University of Southampton

University of Southampton Research Repository

Copyright © and Moral Rights for this thesis and, where applicable, any accompanying data are retained by the author and/or other copyright owners. A copy can be downloaded for personal non-commercial research or study, without prior permission or charge. This thesis and the accompanying data cannot be reproduced or quoted extensively from without first obtaining permission in writing from the copyright holder/s. The content of the thesis and accompanying research data (where applicable) must not be changed in any way or sold commercially in any format or medium without the formal permission of the copyright holder/s.

When referring to this thesis and any accompanying data, full bibliographic details must be given, e.g.

Thesis: Author (Year of Submission) "Full thesis title", University of Southampton, name of the University Faculty or School or Department, PhD Thesis, pagination.

Data: Author (Year) Title. URI [dataset]

University of Southampton

Faculty of Engineering and Physical Sciences

School of Chemistry and Chemical Engineering

Investigating Biological Optical Transparency Windows in the Near and Shortwave Infrared for Diagnosis and Therapy

by

Hiroki Marius Oswald Cook

MPhys

ORCID ID 0009-0003-8984-0021

Thesis for the degree of Doctor of Philosophy

May 2025

University of Southampton

Abstract

Faculty of Engineering and Physical Sciences

School of Chemistry and Chemical Engineering

Doctor of Philosophy

Investigating Biological Optical Transparency Windows in the Near and Shortwave Infrared for Diagnosis and Therapy

by

Hiroki Marius Oswald Cook

Osteoarthritis (OA) is the most common degenerative joint disease and a leading cause of disability worldwide, presenting as the loss of the lubricating and shock absorbing layer of articular cartilage. This results in pain and loss of mobility, and in the absence of definitive cures requires early detection and intervention. Current clinical imaging paradigms fall short and rely on heuristic markers (pain, inflammation), ionising radiation (CT), and/or exogenous contrast (MRI). Radiologically presenting tissue changes are only indicative of advanced and irreversible degradation. Alternatively, vibrational spectroscopy utilising non-ionising near- and shortwave infrared (NIR, SWIR) light offers deep penetration into tissue and label free "chemical fingerprinting". This utilises empirically derived "biological transparency windows" wherein NIR-SWIR light experiences reduced scattering and regions of reduced absorption. Raman scattering and absorption spectroscopy in this range offer potent tools for the detection of OA. Selectively targeting the absorption of certain NIR-SWIR chromophores can also allow for efficient and highly precise photoablation for therapeutic microsurgery applications.

A novel approach for improved detection of OA in human femoral head cartilage by fusing Raman scattering and NIR-SWIR absorption spectral data, termed "spectromics", is explored first. In this proof-of-concept, tissue was classified to high precision under multivariate statistical analysis (100 % class segregation) and supervised machine learning (80% OA, 95% control), where the enhanced spectromics fingerprint consistently outperformed Raman and NIR-SWIR alone. Clinically relevant tissue components were identified through discriminatory spectral features and proposed as OA spectromics biomarkers.

A first demonstration of a novel 3D multimodal hyperspectral scanning system is presented next, with colocalised Raman and NIR-SWIR spectral measurements across the surface of human OA osteochondral samples. The system was proven suitable sensitive to OA associated spectral features and capable to map natural and pathological heterogeneities in 3D, proffered as a platform to further understand the complex effects of OA.

Finally, an advance in NIR-SWIR mediated photoablation is presented demonstrating single-cell scale ablation of human cell samples on a microsurgery system enabled by a nano-second pulsed thulium-doped fibre laser. Precise control of pulse parameters achieved unprecedented precision of 31.3 ± 0.1 µm on onion epidermal and 19.9 ± 0.1 µm on SH-SY5Y cells with such a laser.

The research presented in this thesis focuses on new methodologies for the diagnostic assessment and therapeutic treatment of tissues harnessing the NIR-SWIR optical regime, proposed for paradigm shift in current clinical practices. A general report for concept and delivery of public outreach and science communication activities during my candidature with the Molecular Biophotonics and Imaging group is also included.

Table of Contents

Table of Tables

Table of Tables

Table of Figures

Table of Figures

Table of Figures

Table of Figures

Table of Figures

Research Thesis: Declaration of Authorship

Print name: Hiroki Marius Oswald Cook

Title of thesis: Investigating Biological Optical Transparency Windows in the Near and Shortwave Infrared for Diagnosis and Therapy

I declare that this thesis and the work presented in it are my own and has been generated by me as the result of my own original research.

I confirm that:

1. This work was done wholly or mainly while in candidature for a research degree at this University;
2. Where any part of this thesis has previously been submitted for a degree or any other qualification at this University or any other institution, this has been clearly stated;
3. Where I have consulted the published work of others, this is always clearly attributed;
4. Where I have quoted from the work of others, the source is always given. With the exception of such quotations, this thesis is entirely my own work;
5. I have acknowledged all main sources of help;
6. Where the thesis is based on work done by myself jointly with others, I have made clear exactly what was done by others and what I have contributed myself;
7. Parts of this work have been published as:-

Hiroki Cook, Anna Crisford, Konstantinos Bourdakos, Douglas Dunlop, Richard O. C. Oreffo, and Sumeet Mahajan, *"Holistic vibrational spectromics assessment of human cartilage for osteoarthritis diagnosis*", Biomed. Opt. Express 15, 4264-4280 (2024) [1]

Hiroki Cook, Anna Crisford, Jitendra Nath Acharyya, Konstantinos Bourdakos, Janos Kanczler, Douglas Dunlop, Richard O. C. Oreffo, Sumeet Mahajan, *"Label-free 3D NIR-SWIR "Spectromics" mapping of human hip cartilage for diagnosis of osteoarthritis,"* Proc. SPIE PC13006, Biomedical Spectroscopy, Microscopy, and Imaging III, PC1300605 (2024) [2]

Matthew D. Gerard [†], Hiroki Cook [†], James A. Read, Ibrahim H. Abughazaleh, Panuwat Srisamran, Siddhi Chugh, Sijing Liang, Qiang Fu, Richard O. C. Oreffo, David J. Richardson, Sumeet Mahajan, Lin Xu, *"Single-cell high-precision ablation using nanosecond-pulsed thulium-doped fiber laser,"* Opt. Eng. 63(8) 086102 (2024), [†] Joint First Authors [3]

Signature: ..... Date:

Acknowledgements

"Squiggly lines can tell you if you are diseased"

– Wren, aged 12, wise science festival attendee

First and foremost, with heartfelt thanks to my project supervisors Professor Sumeet Mahajan and Professor Richard OC Oreffo for their steady guidance and inspiring example throughout this project. You have taught me, through consistent practice, "doing your best and forgetting the rest", the vital importance of collaboration, and living out science as the "highest form of creative art".

I would like to acknowledge, particularly, contribution to this project from:

Dr George Devitt for tutorials in IRootLab software

Dr Anna Crisford for retrieval and Raman measurements of human articular cartilage slices employed in the spectromics study

Dr James Read for all things cell culture

Dr Janos Kanczler for the retrieval and preparation of human femoral head tissues

Dr Jacob Trend for tutorials in PolyCam and Dragonfly software (and in building a wardrobe entirely from UniQlo)

Dr Simon Lane for early advice in Python software development and tutorials in 3D CAD, 3D printing and laser cutting (and the virtue of general handyman-ery)

Dr Niall Hanrahan for help in taming the Raman microscope

Matthew Gerard for close collaboration and discussion in the photoablation studies

Ibrahim Abughazaleh for help in autofocusing ventures

I would also like to acknowledge members and collaborators from the EPSRC Transformative Healthcare "InLightenUs" team from the University of Southampton, University of Edinburgh, University of Nottingham, and now Queen Mary University, whose drive for interdisciplinary excellence has been a source of great motivation and a lot of fun science. This includes special thanks to InLightenUs team members:

Dr Anna Crisford for her kind support and indomitable optimism

Dr Kostas Bourdakos for his formative technical advice and clandestine discussions on cool physics

Siddhi “Behena” Chugh and the ORC crew; Ibrahim Abughazaleh, Matthew Gerard, Panuwat Srisamran, Dr Lin Xu, and Prof. David Richardson

Shufan Yang for teaching me the alchemical joys of light roasted coffee

Tommy Loan, Fizza Haseeb, and Janet Kok, who also started this journey with me

I would like to thank the wider Molecular Biophotonics and Imaging group, now past and present. It has been a privilege to work with such talented friends.

With special thanks also to

Dr Peter Johnson, Dr Adam Lister, Dr Niall Hanrahan, and Dr Simon Lane for their advice and support on any and all topics, particularly during a difficult start under lockdowns and beyond.

The original weenies: Jake Kleboe whose heart is as warm as his record-breaking banana breads and Dr Belle Creith who has become my mum’s favourite honorary niece

Lysanne Michels and Theo Hornsey who know what they did

Fiona Haigh, Yoshiki Cook, and Andrew Rawlings: “tabula ludus” is all I am permitted to say

The Rockstone graduates Jonny Reid, Dion George, Dr Maria Elena Vilar Alvarez, Euan Sargent, Ray Kinsella, Yuan Zheng, and Navya Sara Shine

Emiliana, Yadira, Valentina, Issy, a powerhouse of sisters

Finally, my utmost gratitude and appreciation to Joanne Graham and to my family: your love, humour and encouragement sustain me, and inspire me to be a better man.

In loving memory of Augustine Cook

Definitions and Abbreviations

AA..... Ablation Area

AC ..... Articular Cartilage

AE..... Ablation Efficiency

API..... Application Programming Interface

AO ..... Adaptive Optics

BMD ..... Bone Mineral Density

BS..... Beam Splitter

CARS ..... Coherent Anti-Stokes Raman Scattering

CCD ..... Charge-Coupled Device

CLSM..... Confocal Laser Scanned Microscopy

CMOS..... Complementary Metal–Oxide–Semiconductor

CSV ..... Comma-Separated Values

CT..... [X-Ray] Computed Tomography

CW ..... Continuous Wave

DBMS ..... Difference Between Mean Spectra

DCLS ..... Direct Classical Least Squares Component Analysis

DM..... Dichroic Mirror

DMEM..... Dulbecco's Modified Eagle's Medium

DMM..... Deformable Membrane Mirror

DNA..... Deoxyribonucleic acid

DZ..... Deep Zone

ECM..... Extracellular Matrix

Er:YAG ..... Erbium-doped Yttrium Aluminium Garnet

EVLA..... Endovenous Laser Ablation

EYFL ..... Erbium-Ytterbium Fibre Laser

FBS..... Fetal Bovine Serum

FFS ..... Feature Forward Selection

FN ..... False Negative

FP ..... False Positive

FT ..... Fourier Transform

FWHM..... Full Width at Half Maximum

GAG ..... Glycosaminoglycan

GUI ..... Graphical User Interface

Hb ..... Haemoglobin

HbO_2..... Oxygenated Haemoglobin

HCA..... Hierarchical Cluster Analysis

Ho:YAG ..... Holium-doped Yttrium Aluminium Garnet

HWP ..... Half Wave Plate

IfLS ..... Institute for Life Sciences

InGaAs..... Indium Gallium Arsenide

IR..... Infrared

KMC..... K-Means Clustering

LD..... Linear Discriminant

LDA..... Linear Discriminant Analysis

LMA ..... Large Mode Area

LP ..... Long Pass

MAA..... Mechanically Altered Area

MCR ..... Multivariate Cluster Resolution

MIR ..... Mid Infrared

ML ..... Machine Learning

MOPA ..... Master Oscillator Power Amplifier

MPM ..... Multiphoton Microscopy

MRI ..... Magnetic Resonance Imaging

MZ ..... Middle Zone

NA ..... Numerical Aperture

ND ..... Neutral Density

NADH ..... Nicotinamide Adenine Dinucleotide Hydrogen

Nd:YAG ..... Neodymium-doped Yttrium Aluminium Garnet

NIR ..... Near Infrared

OA ..... Osteoarthritis

OCT ..... Optical Coherence Tomography

OP ..... Osteoporosis

ORC ..... Optoelectronics Research Centre

PB ..... Polarisation Beam Splitter

PBS ..... Phosphate Buffer Solution

PC ..... Principal Component

PCA ..... Principal Component Analysis

PFA ..... Paraformaldehyde

PG ..... Proteoglycan

PLA ..... Polylactic Acid

PLS ..... Partial Least Squares

PLSDA ..... Partial Least Squares Discriminant Analysis

PS-OCT ..... Polarisation Sensitive Optical Coherence Tomography

QUS ..... Quantitative Ultrasonography

QWP ..... Quarter Wave Plate

SBS ..... Stimulated Brillouin Scattering

SDK ..... Software Development Kit

SERS ..... Surface Enhanced Raman Spectroscopy

sGAG ..... Sulphated Glycosaminoglycan

SHG ..... Second Harmonic Generation

SIF ..... Standard Interchange Format

SNR ..... Signal to Noise Ratio

SORS ..... Spatially Offset Raman Spectroscopy

S-OCT ..... Spectroscopic Optical Coherence Tomography

SP ..... Short Pass

SPM ..... Spherical Parallel Manipulator

SVM ..... Support Vector Machine

SWIR..... Shortwave Infrared

SZ ..... Superficial Zone

TAA ..... Thermally Altered Area

TDF ..... Thulium Doped Fibre

TDFL ..... Thulium Doped Fibre Laser

TEC..... Thermoelectric Cooler

THA..... Total Hip Arthroplasty

Ti:S ..... Titanium:Sapphire

TKA ..... Total Knee Arthroplasty

TP ..... True Positive

TPF ..... Two Photon Fluorescence

TRL ..... Technology Readiness Level

TN..... True Negative

UV ..... Ultraviolet

WDM ..... Wavelength Division Multiplexer

Chapter 1 Introduction

Non-invasive assessment of the body from the outside has marked a paradigm shift in the diagnostic capability of modern medicine. Generational development of clinical imaging technologies (x-ray, CT, MRI, ultrasound) and their derivatives provide a repertoire of techniques that form an integral part of clinical practice. However, each of these established modalities have their limitations, including exposure to ionising radiation, reliance on exogenous contrast agents, and low spatial and temporal resolution.[4] Repeated exposure to ionising radiation carries risk of carcinogenesis, and contrast dyes employed for non-ionising MRI scans risk induced nephropathy for patients with impaired renal capacity or deposition of rare earth metals in the body. [5–9]

Osteoarthritis (OA) is a leading cause of disability world-wide, presenting as loss of the lubricating and shock-absorbing layer of articular cartilage within joints. A degenerative disease, OA leads to increased pain and loss of mobility, an overall decrease in quality of life, and presents a growing pressure on health care systems for increasingly aging populations. [10,11] OA diagnosis under the conventional modalities falls short due to reliance on detection of radiographically presenting changes in tissue morphology, insensitive to fine soft tissue changes, and on heuristic markers such as pain, indicators of advanced stage degradation. With no definitive cure, early detection is vital for effective intervention (surgical procedures such as femoral head reshaping) or symptom management (lifestyle change, pharmaceuticals).

Optical approaches combat some such limitations through use of relatively benign, non-ionising radiation, capacity for subcellular resolution, and “chemical fingerprinting” through spectroscopy. These facilitate highly detailed interrogation for tissue composition assessment and in diagnostic applications. Typical operating wavelengths in the visible and UV regimes are non-ionising lending themselves to patient friendly paradigms, however, photon scattering and absorption may limit spatial resolution and depth of penetration. Thus, destructive *ex vivo* approaches may be employed including biopsies and histochemical assays with significant patient inconvenience.

Alternatively, techniques operating in the Near- and Shortwave Infrared (NIR, SWIR) regimes benefit from reduced scattering and from reduced absorption in certain ranges, characterised empirically as “biological transparency windows”. [12–14] Label free vibrational spectroscopy approaches utilising NIR-SWIR light can elucidate rich and clinically relevant endogenous chemometric information. Exploiting the biological transparency windows can allow for deeper interrogation into tissue to highlight inherent differences in optical absorptions and scattering

caused by diseases such as OA. Detection and monitoring of chemical precursors to OA or prepathomorphological changes otherwise invisible to radiographic assessment approaches would prove highly valuable for patient care.

Further exploiting the NIR-SWIR regime, absorption chromophores inherent to biological tissue may be utilised for efficient photoablation. Water has its highest absorptions in the NIR-SWIR range, common to all tissue *in vivo*, and capable of efficient energy transfer to tissue. Exposure under finely tuned laser pulse characteristics could control the precision of photodamage and/or incisions into tissue for microsurgical applications. Increased precision of such therapies reduces risk of recurrence (such as in cancer treatment) or revision surgery, and reduction of collateral damage improves recovery times and patient quality of life.

This thesis is presented in a three-paper format with supporting background and theory first delivered in Chapter 2. This includes discussion of the current clinical paradigms for diagnosis of OA and their respective shortcomings, and how vibrational spectroscopy may offer a suitable alternative in the clinic. The light-matter interactions for assessment of tissue are laid out, including empirical and theoretical foundations for the NIR-SWIR windows and vibrational spectroscopy techniques used in this project. Finally, current approaches for clinical photoablation are described as well as theoretical foundation in strategies for precise thermolysis.

In Chapter 3, a comprehensive review is carried out for the literature surrounding NIR-SWIR absorption and Raman scattering spectral characterisation of osteoarthritic articular cartilage, including spectral acquisition and data analysis approaches, clinical viability, and the call for new techniques in this area. Also, a review of the state-of-the-art in photoablation approaches will be carried out, considering established approaches within the clinic and new contenders enabled by emerging laser technologies. This will serve to highlight the importance of advances in NIR-SWIR technologies, and inform the overarching hypotheses and objectives interrogated by this thesis, detailed in Chapter 4.

Chapter 5 presents results of a novel approach for data fusion of Raman scattering and NIR-SWIR absorption spectra, dubbed “spectromics”. This is applied to the assessment of human articular cartilage tissues resulting from total hip arthroplasties of patients with osteoarthritis (diseased tissue) and osteoporosis (control tissue). Multivariate statistical analysis and supervised machine learning methods are applied to assess classification performance of and probe the information contained within the spectromics fingerprint.

Chapter 6 details the construction and development of a spectromics 3D mapping system capable of co-localised Raman scattering and NIR-SWIR absorption measurements. The

system will be tested for its capacity to detect pathological heterogeneities across human joint tissues, and to further biological and medical understanding of the complex effects of OA.

Precise photoablation utilising the 1.95 μm water absorption peak is explored in Chapter 7. This work investigates whether fine control of laser pulse characteristics could allow for efficient photoablation with minimal collateral damage on human cell samples, employing a microsurgical system constructed around an in-house ns-pulsed thulium-doped fibre laser (TDFL).

Finally, Chapter 8 presents a general report of the public engagement and science communication activities carried out over the course of my candidature with the Molecular Biophotonics and Imaging group. In particular, the concepts and delivery of the “From Mars to Humans” activity for which I was a key developer and its delivery to the public as part of the Royal Society Summer Science Exhibition in 2023. The elements of the interactive stand, attitudes for public engagement, and some gathered audience response data will be described.

The approaches described in this thesis help to advance and improve contemporary practice in NIR-SWIR vibrational spectroscopy assessment of OA and in efficient and precise NIR-SWIR mediated photo-ablation. Ultimately, these advancements hope to provide the foundation for improved patient outcomes through accurate diagnosis and understanding of OA, and for more effective therapeutic interventions through microsurgery.

Chapter 2 Background & Theory

2.1 Current Clinical Paradigms for OA Diagnosis

The following seeks to contextualize and establish motivation for new approaches for the diagnosis of osteoarthritis under NIR-SWIR vibrational spectroscopy – the state of the art in practice and a vision for diagnosis in the future.

Osteoarthritis (OA) is a degenerative joint disease leading to the loss of the shock absorbing and lubricating inter joint layer of articular cartilage. This leads to pain and loss of mobility and is a leading cause of disability world-wide. OA affects one third of people over the age of 46 in the UK, where it is the primary cause of 90% of hip replacement surgeries, and affects approximately 28% of the global population over 60 years old.[10] OA presents a major public health challenge recognised as a serious burden for the individuals affected, healthcare systems, and national and global socioeconomic costs.[10,11]

Cartilage is susceptible to degenerative joint conditions due to its weak repair capacity, attributed to its lack of vascular, neural, and lymphatic networks.[15] OA is characterised by a damaged collagen network, loss of proteoglycan starting at the surface, and increase in water content. This will often result in the fibrillation, thinning or even dissolution and fragmentation of articular cartilage, reduced elasticity, decrease in joint lubricity, and present as debilitating and painful symptoms.[16–21]

There is currently no definitive cure, with treatments favouring lifestyle and diet changes as preventative or maintaining responses. Catching the disease in the elusive pre-OA stage, some argue, can maximise the efficacy of available pharmacological interventions before relying on diseases tissue removal in total hip or knee arthroplasty (THA, TKA). [22] Reliance on prosthetic implant is then subject to limitations such as bleeding, infection, longevity of implants and as such higher morbidity in older patients. Current diagnosis depends on heuristic markers such as pain or radiologically presenting structural changes to assess the severity of OA disease progression, such as inter-joint space narrowing between skeletal tissue (radiopaque) implicative of cartilage thinning and thus degradation. OA diagnosis may rely on a number of clinical imaging paradigms, each with their own shortcomings, summarized in the table below:

Table 2.1 Comparative summary of the traditional imaging methods employed in osteoarthritis (OA) treatment pathways

Modality	Main Inspection Site	Advantages	Disadvantages
X-ray	Joint appearance [21]	Low cost, high benefit, combined with arthroscopy to assist doctors in diagnosis [21]	Unable to show early symptoms of OA [21]
CT	Intra-articular structures, dye mediated for soft tissue contrast [23]	Potentially sub-micron precision [23] Quantitative GAG content assays, correlate with MRI [23]	Unable to show early symptoms of OA without dyes [23]
MRI	Structure of cartilage	Observe structural features related to cartilage integrity, no ionisation [21] Quantitative sGAG content assays [19]	Expensive, long scan time Heavy element exogenous contrast agents [21,24]
Quantitative Ultrasound	Periarticular soft tissue[21] Inter-articular arthroscopic probes [23]	Visible image information, low cost[21] Sensitive to scattering from chondrocytes and collagen[23]	Poor penetration of bone, poor reproducibility (user and patient) [21]

X-ray imaging today is a cornerstone of clinical diagnosis: widely available, comparatively inexpensive, relatively low in ionising radiation dosage, and simple to interpret. [25–27] Through-body imaging offers clinicians direct visual assessment of structural changes associated with orthopaedic diseases rather than rely on indirect symptomatic signs such as joint pain and swelling.[24] Images are formed from the projection of all radiopaque objects in the x-ray's path, with inherent loss of depth information and requiring exposure to ionising radiation. Typical images are unable to delineate soft tissue detail without introducing radiopaque contrast media [25] X-ray utility in orthopaedic application is somewhat limited since indicative radiological features for OA (joint-space thinning, spurs) will appear only at very late stages of the disease and some densitometric studies for assessing osteoporosis are unsuitable for children. [27,28]

Computed tomography (CT) offers capacity for reconstruction of 3D images from x-rays. [25] Overlapping of tissues, which can obfuscate 2D radiographs, is eliminated and image contrast not overwhelmed by x-ray absorption by the skeleton. This enables clinicians to clearly distinguish internal structures of the body including enhanced visualisation of soft tissues for morphological assessment, aiding diagnosis.[25] Material studies can also be made via measurements of radiolucency to indicate tissue densities, but again rely on ionising radiation, typically at higher dosage than for simple 2D x-ray.[27] Microscale spatial resolution can be achieved through combination of higher X-ray intensities and longer exposure times (micro-CT)

though require prolonged scanning times (children may require sedation) and high radiation dosages to achieve good signal to noise resolution. [25] Mitigating the effects of damaging radiation can be cumbersome and inhibit treatment planning, incentivising rapid and non-ionising methods for assessing orthopaedic tissues.

Magnetic resonance imaging (MRI) employs the intrinsic spin characteristics of different tissue species to generate imaging contrast. Morphological imaging of soft (such as cartilage) and hard (such as bone) tissues can occur again for joint space narrowing assessment or some limited macromolecule assessment but lacks high spatial and temporal resolution. [29–31] Semi-quantitative scoring methods have been developed, which incorporate a range of OA features within MRI images such as cartilage signal and morphology, cysts, bone attrition, osteophytes etc. shown to correlate with gold-standard radiographic scoring (Kellgren-Lawrence, KL).[32,33] However, these prove expensive in time, money, and personnel, and lack specific chemical analysis.[34] Some tissue composition studies often necessitate intravenous or intra-articular administered contrast agents, for example exogenous gadolinium compounds for quantification of glycosaminoglycan (GAG) as an indicator of cartilage health in OA patients.[19] This may be prohibitive to patients with impaired renal function and can lead to unwanted retention of heavy metals. [6]

Quantitative ultrasonography (QUS) offers non-ionising subsurface imaging with contrast capable of delineating interfaces of tissue with different acoustic densities.[28] Functional real time measurements can observe soft tissue movements and vascularity such as blood flow velocities. Signal is captured *via* use of non-invasive, skin contact transducers to interrogate tissue at depth. However, compromise is made between use of shorter wavelengths that may describe fine detail (up to 20 MHz) and longer wavelengths that penetrate deeper into tissue.[35] Standardised protocols have been proposed benefiting from dynamic imaging to assess inflammatory changes in OA, as well as observations of osteophytes and cartilage, correlating with KL and pain scoring.[34,36] However such methods are proposed as supplementary to standard radiographic assessment, and rely again on morphological assessment without quantifiable measure of tissue composition.

Thus, commonly used methods are often time-consuming, expensive, employ ionising radiation, or destructive assays, and as such may not be considered patient friendly.[21] Additionally these methods are limited in spatial resolution and likely to underdiagnose microscopic cartilage damage. [23] Techniques employing light in the optical ranges may instead offer assessment of cartilage under non-ionising radiation (visible to infrared wavelengths) and with capacity for microscale resolution.

Optical Coherence Tomography (OCT) produces cross-sectional subsurface images into tissue, non-invasively, under broadband visible or near infrared illumination. This is directly analogous to B-mode clinical ultrasound, though with significantly higher spatial resolution (2 – 10 um, rather than 10 – 100 um), and shallower imaging depths (1 – 2 mm, compared to 10 – 100 mm). [37,38] OCT image contrast is produced through Michelson interferometry of back-reflected light at interfaces between tissue layers with differing refractive indices, offering microscale morphological and structural assessment. First reported in 1991 by Huang et al., OCT is currently only a routine clinical choice for ophthalmic measurements (e.g. retinal layer structure) [39,40] but has seen active preclinical research as a tool for detecting microstructural irregularities associated with early OA. [37]

Polarisation-sensitive OCT (PS-OCT) imaging has shown particular promise, offering sensitivity to collagen matrix organisation (birefringence patterning) which may be interrupted or lost in early OA [37,41] or associated with potentially reversible metabolic changes. [38] PS-OCT via a handheld endocatheter has demonstrated feasibility for intraoperative use (such as during arthroscopy) [42] and proven sensitive to pre-OA structural changes missed by MRI in a pilot study with 2.5 year follow up. [43] That said, depth of penetration is limited to imaging only the superficial layers of cartilage and no indication of the highly scattering underlying bone. [37]

Spectroscopic OCT (S-OCT), a post-processing technique performed on OCT interferograms [44] may yield limited chemical information about tissue, demonstrated particularly for optical blood oximetry. [44,45] However, to capture high spectral resolution sacrifices depth (axial) resolution, due to the fundamental limits of the Fourier transform. Instead, the most indicative approaches have leveraged Raman scattering spectroscopy to supplement OCT analyses by revealing chemical differences (molecular vibrations). [46,47] Ran et al. propose surface enhanced Raman spectroscopy (SERS) to provide further diagnostic judgement criteria to OCT images and improve reliability of OA disease detection in cartilage. [46] But it is noteworthy that SERS would rely on contrast enhancing agents (e.g. gold nanoparticles) whereas an ideal detection paradigm would be carried out “label free”.

Vibrational spectroscopy operating in the NIR-SWIR holds great capacity for label free interrogation of articular cartilage, capable of answering the urgent need for rapid, non-destructive methods for diagnosis.[21]

Raman scattering and NIR-SWIR absorption spectroscopic techniques are sensitive to the physiological and biomechanical properties of articular cartilage, able to predict to a high degree of accuracy characteristics such as biochemical content, thickness, and clinical scoring of OA severity.[20,21,48–51] The main characteristics are identified in the table below.

Table 2.2 Comparative summary of the application of Raman scattering and NIR-SWIR absorption spectroscopy for assessment of osteoarthritis. Adapted from Yu et al, in adherence to CC BY.[21]

	Working Principle	**Advantages**	**Disadvantages**	**Application in OA**
NIR-SWIR absorption	Reflects overtones and/or combination bands of stretching and bending vibrations of C–H, N–H, and O–H bonds ranging 4000–12500 cm^{-1}	Fast, accurate, non-destructive, labour-saving	Wide band, high spectral overlap, difficult to distinguish characteristic peak	High penetration depth for a full spectral signal of the cartilage
Spontaneous Raman scattering	Reflects vibrational information between molecules based on the principle of Raman scattering	Weak water signal, fast, simple, reflects biological signal	Raman scattering area can be affected by fluorescence interference	Reflects physiological changes of OA at tissue, cell, and molecular levels

Thus, these techniques have capacity to show changes in the early stages of OA wherein cartilage deformities manifest as complex changes in the extracellular matrix (ECM), GAG, moisture and collagen. [21] Indeed, Hofmann et al. report that when comparing degree of accuracy for techniques including arthroscopy, OCT, MRI, and NIR spectroscopy for early OA markers, only NIR spectroscopy showed good correlation with the Knee Injury and Osteoarthritis Outcome Score (KOOS).[21]

2.1.1 Optical Interrogation of Tissue Can Detect OA

Articular cartilage lines the subchondral bone in diarthrodial joints to provide frictionless motion and shock absorbance, composed primarily of type-II collagen, proteoglycans (PG), chondrocytes, and water.[20] The extracellular matrix (ECM) makes up the bulk of articular cartilage (>95% by volume), itself consisting of collagen fibrils (two thirds of dry cartilage mass), non-collagenous proteins including PG, and a sparse population of chondrocytes (only 1–5% volume). [19,50,52,53] Collagen fibrils provide tensile strength and shear stiffness of the tissue (structural, 3D framework) and PG provide compressive stiffness. [20,50]

Cartilage PGs account for 5–10 % of the dry mass of articular cartilage, mainly consisting of aggrecans, themselves containing negatively charged glycosaminoglycan (GAG) side chains which attract free ions and water into the tissue ECM. [50] In healthy cartilage, hydrophilic PG macromolecules swell to put the collagen network under intrinsic tension.[19,20,50] Water accounts

for over 70–80% of normal hyaline cartilage and offers shock absorbance during loading, lubrication, and transport of nutrients. [20,21,50]

Zonal organisation with respect to depth means water and collagen content are greatest at the surface and decrease to lowest in the deeper zone, PG and aggregan content is lowest at the surface and higher in deeper zones. [18–20] Toward the cartilage to subcortical bone junction collagen transitions gradually in orientation from parallel to the articular cartilage surface, to random orientation, to perpendicular to the surface. [20,54] The superficial zone (SZ), middle zone (MZ), deep zone (DZ), and calcified zones demarcate and describe regions with varying collagen fibre orientation and composition. [18,53,54] Collagen fibres have been noted with angular orientations 0 − 15° in SZ , 15 − 45° in MZ, and 45 − 90° in DZ, illustrated in Figure 2.1.[15]

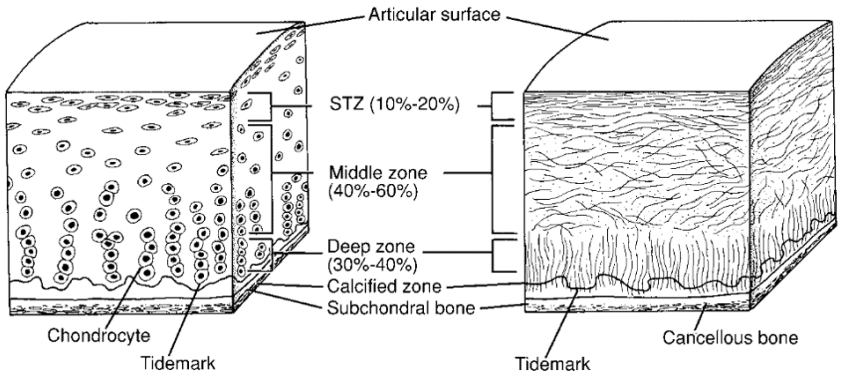

Figure 2.1 Cross-sectional diagram showing the three salient zones of articular cartilage, namely superficial tangential zone (STZ), middle zone, and deep zone. The tidemark represents the interface between calcified- and non-calcified cartilage, and below that is subchondral bone. Left: Chondrocyte organisation; Right: Collagen fibre architecture. Adapted from Buckwalter *et al*.[54] Reproduced with permission from Wolters Kluwer.

NIR- SWIR absorption spectroscopy directly interrogates harmonics of vibrational modes of tissue, sensitive to relevant moieties such as bound and free water, and overtones of C-H and O-H stretching associated with collagen and proteoglycans. [20,50] Intrinsic chemical information of tissue can be obtained, label-free, and has been demonstrated for assessment of degenerative disease in cartilage.[16,17,48,55]

Spontaneous Raman scattering spectroscopy interrogates vibrational modes of molecules to extract chemical information indicative of the constituent tissue moieties. The “fingerprint” region, Raman shifts between 800 – 1800 cm^{-1}, is particularly rich in biochemical information and, crucially, insensitive to water, ideal for characterisation of connective tissues.[49,56]

Overall, label-free assessment in the NIR and SWIR offers significant promise to enable clinically significant interrogation of cartilage tissue to assess disease state.[20,21,49,51] Strategies to date will be explored in Chapter 3.

2.1.2 Spectroscopic Tools in the Clinic

Spectroscopic techniques have long been adopted into the clinical pathways for diagnosis and patient assessment but in an arguably more hidden role than the conventional modalities identified above. Nevertheless, maturity of these optical techniques including miniaturisation of gratings, detectors, sources, and efficient processing has resulted in desktop and newly developing theatre-operated instruments for rapid and user-friendly sample assessment.

Plate readers and fluorescent analysers are a mainstay of many preclinical pathways and biopsy sampling protocols rely typically on UV-visible spectroscopy. This highlights the general agnosticism of excised tissues and other *ex vivo* medical analytes to whichever optical wavelengths may be used to interrogate. Depth of penetration or patient exposure to radiation is of no concern, and samples may be cut to shape (histology, cores) for use with standard mountings in commercial instruments. Such instruments play a vital part of healthcare pathways but may not assess live intact tissue, may rely on fluorescence mechanisms (limiting sensitivity for some chemical interrogations), or use exogenous markers (limiting applicability to biological systems).

NIR-SWIR techniques, by contrast, offer direct interrogation of endogenous chemical vibrations for label free, and largely non-perturbative assessment of biological tissue. Pulse oximetry is a prevalent example of NIR spectroscopy utilised for live, non-invasive assessment of tissue, and thus of patient health. Here, the differential absorption of oxygenated and deoxygenated haemoglobin can be assessed with only benign NIR light and is regarded a gold standard for medicine, from first response to on-ward monitoring. Pulse oximetry may be safely attributed to the saving of a vast number of lives in the 90 years since its inception, prominent recently in the treatment of COVID-19, and will continue to do so.[57]

Wider implementation of spectroscopic techniques in clinical practice is still in its infancy but promises a repertoire of potent and sensitive tools. A recent review from Kim et al. graded emerging probe based spectroscopic techniques by their technology readiness level (TRL) to be in the hand of a physician in theatre. Their meta-analysis categorized feasible *in vivo* techniques that have matured beyond the initial conceptualization (TRL ≥ 3), toward preliminary lab/animal models (TRLs 3-4), to multi-centre clinical trials (TRLs 5-7), to a marketed/distributed product (TRL 8-9). Minimally invasive applications of fluorescence spectroscopy were between TRLs 5-9,

though most still needing to prove clinical feasibility, and almost all ahead of similar Raman spectroscopic attempts with TRLs 3-7. [58]

There is promising trajectory for harnessing the potent and informative capacities of Raman scattering and NIR-SWIR absorption spectroscopic tools for the treatment of patients. Recent endeavors for the sensitive appraisal of OA in connective tissues will continue to be explored in Chapter 3.

The work detailed here is motivated by clinical, point-of-care applications of NIR-SWIR techniques conducive to patient friendly (benign radiation, label free, minimally invasive) assessment of tissue. This may be envisioned as a sensitive, multimodal handheld probe capable of microscale chemical fingerprinting, ideally able to assess tissue *in vivo* and at depth, entirely non-invasively. NIR-SWIR light is the most promising candidate for such a task, and as such it is incumbent upon new developments in this area to prove capacity to detect disease in tissue (by assessing molecular vibrations) whilst optimising capacity for deep tissue penetration (through optical transparency windows).

Depth penetrations of light into tissue up to 5 mm within the NIR-SWIR range describe particular suitability for optical assessment of cartilage tissue.[18,51] The goal herein is to utilise the native NIR-SWIR transparency windows to extract valuable chemical information for non-invasive, diagnostic appraisal.

2.2 Light-Matter Interactions for Tissue Assessment

2.2.1 Optical Windows in Biological Tissue Allow Deep Interrogation

For imaging of deep tissues, there are two broad approaches: “inside out” where samples are artificially excised from deep within tissue and imaged *ex vivo,* or “outside in” where tissue is imaged natively *in vivo*. “Inside out” approaches are wavelength agnostic and as such compatible with most optical imaging modalities. Morphological imaging of structures from within deep tissue are achieved with chemical fixing and histological analysis, but functional assessment of living tissues would require preservation of physiological conditions *in situ*. [59] “Outside in” approaches may involve removing obscuring biological layers such as skin and bone in craniotomy (hugely invasive) or insertion of fibre probes such as in endoscopy or arthroscopy (minimally invasive). For example, in most animal neurology models to date, long term *in vivo* optical monitoring is enabled through artificial thinning of the skull or installation of chronic cranial windows. The scattering effect of the skull and soft tissue on excitation and emission reduces spatial resolution prompting the destructive procedure. [60]

The idealised “outside in” approach, however, is non-destructive - without removal of any endogenous or introduction of any exogenous material, to avoid interruption of the natural vital system. Thus the vision is for entirely non-perturbative, *in vivo,* compositional, and functional assessment of the body from outside.[61] For non-ionising optical wavelengths to penetrate deeply, thought must go into the wavelength dependent transmission of tissue layers. Depth limits may be geometric, determined by the numerical aperture (NA) and working distance of a focusing lens, or more fundamental through attenuation of light in absorption, scattering, and/or wavefront distortion.[4]

The transparency windows thus far alluded to may be empirically defined by tissue type (particular and relative compositions of chromophores) but follow general trends. Light interacting with turbid biological media experiences reduced scattering with increasing incident wavelength, observing a power law model defined by theory from Mie and Rayleigh.[62,63] When extending from the UV to visible to NIR-SWIR, reduction in the scattering coefficient causes absorption to be the main determinant in focusing quality (image formation, spectroscopic interrogation etc).[64]

In various native tissues there exist continuous wavelength regions in the NIR and SWIR regime for which light experiences significantly minimised absorption. The so-called transparency windows are categorised in four distinct ranges termed

- NIR-I (~650 – 1000nm);
- NIR-II (~1000 – 1350 nm);
- NIR-III or SWIR-I (~1550 – 1870 nm);
- and SWIR-II (~2100 – 2350 nm),

displayed in Figure 2.2.[12] The 1980’s saw first characterisation of NIR-I as “the” diagnostic and therapeutic optical window, and which has since facilitated non-invasive optical bioimaging of small animals and for image guided phototherapy and drug delivery.[12,65]

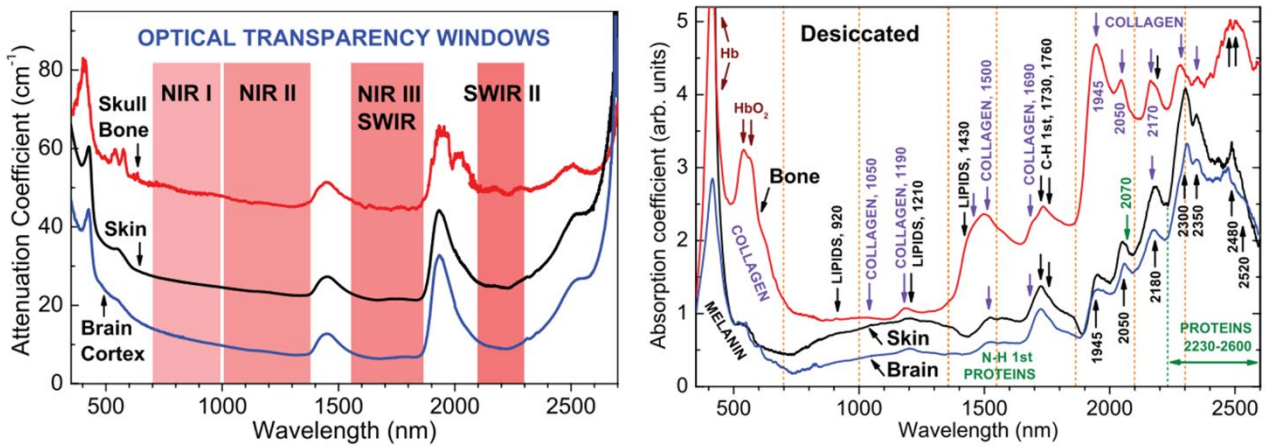

Figure 2.2 Absorption in Near Infrared and Shortwave Infrared optical windows characterised for mouse skull bone, skin, and brain cortex tissue. (Left) Optical windows with high transparency (low attenuation coefficient) are highlighted, (Right) Peaks in absorption coefficient associated with key chromophores in biological tissue are labelled. Modified from Golovynskyi et al.[12] Reproduced with permission from John Wiley & Sons.

These empirically derived windows consider the cumulative effect of wavelength dependent scattering and absorption by moieties common in native tissue, such as attenuation by water and blood. Wilson et al. identified notable biological absorptions in the region ~1.1 – 2.5 μm including water peaks at ~1150, 1450, 1900 nm; lipids at ~1040, 1200, 1400, 1700 nm; and collagen protein at ~1200, 1500 nm.[62] Sordillo et al. also report absorbance by collagen protein in the optical windows is highest and second highest in SWIR-II and SWIR-I, respectively. [65]

Working around known absorbing chromophores within the NIR and SWIR windows can allow for improved penetrative performance, but also hold inherently informative biomarkers of the target tissue .[12,66] For example, haemoglobin absorption *in vivo* in the visible-NIR (420, 540, 577 nm) is greatly reduced within the SWIR regime, whilst absorption of water and lipids increases from NIR to SWIR.[62] This indicates an enhanced sensitivity to spectral features of water and lipids which may be used as metrics of atherosclerosis plaque and breast cancers, unencumbered by presence of blood.[62]

Figure 2.3 describes the typical optical densities across the visible to NIR-SWIR regimes for soft tissues, here benign and malignant human breast and prostate, from which the transparency windows may be identified between the major water absorption peaks.[13] Excised tissue would be characterised with an integrating sphere (diffuse and collimated, transmittance and reflectance) or within commercially available spectrophotometers. Optical parameters including attenuation lengths, absorption, and scattering coefficients, may be quantified, suitable for planning and simulation of approaches reliant on NIR-SWIR light penetration. [12,13,65]

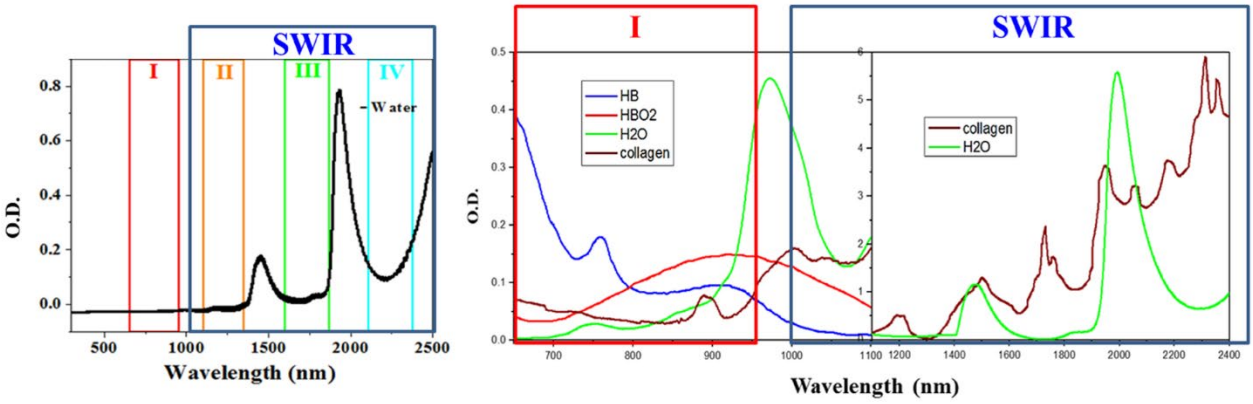

Figure 2.3 Characterisation of wavelength dependent absorption in key biological chromophores in tissue highlighting water, collagen, haemoglobin (Hb) and oxygenated haemoglobin (HbO_2). Notable reduction in water absorption is demarcated to regions 1550 – 1870 and 2100 – 2350 nm, defining the NIR-III or SWIR-I, and SWIR-II transparency windows, respectively. Modified from Sordillo et al.[13] Reproduced with permission from SPIE.

Light may be scattered in native tissues due to an abrupt change of refractive index on small length scales from sub-micron particles, lipid droplets, protein assemblies, etc. and/or longer scale variation in turbid media. Optical pulse propagation in highly scattering turbid medium may be categorised into ballistic and diffusive photon components. [58,64]

Biological turbid media may be modelled as spherical particles embedded and distributed heterogeneously in a non-absorbing host medium of constant refractive index. [67] More detailed modelling may consider influence from the host medium with a continuous fluctuation in refractive index with interspersed scattering structures (plum pudding model). [68] The scattering coefficient, μ_s, has spectral dependency

$$\mu_s(\lambda) = \alpha \cdot \lambda^{-\omega} + b \cdot \lambda^{-4}$$

where α and b are the fractional concentration of scattering particles in the media, large particles described by α contributing to Mie scattering and b to Rayleigh. The parameter ω varies with particle size and assumes Mie scattering makes the larger contribution for longer wavelengths and Rayleigh for shorter wavelengths.[12]

The optical transparency windows consider the cumulative effect of scattering and absorption acting on incident light. The attenuation of ballistic photons through turbid medium of length L is estimated as

$$I_b = I_i \exp\left[-\left(\frac{L}{l_a} + \frac{L}{l_s}\right)\right]$$

where l_a is absorption length or distance a photon travels before being absorbed, l_s the scattering mean free path or mean distance between consecutive scattering events, I_i the intensity of the incident beam, and I_b ballistic beam intensity. The absorption and scattering coefficients are determined as $l_a = \mu_a^{-1}$ and $l_s = \mu_s^{-1}$, respectively. The total attenuation coefficient can then be formulated as $\mu_T = \frac{1}{l_a} + \frac{1}{l_s} = \frac{1}{l_T}$, where l_T is the total attenuation length.[4]

The transport mean free path is the distance beyond which a photon is fully randomised from its original direction of motion having encountered numerous scattering events,

$$< l_{tr} >= \Sigma l_s \hat{n} = \frac{l_s}{1-g}$$

where $\hat{n}$ represents the vector displacement of the photon within the turbid media and g the anisotropy factor defined as $< \cos\theta >$, where θ is the scattering angle. From this is defined the reduced scattering coefficient, $\mu_s' = \mu_s(1-g) = (l_{tr})^{-1}$. In regions where absorption is comparable to or greater than scattering multiply scattered photons are selectively attenuated, while ballistic and near-ballistic photons survive. Yoo et al. offer this as rationale for using any wavelength where $\mu_s \geq \mu_s'$ to allow for deep photon penetration.[4,66]

The values for μ_a, μ_s', and g are of particular interest since these may be adopted in simulation models of photon propagation (e.g. Monte Carlo describing multiple scattering events) or in development of optical phantoms, both to inform the design of new optical techniques. The cartilage layer of connective tissues has been modelled with $\mu_s'(\lambda) = 0.016\lambda^{-2.4}$ and $g(\lambda) = 1.1 - 0.58\lambda$ for the production of optical tissue phantoms and to inform finite element modelling of NIR light fluence, employed in the development of diagnostic fibre-optic Raman spectroscopy. [56] The results of Chapter 7 also utilise the high μ_a in the NIR-SWIR profile of water in biological tissues for precise, effective photo-ablation, discussed in the following sections.

Finally diffusive photons have travelled long distances through a scattering medium ($> l_{tr}$) and may hold valuable information for the tissue encountered along is path. Following repeated scattering events, diffuse intensity is defined as

$$I_D = I_i \exp(\mu_{eff} z)$$

using the effective scattering coefficient parameter,

$$\mu_{eff} = \sqrt{3\mu_a(\mu_s' + \mu_a)}.$$[4,12,69]

Scattered diffusive photons dominate signal beyond a certain depth in turbid tissue, known as the transition depth, z_c. As such, z_c will be dependent on g, l_s, l_t, specific for tissue and incident wavelength.

The diffusive photons transmitted through a turbid medium are modelled to interact with a "banana shaped" volume along its long path. This forms the basis for spatially offset Raman scattering (SORS) and absorption spectroscopy paradigms, and, though beyond the scope of this work, is described here to further complete the picture for NIR-SWIR and deep interrogation approaches.

Here a continuous, low intensity beam may illuminate tissue from its surface and spectral signal collected at discrete lateral distances away from the illumination, depicted in Figure 2.4. Deeper penetrating photons are likely to have further migrated laterally following a random walk pattern (subject to g, μ'_s, μ_a), such that scaled subtraction of signals at discrete distances indicate subsurface layers (depths of the order of mm). [70,71] Optical paths may be modelled with further detail with diffuse optical tomography software (e.g. NIRFAST) with specific μ'_s and μ_a. [56]

Such approaches have been applied to study of bone disease, neurotransmitters, and cancer, though typically must contend with weak signal intensities. [71] The work of Dooley et al. offers demonstration of SORS for monitoring of bone mineralization (collagen and hydroxyapatite concentration) in implanted scaffolds for bone tissue regeneration (*in vivo,* up to 8 mm deep in animal models). [72,73]

The conclusions for Chapter 5 (furthered in Chapter 6) offer technique level development and innovation employing back scattered (isotropic) spectroscopy but are anticipated to be directly compatible with offset geometries, and warrant further investigation.

Figure 2.4 depicts an overview of light-matter interactions considered in this thesis, which may be utilised for optical interrogation of tissue at varying depths. Each incident photon may undergo absorption and scattering events as they travel through the tissue medium and give rise to characteristic spectral signal, described in the following section. [58,64]

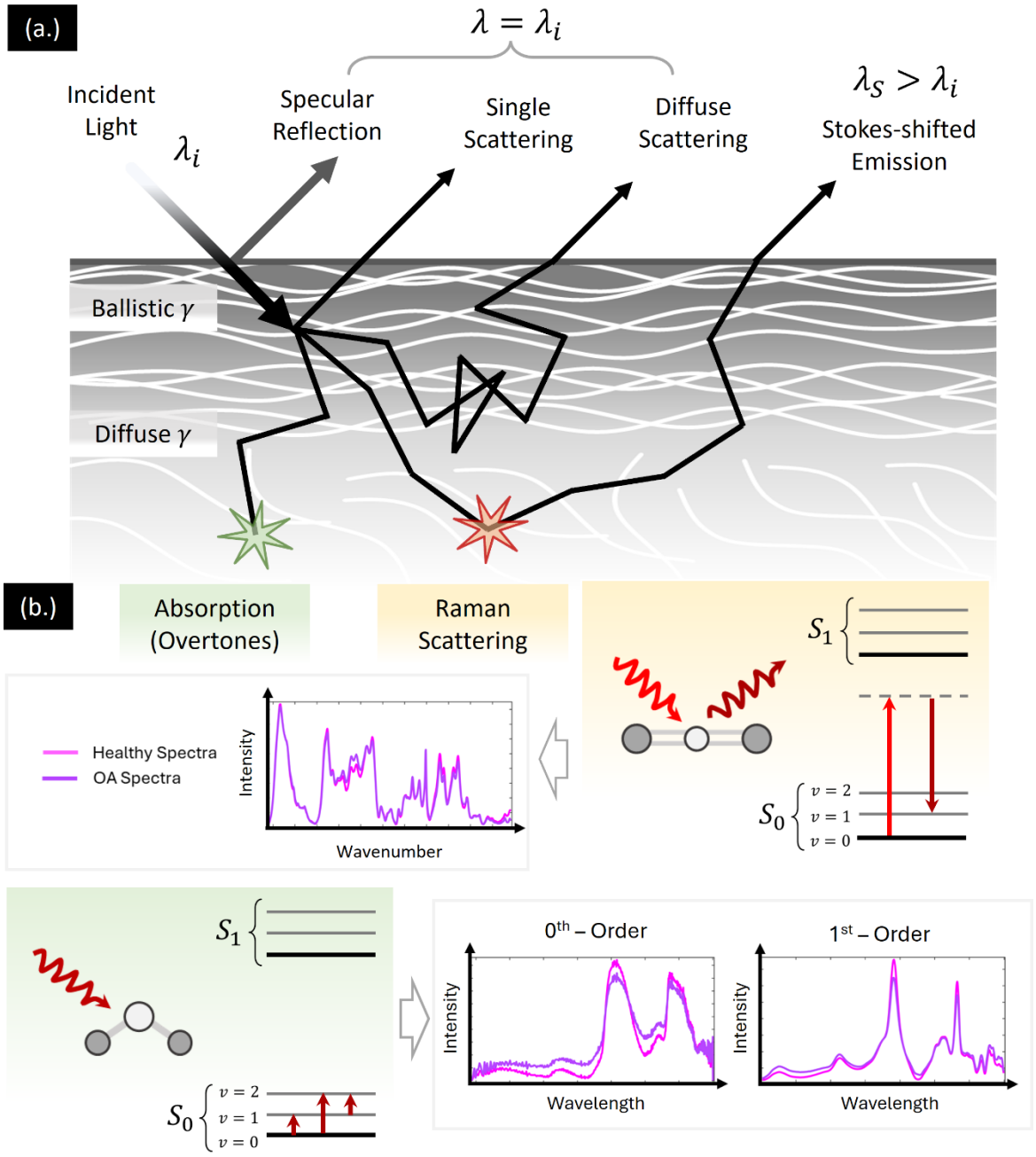

Figure 2.4: Overview of light-matter interactions considered in this thesis, defining (a.) photon propagation into turbid, scattering tissue to undergo scattering and absorption which can give rise to (b.) characteristic spectral signals. Incident light at wavelength λ_i may penetrate into the tissue (ballistic photons) and undergo multiple scattering events (diffuse photons) before reemitting from the tissue. Absorption of NIR-SWIR light is mediated by overtones of IR-active vibrational modes giving rise to characteristic spectral response in healthy and osteoarthritic tissue. Scattering of light may result in emission at $\lambda = \lambda_i$ (elastic Rayleigh scattering), at $\lambda_S > \lambda_i$ (inelastic Stokes shifted scattering), or $\lambda_{AS} > \lambda_i$ (inelastic anti-Stokes shifted scattering). Rayleigh scattering is the most dominant, followed by Stokes shifted Raman scattering, then anti-Stokes Raman at ambient

temperatures. Raman scattering spectra is also mediated by certain vibrational modes, sensitive to characteristic optical responses in healthy and diseased tissue.

2.2.2 Spectroscopic Optical Assessment Techniques

In the classical description, the electric field of incident light interacts with the charged particles of a material. Bound electrons are driven into motion by the rapidly oscillating applied field, inducing an electric dipole moment. Within the weak field limit and assuming a rapid response, the induced polarisation can be considered linearly dependent to the applied field. Under stronger electric fields higher order of polarisation response can be induced. [4,61] This behaviour is formulated as

$$\tilde{P}(t) = \epsilon_0 \chi^{(1)} \tilde{E}(t) + \epsilon_0 \chi^{(2)} \tilde{E}(t)^2 + \epsilon_0 \chi^{(3)} \tilde{E}(t)^3 + \cdots$$

where $\tilde{P}(t)$ is induced polarisation due to electric field $\tilde{E}(t)$, ϵ_0 is the permittivity of free space.[74] The first term relates to first order susceptibility, $\chi^{(1)}$, responsible for refractive index and linear optical phenomena such as absorbance, scattering, reflectance, and fluorescence. The second term ($\chi^{(2)}$) describes second-order optical responses such as in second harmonic generation (SHG). The third term ($\chi^{(3)}$) is associated with third-order responses such as coherent anti-Stokes Raman scattering (CARS) and two-photon fluorescence (TPF).

These interactions form the basis for a repertoire of optical techniques capable of structurally, molecular, and chemically selective interrogation of tissue. This thesis concerns primarily the application of one-photon Raman scattering and NIR-SWIR absorption phenomena, as well as linear absorption for targeted photo-ablation. The non-linear, multiphoton techniques are named above only to complete the picture for NIR-SWIR operable optical approaches employed for label free interrogation in tissue.

Multi-photon microscopy (MPM) has been harnessed for the label free interrogation of native and tissue-engineered cartilage, benefiting from high spatial resolution, high molecular contrast, and 3D sectioning capability.[61,74] Processes with emission intensity proportional to $I^{(n>1)}$ signal will originate predominantly from the focus of the excitation beam where I is highest, offering high spatial resolutions.[4,74] High intensities may be delivered under short coherent laser pulses but must maintain low average powers incident on the sample in order to minimise photodamage.[61] Typical NIR-SWIR operating wavelengths (photon energy below that required for electronic transitions), and with processes occuring only within a small focal volume, also mean photodamage may be avoided.[4]

Simultaneous, multimodal imaging may be operated under the same (typically fs) pulsed source. [75,76] The work of Costa Moura et al. offers demonstration of the potent combination of multimodal label-free MPM for live assessment of engineered cartilage, capable of imaging sensitive to collagen (SHG), lipids (CARS), and endogenous auto-fluorescent structures (TPF). [52,77,78]

Returning to the one-photon vibrational spectroscopy techniques employed in this thesis, the light-matter interactions of NIR-SWIR radiation with molecular vibrations will be explored.

NIR-SWIR Absorption

One of the most fundamental photophysical processes, absorption involves a transfer of energy from an incoming photon to a molecule. The photon transfers all energy and ceases to exist, whereupon the molecule may be promoted to a higher quantum energy level, depicted in Figure 2.6 The elevated energy level that the molecule reaches depends on the energy of the photon and thus the frequency of the incoming light.

The lowest energy of a molecule is its electronic ground state (S_0) and may be promoted to occupy higher discrete electronic energy levels ($S_1, S_2, \dots, S_n$). Each electronic state may be finely resolved into sublevels of discrete vibrational states ($v_0, v_1, \dots, v_n$), described in Jablonksi energy level diagrams in Figure 2.5. Broadly speaking, absorption of ultraviolet (UV) light is mediated by electronic energy levels, IR absorption by vibrational modes which experience a change in dipole moment, and NIR-SWIR absorption by harmonics of these vibrational modes. Interaction with the electronic excited state may give rise to photoluminescence and fluorescence phenomena with characteristic emission. Interaction with vibrational modes can elucidate specific chemical bonds presiding in the sample. Thus, spectroscopic investigation may identify characteristic absorptions to evaluate chemical composition of a sample.

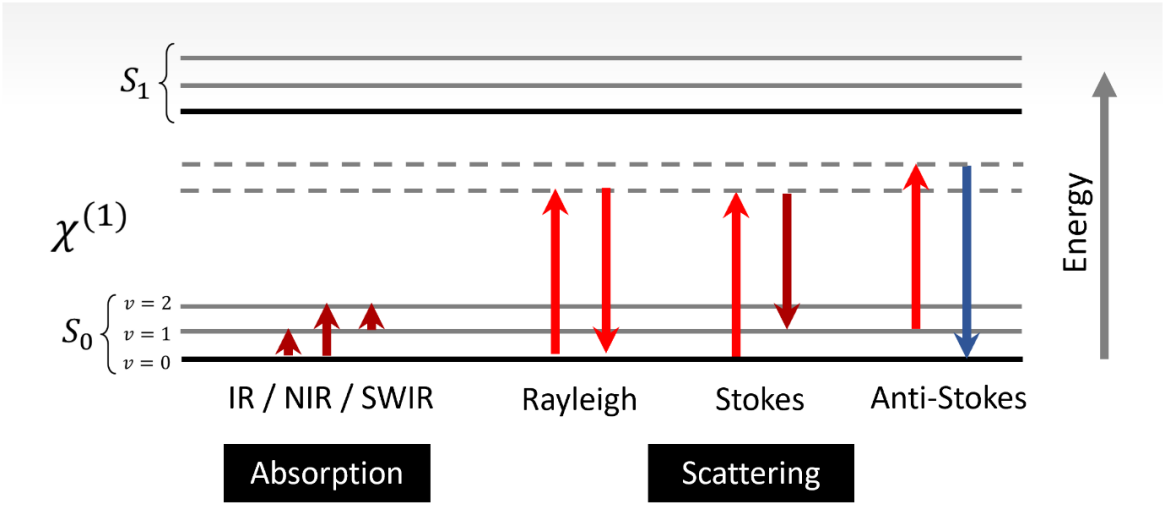

Figure 2.5 Jablonksi energy level diagrams for the light-matter interactions regarded in this thesis. Absorption of a photon results in molecular excitation to a higher energy state dependent on the frequency of the incident light. IR absorption results in promotion from the ground vibrational state ($S_0, v = 0$) to an excited vibrational state ($v = 1$), weaker NIR-SWIR absorption by overtones of the fundamental IR vibration ($v = 0 \rightarrow 2, 0 \rightarrow 3$, etc.). Scattering processes involve the molecule being promoted to a virtual state (dotted line) below the electronic excited state (S_0) by an incident photon. Instantaneous relaxation may then return the molecule to its original state (elastic Rayleigh scattering), a higher vibrational excited state (inelastic Stokes shifted scattering), or lower state (inelastic anti-Stokes shifted scattering). The emitted photon would have equal, lower, or higher energy than the incident photon, respectively.

It is worth noting that in a simplified and oft adopted model, absorbance is measured from the diffusely reflected light from a sample (sample spectrum) relative to that obtained from a diffuse or directly reflecting standard (reference spectrum), using Beer-Lambert theory. Absorbance, A, may be determined as

$$A = \log_{10} \frac{I_0}{I} = \epsilon c l$$

where I_0 and I denote the intensities of the incident and back-detected beams, respectively, ϵ is molecular absorption coefficient, c is sample concentration, and l the photon path length in the tissue sample.[79] In reality, this measure incorporates both specular reflection, absorption, and scattering events, characteristic to the sample, which result in loss of intensity. A more apt term may be "attenuation" but absorbance is usually quoted, with intensity recorded in arbitrary units.[17,20,51,80] Practical consideration must be made for the photon beam path through the tissue analyte, for example under diffuse, transmitted, or transreflected absorption spectroscopy. The

latter is adopted for the study detailed in Chapter 5 wherein the sample is placed on a highly reflective substrate and as such considers an idealised beam path for photons through cartilage tissue of twice the tissue thickness.

Transfer of IR energy to a molecule through absorption requires the incident oscillating electromagnetic field to match the frequency of a normal mode of vibration, and for this vibration to cause a change in dipole moment, μ. The dipole moment for a molecule is defined as

$$\mu = \sum e_i \, r_i$$

resulting from the magnitudes, e_i, and relative positions, r_i, of all of its atomic charges.[81]

NIR-SWIR absorption is mediated by excitation of overtones, combinations, and resonances of the fundamental IR-active vibrational modes.[82] Overtones occur when a vibrational mode is excited from ground state with quantum number $v = 0$ to state $v = n$ where $n > 1$. These transitions are labelled the fundamental $(0 \rightarrow 1)$, first overtone $(0 \rightarrow 2)$, second overtone $(0 \rightarrow 3)$ etc. and their probability rapidly decreases with number of quanta n, where $\Delta v = \pm n$. Combination and difference bands are the result of simultaneous excitation of two or more fundamental vibrations, with typically small intensities. [83,84]

Spontaneous NIR Raman Scattering

Scattering behaviour is determined through the radiation produced by oscillating dipoles induced in the molecule under an incident photon. The electromagnetic field of the incident photon will perturb the charges within the molecule to induce a dipole moment such that

$$\mu = \alpha E$$

where α is polarisability, and E the incident electric field which oscillates with frequency, f_0. The induced dipole moment will oscillate at the same frequency, f_0.[81] The magnitude of the molecular polarisability may be made to vary in time though at a considerably slower frequency, f_m.

The resultant amplitude modulation of the permanent and induced dipole moment may be resolved into three oscillating components with steady amplitude and frequencies f_0, $f_0 + f_m$, and $f_0 - f_m$, giving rise to Rayleigh, anti-Stokes Raman, and Stokes Raman scattering, respectively.[79,81] The Jablonksi energy level diagrams for each are described in Figure 2.5.

Rayleigh scattering is the dominant interaction, occurring for 1 in 10^4 incident photons, and is considered an elastic scattering process since no energy transfer occurs. Should the incident

photon energy, hf_0, be insufficient for electronic excitation, the irradiated molecule would be promoted to an intermediate virtual state, before immediate relaxation to the original vibrational energy level. [79] Under NIR irradiation this virtual state exists close to the ground state.

By comparison, only 1 in 10^6 - 10^8 photons would undergo Raman scattering whereupon the molecule would lose or gain energy, resulting in a Stokes or anti-Stokes shifted signal emission, respectively. Molecules initially in the ground vibrational state may be promoted to a virtual state, relax to a vibrational excited state, and produce a Stokes shifted signal ($f_0 - f_m$), while molecules initially in a vibrational excited state would give rise to an anti-Stokes shifted signal ($f_0 + f_m$) .[81]

The population ratio of the ground ($v = 0$) and excited ($v = 1$) vibrational states is defined by the Maxwell-Boltzmann distribution such that

$$\frac{N_{v=0}}{N_{v=1}} = \exp\left(\frac{\Delta Energy}{k_B T}\right)$$

where $\Delta Energy$ is the difference in energy between the vibrational states, k_B is Boltzmann's constant, and T is absolute temperature.[79] The strength of Stokes shifted signal, I_S, compared to anti-Stokes shifted signal, I_{AS}, is determined as

$$\frac{I_S}{I_{AS}} = \frac{(f_0 - f_m)^4}{(f_0 + f_m)^4} \exp\left(\frac{hf_m}{k_B T}\right)$$

where h is Planck's constant.[79] The Stokes shifted Raman lines in spectral measurements have much higher intensity than anti-Stokes at ambient temperatures since most molecules may be found in the ground state. [81] Collected spectra are represented as the frequency shift between incident and emitted light, displayed in wavenumbers (cm^{-1}) indicative of the change in energy.[61,85]

The intensity of the Raman scattered radiation can be expressed as

$$I_R \propto f_0^4 I_0 N \left(\frac{\delta\alpha}{\delta Q}\right)^2$$

where I_0 is the incident laser intensity, N is the number of scattering molecules in a given vibrational state, and Q is the vibrational amplitude.[81] A number of important parameters may be gleaned from this. Raman signal intensity is dependent on concentration of scatterers and as such can be used to quantify chemical composition within a sample. Spontaneously generated signal is isotropic being the incoherent addition of scattering from the irradiated molecules. Raman signal intensity may also be increased with higher laser flux power density, though

requires a balance for sufficient signal generation whilst mitigating photodamage to the tissue sample (or patient).[81]

Raman signal intensity is also inversely proportional to excitation wavelength ($1/\lambda^4$), and so spectroscopy under excitation in the NIR is expected to have reduced sensitivity compared to visible and UV. However, NIR excitation benefits are two-fold. Photoluminescence has a much higher probability than Raman scattering events that, even at low quantum efficiencies, may overwhelm the Raman spectra. Moving out of an excitation manifold into the NIR, e.g. 785 nm or 830 nm, would avoid inducing fluorescence and ensure good Raman signal-to-noise ratio. Secondly, use of less energetic photons reduces risk of phototoxicity and photodamage under prolonged exposure. [56,86] As such, 785 nm mediated Raman spectroscopy is adopted in this work, benefiting from operation in the NIR-SWIR transparency windows for both excitation and Stokes-shifted emitted light.

Finally, for the generation of Raman signal the change in polarisability with respect to change in the vibrational amplitude must be non-zero, or equally

$$\left(\frac{\delta\alpha}{\delta Q}\right) \neq 0$$

Thus, Raman scattering is mediated only by molecular vibrations which may experience a change in polarisability, that is the ease with which the electron cloud around a molecule could be distorted by an electric field.[85]

The phenomena described above give rise to a rule of mutual exclusion for centrosymmetric molecules, best exemplified by the carbon dioxide molecule, which is non-polar, linear, and with a centre of symmetry. Each molecule may have 3N degrees of freedom (DoF) where N is the number of atoms. The triatomic CO_2 molecule has three translational and two rotational (linear structure) DoF, leaving four (3N-5) possible normal modes of vibrations. Each normal mode produces a fundamental transition with characteristic frequency, from whose combinations allow for the overtone bands. It is worth noting that, similar to absorption, signal from overtones of Raman-active modes decreases with increasing quantum number, and may be safely ignored given the already low intensities of Raman scattered light.[84]

The CO_2 molecule may undergo symmetric stretching, asymmetric stretching, and in-plane and perpendicular bending, described in Figure 2.6.

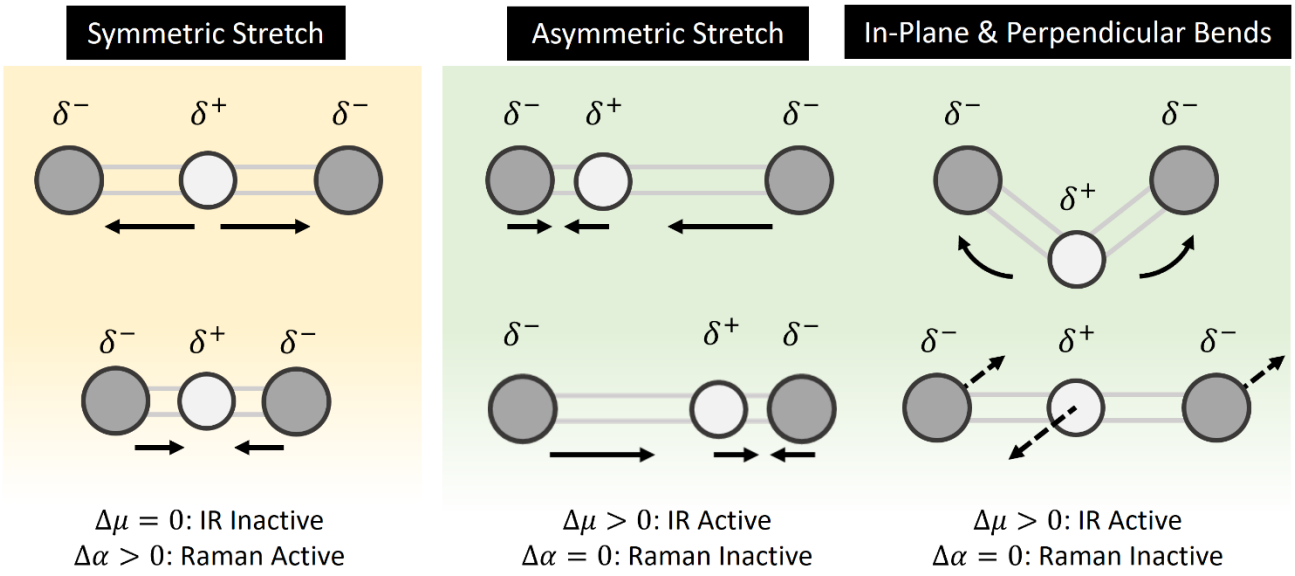

Figure 2.6 Vibrational modes of the linear triatomic carbon dioxide molecule. As a centrosymmetric molecule, IR and Raman activity of the vibration modes are determined by a mutual exclusion rule. The symmetric stretch vibration mode experiences a change in polarisability (Raman active) but no change in dipole moment when partial charges ($\delta^{\pm}$) are moved (IR inactive). The asymmetric stretch, in-plane bend, and perpendicular bend vibration modes experience no change in polarisability (Raman inactive) but see a change in dipole moment (IR active).

The symmetric stretch (relative to the centre of symmetry) vibration is Raman active since the lengthening of the bonds causes an increase in polarisability, as the electron cloud may be more easily distorted when stretched, but the overall dipole moment is unchanged meaning no IR activity. The asymmetric stretch is IR active due to an overall change in the dipole from an uneven distribution of partial charges, but since an increase in polarisability of one bond is countered by decrease in the other (or vice versa) there is no net change and the vibration is Raman inactive. The two bending modes similarly would cause a net change for dipole moment and so are IR active, but experience no change in the polarisability of the bonds throughout its vibration so remain Raman inactive.[79,81,84]

This may be extended to rule that for all centrosymmetric molecules Raman active vibrations are IR inactive, and vice versa, offering complementarity between the two spectroscopic techniques. For molecules without a centre of symmetry, some vibrations may show both Raman and IR activity, though other suitable symmetry elements may determine their behaviour as only Raman or only IR responsive. Non-centrosymmetric water molecules with permanent dipole have all three (3N-6) vibrational modes as highly IR active (highly polar), whilst displaying weak Raman scattering with no influence on IR spectra. [79,84]

The argument will be made within this thesis for exploiting of this complementary behaviour for the holistic assessment of biological tissue. A combined approach may elucidate a full view of the vibrational bonds in a sample under water rich conditions. [85]

2.2.3 In Vivo Optical Processes Require Efficient Introduction and Retrieval of Light

Finally, a general methodology for NIR-SWIR and/or deep optical interrogation into tissue is considered. Optical systems must be optimised for back-reflected signal collection in order to analyse subsurface tissues *in vivo*. Excitation light may be focussed onto the sample via an objective lens, emitted signal light collected through this same objective, directed *via* some beam splitting element, a spectrum analyser (spectrograph), and onto a CCD detector. Aforementioned offset spectroscopy approaches see the signal collected by an adjacent optic (lens or fibre optic) and onto the detector. In either case it is clearly prudential to consider the fate of photons travelling through the tissue medium when analysing under spontaneous Raman scattering and NIR-SWIR absorptions.

Raman scattered signal is spectrally distinct from its excitation laser (wavenumber shift relative to excitation) and can be discriminated through suitable long-pass dichroic optics, with cut-off close to the laser frequency. Isotropically emitted Stokes-shifted signal light may be produced backwards, directly towards the detector, or travel to the detector after a number of scattering events within the tissue medium. Spectral intensity is the cumulative count of Raman scattered photons travelling back toward the detector having interacted with a small focal volume of tissue.

NIR-SWIR absorption signal by contrast would consider the intensity of reflected light having interacted with the sample within a small volume, regarding excitation and signal light across a broad wavelength range, between 900 – 2500 nm.[87] Optimal optics require flat spectral response curves (high transmission, low chromatic aberration) across this broad range to maximise signal collection. Metallic reflective optics (planar and focussing mirrors) offer high performance across the NIR-SWIR with typical transmission >95%, across ranges UV to MIR. Though absorption may be considered a more “photon efficient” process than Raman scattering, weak overtone responses (broad spectral features, subtle peaks) would benefit from efficient detection pathways to allow for suitable signal-to-noise ratio. InGaAs based detectors are common, with optical sensitivity at wavelengths beyond the typical 1.1 μm limit of Si-based detectors, actively cooled to mitigate thermal noise.

Aberration effects have been reported to increase exponentially with the order of nonlinearity in a thick sample or, equally, measurements at depth.[88] The maximum imaging depth of MPM processes is related to the ability of ballistic photons to target the focal plane in a diffraction

limited volume. [59] Photophysical phenomena with quadratic and higher order dependence on excitation intensity will have increased sensitivity to distortions caused by the tissue.[88] Longer length scale variation in refractive index (greater than scatterer diameter) can be pre-compensated with adaptive optics (AO). [4,59] Though beyond the scope of this study, a description of AO technology completes the picture for the strategies available for optical interrogation at depth.

Briefly, a phase modulating optical component (typically a deformable membrane mirror (DMM)) is placed in a position conjugate to the back focal plane of the objective. Tens to hundreds of actuators in the DMM are capable of precise shaping of the laser wavefront. The correct deformation can be estimated with a wavefront sensor (typically Shack-Hartmann design) as part of a closed control loop or iteratively (sensorless, algorithmic) to achieve highest intensity within the tissue.[4,59,89] This concept treats the medium as a scattering "lens" and a transmission matrix is computed that relates the actuators of the wavefront-shaping element to the pixels on an imaging camera. [59,90] Sensor-less approaches quantify the pre-compensation effects via some metric such as intensity or image sharpness, though may suffer from long optimisation times (order of minutes) compared to direct wavefront sensing.[59,89,91] With the optimal pre-compensation the excitation wavefront could be focused perfectly up to hundreds of microns deep *in vivo*.[88]

2.3 Current Approaches towards Tissue Photo-ablation

Clinical photo-ablation in general terms seeks to raise the temperature of a target tissue beyond an irreversible threshold for precise thermolysis or incisions with little to no collateral damage. Laser systems for clinical ablation differ in operating wavelength and pulse characteristics, dependant on choice of absorption chromophore within the target tissue. Commonly employed clinical laser systems (and their wavelengths) include argon (350 – 514 nm), diode (630 – 980 nm), neodymium-doped ytrrium aluminium garnet (Nd:YAG, 1064 nm), holmium: YAG (Ho:YAG, 2100 nm), erbium:YAG (Er:YAG, 2940 nm), and CO_2 (10,600 nm), described in the Figure 2.7.[92] These have diverse surgical application such as lithotripsy, oral surgery/dentistry, oncology, neurology, and ophthalmology. There is substantive argument for the adoption of new Thulium-doped fibre laser systems (~1950 nm), further explored in Chapter 3. Here will be discussed the beneficial move to laser ablation operating within the NIR-SWIR, and the facilitating theory underpinning thermolysis of biological tissues.

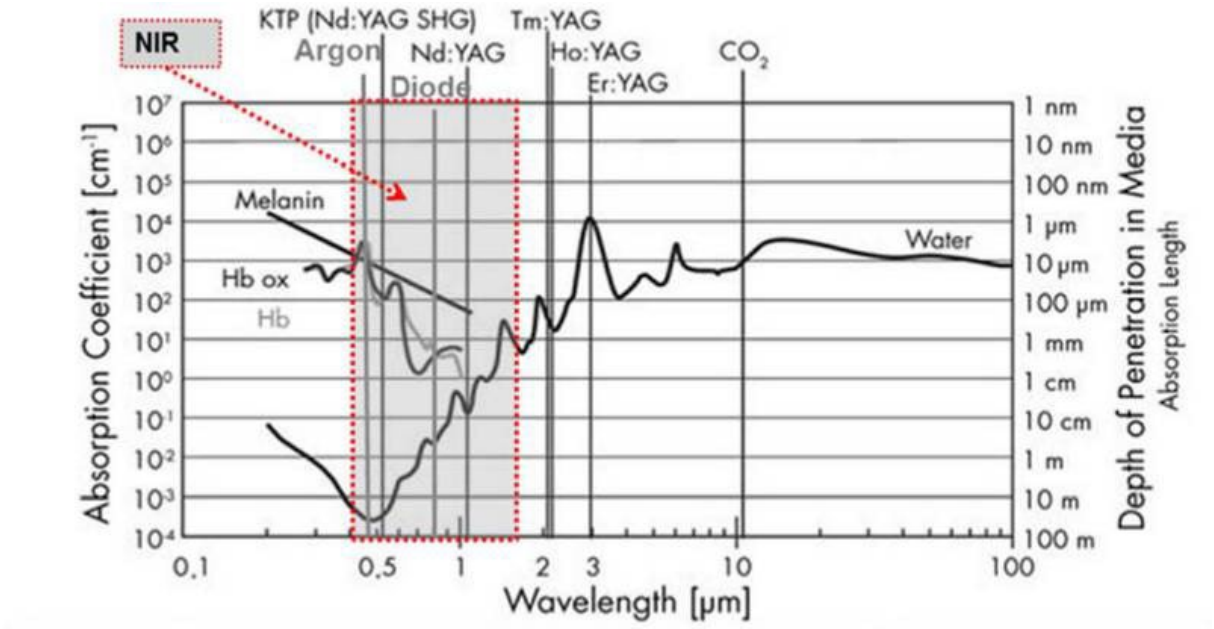

Figure 2.7 Absorption coefficient and corresponding depth of penetration expected from common chromophores in biological tissues relative to commonly employed medical lasers. Adapted from Schena et al. [93] Reproduced in adherence with CC BY 4.0.

Key absorption chromophores within biological tissues have been mapped across the UV to visible to NIR-SWIR and MIR ranges, informing choice of laser systems for specific treatments. UV absorption is mediated chiefly by peptides present in the backbone of all proteins, by DNA, and by melanin, with negligible absorption by water. Attenuation due to melanin drops monotonically from its peak at 335 nm into the IR. Haemoglobin in vascularised tissues – oxygenated (HbO_2) and deoxygenated (Hb) – contributes significantly to the overall optical absorption in the NIR to wavelengths ~1 µm.

Water then begins a significant contribution from ≳ 900 nm, with μ_a increasing rapidly, and its maximal value at 2.94 µm (μ_a = 12,000 cm^{-1} at 25 °C).[94,95] Water absorption due to symmetric and asymmetric stretch modes, symmetric bend mode, and their combinations result in μ_a peaks at λ = 0.96, 1.44, 1.95, 2.94, 4.68, and 6.1 µm. Finally, collagen displays peaks between ~ 6 – 8 µm, sharing a peak at 6.1 µm with water, though at half the peak value of water.[94]

However, low-loss transmission of radiation at 2.94 µm may only be mediated by soft-glass-based optical fibres, that suffer poor physical and chemical properties compared to conventional silica-glass components. Tm-doped laser systems may target the 1.95 µm peak to induce effective photo-ablation of a wide range of biological tissues, benefiting from the highest water peak available for targeting through silica fibres. Additionally, Tm-fibre lasers offer compactness, flexibility, and robustness than their bulky solid-state counterparts.

Fine control over fundamental pulse parameters such as duration and pulse parameters would allow for precise ablation effects (minimized collateral) and adaptability for various tissue types (target cells within a heterogeneous *in vivo* environment). The approach for tailoring ablation affects through pulse characteristics is informed by the theory laid out below. Here the argument is made for the development of a microsurgical system with a single-mode TDFL with a pulsed output at 1.95 μm for precise and effective laser ablation of biological samples with differing morphologies, at single-cell scale resolution.

2.4 Light-Matter Ablation Interactions

Ablation, from "ablatus" or "carried away", describes tissue incision or material removal under laser irradiation, and can be mediated by various photothermal or photochemical processes depending on laser pulse characteristics, tissue type, and tissue environment. The work carried out in this study will focus on pulsed laser irradiation (pulse duration < 1 μs) on soft (non-mineralised) biological tissue, and will utilise models for linear thermomechanical response of the tissue (all energy absorbed by tissues converted to temperature rise) to inform parameters for effective ablation. [94]

A crude mechanistic model of soft tissue describes composition mainly of extracellular matrix, with some cells within and attached to the ECM. The ECM ensures structural integrity and would resist material removal under laser ablation phenomena. Overall, soft tissue is made up of water (55 – 99 %) and collagen (0 – 35%). Collagen makes up 25% of all protein in the human body, and has hierarchical fibrillar structure wherein three α-chains (amino acid sequences) associate in a triple-helical structure, forming fundamental units known as tropocollagen (TC). "Ground substance" describes matter between fibrils, made up of water, GAG, PG (sGAG covalently linked to a core protein), non-fibrillar collagen and cell adhesion proteins.

Both collagen and ground substance are hydrophilic. Collagen exists in a highly swollen state, and PG / GAG, though only accounting for 1% of connective tissues, may hold around 1000 times their volume of water. [94] Structural (directly associated with protein) and bound (indirectly associated) water accounts for 35% of collagen by mass. Thus, the NIR-SWIR water absorption band offers a prime candidate as a chromophore for laser ablation.[94] Within the crude model above, therefore, spatial scales for soft tissue ablation relate to the diameter and spacing of collagen fibrils.

Thermal denaturation of protein is a key concept when measuring the effects of laser ablation on tissues, generally considering the denaturation of fibrillar collagen. Under laser irradiation, temperature rise due to the increased kinetic energy of constituent molecules may overcome

the weak hydrogen bonds and van der Waals interactions responsible for stabilising the helical structures of α-chains in TC (triple-helical to "denatured" random coil structure). Tissue heating would lead to tissue shrinking (e.g. along the axis of collagen fibrils) and to total mechanical failure of the fibrillar tissue structure (ECM), depending on melting temperatures and latent enthalpy characteristic of that tissue type (e.g. relative amount of proline and hydroxyproline which resist ablation pressures). [94]

Thermal denaturation is considered a time-resolved process, dependent on transient temperature and duration of laser exposure, and accumulation of thermal injury modelled as

$$\Gamma(t) = \int_0^t A\exp\left(-\frac{\Delta E}{k_B T(t')}\right) dt'$$

where $\Gamma(t)$ is a dimensionless parameter for thermal injury dealt over time t, k_B is Boltzmann's constant, ΔE is the activation energy for denaturation to occur, and A is a decomposition rate factor of the target molecule. [94,96] This serves to describe how if exposure time is reduced, significantly higher temperatures are required to initiate denaturation, reportedly >> 100 °C under ns pulses.[94] Since the aim here is efficient and precise delivery of damage to tissue, and avoiding collateral damage (excessive energy deposition), laser pulse parameters must be finely tuned to find this balance.

The most direct strategy is to minimise heat diffusion from the volume of tissue in which energy is directly deposited to the surrounding (e.g. healthy) tissues, by shortening pulse duration, τ. The heated volume is typically a layer of tissue with thickness equivalent to $1/\mu_a$ (wavelength and tissue specific absorption length, l_a) such that the characteristic thermal diffusion time is expressed as

$$t_d = \frac{1}{\kappa \mu_a^2}$$

where κ is thermal diffusivity. As such, "thermal confinement" may be achieved when the ratio of laser pulse duration to thermal diffusion time, τ / t_d ≤ 1. Should pulse duration be too high, thermal diffusion would redistribute energy over a large volume, reducing peak temperature in the sample, perhaps below the ablation threshold. [94] This is also dependent on the operating wavelength and its absorption profile within the target tissue. However effective tissue denaturation must consider this in balance with the breakdown rate of the target protein, ensuring that sufficiently elevated temperatures are maintained for the required length of time. [96]

The ablation processes may be considered through the "blow off model" wherein thermal enthalpy increases monotonically during irradiation. Ablation efficiency is maximal at moderate

exposure and at high exposure, excess energy is wasted as overheating of superficial tissue layers. [94] The model stipulates that

a. Beer-Lambert relationship accurately describes the spatial distribution of laser energy
b. Energy in excess of a threshold is required to initiate ablation (anything less serves to only heat the tissue)
c. Material removal only commences after the laser irradiation
d. Thermal confinement conditions are satisfied

As such this is appropriate for the linear ablation processes considered here, with pulse durations ≤ 100 ns and in targeting of the strongly absorbing water NIR-SWIR chromophore (higher μ_a), requiring only relatively low radiant exposures for ablation (lower threshold).[94]

A more comprehensive model may also consider the generation and propagation of thermoelastic stress caused by rapid heating of tissue under pulsed laser radiation. Here "stress confinement" is achieved when τ / t_m ≤ 1, where the characteristic time for a stress wave to propagate through a heated volume, t_m= (1/$\mu_a c_a$), dependent on the longitudinal speed of sound in the tissue medium, c_a.[94] Suffice to say that short pulse durations are conducive to confining the overall impact of laser ablation.

Repetition rate, R, must be suitably low to avoid excessive accumulation of heat in the target tissue (only enough to cross the ablation threshold) for a given exposure time, t_{exp}. [94,97] In addition to this, Vogel et al. recommend that for a given average power, P_{avg}, the highest ablation efficiency may be achieved for a series of short pulses with high peak power than for continuous or long-pulsed (100 µs to ms) exposure. [94]

Four fundamental pulse parameters are identified here for precise control of the laser ablation effects, namely:

1. Average power, P_{avg}
2. Pulse duration, τ
3. Repetition rate, R
4. Exposure time, t_{exp}

These pulse parameters form the variables of interest for the photo-ablation study detailed in Chapter 7.

Chapter 3 Literature Review: NIR-SWIR Diagnosis and Therapy

Within this work, ideal optical interrogation for a patient friendly paradigm of diagnosis is defined as minimally perturbative, *in vivo*, morphological, and chemically sensitive assessment of the body from the outside. The "outside in" microspectroscopic approach is one without removal of any endogenous or introduction of any exogenous material that would interrupt the natural vital system. Vibrational spectroscopy techniques in the NIR-SWIR are capable of extracting rich chemical information at subcellular spatial resolutions.

Light-matter interactions of optical light with biological tissue are predominantly considered in terms of scattering and absorption, which prove detrimental to maintaining photon characteristics such coherence and power. Operating in regions of biological tissue transparency can allow deeper penetration of the order of millimetres. Specific chromophores within these transparency windows can allow diagnostic assessment (spectral biomarkers) and selective ablative therapies (efficient heating by targeting absorption bands). In addition, ablation therapies of tissue through pulsed laser in the NIR-SWIR benefit from efficient thermolysis *via* the water absorption chromophore.

Thus, the review of literature below seeks to contextualise and highlight optical techniques that have enabled effective diagnosis and treatment in the NIR-SWIR, intended for precise clinical tools. The current state of field will be explored for NIR Raman scattering and NIR-SWIR absorption spectroscopies for diagnosis of OA, and approaches for data analysis and enhancement (data fusion) and viable clinical implementation (arthroscopy). The state of art for NIR-SWIR operating photo-ablation therapies in practice and proposed new directions for clinical practice will be highlighted.

3.1 Measurements through the NIR-SWIR windows

3.1.1 NIR-SWIR Absorption correlates with OA progression

NIR-SWIR absorption spectral measurement of articular cartilage is considered the sum total of optical interactions with the tissue micro- and ultrastructure, sensitive to structural and compositional changes resulting from loss or alteration of the tissue ECM.[50] Absorption in this region results from combination of 1st and 2nd overtones of MIR fundamental vibrations, giving rise to low signal intensity (inversely proportional to overtone order) and broad spectral

features.[18] First- and second-order derivatives of NIR-SWIR spectral fingerprints are commonly employed in order to elucidate subtle features in the absorption spectrum.

Nonetheless, NIR-SWIR absorption spectroscopy can offer a non-destructive method to determine thickness and composition of articular cartilage for evaluation and monitoring of OA progression.[16,17] Operating within the biological transparency windows, this offers an attractive suite of optical characterisation technologies that may be employed for label free, deep tissue assessment.[4]

Specifically, absorbance bands in the NIR- SWIR are overtones and combinations of the fundamental vibrations of O-H, C-H, N-H, and S-H bonds which form the molecular framework of the tissue. [50,51] Some key NIR-SWIR absorption bands are identified in summary Table 3.1 below, collected from intact tissue and from its major components, PG and collagen. [20,50]

Table 3.1 NIR and SWIR absorption peaks of native articular cartilage and solid matrix components.[20,50]

Wavenumber (cm^{-1})	Wavelength (nm)	Assignment
Native Cartilage Tissue		
8820 – 8060	1134 – 1241	C–H stretching (2nd overtone)
7280 – 6780	1374 - 1475	O–H stretching (1st overtone)
6890	1450	Free Water
5720 – 5500	1748 - 1818	C–H stretching (1st overtone)
5200	1923	Bound and free water
Cartilage Solid Matrix Components		
Proteoglycan		
8250	1212	C–H stretch (-CH_2, 2nd overtone)
6352, 6863	1574, 1457	N–H stretch (-CONH, 1st overtone)
5890	1698	C–H stretch (-CH_2, 1st overtone)
5623	1778	C–H stretch (-CH_2, 1st overtone) + S–H stretch (-SH, 1st overtone)
4228, 4730	2365, 2114	O–H bend, C–O stretch combination
Collagen		
8430	1186	C–H stretch (-CH_2, 2nd overtone)
6682	1497	N–H stretch (-NH, 1st overtone)
4902	2040	N–H (amide II [-CONH] or [-$CONH_2$])
4594	2178	N–H bend (protein, 2nd overtone); C–H stretch/C=O stretch combination
Combined Collagen and Proteoglycan		
5790	1727	C–H stretch (-CH_2, 1st overtone)
5154	1940	O–H bend (2nd overtone)
4350	2300	C–H bend (protein, 2nd overtone)

Padalkar et al. have quantified the varying depth of penetration of optical light into cartilage across the NIR-SWIR range. These were categorised into first region (wavenumbers 4000 – 5000 cm^{-1}) with depth limit of 2 mm, second region (5000 – 7000 cm^{-1}) ~3 mm, and third region (7000 – 9000 cm^{-1}) >4 mm. The authors suggest that, as the normal thickness of human cartilage is 1 – 3 mm, the ideal spectral range for cartilage assessment is wavelengths 1.4 – 2.5 µm (wavenumbers 7143 – 4000 cm-1), since wavelengths able to penetrate deeper may also experience absorption due to the underlying subchondral bone.[18] It is worth noting here that spectra were captured for *ex vivo* cartilage samples with a reflective substrate, referred to as transreflectance spectroscopy.

Corroborating studies demonstrate how interrogation under NIR-SWIR light may retrieve optical responses from all depths in the cartilage layer, giving a chemical fingerprint indicative of specific layers in joint tissues, as shown in Figure 3.1. [98]

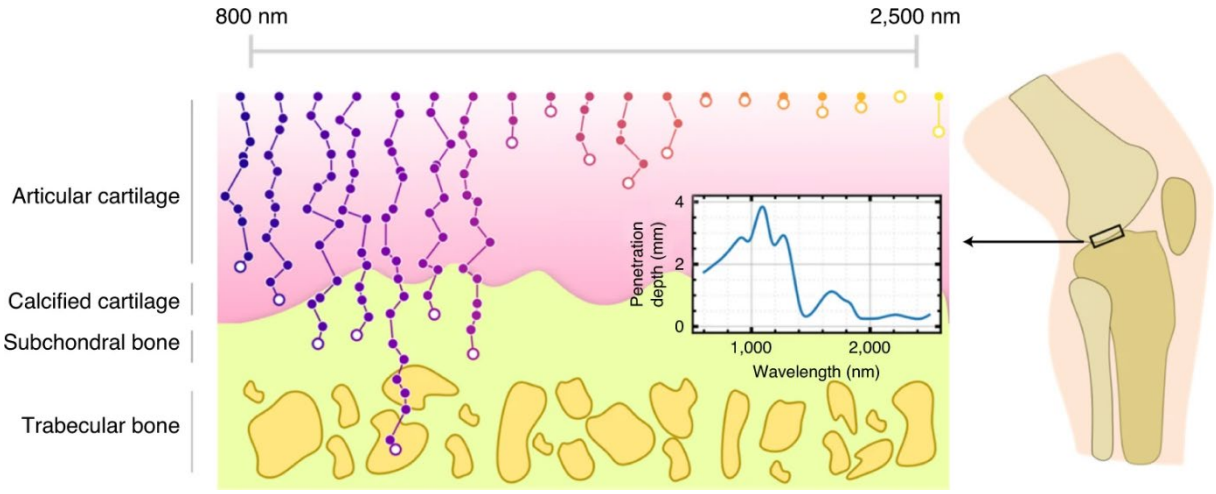

Figure 3.1 NIR-SWIR wavelength dependent interaction with osteochondral tissue - articular cartilage, calcified cartilage, subchondral and trabecular bone – showing capacity for light to interrogate through the various tissues across the osteochondral junction. From Afara et al.[98] Reproduced in adherence to CC BY.

In general terms, approaches to date have sought to utilise NIR-SWIR absorption spectral data in regression and other statistical models (e.g. PLS) to investigate the correlation between the broad spectral features and an OA relevant metric, such as relative water content, protein composition (collagen, PG, GAG), biomechanical property (reswelling after compression) or a gold-standard clinical grading score (KOOS, Mankin, Kellgren-Lawrence). [20]

Diagnosis of early OA may be facilitated by detection of prepathomorphological chemical and compositional changes in the cartilage layer. This may then serve to highlight tissue changes invisible to the eye or to typical diagnosis pathways, such as within soft tissue not detectable via

x-ray. NIR-SWIR spectroscopy may also be preferred for a patient friendly diagnosis approach, offering non-destructive and label free chemical fingerprinting.

The predictive capacity of the chemical fingerprint is determined by accuracy of the statistical modelling, from which the most informative spectral regions could be identified, marked as "spectral biomarkers". Tracing back such biomarkers to their chemical vibration and thus to their biological assignment (protein composition etc.) can give insight to the pathological changes within the tissue.

Quantitative tracking of relevant chromophores can allow for accurate biochemical assessment of OA, for example in the mapping of PG reduction in animal models (e.g. enzymatically degraded bovine patella) or human samples (e.g. lesions in human TKA samples). [20] Pertinent chromophores and their capacity to detect and monitor OA are reviewed below.

A direct manifestation of OA is thinning of articular cartilage, which may be monitored with changes to NIR-SWIR spectral response as a potential diagnostic marker.[16,21] Afara et al. collected absorption spectra between 4000 – 12000 cm^{-1} from bovine patallae and murine cartilage models with 1.2 – 2.4 mm thickness, to develop a partial least squares (PLS) model to correlate the spectra with tissue thickness.[20] The authors report that absorptions in the region 6102 – 5446 cm^{-1} are optimal for correlation with cartilage thickness, indicative of collagen and PGs (first overtone CH_n and SH absorptions). [16] This approach considered an idealised model of cartilage thickness, considering an effective path length for photons travelling through the translucent cartilage matrix to the opaque subchondral bone, which accounts for higher absorptions in thicker tissue layers. [16]

NIR-SWIR bands at 5200 cm^{-1} and 6890 cm^{-1} have been attributed to free and bound water, and free water, respectively, and PLS regression models have successfully employed to predict total and free water contents in bovine nasal cartilage. The peak ratio has also proven to correlate with KOOS in a clinical knee pain study, and to weakly correlate with mechanical properties (Young's modulus) of cartilage. [20]

Elsewhere, absorption signal <5250 cm^{-1} was excluded to avoid signal saturation from the water overtone in order to build accurate models via PLS, principal component analysis (PCA), and support vector machines (SVM), of surgically-induced OA murine knee samples. [17] Spectral data was obtained via a single-point spectroscopic set up consisting of a fibre optic probe (six peripherally positioned for NIR illumination, one centrally placed for collecting the diffusely reflected light), in contact with tissue and relaying signal to an FT-NIR spectrometer. The authors report use of "shaving" and "genetic" algorithms to test the spectral contributions to

the PLS models for Mankin score and GAG content prediction. Figure 3.2 displays the indicative NIR-SWIR response from articular cartilage as well as the most informative spectral variables. [17]

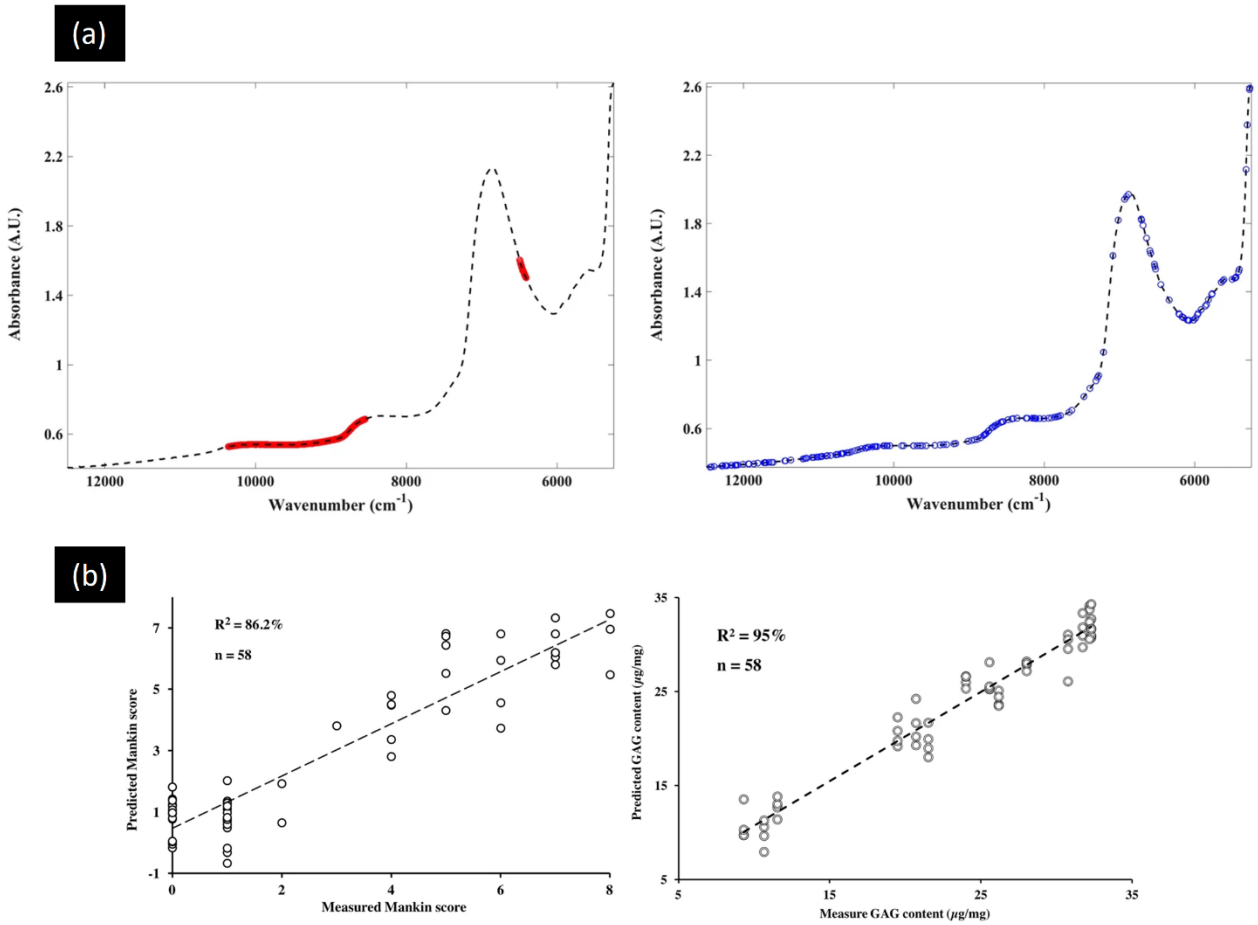

Figure 3.2: Predictive models of OA cartilage have been built upon NIR-SWIR absorption data. (a) NIR spectral plots of murine OA models highlighting most informative variables obtained from variable selection algorithms for optimal PLS regression model to predict Mankin score (red) and GAG content (blue). (b) PLS correlation between NIR spectral predicted and measured (a) Mankin score and (b) GAG content. Adapted from Afara et al, in adherence to CC BY.[17]

Mankin score prediction relied on spectral features in ranges 8547 – 10361 cm^{-1} and 6411 – 6496 cm^{-1}, attributed to combined PG and collagen absorption (2nd overtone CH_n) and to PG related absorption (1st overtone CH_n and SH stretch), respectively. [17] This largely corroborates previous studies for highly accurate PCA and PLS modelling of surgical and enzymatically degraded murine cartilage when utilising these NIR-SWIR spectral regions.[16] Features contributing to prediction of GAG content were dispersed across the spectrum, which the authors attributed to the close relationship between PG and water contents, and increasing overall absorption with OA progression.[17]

Further corroborating results have been reported for NIR absorption spectra of human cadaveric knee cartilage indicative of cartilage health, measured from excised osteochondral cores [48] and through insertion of ferrule fibre optic probe into the joint, in contact with cartilage tissue. [99] Afara et al. correlated visible-NIR absorption spectra (400 – 1100 nm) of cartilage cores with biochemical composition (water & uronic acid), clinical score (Mankin), thickness and biomechanical properties for accurate prediction under PLS regression models ($p < 0.0001$). [48] Developing this work, Prakash et al. built multivariate regression models based on PCA and linear mixed effects modelling to accurately predict cartilage thickness and biomechanical properties with NIR spectra between 710 – 1850 nm captured from within the ex vivo joint. Outlier measurements associated with non-optimal probe-cartilage contact were removed for these models, as well as spectral data in the visible range (400 – 710 nm) and from pronounced water peaks (1350 – 1450 nm and 1850 – 2500 nm) which saturated signal. [99]

The argument will be made here for characterising absorption of human articular cartilage across the entire NIR-SWIR regime, 900 – 2500 nm or 11,000 – 4000 cm^{-1}. Spectral assessment may then be sensitive to all subtle features (weak overtone intensities) within this range, ensuring probing of both ECM chromophores and influence of water, both shown as crucial OA markers. This will be conducive to exploratory assessment of cartilage from mature human samples, and maintain a holistic view of all possible features that could be employed in multivariate analysis (such as PCA and PLS) and in machine learning (SVM etc.) [21,100] The importance of spectral features may then be evaluated to give potential diagnostic insight into changes within the tissue.

3.1.2 Spontaneous Raman Scattering correlates with OA progression

Similarly, Raman scattering spectroscopy of connective tissues has proven a potent technique for the detection and chemometric analysis of OA pathologies. Discriminating spectral features have been identified capable of diagnostic assessment. In comparison to NIR-SWIR absorption, Raman responses result from fundamental vibrational modes, presenting as sharper spectral features and with intensity directly dependent on the number of scatterers, lending itself to chemometric assessment approaches with simple interpretation.

The “fingerprint region” in the Raman spectrum describes wavenumbers between 800 - 1800 cm^{-1} and is considered rich in biochemical information, with bands associated with the chemical functional groups attributed to tissue proteins and lipids. Costa Moura et al. identified within articular cartilage that the band at 1061 cm^{-1} is typical for GAG with sulphate groups (OSO^{3-} symmetric stretch); the band at 1668 cm^{-1} for collagen (amide I); and also at 1450 cm^{-1} for collagen and proteins (CH_2 and CH_3).[52] The peak at 1375 cm^{-1} is also considered a suitable

choice for evaluating GAG (CH_3 symmetric deformation peak), unobscured by peaks associated with calcified cartilage. [20] Some key Raman scattering chromophores within native cartilage tissues are presented in Table 3.2.

Table 3.2 Raman scattering peaks of native articular cartilage. [20,49]

Wavenumber (cm^{-1})	Assignment
Native Cartilage Tissue	
1630 – 1690	C=O stretching (Amide I)
1606	Phenylalanine, tryptophan
1550 – 1600	N–H and C–N deformation (Amide II)
1450	CH_2/CH_3 scissoring; collagen & other proteins
1441 – 1460	CH_2 deformation/scissoring; protein & lipids
1424	COO^-, GAGs
1375 – 1380	CH_3 symmetric stretching; GAGs, PGs
1342	CH, GAGs
1230 – 1280	C-N stretching (Amide III)
1269 – 1270	NH_2 bending; α-helix (Amide III), functional collagen
1241 – 1245	NH_2 bending; random coil (Amide III), defective collagen
1127 – 1163	Pyranose ring
1070 – 1090	CO_3^{2-}, asymmetric stretching
1060 – 1064	SO_3^- stretching of sulfates in GAGs
1047 –1055	P–O–P symmetric stretching, CPPD
1039 – 1042	C–O–C stretching, Pyranose ring
1002 – 1004	Aromatic ring stretching, Phenylalanine
954 – 962	PO_4^{3-}, symmetric stretching
932 – 941	C–C deformation of aggrecan / C–O–C stretching of GAGs
920 – 928	C–C stretching, Proline, Collagen
875 – 880	C–C Stretching, Hydroxyproline, Collagen
856 – 858	C–C Stretching, Proline, Collagen

Unal et al. have demonstrated classification of water fractions in articular cartilage of mature bovine knee joints under NIR Raman interrogation (excitation at 847 nm), quantifying water loss as an early indicator of OA. Peaks at 3200 and 3650 cm^{-1} (OH vibrations) were monitored, associated with organic matrix (both collagen and PG) and matrix-bound water molecules. Bands at 3250, 3453, and 3630 cm^{-1} were also associated with collagen and collagen-related water molecules, and at 3520 cm^{-1} with PG and PG-related water molecules.[101]

The optical responses of proteins are amongst the most indicative for tracking OA associated changes in articulate cartilage, Kumar et al. have described how contents of amide I (1612–1696 cm^{-1}) has been shown to decrease, and the band associated with lipids (1302–1307 cm^{-1})

increase, with severity of OA.[21] Employing porcine models, Lim et al. observed a decrease of 1042 cm^{-1} (GAG-related pyran saccharide band) which indicated a decrease in GAG content in OA patients.[21] The authors also demonstrate a red shift of the amide III band from 1264 to 1274 cm^{-1} when porcine cartilage was subject to impact compression, establishing sensitivity of Raman signals also to mechanical changes. [21,102]

Changes in the amide III band ratio (1241/1269 cm^{-1}) have been reported between patients with different stages of OA, proposed as a sensitive indicator of structural and direction changes in collagen fibre bundles, relevant for early detection of OA.[21] This ratio corresponds to random coil content/alpha-helix content and can measure the degree of disorder in the collagen secondary structure, demonstrated to assess difference between healthy control and OA human knee tibial plateau, evaluated as a function of the OA grading.[20] Other major spectral differences between control and OA human knee cartilage were mapped by Oshima et al. who highlighted peaks attributed to proline (855 cm^{-1}), hydroxyproline (C-C 920 / 939 cm^{-1}), amide III (C–N / N–H, 1247/1275 cm^{-1}), and amide I (C=O, 1668 cm^{-1}). The authors' analysis suggests the spectral results describe loss of type II collagen in OA and change to the proteoglycans indicated by alteration of the GAG assigned peak at 1384 cm^{-1} (CH_3). [103]

The work of Casal-Beiroa et al. offers substantive evidence in the form of spectral biomarkers within the fingerprint region for assessing degradation of cartilage on human femoral head tissues, cross-validated with biochemical assays for quantifying sulphated-GAG and total hydroxyproline collagen. Cartilage plugs (6 mm diameter, ~1 – 1.5 mm thickness) were extracted from excised femoral heads and analysed under confocal Raman microspectroscopy using 785 nm excitation. Figure 3.3 displays the typical Raman scattering response from articular cartilage at varying Kellgren-Lawrence grades of OA severity, along with results of Spearman's correlation between the proposed biomarkers for sGAG and hydroxyapatite (HA).[49]

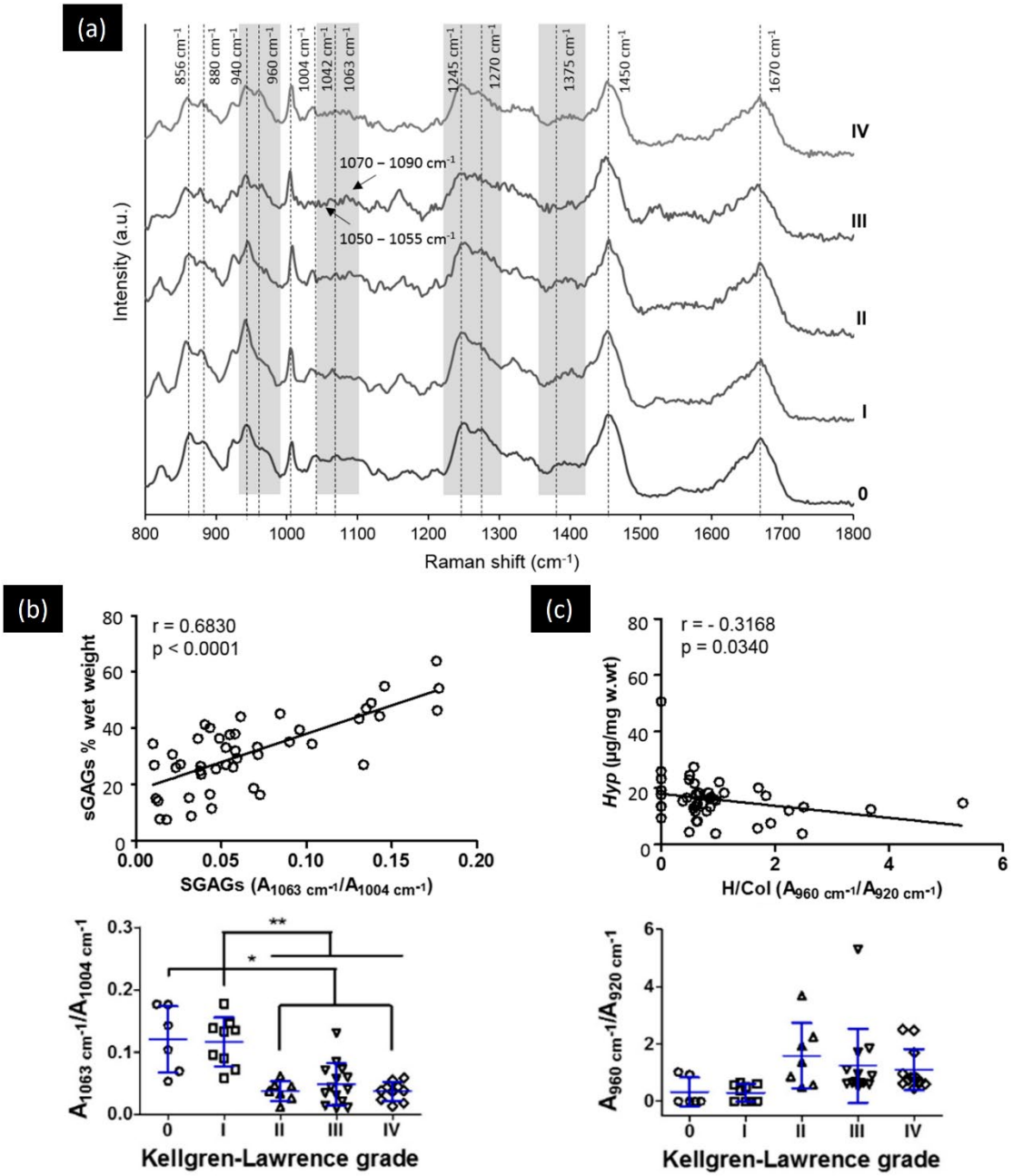

Figure 3.3**:** Correlative models of OA cartilage have been built upon NIR Raman scattering data (a.) Raman spectral response of articular cartilage of human femoral heads with increasing severity of OA marked by Kellgren-Lawrence (KL) score, 0 to IV (b.) Spearmen's correlation between sGAG content and proposed spectral biomarker, and change with KL score. (c.) Spearmen's correlation between total collagen content and proposed hydroxyapatite/collagen spectral biomarker, and change with KL score. For Spearmen's correlation: dots represent individual samples, significance is indicated as * $p < 0.05$ and ** $p < 0.01$. Raman signal obtained under 785 nm excitation. Adapted from Casal-Beiroa et al.[49] Reproduced in adherence to CC BY.

The authors propose peak area ratios as spectral biomarkers based on Gaussian fitting of peaks normalised to the phenylalanine (1004 cm^{-1}) peak, a selection presented in Table 3.1. Employing such ratios, various tissue moieties may be tracked to allow for grading of OA progression. Indeed, the authors offer the sGAG/hydroxyapatite ratio (A1063 cm^{-1}/A960 cm^{-1}) which may assess functional matrix (PG) to mineralised matrix (HA), which lowers significantly for late stage OA, and the mineralised to collagenous matrix ratio (A960 cm^{-1}/A920 cm^{-1}) which increases.[49]

Table 3.3: Optical biomarker candidates for osteoarthritis (OA) in human cartilage derived from the femoral head. Adapted from Casal-Beiroa et al.[49] Reproduced in adherence to CC BY.

Proposed Biomarker (Peak Area Ratio)	**Assignment**
A960 cm^{-1} / A1004 cm^{-1}	Mineralisation - Phosphate groups present at hydroxyapatite
A960 cm^{-1} / A920 cm^{-1}	Phosphate, Hydroxyapatite/Collagen Total – bone to collagen
A1039 – 42 cm^{-1} / A1004 cm^{-1}	Total glycosaminoglycans
A1063 cm^{-1} / A1004 cm^{-1}	Sulphated glycosaminoglycans (OSO_3^- groups)
A1063 cm^{-1} / A960 cm^{-1}	Cartilage to bone
A1070 cm^{-1} / A1004 cm^{-1}	Mineralization grade-carbonated hydroxyapatite
A1245 cm^{-1} / A1270 cm^{-1}	Collagen randomness: relative amount of random coil (defective collagen) to α-helix structure (functional)
A1375 cm^{-1} / A1004 cm^{-1}	Proteoglycans

Finally, analysis of fresh equine articular cartilage and subchondral bone identified the 1070 cm^{-1} (carbonate) and 959 cm^{-1} (phosphate) peaks as useful for distinguishing non-calcified and calcified cartilage, respectively. [20] This ratio may be employed in the survey of articular cartilage *in situ* such that a healthy (thick) layer of tissue would present a strong non-calcified tissue signal, and a degraded (thinned) layer would start to allow the calcified tissue signal to come through. The argument will be made here for spatially resolved Raman analysis of cartilage across the joint which may detect focal and site-specific degradation that may be invisible to the eye, and to typical radiographic assessment techniques.

This is largely corroborated by Esmonde-White et al. who found on human cadaveric knee tissue, intact cartilage expressed a 1063 : 958 cm^{-1} (cartilage to bone) ratio ~5 times higher and 958 : 920 cm^{-1} (bone mineralisation) ratio ~4 times lower than for areas of eroded cartilage.[56] In areas of partial erosion, a carbonate band would appear at 1072 cm^{-1} attributed to a marker of bone remodelling, proposed as an early stage response to degenerative or traumatic injury. [56]

The argument will be made here for characterisation of human femoral head cartilage under fingerprint region Raman (800 – 1800 cm^{-1}), excited by 785 nm, since this contains information pertinent to detection of OA in biochemical constituents such as mineralised tissue, collagen, GAG, PGs, etc.[49] In a similar fashion as for NIR-SWIR spectra, this may then be subjected to statistical analyses for assessing sensitivity to disease (tissue classification) and insight into biochemical compositional change.

PCA of Raman data has proven successful in distinguishing control and OA groups in murine models, with the phosphate and collagen bands shown to be significantly different. [21] Richardson et al. have demonstrated PCA-LDA on spectra from pairs of materials modelling cartilage disease to create multiple spectral scoring metrics: Human "OA" vs "Normal AC", simple purified collagen type-I vs type-II, rat injury fibro-cartilage vs rat AC. The authors purport that Raman characterisation will be most useful in assessment of patients in pre-clinical and pre-pathomorphological stages of OA which cannot be detected via MRI or other current clinical modalities.[104]

3.1.3 Spectroscopy in Arthroscopic Procedures for OA

Vibrational spectroscopy for the diagnosis of OA can only be proposed should it prove viable for a patient friendly assessment pathway. The studies described above allude to applicability in arthroscopic assessments of articular cartilage within joints *in vivo*. Here a modified fibre optic probe may be utilised, capable of delivering excitation and detection for Raman scattering and NIR-SWIR absorption spectroscopy. This would allow for a minimally invasive approach, capable of overcoming the scattering, obfuscating layers of tissue between the joint (e.g. hip or knee). In future, strategies employing adaptive optics (capable of focusing through overlaying tissue) and diffusive detection (e.g. SORS) may allow for an entirely non-invasive detection paradigm, but in the meantime minimally invasive probing (arthroscopy, endoscopy) could be utilised immediately.

Arthroscopic procedures employ surgical and measurement probes inserted into the joint of a patient via small incision (keyhole surgery). Hip arthroscopy offers minimally invasive access to the tissue of the hip for assessment or treatment, without the need for joint dislocation or cutting of ligaments. Less trauma to the body overall shortens recovery time and increases the success rate of surgical intervention. Recent trends suggest this procedure is gaining popularity over total dislocations. [105] Hip arthroscopy has been proposed as a key strategy for management of early OA, for removal of damaged tissue and areas of femoroacetabular impingement, aiming to preserve tissue before requiring definitive arthroplasty treatments. [106] Early-OA cartilage damage may be prevented or halted through access to the femoral head through arthroscopy or

surgical hip dislocation, in procedures such as femoral head reshaping, with or without cartilage transplant. Deciding the optimal timing of such procedures remains challenging since advanced OA cannot be treated this way. [106]

Other chondral defects of the hip may be treated by arthroscopic debridement, microfracture, or chondrocyte transplantation indicating the various reasons a probe may be inserted into the hip. [107] Thus, spectroscopic measurements in an arthroscopic procedure could offer diagnostic screening, focusing on any chemical precursors for OA that may provide a valuable insight for patient prognosis.

Development of NIR-SWIR absorption spectroscopic analysis of cartilage tissue has been carried out explicitly for arthroscopic intraoperative applications. [55,99] The first NIR arthroscopic study evaluated the relative proportion of water to organic substances by calculating ratio between the 1st overtone OH and CH combination (6780 – 6990 cm^{-1}) and 2nd overtone CH (8195 – 8695 cm^{-1}), found to be significantly higher on cartilage lesions than for intact cartilage. This same ratio was later found to correlate with Mankin score and mechanical stiffness for sheep models. [20]

Ferrule probes with silica optical fibres in the core placed in contact with tissues have allowed for collection of signal from human cadaveric knee *ex vivo*, [99] equine knee *in vivo,* [108] and via point mapping across whole bovine patella and osteochondral cross sections. [98] The latter has been adopted to generate spectral heat maps for assessing the spatial distribution of collagen and water, otherwise invisible to the eye. [98] In each case, quantitative analysis of the broad spectral features (overtones) could be used to assess tissue, cognizant that such features have been shown to correlate with useful OA metrics.

Similarly, Raman spectroscopy has proven efficacious for assessment of various cartilage and subchondral bone samples through ferrule optical fibre probes.[21] The work of Gaifulina et al. has demonstrated optical probe mediated fingerprint-region Raman measurements from patients undergoing exploratory arthroscopy of the knee for suspected cartilage defects, under true clinical conditions.[109] On cadaveric knee specimens with and without macroscopic cartilage lesions, the authors report the application of principal component analysis (PCA) for distinguishing advanced stage OA (grade 4) from other specimens (grades 0,1, and 2/3). Associated loading plots showed protein content was significantly higher in the control and for early lesion stages than for advanced stages. Indicative features were identified, including sGAG (1063 cm^{-1}), tryptophan (570 cm^{-1}), and collagen (C-C stretching, proline in α-helix, 939 cm^{-1}). Late-stage diseased cartilage spectra were dominated by water bands (1622 and 1645 cm^{-1}), which the authors attributed to fibrillar collagen type II.[109]

Under spectroscopic mapping, this approach was sensitive to reduction in GAG content and decreased in fluorescence intensity in cartilage lesions otherwise visually indistinguishable from healthy tissue. [109] It is worth noting that mapping results were obtained from cartilage tissue prepared as cross-sections of the osteochondral junction in 20 µm thick cryosections and placed on super mirror stainless steel slides for microspectroscopy (maps and single point). An approach closer emulating clinical *in vivo* measurements would instead see cartilage assessed at full thickness from the "superficial" surface (intact) and *in situ* on a naturally occurring substrate (subchondral bone). The practical implications of this will be further explored in Chapter 5 and answered in Chapter 6.

Esmonde-White et al. have demonstrated arthroscopic Raman assessment of cadaveric human knee and optical phantoms of connective tissues to determine the influence of cartilage thickness on signal collection. [21,56,110] The authors purport that the 850 – 1100 cm^{-1} region provides the highest spectral contrast between cartilage (consisting of type II collagen and sGAG) and subchondral bone (apatite mineral and type I collagen). Raman signal of femoral condyles was compared between regions with intact cartilage, focal lesions (partial erosion), and full thickness erosion. Both cartilage and bone signals were observed from the intact cartilage, stronger bone signal from focal lesions, and only from subchondral bone where fully eroded.[56]

Therefore, it follows that spectral profiling across the surface of the articular cartilage on human joints could allow detection of OA severity, conducive to early-stage detection and conceivably as part of routine, exploratory clinical assessment like arthroscopy. Here, in this thesis, the argument will be made for mapping of cartilage under both NIR-SWIR absorption and Raman scattering across the surface of intact human femoral head tissues. It is expected that the superolateral and inferomedial regions are the most and least weight-bearing surface of the femoral head, respectively, with Raman signal sensitive to the slight decrease in mineralisation within the inferomedial region.[111]

The step change proposed here would see application of data fusion to gain the best of Raman and NIR-SWIR sensitivity and 3D hyperspectral characterisation of the whole femoral head. Indicative approaches in literature related to data fusion of spectroscopic signals are detailed in the next section.

3.1.4 Data Fusion Approaches

Data fusion approaches seek to combine information from different modes of spectroscopic interrogation such as Raman scattering and absorption in the UV, visible, NIR-SWIR, mid-IR to IR. Since each modality harnesses different light-matter interaction phenomena, these allow for

a repertoire of interrogative tools. These approaches are classified according to the level of abstraction. Low -level abstraction of spectral data sees minimal processing and preservation of dimensionality to remain closest in form to the original measurement, e.g. intensity (y) vs wavelength (x). Mid- and high-level abstraction involve feature or trend extraction via mathematical transformation, as a summary or interpretation of the spectral data, and then characteristic features merged together. This is described as analogous to the human multisensory system, retaining perception of each sense whilst merging together for complex decision making. [112]

The intermodal combination of Raman scattering and NIR-SWIR absorption measurements has precedent in industrial and agricultural application for quantitative assessment of molten polymer beads, methanol-gasoline composition, and polyphenols content in cocoa beans. [112–114] Low-level abstraction saw a simple, arguably elegant, concatenation of the two modes of spectral data. The independent variable (wavenumber Raman shift or absorption at that NIR-SWIR wavelength) is abstracted to an index, x, and the spectral shape preserved to indicate relative spectral response (Raman scattered intensity or absorbance) at x.

Higher order abstractions allow for various, holistic combinations, extracting a summative metric or indicative features which may then be combined for multivariate or machine learning modelling. Multi-block PLS modelling can extract complementary information from results offered by different optical phenomena (e.g. NIR and MIR) or different equipment (e.g. different NIR sensors), to generate a predictive model.[115] The abstract block is built through regression of a matrix describing the tissue class (e.g. normal or damaged cartilage) to a matrix containing the spectral data. Various combinations of the blocks may be considered at a time to optimise the classification performance of the multi-block model.[116] However this and some machine learning (ML) approaches (deep learning, neural networks etc.) suffer loss of interpretability when relying on data compression methods, resulting in a “black box” model.

Here the argument will be made for use of low abstraction data fusion to retain interpretability of results – ability to directly “read” the spectrum – and compatibility with the suite of spectroscopic data analysis tools available, including feature selection and predictive modelling. The concatenated data preserves its dimensionality and relative spectral shape, whilst allowing multimodal data to be considered holistically. “Spectromics” detailed in Chapter 5 refers to the fusion of complementary Raman scattering and NIR-SWIR absorption spectral data, thus incorporating a total view of optically responsive chemical vibrations within the NIR-SWIR windows.

It is worth noting that recent work since inception of the spectromics study (Chapter 5) from Shaikh et al. has seen high level abstraction fusion to combine MIR (contact probe), NIR

(contact probe) and Raman (microspectroscopy) data for characterisation of animal models for mechanically and enzymatically damaged cartilage. [116] Spectra were collected from osteochondral plugs of bovine patella under separate protocols and equipment, which formed abstracted data blocks via PLS discriminant analysis (PLS-DA) for a predictive multi-block model (NIR + MIR, or NIR + Raman, etc.). The authors propose advantages of the multi-block approach not in its increased classification accuracy but in interpretability over other highly abstracted models, e.g. under machine learning. Correlation loadings plots allowed some insight into the chemical features of the samples "within" the black box for the contributions of different spectral regions. Thus, the spectromics argument for inherent interpretability is still valuable, and the low-level abstracted data still offers the greatest compatibility for any further statistical analyses, described in Chapter 5. This work has the added novelty of directly assessing human osteochondral samples resulting from OA specific surgeries in order to derive useful optical biomarkers.

The work of Chapter 6 pertains to construction and development of a 3D surface scanning rig able to capture co-localised Raman scattering and NIR-SWIR absorption data from tissue *in situ* rather than from excised samples (cartilage slices or osteochondral plugs) in a single multimodal system. Here a system is developed for characterising the spectral response across the surface of (largely spherical) whole human femoral heads, offering understanding of the natural and pathological heterogeneity in biochemical composition. Diagnostic potential and clinical relevance may be assessed through measurements of mature, human, in-tact tissue, classified by the attending orthopaedic surgeon.

Once more drawing inspiration from agricultural studies, the work of Huang and colleagues lays out an approach for multimodal, hyperspectral (visible and NIR absorption) measurements across the surface of apples, described in the figure below.

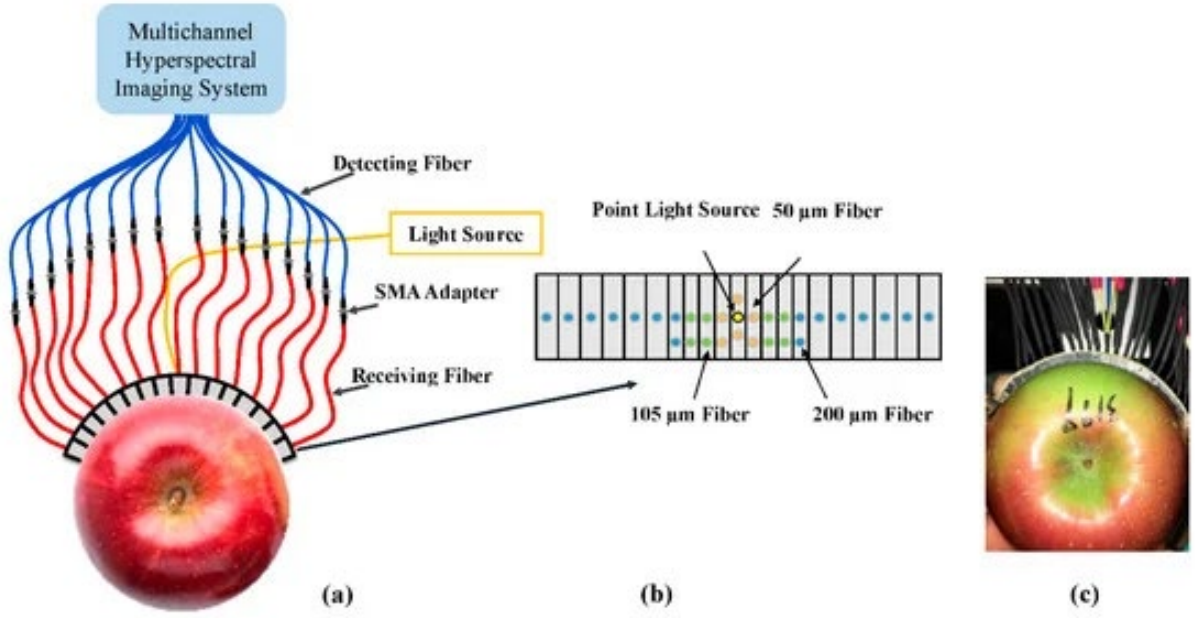

Figure 3.4 Label-free hyperspectral measurements of the surface of apples for classifying variety and quality. (a) The multichannel hyperspectral imaging (MHI) system for spatially offset reflectance spectra at light source–detector distances 1.5 – 36 mm, (b) the arrangement of optical fibres on a flexible probe, and (c) the experimental testing image. From Huang et al. [117] Reproduced in adherence to CC BY.

The multichannel system comprised an optical fibre array with a central excitation source and multiple collection fibres at discrete lateral distances from the excitation fibre (offset spectroscopy). PLSDA modelling of the visible (550 – 780 nm), NIR (780 – 1650 nm), and full region (550 – 1650 nm) of absorption data offered modelling capable of differentiating apple variety and correlating with some quality analysis metrics (firmness and soluble content refractometry value). Variety classification reported close to 100% accuracy, with better overall accuracy under combinations of the spatially resolved spectra (different depths). [117] Exact chemical changes were not explored in detail (inside the black box) though arguably agricultural practice may only need concern itself to apple variety rather than deep compositional analysis.

Such a system is informative but falls short of an ideal scanning system for assessing whole human femoral heads. Fibre channels shown here allow mapping of subsurface changes in a spherical sample but could not map with high precision changes in surfaces (apple skin or articular cartilage) with largely varying diameter. It is anticipated that the mechanical loading and lifestyle influence on joint tissue in the hip contribute to differential wearing, evidenced by focal lesions that may appear across the femoral head.

As such the system developed in Chapter 6 offers full 3D degrees of freedom for automated and contact-less scanning of the tissue surfaces. Full freedom also afford the system adaptability for a range of tissue shapes, here applied to cylindrical bone cores and largely spherical (though

practically with some prominent asymmetry) femoral heads. The literature review outlined above allows the formulation of the following hypotheses which are addressed in Chapter 5 and Chapter 6.

Hypothesis: Diagnostic performance of optical assessment of osteoarthritis in human articular cartilage is improved by enriching the spectral fingerprint with low-level abstraction data fusion, namely through concatenated Raman and SWIR data, compared to that obtained from Raman and NIR-SWIR data alone.

Hypothesis: The spectromics approach can be translated to 3D and a multimodal microspectroscopy system for 3D mapping will allow for inherently correlative measurements of Raman scattering and NIR-SWIR absorption

Here the argument is made for application of spectromics to classify samples of diseased (osteoarthritic) and control cartilage in situ on human femoral head samples (atop subchondral bone). This would answer some limitations of measurements of cartilage slices on separate systems (Raman microscope and NIR-SWIR probe) and on unnatural substrates (slices on a sample slide). The vision is to develop an integrated scanning system capable of collecting a library of spectra as ex vivo ground truth from which a clinician may assess cartilage tissue arthroscopically under spectromics, in which spectral data may be collected with a ferrule fibre optic probe inserted into the joint. This will allow detailed insight into the site-specific pathological heterogeneities expected from OA, which present under label-free non-ionising vibrational spectroscopy through clinical assessments like arthroscopy.

3.2 Photo-Ablation Therapies in the NIR-SWIR

Having established above the facilitating mechanisms of biological tissue ablation, the following review seeks to describe the trajectory of photo-ablation systems utilising the NIR-SWIR regime. The argument will be made here for the selective targeting of the water absorption peaks in this range for efficient and precise thermolysis of human tissue, at single cell precision.

As alluded to above, among the commonly employed surgical laser systems are argon (350 – 514), diode (630-980), neodymium-doped ytrrium aluminium garnet (Nd:YAG, 1064 nm), holmium: YAG (Ho:YAG, 2100 nm), erbium:YAG (Er:YAG, 2940 nm), and CO_2 (10,600 nm). Each target a specific absorption chromophore for precise cuts under a surgeon's hand in diverse applications as lithotripsy, oral surgery/dentistry, and cataract surgery. [92]

For example in soft tissue dissection, the CO_2 laser has proven most practical for its capacity to ablate and cauterize simultaneously, mediated by the MIR water absorption peak.[94] Novakovic

et al. report the effects on treatment of premalignant lesions of the tongue employing either water targeting CO_2 and thulium (Tm, 2013 nm), or haemoglobin targeting (532 nm and 940 nm) laser systems. The authors express preference for the Tm-based diode laser for its optical fibre delivery and superior haemostatic properties over the bulky CO_2 systems. [118] In hard tissue applications such as lithotripsy, Ho:YAG has proven the equipment of choice for treatment of kidney stones, but now thulium-doped fibre laser (TDFL) systems pose as promising contenders by virtue of their integration into smaller fibres, use of lower pulse energies, and high repetition rates. [119] In general, TDFL systems targeting the NIR-SWIR ~1950 nm water absorption peak promise highly efficient energy delivery suitable for accurate ablation outcomes (minimal collateral) under non-contact modes. [92]

Today, the most compelling systems in practice for single-cell level excisions employ UV lasers, which may utilise photochemical and plasma phenomena for selective thermolysis. The maturity of this technology and ease of implementation is exemplified in commercial tools for UV diffraction limited nanosurgical incisions of *ex vivo* cell samples such as the MMI "CellCut" system from Olympus. Semi-automated isolation of cells from a monolayer sample or for simple organisms may be carried out under a ns-pulsed 355 nm laser through an operator friendly interface, sample area marked in software via a stylus and collected in an adhesive vial through automated motorised stages.[120,121]

Photoablation in the UV range (~315 – 400 nm) under ps pulses offers non-linear ablation (ionisation) through plasma generation (solid to gas sublimation) for subcellular effects on tissue. [122] However careful selection of the incident wavelength is crucial since UV-B (~280 – 315 nm) is strongly absorbed by DNA provoking irreversible damage and mutations *in vivo*, and UV-C (~100 – 280 nm) suffers from very high attenuation in turbid media and requires specialised, expensive optical elements. [123] Choice of wavelength is also not the sole determinant of ablation precision. Van Acker et al. report ablation of cancer cell lines for plasma-mass spectrometry using an ArF excimer (193 nm), but state that under a 30 μm spot size, single cell ablation from a cluster could not be guaranteed. [124]

Thus, attention is turned to precise and effective ablation under NIR-SWIR radiation. A strong case has been made for utilising NIR-SWIR wavelengths for endovenous laser ablation (EVLA) applications, mediated by inserted fibre probes, such as in treating chronic vein insufficiency through catheters in incompetent truncal veins (varicose veins). Here haemoglobin was typically employed as a major absorption chromophore, targeted by lasers at 810 nm and 940 or 980 nm, but increasingly favouring the 1470 nm water absorption local maximum. [125]

Extending this argument, there is evidence for shifting radiation toward the 1940 nm absorption maximum, boasting over fourfold increase in μ_a over 1470 nm.[126] In a recent review, Setia et al

contend that EVLA with 1920/1940 nm systems offered patients high occlusion rates and low post-operative complications, attributed to reduced collateral to perivenous structures. The latter is attributed to the high absorption of >1900 nm laser light by water limiting unwanted penetration depths into the vein wall. [126] The benefit of 1940 nm has been further corroborated in multicentre patient follow-up studies after 2 years [127] and proven at least comparable to 1470 nm in porcine liver models, itself shown to correlate with 1-year clinical outcomes. [128]

In the latter case, Whitely et al. cast doubt on the claim that the higher absorption profile reduces the amount of power needed at 1940 nm over 1470 nm, with small differences presenting at low incident powers, some greater spread of effects at 1470 nm, but some higher carbonisation at 1940 nm. [128] Nonetheless, ~1900 nm targeting systems have grown in prevalence for diverse cases such as oral ablation [118,129], liver ablation [130], and as a contender for effective lithotripsy [119,131], each citing this claim.

Indeed Ho:YAG systems have been the longstanding preference for photoablation of kidney stones, targeting intercrystalline water at ~2100 nm to induce thermal expansion, vaporisation and stone fragmentation. [119,132,133] Recent trends show a move towards the 1950 nm peak via Tm-fibre systems, boasting a similar four times increase in μ_a (14 mm^{-1} vs 3 mm^{-1} attenuation at 22 °C), offering faster stone ablation and reduced penetration depth for an improved safety profile. [119] Low pulse energies are preferred for equivalent ablation under Ho:YAG and continuous wave (CW) systems. Pal et al. reported a Q-switched Tm-fibre laser for both effective urinary stone fragmentation and soft tissue ablation, demonstrating two-fold narrower soft tissue damage and four-fold lower charring under pulsed irradiation (350 – 750 ns, 55 – 135 kHz) over CW ablation.[134] This is indicative of the thermal confinement process described in the preceding chapter and lays motivation for a pulsed TDFL system for achieving precise NIR-SWIR photoablation.

Finally, it is worth noting that though the absolute maximum for water absorption in the NIR to MIR range is found at 2.94 μm (Er:YAG) [135], radiation here (as for 10.6 μm CO_2 systems) cannot be transmitted by silica based optical fibres.[129] Highly precise pulsed laser photo-ablation for studies in ophthalmology (keratoplasty [136,137] and trephination [138]), wound healing, [139] and dental surgery [140] have been demonstrated offering clear benefit to both clinician and patient. These works are still of benefit as they substantiate the overall aim of targeting water absorption peaks, under tuned pulse durations and repetition rates, for effective ablation of a range of tissue types.

The literature describes that single-cell level ablation with ~1950 nm in the ns pulsed regime has yet to be demonstrated. It is anticipated that short pulses would maximise thermal and

mechanical confinement for high precision, and benefit from the lowered ablation threshold afforded by high absorption cross section.

Zhao and colleagues employed 805 nm 250 fs pulses for axotomy of neurons from C. Elegans samples (<3 μm in diameter), capable of incisions down to 2 μm. The authors contend the advantage of fs pulsed ablation for the confinement of laser absorption to submicron focal volumes below the surface and avoiding out of focus damage. [141] Mangione and colleagues utilised 780 nm fs pulses for photoablation of single cells in Drosophila epidermis reporting precision of < 5 μm and capacity to monitor samples (cell shape change) during and after ablation. The authors employed a commercial laser scanning microscope with proprietary photo-bleaching programme (controlling laser power percentage and pixel dwell time) which exposed a set pattern over 1-3 iterations. [142] This shows exciting application for precise ablation of targets within a heterogeneous, *in vivo* cell environment. However, an ideal system would have control over laser parameters (repetition rate, pulse duration) such that the system may be adapted for a range of human cells with differing thermal and mechanical diffusion times.

The literature review outlined above leads to the formulation of the following hypothesis, examined in Chapter 7.

Hypothesis: Targeting the NIR-SWIR water absorption peak with 1950 nm laser pulses through a novel ns-pulsed Tm-doped laser can allow for precise single-cell scale ablation for clinical application.

Here the argument is made for a Tm-doped fibre laser with precise control over fundamental pulse parameters that allows for step-change single-cell scale resolved ablation in human cell samples. This answers the need for tunable photoablation operating in the NIR-SWIR regime, conducive to optical strategies which benefit from reduced scattering of light. Maintaining compatibility with conventional silica optics by targeting the 1.95 μm water peak should offer easy integration into both microscope-based and potential clinic-based, *in vivo* applications for precise treatments.

Chapter 4 Hypothesis and Aims

HYPOTHESIS 1: Diagnostic assessment of OA is improved using fused Raman scattering and NIR-SWIR absorption data, compared to that obtained from Raman and NIR-SWIR data alone.

Aim: Optimisation of Raman and NIR-SWIR spectroscopy and analysis of human articular cartilage via data fusion to classify diseased (osteoarthritic) and control tissue samples *ex vivo*.

I. Development of Raman scattering and NIR-SWIR absorption spectroscopy protocol for slices of cartilage tissue excised from human femoral heads, including acquisition parameters and equipment.
II. Investigate spectral processing and analysis methods for data fusion, multivariate analysis, and machine learning modelling for accurate tissue classification.
III. Determine whether fused data can provide enhanced information for precise and reliable OA detection.
IV. Determine spectral features useful for clinical assessment (diagnostic spectral biomarkers).

HYPOTHESIS 2: The spectromics approach can be translated to 3D and a multimodal microspectroscopy system for 3D mapping will allow for inherently correlative measurements of Raman scattering and NIR-SWIR absorption

Aim: Development of a novel multimodal 3D microspectroscopy system for co-localised Raman and NIR-SWIR hyperspectral mapping of pathological heterogeneities across diseased and control tissue surfaces for diagnostic application.

I. Investigate spectral response of osteoarthritic cartilage tissue *in situ* on human femoral head subchondral bone.
II. Development of protocol and optimization of equipment for handling whole femoral head and bone core samples and carrying out precise sample-scanned microspectroscopy and photogrammetry.
III. Determine whether this system is suitably sensitive to vibrational spectral features in the NIR-SWIR range conducive to biochemical assessment.
IV. Investigate the spectromics concept on whole cartilage surfaces for an *ex vivo* ground truth for future clinical application.

HYPOTHESIS 3: Targeting the NIR-SWIR water absorption peak with 1950 nm laser pulses through a novel ns-pulsed Tm-doped laser can allow for precise single-cell scale ablation for clinical application

Aim: Development of a microscope laser ablation system with precise targeting and pulse parameter control for ablation with minimal collateral damage.

I. Development a precise ablation platform integrating a custom Th-doped fibre pulsed laser into a microscope system
II. Optimisation of optical system for targeting samples with single-cell scale precision.
III. Optimisation of pulse parameters (pulse duration, exposure time, average power, repetition rate) for effective ablation with minimal collateral damage.
IV. Determine whether 1950 nm ablation can achieve single-cell scale precision on a clinically relevant human sample (neuroblastoma, SH-SY5Y).

Chapter 5 Holistic vibrational spectromics assessment of human cartilage for osteoarthritis diagnosis

This chapter details results published in part as a research article with Biomedical Optics Express, for which I was first author and primary contributor. Reproduced in adherence to CC BY 4.0

Hiroki Cook, Anna Crisford, Konstantinos Bourdakos, Douglas Dunlop, Richard O. C. Oreffo, and Sumeet Mahajan, *"Holistic vibrational spectromics assessment of human cartilage for osteoarthritis diagnosis"*, Biomed. Opt. Express 15, 4264-4280 (2024) [1]

I would also like to acknowledge Dr George Devitt for training in use of the IRootlab toolbox.

5.1 Abstract

Osteoarthritis (OA) is the most common degenerative joint disease, presented as wearing down of articular cartilage and resulting in pain and limited mobility for 1 in 10 adults in the UK.[10] There is an unmet need for patient friendly paradigms for clinical assessment that do not use ionising radiation (CT), exogenous contrast enhancing dyes (MRI), and biopsy. Hence, techniques that use non-destructive, near- and shortwave infrared light (NIR, SWIR) may be ideal for providing label-free, deep tissue interrogation.

This study demonstrates multimodal "spectromics", low-level abstraction data fusion of non-destructive NIR Raman scattering spectroscopy and NIR-SWIR absorption spectroscopy, providing an enhanced, interpretable "fingerprint" for diagnosis of OA in human cartilage. This is proposed as method-level innovation applicable to both current arthro- or endo-scopic (minimally invasive) or potential exo-scopic (non-invasive) optical approaches.

Samples were excised from femoral heads post hip arthroplasty from OA patients (n = 13) and age-matched control (osteoporosis) patients (n = 14). Under multivariate statistical analysis and supervised machine learning, tissue was classified to high precision: 100% segregation of tissue classes (using 10 principal components), and a classification accuracy of 95% (control) and 80% (OA), using the combined vibrational spectroscopy data. There was a marked performance improvement (5 to 6-fold for multivariate analysis) using the spectromics fingerprint compared to results obtained from solely Raman scattering or NIR-SWIR absorption spectroscopy data.

Furthermore, clinically relevant tissue components were identified through discriminatory spectral features – spectromics biomarkers – allowing interpretable feedback from the enhanced fingerprint. In summary, spectromics provides comprehensive information for early OA detection and disease stratification, imperative for effective intervention in treating the degenerative onset disease for an aging demographic. This novel and elegant approach for data fusion is compatible with various NIR-SWIR optical devices that will allow deep non-destructive penetration.

5.2 Introduction

Osteoarthritis (OA) presents a major public health challenge recognised as a serious burden for the individuals affected, healthcare systems, and resulting in significant national and global socioeconomic costs.[10,11] Current modes of assessment of articular cartilage (AC) in the clinic are typically invasive (endoscopy, arthroscopy), or destructive (biopsy, histochemistry), incorporating ionising radiation and/or exogenous contrast (CT, X-ray, MRI).[23,53] Each modality provides different levels of qualitative morphological information of connective tissues to assess the health of the patient. Critically, none of these indicated techniques provide a definitive diagnosis for OA, which needs to be confirmed by secondary methods.

Current gold standard approaches for diagnosing OA rely on the detection of pain, radiologically presenting morphological changes (joint space narrowing, osteophytes formation), or accumulation of synovial fluids.[35,143] OA presents degradation and loss of articular cartilage, the lubricating and shock absorbing inter-joint layer, developed over many years, and which can pre-date symptoms over decades.[144] Hence, early diagnosis is crucial for effective and timely intervention to reduce pain, improve mobility, and patient quality of life. To date, there is no cure for OA, rather treatments are focused on alleviating inflammatory symptoms or interventional surgery including arthroplasty and prosthetic joint implant.[145–147] Detection of pre-pathomorphological and biochemical changes will inform new and earlier forms of pharmacological and lifestyle interventions to alter the course and progression of the disease.[148,149]

Near- and Shortwave Infrared (NIR, SWIR) absorption and spontaneous Raman scattering are highly sensitive to structural and biochemical changes offering an innovative approach for early detection associated with the onset of OA, using spectral biomarkers. This can be ideal as both Raman and NIR-SWIR absorption spectroscopy can be carried out with minimal sample preparation, conducive to native *in situ* tissue assessment. Moreover, both NIR-SWIR absorption and Raman spectroscopies can utilise the biological 'optical' transparency windows. Such windows exist in various native human and animal tissue types and are quantified by the absorptive and scattering effect of common endogenous chromophores. In these regions, optical light undergoes reduced scattering and absorption, facilitating deep penetration of inherently non-ionising radiation.[12,13,66]

Depth of penetration for NIR-SWIR light into AC tissue has been recorded up to 5 mm, indicating high suitability for clinical assessment.[18,51] Since the normal thickness of human cartilage is 1 – 3 mm, optical interrogation in the spectral range of 1.4 – 2.5 μm is considered optimal for AC tissue assessment.[18,20] Thus, spectroscopic techniques such as NIR-SWIR absorption and

Raman spectroscopy (if carried out with NIR or SWIR excitation) offer valuable chemometric and structural information at depth for non-destructive, potentially non-invasive, *in vivo* clinical assessment.

The goal herein is to utilise the inherent transparency windows of tissue to extract valuable chemometric and structural information for non-invasive appraisal to enable useful clinical assessment.

NIR-SWIR absorption spectroscopy has been shown to be sensitive to structural and compositional changes resulting from loss or alteration of the tissue extracellular matrix (ECM).[50] The spectral response provides information relevant to structural and functional characteristics, important in the assessment of degeneration of cartilage.[16,17,48,55] Specifically, absorbance bands in the NIR and SWIR are overtones and combinations of the fundamental vibrations of O-H, C-H, N-H, and S-H bonds which form the molecular framework of the tissue.[50,51,150] As such, NIR-SWIR absorption spectroscopy can offer a non-destructive method to determine thickness, biomechanical properties, and composition of articular cartilage especially water fractions for evaluation, prediction, and monitoring of OA progression.[16–18,20,21,100]

Spontaneous Raman scattering spectral signal between 1800 – 800 cm^{-1}, the "fingerprint region", is relatively insensitive to water (only O-H bending ~1640 cm^{-1}), whilst particularly sensitive to structural and skeletal vibration modes, thus ideal for biological tissue characterisation.[151] Raman spectroscopy using NIR excitation has been employed by a number of groups in the diagnosis of osteoarthritis, with biochemical and biomechanical change in human and preclinical models correlating with gold standard assays.[20,21,49] Spectral features including those associated with collagen, GAG, and PG (major proteins of the ECM), water fraction, lipid and amides have proved efficacious as preclinical and prepathomorphological biomarkers.[101,103,104] Specific biochemical distributions have been mapped up to depths of 0.5 mm with NIR excitations[151–154] and OA relevant signals (depth and GAG content) collected at depths >10 mm using spatially offset Raman spectroscopy (SORS).[155]

NIR-SWIR absorption and NIR-excited Raman spectroscopy have been used to interrogate cartilage and have shown potential for OA diagnosis, especially through evaluation of depth-dependent features.[156] Given these techniques are mediated by different optical phenomena, namely changes in dipole moment (overtones of vibrational modes) and changes in polarization, respectively, NIR-SWIR absorption and NIR-excited Raman spectroscopy offer complementary information. As such, these modalities can be combined to yield a more holistic chemical 'fingerprint' of the sample of interest. This study presents the first demonstration of an elegant combination of vibrational spectroscopy techniques operating in the transparency windows to

augment their diagnostic assessment potential of human articular cartilage. Raman scattering(sensitive to change in polarisability) and NIR-SWIR absorption (change in dipole moment) signatures are concatenated through low-level abstraction data fusion, into a new “spectromic” fingerprint. [112–114]

The fused data was subjected to statistical and machine learning analysis, namely supervised Principal Component Analysis – Linear Discriminant Analysis (PCA-LDA) and supervised support vector machine (SVM).[112] The new fingerprint facilitated improved classification accuracy and delineation between control and osteoarthritic AC tissue compared to spectra from each technique individually. The low-level abstracted data is directly interpretable since significant spectral features used to classify the tissue can highlight clinically relevant biomarkers, and is compatible with various statistical and machine learning assessments.

The current studies demonstrate the efficacy and power of a spectromics approach to provide a holistic assessment of human cartilage tissue for OA diagnosis, with therapeutic implications for an increasing aging population. This is directly compatible with current minimally invasive procedures (arthroscopy, endoscopy), and potentially with completely non-invasive implementations using NIR-SWIR wavelengths.

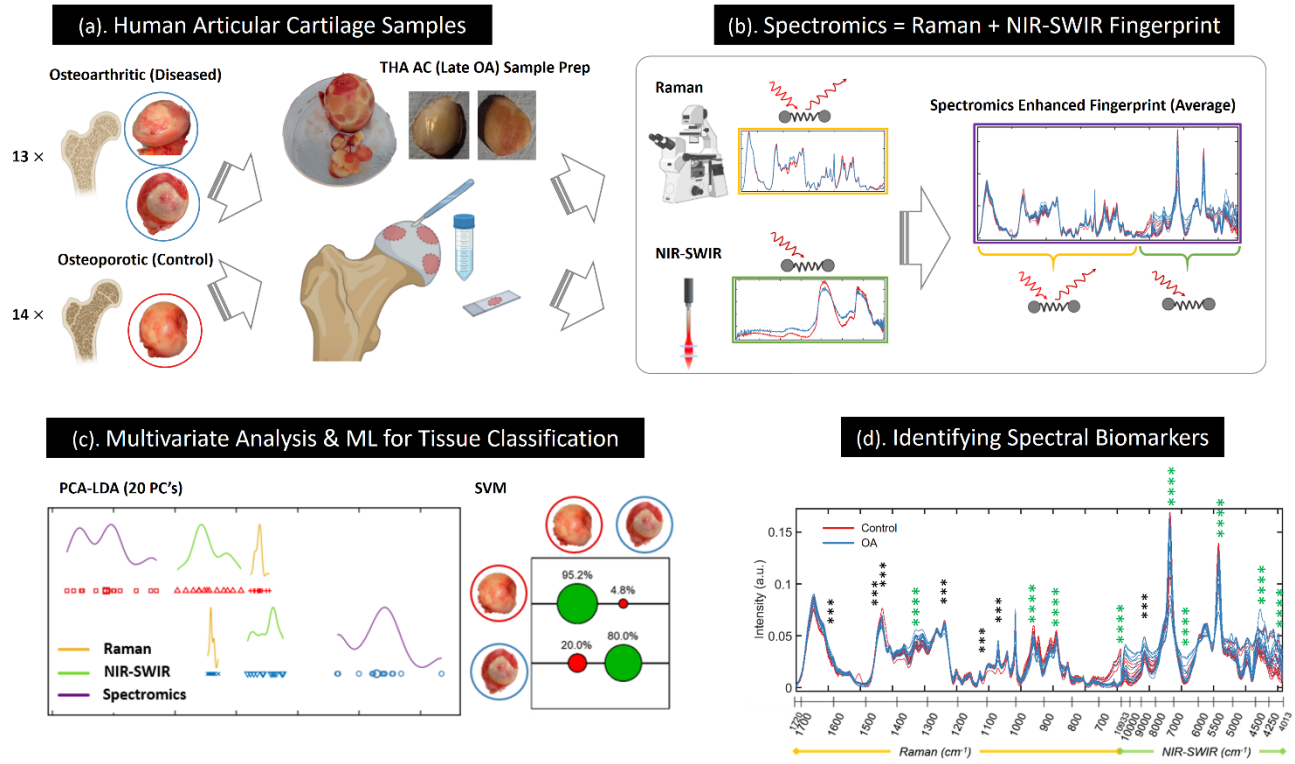

Figure 5.1 Spectromics Concept: More than the sum of its parts (a). Cartilage samples excised from femoral heads post arthroplasty, control and diseased tissue model represented by OA and OA tissue, respectively. Superficial side of cartilage characterised by Raman scattering spectra and SWIR absorption spectra on

separate systems. (b). Spectromics fingerprint constructed via pre-processing and concatenation of both spectral modes. (c). Multivariate analyses and supervised machine learning allow tissue classification and (d.) identifying spectral biomarkers. Created in part with BioRender.com.

HYPOTHESIS 1: Diagnostic assessment of OA is improved using fused Raman scattering and NIR-SWIR absorption data, compared to that obtained from Raman and NIR-SWIR data alone.

Results described here relate predominantly to Aim 1 wherein proof-of-concept for a new diagnostic spectroscopic paradigm will be demonstrated, as well as establish the motivation for Aim 2 for developing a multimodal microspectroscopy system as a platform to facilitate this paradigm, detailed in Chapter 6.

5.3 Methodology

5.3.1 Cartilage Samples and Preparation

Articular cartilage samples, obtained with full ethical approval and patient consent, were excised from human femoral heads manually using a scalpel blade. Cartilage tissue slices were taken parallel to the femoral head surface, as deep as the subchondral bone. Cartilage slices were washed (phosphate buffered saline, PBS) fixed in 4% paraformaldehyde (PFA) for 72 hrs (4 °C, gentle shaking), washed (PBS 3x), and stored, refrigerated, in PBS. Tissue storage conditions were found to be compatible with vibrational spectroscopy characterisation, with consistent Raman spectral responses reproduced despite storage periods approaching 6 months.

This work was approved under the University of Southampton's local Ethics and Research Governance Office (ERGO 71875) and by the National Health Authority – North West – Greater Manchester East Research Ethics Committee (18/NW/0231) and conformed to the ethical guidelines of the Helsinki Declaration.

For spectroscopic analysis, AC samples were cut into square slices, side lengths of the order of 10's of mm, thickness between 0.8 – 1.2 mm, dimensions determined by Vernier calipers. For each sample, the "superficial surface" describes the outermost layer of cartilage on the femoral head (in contact with the acetabular cup) and "deep side" the layer proximal to the subchondral bone. This terminology reflects the zonal stratified structure reported for cartilage wherein the superficial- , middle-, and deep zones (SZ, MZ, DZ) and calcified zones contain varying collagen fibre orientation and composition.[18,53,54,156]

Samples obtained from osteoarthritic (OA) femoral heads served as the diseased AC model, while samples from osteoporotic (OP) femoral heads, with no detectable OA or sign of other cartilage degeneration, served as the control model.[157,158] Both classes of whole femoral head tissue were obtained as consequence of interventional total hip arthroplasty (THA) surgery. Patient information included only patient age and gender, and classification as "OA" or "OP" joint tissue.

Classification was confirmed by the consultant orthopaedic surgeon (Prof. Douglas Dunlop, University of Southampton) with OA samples typically Grade 3 & 4 under Mankin scoring, indicating late-stage progression. OA pathologies result in severe thinning of AC around the femoral head such that the subchondral bone is typically exposed in large regions. OA samples were taken from areas where articular cartilage remained present. OP (non-OA) samples resulted from THA of patients with compromised bone integrity leading to femoral neck fracture, and presented with thicker and smoother layers of cartilage across the femoral head surface.

It is worthy to note that human cartilage from patients with OP may be considered an imperfect model for control cartilage since the osteochondral samples ultimately derived from age-related health conditions. This was justified in first part by the limited availability of truly healthy aged human cartilage due to ethical and practical constraints. Analysis of human osteochondral explant samples is particularly needed for enabling development of clinically feasible paradigms. [159] More crucially, the femoral head joint samples chosen from OP patients presented with full-thickness articular cartilage and with no OA pathology or sign of other degenerative disease. Confirmation by the consultant orthopaedic surgeon offers a gold standard classification. Thus, the relative preservation of tissue in the OP patient samples makes this a practical control model of articular cartilage.

This line of reasoning has some precedent in the literature and has also been successfully employed in related publications from our collaborators. Buchwald et al employed femoral head samples from THA of adult patients (49 – 88 years) with radiologically presenting OA (KL Grades 2-4) and after traumatic femoral neck fracture (post-hoc assessment, KL Grades 0-1), as the diseased and control model, respectively, in significant classification of subchondral and spongy bone under Raman microspectroscopy. [111] Casal-Beiroa et al. also report Raman spectral classification of femoral head articular cartilage between that from THA of adult patients (42 – 92 years) with OA (KL Grades 1-6) and those classified as "healthy" (KL Grade 0) by attending clinical doctors. [49] Finally, OP samples, classified as non-OA by orthopaedic surgeon, formed the control model for Crisford et al. who characterised depth-dependent Raman signatures and non-linear microscopy of osteoarthritic articular cartilage, [157] and for Kok

et al. who employed novel machine learning classification of Raman signals for OA diagnosis of cartilage. [158]

Samples from both OA and OP patients were selected in order to match and be equally distributed across anthropometric parameters. Spectra were collected from tissue from n = 13 OA patients and n = 14 OP patients for this proof-of-concept study. The OA population consisted of three women and ten men between 57 and 83 years of age, and the control (OP) population of nine women and five men between 40 and 88 years of age. The average age (mean ± SEM) for OA and control patients was 67.5 ± 2.8 and 68.1 ± 4.7, respectively.

5.3.2 Raman Scattering Microspectroscopy

Raman spectroscopy of the cartilage samples was carried out *via* modification of a previously reported protocol. [156] Spectral measurements were carried out by Dr Anna Crisford, University of Southampton. Samples of AC were placed on a quartz slide, "superficial" side up, and their spectra centred at 1200 cm^{-1} (614 – 1722 cm^{-1}) captured in reflectance geometry. Measurements were carried out on a Renishaw InVia microscope system with samples excited using a 785 nm laser focused through a Leica 50x (0.75 NA) short working distance (~200 μm) objective. Renishaw WiRE 4.1 software was used to collect data and set measuring parameters. The instrument was calibrated (pixel wavenumber calibration) to the 520 cm^{-1} peak of a silicon reference sample before each experiment, dark background signal subtracted, and cosmic rays removed after acquisition using WiRE. Spectral resolution was recorded as $\Delta\lambda$ ~1.1 cm^{-1}.

Spectral data was acquired across the tissue surface through translation of the sample stage in random steps of the order of 100's μm. For each position, a mean average spectrum of 3 acquisitions with exposure time of 5 s was recorded. A modal average of 3 samples were investigated for each patient with 10 spectra measured from each sample.

5.3.3 NIR-SWIR Absorption Spectroscopy

NIR-SWIR spectroscopy of the cartilage samples was carried out on a homemade benchtop system, described in Figure 5.2. Samples of AC were placed on a gold-coated mirror slide, "superficial" side up, and spectra between 11,127 – 3993 cm^{-1} (899 – 2504 nm) captured in transreflectance geometry. Incident excitation light was provided by a broadband halogen lamp (HL-2000-FHSA-LL, Ocean Insight) emitting as a blackbody across the NIR-SWIR range, and signal collected via an NIRQuest2.5+ (Ocean Insight) spectrometer. Both were coupled to a ferrule fibre optic reflectance probe (R400-7-VIS-NIR, Ocean Insight) with a profile of 6 annular fibres for excitation and 1 central fibre for collection. [17] Two planoconvex uncoated lenses

collimated and focused light onto sample, allowing for contact-less measurements. Spectral resolution of the spectrometer was quoted by the manufacturer at Δλ ~6.3 nm.

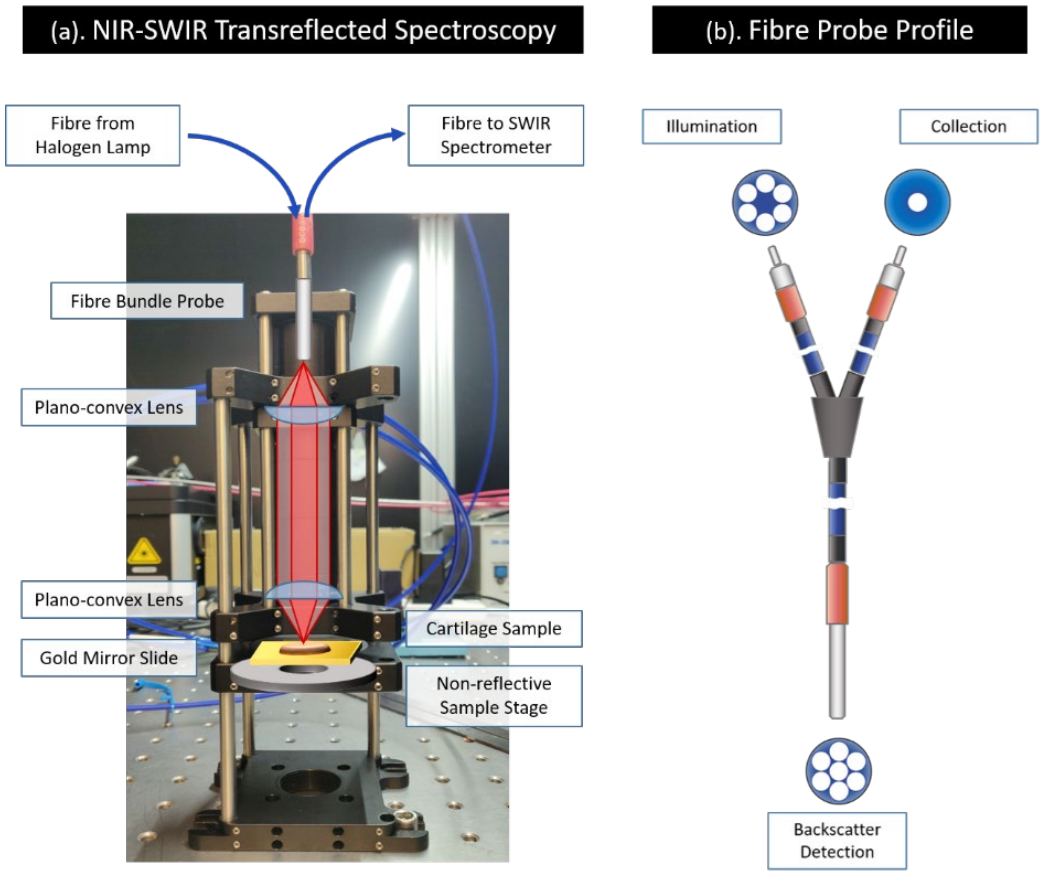

Figure 5.2 NIR-SWIR Absorption Spectroscopy Experimental Setup: (a). Articular cartilage sample placed on highly reflective gold slide for transreflected absorbance measurements with broadband illumination from halogen lamp collimated and focused onto sample via uncoated plano-convex lenses, signal measured with SWIR spectrometer (b). Broadband illumination and signal collection mediated by ferrule backscatter detecting fibre bundle probe, with 6 annular fibres for illumination and 1 central fibre to transport spectral signal.

Spectral data was acquired across the tissue surface through translation of the sample stage in random steps of the order of 100's μm. For each position, a mean average spectrum of 100 acquisitions with exposure time of 10 ms was recorded. A modal average of 3 random samples were investigated for each patient and 10 spectra measured from each sample. It should be noted that, for this study, cartilage samples for each patient were measured on separate Raman scattering and NIR-SWIR absorption spectroscopic instruments, and measurement points were not spatially correlated between instruments.

Wavelength dependent absorbance was calculated assuming propagation of light into sample following Beer-Lambert theory, namely

$$A = \varepsilon cl = -log10\left(\frac{I}{I_0}\right)$$

where ε is molar absorptivity, c is concentration of the attenuating species, l is optical path length, I is total transreflected intensity measured with sample on the mirrored slide, and I_0 is total intensity reflected solely from the slide. This also assumes "absorbance" accounts for both absorption and scattering events, characteristic to the sample, which result in loss of intensity. A more apt term may be "attenuation" but absorbance is oft quoted in this field with intensity recorded in arbitrary units.[17,20,51,80]

This theory also prompted measurements be taken from samples with an average thickness between 0.8 and 1.2 mm, such that l can be kept consistent and chemical differences be evident between samples. Thickness was determined via Vernier callipers with resolution down to 0.01 mm. Measurements were taken in a transreflectance geometry by virtue of the highly reflective gold substrate, meaning that maximum photon path length is twice the sample thickness since penetration depths of 2 mm into articular cartilage have been recorded for wavelengths between 900 – 2500 nm.[18]

5.3.4 Spectral Pre-processing

Spectra were labelled with the patient's age, sex, and OA/OP classification. The modal average was 30 spectra per patient (10 spectra per sample, 3 samples per patient). Spectral data underwent pre-processing transformations prior to classification via multivariate analysis, carried out in iRootLab (0.15.07.09-v) toolbox within MATLAB R2020a software (MathWorks).[160] Pre-processing methodology was developed from preceding literature, with optimal parameters chosen manually to achieve best performing classification models built separately on the Raman and the NIR-SWIR spectral data sets. Since the spectral data sets arose from different physical phenomena, pre-processing steps were accordingly chosen to best represent the data.

Raman spectra represent the magnitude of scattering due to interaction with a given vibrational mode (energy represented as wavenumber shift) such that an ideal signal displays narrow and defined peaks with minimal non-scattered or fluorescence interference background signal. [161] Conversely SWIR spectra represent the absorption of light mediated by overtones of vibrational modes (absorption of light of a given wavenumber), possessing much broader features resulting from overlap of overtone and combination bands.[51,161] The superposition of these bands results in lower specificity and structural selectivity than that of IR absorption or Raman scattering, prompting the use of 1st-derivative spectra to ensure subtle features could be retrieved effectively.

Raman scattering spectra were treated with 5th-order polynomial baseline correction, to eliminate slow varying offset attributed to interference of fluorescence and Mie scattering.[161–163] Wavelet de-noising via 6 level Haar wavelet thresholding minimised random spectral noise without affecting signal quality.[160,164] Rubber-banding baseline correction anchored the primary and terminal ends of each spectra to the horizontal axis, before vector normalisation. [163,165,166] The former transformation connects the minima of the spectral curve (y) with a straight or spline line to create a baseline. This "rubberband" is "stretched" over the curve and subtracted, effectively anchoring the start and end points to $y = 0$. The latter sees signal intensity divided by a normalisation factor, here the square root of the sum of squared signal intensities.

NIR-SWIR absorbance spectra were first treated with a 1st-derivative transformation to elucidate subtle features, as well as eliminate baseline offset, linear trends, and interference from light scattering.[51,161] To mitigate subsequently increased noise (reduced SNR), a 2nd order Savitsky-Golay smoothing filter was applied (suitable for vibrational spectroscopy data) with 9 filter coefficients (reducing noise whilst preserving information). [51,161,166] This algorithm follows a moving-window iteration which replaces spectra in a given window (spectral points) with a low-degree polynomial via a least-squares approach. Here a larger window may produce less noise but would sacrifice more subtle peaks. Then, a rubber-banding baseline correction was also applied, suitable for later concatenation since the terminal value of the Raman region could marry with the starting value of NIR-SWIR. Finally, a further application of a 6 level, Haar wavelet de-noising transformation, before vector normalisation served to make Raman and NIR-SWIR spectral peaks a compatible magnitude whilst retaining pertinent spectral features.

5.3.5 Concatenation

The spectromics fingerprint was built for each patient by concatenation (data fusion) of Raman scattering spectra and NIR-SWIR absorption spectra. Concatenation is thus a low-level abstraction of the data wherein the overall spectral shape is preserved (Raman scattering and NIR-SWIR absorbance) and the independent variable becomes a reference point in the spectromics fingerprint. This data fusion process resulted in Raman spectra accounting for the first 1011 independent variables (data points) and NIR-SWIR spectra the last 512 points. [112–114]

For each patient, the mean averaged pre-processed Raman scattering was fused to the mean averaged pre-processed NIR-SWIR absorption spectral data. This was motivated by the fact that slices of cartilage were preserved and stored together per patient and measured on separate optical systems, so that a particular Raman mode spectrum and a particular NIR-SWIR mode spectrum could not be spatially correlated to a position on the femoral head of that patient. As such one averaged Raman mode spectrum, one averaged NIR-SWIR mode spectrum, and one

concatenated spectrum was produced for each patient, representative of the chemical composition of the whole femoral head cartilage.

Previously we have reported on the low level fusion between two Raman spectra excited at different wavelengths for accurate, label-free characterisation of bacterial pathogens.[164,167] Low level abstraction has the added benefit of direct interpretability and compatibility with numerical processing using established spectral analysis tools such as iRootLab [160], and other recent promising resources such as nippy [168] and RamanSpy. [169]

5.3.6 Multivariate Analysis

PCA-LDA

Each of the pre-processed Raman scattering, NIR-SWIR absorption, and spectromics data set was mean centred before Principal Component Analysis (PCA).[51] The PCA process decomposes the spectral data under the form:

$$\mathbf{X} = \mathbf{T}\mathbf{P}^{\mathrm{T}} + \mathbf{E}$$

where $\mathbf{X}$ describes the pre-processed spectral data, $\mathbf{T}$ the PCA scores, $\mathbf{P}$ loadings of each PCA score, and $\mathbf{E}$ any residual values.[161] PCA scores represented the projection of sample spectra onto the principal components (PC's) that accounted for most of the variance in the spectral data. Plotting of these scores may reveal clustering patterns associated with chemical similarities and differences between samples.

PCA loadings describe the contributions (weightings) across the original independent variable (wavenumbers) for a given principal component. The highest absolute loading coefficients (positive and negative peaks) can then identify the spectral regions most responsible for the PCA scores distribution.[161,170] Residuals describe difference between the original pre-processed data and the decomposed, dimensionally reduced data, indicative of experimental errors and ideally random and close to zero.[161]

PCA was employed for dimensionality reduction of the spectral data, from many hundred wavenumbers to a limited number of principal components to match the scale of the patient cohort. PCA could not systematically classify samples alone and instead required further classification techniques.[171] Namely, the first 20, 10, and 5 PC's (responsible for the majority of variance in the dataset) were selected for supervised classification via Linear Discriminant Analysis (LDA) which maximised differences between the predefined classes. The cumulative explained variance for up to 20 PC's considered for each of the spectral modalities is displayed in Figure 5.3.

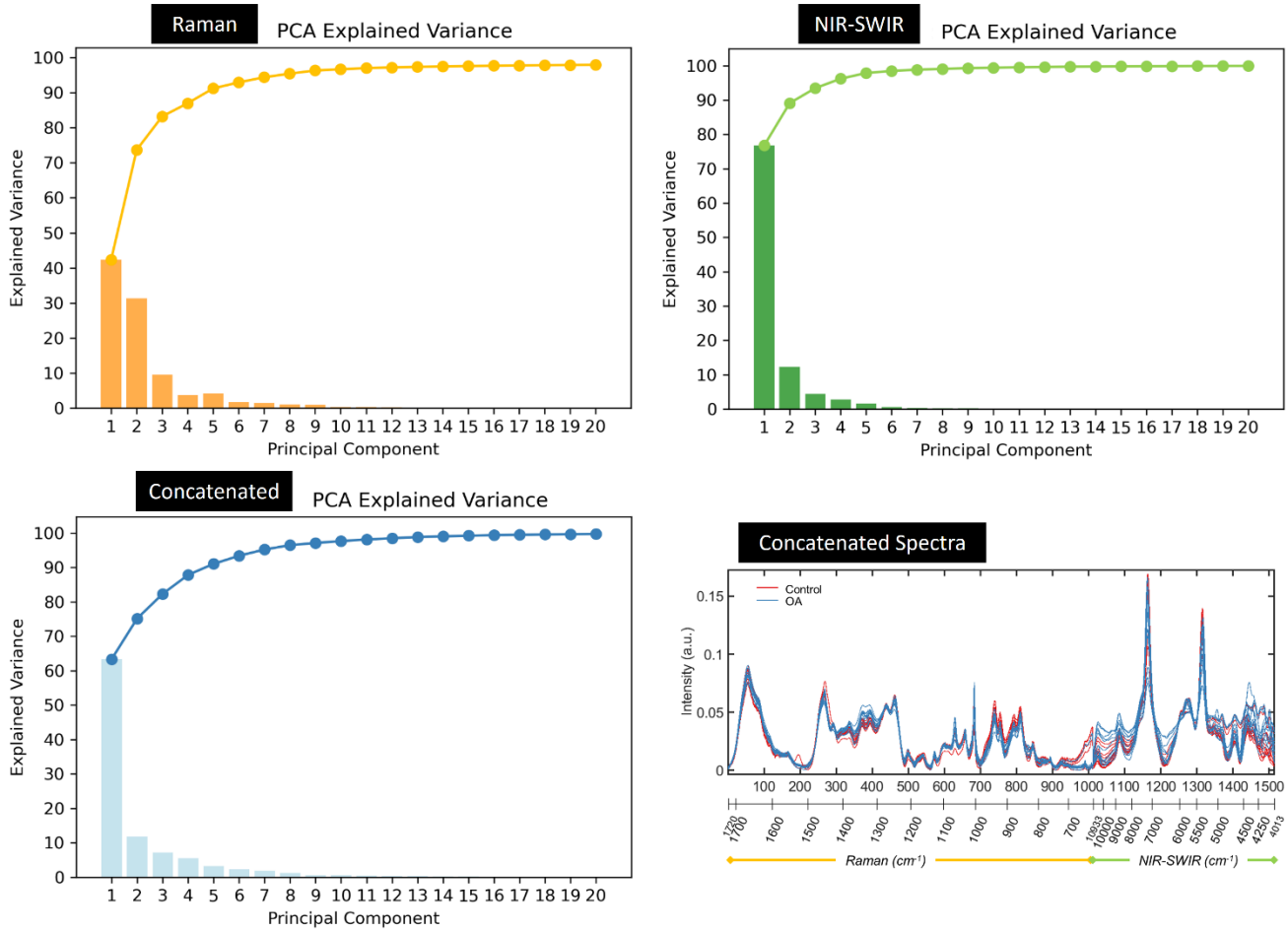

Figure 5.3 Cumulative Explained Variance for increasing number of Principal Components considered for each spectroscopic modality, Raman, NIR-SWIR and Concatenated spectral data. Bottom Right: Class means for concatenated spectra from all patients, with Raman (614 – 1722 cm-1) and NIR-SWIR (11,127 – 3993 cm-1) spectral regimes demarcated in the abstracted Spectromics fingerprint.

PCA-LDA analysis assigns each patient sample to their predicted group, “Control” or “OA” cartilage.[172] This algorithm calculated the Mahalanobis distance between samples for each class as a measure of tissue class segregation.[161] Classification for diagnosis here was supervised, labelled a priori via gold standard assessment from the consultant orthopaedic surgeon. Though LDA is a parametric method and assumes samples hold a normal distribution, it was considered robust enough for spectroscopic data, and by applying to the foremost principal components maintains that the number of spectral variables was smaller than the number of samples (n = 27).[161]

SVM

Support Vector Machine (SVM), a supervised binary linear machine-learning classifier, was applied to each the Raman, NIR-SWIR, and spectromic fingerprints to quantify classification

accuracy. A k-fold cross validation method was used to train the Gaussian classifier to model "Control vs OA Cartilage", with the optimal values for the parameters for c and γ determined via a grid search function. [160,172] This was carried out for k=3 and leave-one-out cross validation to determine training and test sub-datasets, chosen from the 27 patient spectra (one spectrum for each patient, labelled "Control" or "OA"). As such, the model training had no sight of the test subset, nor from data from the same patient, validation carried out on unseen data. Confusion matrices of each SVM model, built on the Raman, NIR-SWIR and spectromics fingerprints, describe the rate of correct group assignation when applying the trained model to the test dataset.

Quality Parameters

Quality parameters were calculated using the accumulative hits of the classification models, describing number of true positives (TP), true negatives (TN), false positives (FP), and false negatives (FN). This quantified the classification accuracy of the respective models (Raman, NIR-SWIR, spectromics) on a test dataset (no *a priori* indication). [161] The comparator metrics, equations, and relevance to the technique are summarised in Table 5.1.

Table 5.1 Quality parameters used to evaluate model classification performance. Here TP means True Positive, FP false positives, TN true negatives, and FN false negatives. Adapted from Medeiros-De-morais et al. [161]

Quality Parameter	Equation	Meaning
Accuracy / %	$\frac{\mathbf{TP}+\mathbf{TN}}{\mathbf{TP}+\mathbf{FP}+\mathbf{TN}+\mathbf{FN}} \times \mathbf{100}$	No. of samples correctly classified considering true & false negatives. Optimal = 100%
Sensitivity (SENS) / %	$\frac{\mathbf{TP}}{\mathbf{TP}+\mathbf{FP}} \times \mathbf{100}$	Proportion of positive samples (e.g. OA) correctly classified. Optimal = 100%
Specificity (SPEC) / %	$\frac{\mathbf{TN}}{\mathbf{TN}+\mathbf{FP}} \times \mathbf{100}$	Proportion of negative samples (e.g. control) correctly classified. Optimal = 100%
F-Score	$\mathbf{2} \times \frac{\mathbf{SENS} \times \mathbf{SPEC}}{\mathbf{SENS}+\mathbf{SPEC}}$	Model performance considering imbalanced classes. Optimal = 100%

5.3.7 Feature Extraction: Spectral Biomarkers

Feature extraction was performed on the spectromics data set to ascertain potential spectral biomarkers that account for the biggest differences between the OA and control tissue groups. The key biomarkers were identified by observing agreement between the highest weighted results of several independent statistical tests. Each process was carried out within iRootLab. [160]

PCA-LDA Loadings were utilised to identify the most significantly contributing wavenumbers to the PCA-LDA segregation of tissue classes. The first linear discriminant (LD) was selected, describing the direction which maximised inter-class separation and minimised intra-class variation, and the 3 highest absolute (positive or negative) loadings coefficients identified. The coefficients in turn revealed the top 3 PC's, which were plotted to identify the highest absolute peaks in the wavenumber direction. The top 20 wavenumbers were recorded from each PC.

Cluster Vector analysis calculated the centroid (mean) of the OA and Control spectral data clusters in LDA space and determined the vector separating the two centroids, or cluster vector. Operating in LDA space this identified the direction of maximal class separation. The cluster vector was then back-projected onto the original variables (wavenumbers) for each cluster (class) via the PCA and LDA loadings matrices. The back-projected loadings plot could then identify the most significant wavenumbers driving class separation.[160,161,170] The top 20 wavenumbers were recorded.

Differences Between Mean Spectra (DBMS) identified at which wavenumbers were there differences between the mean averaged spectromics fingerprint of the Control tissue (reference) and of the OA tissue (investigated sample), highlighting general biochemical differences. Of the largest absolute (positive and negative) peaks in the wavenumber direction, the top 20 most distinguishing features were recorded.

The Student's T-Test and Mann-Whitney U-Test were each applied to the spectromics fingerprint to determine at which wavenumbers the spectra from the OA and Control tissue samples showed statistically significant differences in signal intensity. The former assumed a normal (Gaussian) distribution of samples and the latter a non-parametric distribution (arguably with less bias), both carried out for completeness.[160,161] The -log10 of the P-value for the T- and U-Test for each wavenumber was plotted. Feature extraction was carried out by identifying the 20 largest peaks above a threshold of $p = 0.01$ (99% confidence interval).[161]

Feature Forward Selection (FFS) was carried out to identify a small, optimal set of spectral features (wavenumbers) which best distinguished between the labelled sample classes. Starting with an empty feature set, the stepwise process evaluated each spectral variable one-by-one via an LDA classifier to find the most discriminating feature, which was then added to the FFS model. Up to 5 wavenumbers were selected in this way, each variable assessed on enabling the best classification together with those already selected. The model was assessed with random subsampling of data with 90% portion for training and tested on the remaining 10% portion. Feature histograms were produced from repeating feature selection 100 times and counting how often each wavenumber was selected. [160] The 7 most used wavenumbers were recorded for feature extraction.

Candidate biomarker spectral features from the concatenated (abstracted) fingerprint were mathematically translated to the corresponding Raman and NIR-SWIR wavenumbers for assignment.[161] NIR-SWIR features were corroborated through comparison to the nearest 1st derivative and corresponding 2nd derivative transformed spectral peaks. This allowed correct attribution to the zero-order NIR-SWIR spectra. Briefly, the derivative transformation shifts spectral band positions by $i \times d$ wavenumbers, where i is the derivative order and d the data spacing resolution. [161] Then a peak fitting algorithm was applied to identify the feature in the 1st-order data and matched to the (inverted) peaks of the 2nd-order data, which match the wavenumber positions of the original data. [173]

5.4 Results and Discussion

5.4.1 Vibrational spectroscopy of articular cartilage using deeply penetrating light

Representative spectra obtained with back-scattered Raman scattering and transreflected SWIR absorption spectroscopy of articular cartilage are shown in Fig 1. Raman spectra are displayed following the convention of low to high wavenumber, NIR-SWIR following the convention of high to low wavenumber. For concatenation, high to low wavenumber was chosen for consistency in both modes, though it is anticipated that the analysis should be agnostic to this. The class means for control and OA tissue from Raman spectra and the corresponding 1st order derivative NIR-SWIR spectra for the same patient are shown, used to form the spectromics concatenated fingerprint. For NIR-SWIR absorption spectra it was found that transreflectance geometry measurements (non-contact, highly reflective substrate) produced the same spectral response as for transmission geometry measurements (illumination and collection from either side of the sample), recorded in-house, and for backscattered fibre probe measurements (in contact, diffuse reflectance), recorded in literature.[16,17,51]

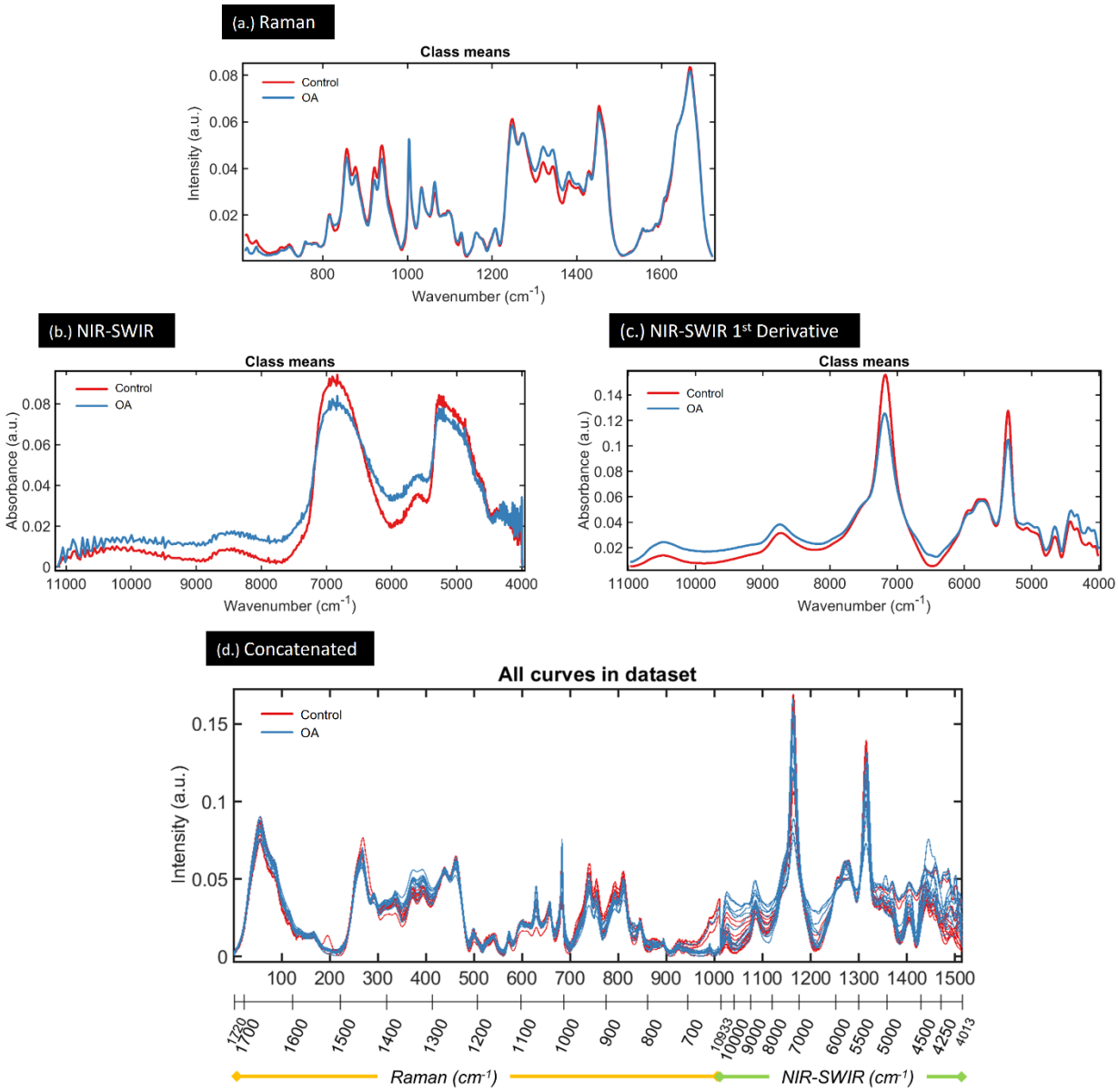

Figure 5.4 Typical vibrational spectroscopy fingerprints of articular cartilage. (a.) Represents Raman spectroscopy (614 – 1722 cm-1) pre-processed to correct background signal and random noise, and vector normalised. (b.) i. Represents typical NIR-SWIR absorption (11,127 – 3993 cm^{-1}) minimally pre-processed to remove extraneous signal, and normalised. (c.) Represents NIR-SWIR spectra with 1st Derivative pre-treatment to elucidate subtle peaks, smoothed and normalised. (d.) Concatenated Spectromics Fingerprint showing abstracted Raman spectra (1011 data points) fused to NIR-SWIR spectra (512 data points)

Regarding resolution and sample uniformity, 10 spectra with separation on the order of 100s µm was considered a suitable sampling size for the level of heterogeneity of the sample since MRI diagnosis of early OA would employ spatial resolutions of 300 × 300 μm^2 (high powered 3.0T scans) to assess radiologically presenting anatomical features such as joint space narrowing and some limited macromolecule compositional assessments of the soft tissue. [29–31,174]

From another perspective, Afara et al. have reported NIR spectroscopic analysis of animal and human knee joint cartilage with a macroscale optical fibre probe, sufficient to differentiate healthy vs diseased tissue and track biochemical changes. Here the probe was pressed against tissue samples with tip window diameter 2 mm (total ø 3.25 mm) to take an average of 10 co-added scans (30 ms exposure) from the centre of each sample. Samples were chosen from biopsy plugs 4 or 8 mm in diameter, or measurements taken from intact tissue with 3.25 mm separation.[175–177]

Methodology employed in this study is consistent with the approaches above as here slices of cartilage tissue up to 10 mm in diameter were taken from across the intact femoral head surface, and 10 single-point spectral measurements captured about the centre of each slice, with separation of the order of 100's µm. However, transreflectance measurements made use of a highly reflective gold mirror substrate. Native *in vivo* tissue classification will require diffuse reflectance measurements (subchondral bone as natural substrate), nevertheless, NIR-SWIR results presented here enable us to provide proof-of-concept. The effect of the substrate material on reflected absorbance is displayed in with results from literature displayed as Figure 5.5 (a.) and first-hand results as Figure 5.5 (b.).

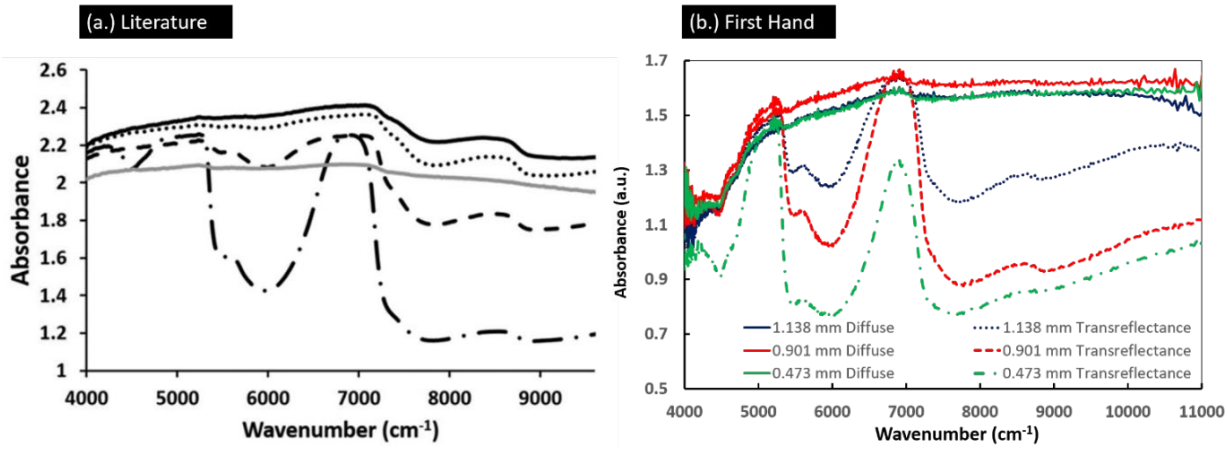

Figure 5.5 Diffuse and Transreflected measurements of absorbance in articular cartilage of varying thicknesses, as reported in literature and from first hand results. (a.) Padalkar et al demonstrate transreflectance absorbance of cartilage plugs from newborn bovine knee joints with thickness of 1 mm (long dash dot), 2 mm (black dash), 3 mm (dots) and 4 mm (solid black, and diffuse reflectance spectrum (solid grey) obtained from 1 mm thick cartilage sample on a dark surface. Adapted from Padalkar et al. [18] Reproduced with permission from the Royal Society of Chemistry. (b.) Transreflectance (dashed) and diffuse (solid) absorbance measurements from human femoral head cartilage samples of average thickness 1.138 mm (blue), 0.901 mm (red), and 0.473 mm (green).

The results from Padalkar et al. describe how for bovine knee cartilage thickness increases beyond 1 mm, diffuse reflectance increasingly dominates the transreflectance spectra.[18] A similar trend was observed when measuring spectra from human femoral head cartilage of varying average thickness from an individual patient (male, 85, OA) mounted on either the gold mirror slide or a non-reflecting substrate. Qualitatively, the transreflectance spectra obtained from thin samples display narrow spectral features with high dynamic range, thicker samples display broader features with relatively shallow peaks. Samples with average thickness around 1 mm (0.8 – 1.2 mm) were selected for SWIR characterisation which served to establish a form of normalisation across the transreflectance spectra.

5.4.2 Multivariate Analysis Modelling: Improved Tissue Classification using Spectromics

Raman scattering spectra, NIR-SWIR absorption spectra, and Concatenated spectra were assessed under multivariate statistical analysis to determine tissue classification accuracy. The data represented a mean average spectra characteristic for each of n = 13 osteoarthritis and n = 14 control model patients (one spectrum per patient).

Classification via PCA clustering alone proved inconclusive for each spectral modality since significant overlap existed between groupings of control and OA patients. This could be due to the relatively small number of total patient samples, exacerbated by the lack of spatially correlated Raman and NIR-SWIR data which motivated the use of one averaged spectrum per patient. Instead, PCA-LDA analysis was carried out to further segregate data classes. LDA based on the first (most informative) 20, 10, and 5 PC's showed sufficient inter-group differences, between control (negative class) and OA cartilage (positive), measured in Mahanobolis distance, displayed in Figure 5.6. [164] Quality parameters were calculated from the corresponding proportion of TP, FN, TN, and FP segregation of samples, summarised in Table 5.2. [161]

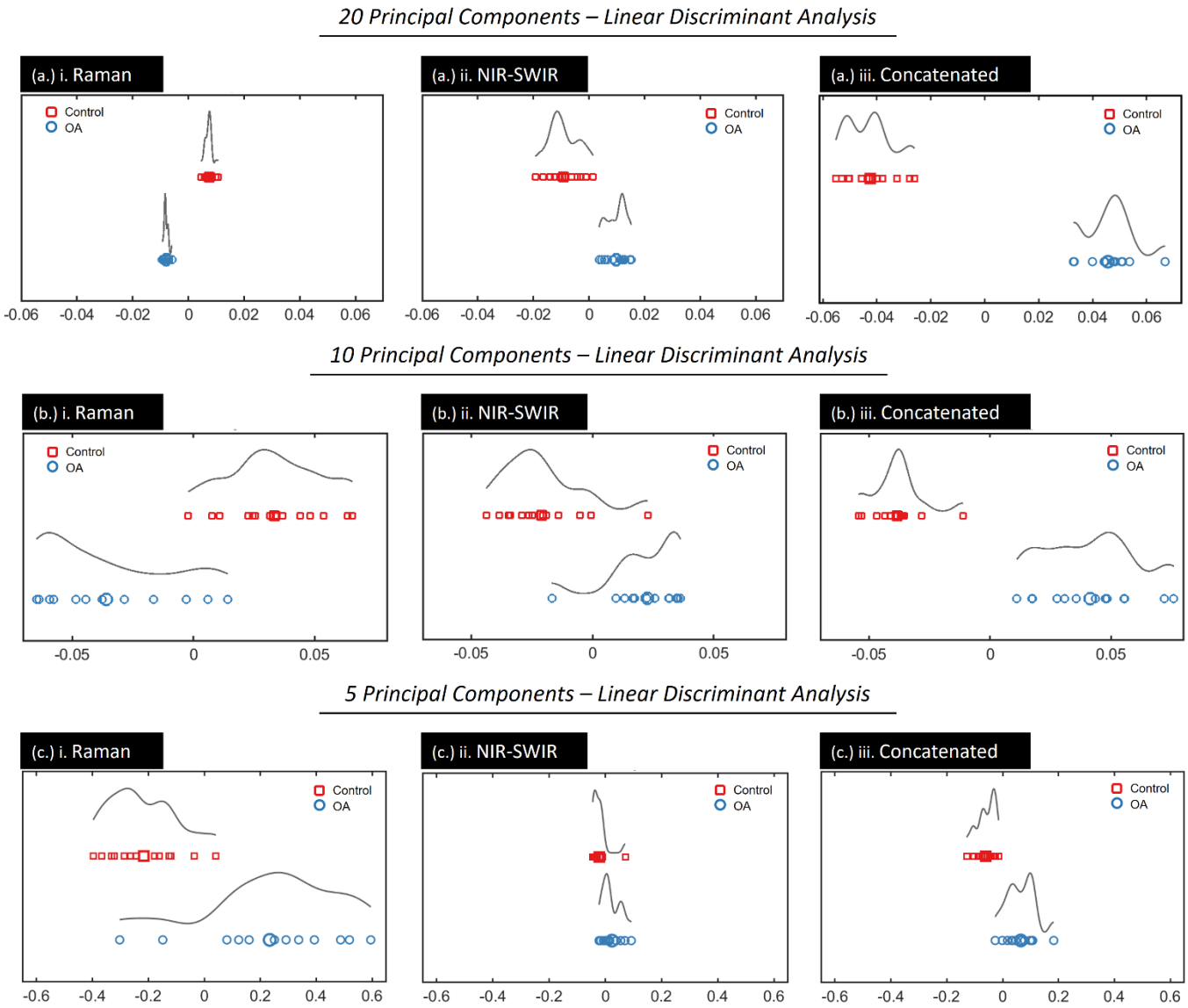

Figure 5.6 Principal Component Analysis - Linear Discriminant Analysis (PCA-LDA) classification of Raman scattering spectra, NIR-SWIR absorption scattering and the Concatenated spectra. LDA based on (a). 20 (b). 10 and (c.) 5 principal components display marked improvement in classification for the combined spectra compared to individual analysis, illustrated by the lack of overlap and/or greater degree of separation (greater Mahanolobis distance).

Table 5.2 Quality Parameters to quantify classification performance of PCA-LDA models built upon the foremost 20, 10 and 5 principal components of the Raman, NIR-SWIR and Concatenated fingerprints. Ideal result is 100% for each.

	Accuracy	Sensitivity	Specificity	F-Score
20 Principal Components				
Raman	100.0	100.0	100.0	100.0
NIR-SWIR	100.0	100.0	100.0	100.0
Concatenated	100.0	100.0	100.0	100.0
10 Principal Components				
Raman	77.8	76.9	78.6	77.7
NIR-SWIR	62.3	53.8	71.4	61.4
Concatenated	100.0	100.0	100.0	100.0
5 Principal Components				
Raman	55.6	84.6	28.6	42.7
NIR-SWIR	33.3	7.7	57.1	13.6
Concatenated	85.2	92.3	78.6	84.9

Results showed a marked performance enhancement in modelling accuracy for the concatenated fingerprint over Raman and NIR-SWIR fingerprints alone. Initially, models built upon 20 PC's were investigated to assess the effect of dimensionality reduction on classification performance, from many wavenumbers to a few components. These showed classes completely segregated (100 %) for all spectral modes and so acted as the positive control.

Working with a reduced number of features was preferred in order to avoid susceptibility to overfitting when modelling data with a high number of predictors (wavenumbers) to samples (patients), referred to as a "big p, little n" scenario. As described in Section 5.3.6, applying analysis to the foremost principal components maintains that the number of spectral variables was smaller than the number of samples (n = 27). The very high performance when using 20 PC's (100% throughout) is likely explained by overfitting, suggesting dimensionality should be reduced further to 10 or 5 PC's ($p \ll n$) to eliminate this risk. Evaluating the cumulative explained variance confirms that 10 PC's would sufficiently account for >95% of differences, 5 PC's for >90%, so 20 PC's may pull out differences due to noise or uninformative spectral features for these samples.

Still, should tissue samples become more complex, approaches to maximise segregation are valuable. Samples with smaller variance, such as when investigating disease type/severity, or factors such as comorbidities, sex, and age, will require more sensitive segregation for clinical application. Thus, the mean and median Mahanolobis distance were quantified as a measure of

tissue classification performance between the spectral modes. The greater the difference, the greater the discrimination between tissue classes. A marked improvement for the concatenated fingerprint over Raman and NIR-SWIR fingerprints alone was observed (summarised in Table 5.3).

Table 5.3 Difference between mean and median Mahalobian distance to quantify tissue classification achieved via PCA-LDA modelling of articular cartilage built upon the 20 foremost principal components of the Raman, NIR-SWIR and Concatenated fingerprints. Ideal result is a larger distance between clusters.

	Raman	**NIR-SWIR**	**Concatenated**
20 PC's PCA-LDA Difference in Mahalobian distance ($x10^{-2}$)			
Median	1.58	1.37	8.98 (570/ 654% increase)
Mean	1.54	0.07	8.81 (572/ 1220% increase)

An approximately 5- to 6-fold improvement in classification was demonstrated with the concatenated fingerprint over Raman and NIR-SWIR alone. These results indicate the augmented information content from both Raman and NIR-SWIR active vibrations may be responsible for improvement in tissue classification.

For models built on 10 PC's, accuracy increased from 77.8 % and 62.3 % for Raman and NIR-SWIR, respectively, to 100.0 % segregation of the concatenated fingerprint spectra, showing proof-of-principal for the added information afforded by multimodal Spectromics.

Finally, for models built using only 5 PC's, both Raman and NIR-SWIR failed to show effective tissue classification, describing poor accuracies (and F-Scores) at 55.6 % (42.7 %) and 33.3 % (13.6 %), respectively. By contrast, Spectromics showed significantly high classification performance with 85.2 % accuracy and an F-Score of 84.9 %.

This highlights the beneficial application of multimodal Spectromics, suitable to work with a reduced number of PC's, a stand-in for poorer fidelity data, showing a spectral analysis approach compatible with reduced computational expense and headroom for greater clinical complexity.

5.4.3 Machine Learning Modelling: Improved Tissue Classification under Spectromics

Spectral fingerprints formed from Raman scattering spectra, NIR-SWIR absorption spectra, and concatenated spectra were used to build a support vector machine for model "Control vs OA Cartilage" to determine tissue classification accuracy. These represented one spectrum for

each of 13 osteoarthritis and 14 control model patients. Classification accuracies of SVM with 3-fold cross validation and with leave-one-out cross validation are shown in Figure 5.7 and summarised in Table 5.4.

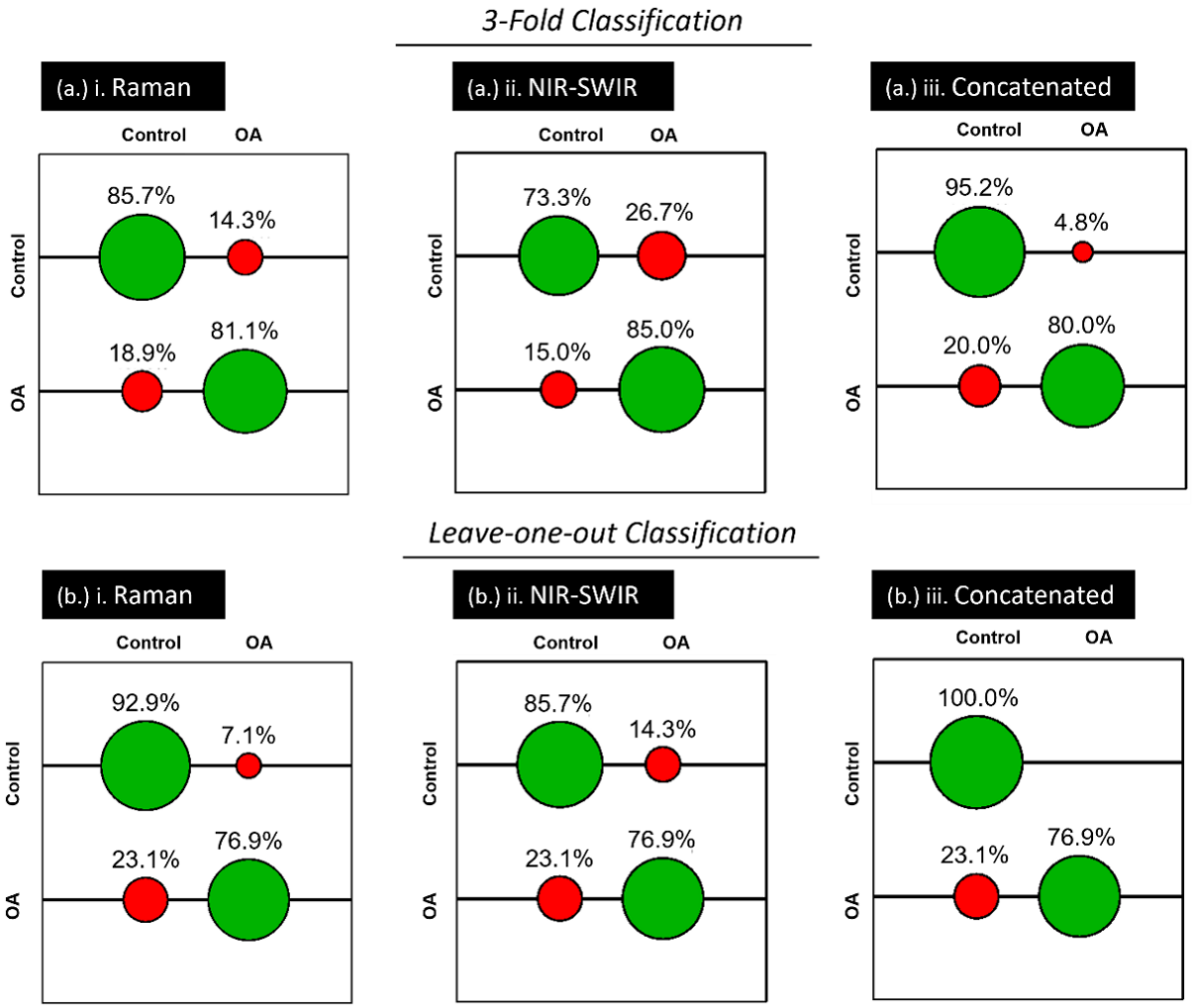

Figure 5.7 Average accuracy of Support Vector Machine classification model (OA vs control tissue) for Raman scattering, NIR-SWIR absorption scattering and the Concatenated spectra. SVM confusion matrices (correct classification in green, incorrect in red) and associated classification rates displayed for the test dataset generated with optimal tuning parameters (c,γ) extracted from a grid search of the training dataset. The algorithm was carried out on a (a). 3-fold and (b). leave-one-out cross validator and shows improved classification when employing the concatenated spectra over Raman and NIR-SWIR alone.

Table 5.4 Percentage Classification Accuracies rating performance of SVM models "Control vs OA Cartilage" based on data of the Raman, NIR-SWIR and Concatenated fingerprints. Ideal result is 100% for Control/Control and OA/OA classes, and 0% for mismatched classes.

	Control/ Control	**Control/ OA**	**OA/ Control**	**OA/OA**
		3-fold Cross Validator		
Raman	85.7	14.3	18.9	81.1
NIR-SWIR	73.3	26.7	15.0	85.0
Concatenated	95.2	4.8	20.0	80.0
		Leave-One-Out Cross Validator		
Raman	92.9	7.1	23.1	76.9
NIR-SWIR	85.7	14.3	23.1	76.9
Concatenated	100.00	0.00	23.1	76.9

The results clearly describe the improved classification under the spectromics fingerprint over modelling with Raman or NIR-SWIR alone. Specifically, recall for the control class (specificity) showed improvement from 85.7% and 73.3% for Raman and NIR-SWIR, respectively, up to 95.2% for the spectromics fingerprint under 3-fold cross validation SVM.

Under leave-one-out cross validation, where each spectrum in turn is treated as the test data and the remaining used to train the model. This approach showed an improvement again from 92.9% and 85.7%, for Raman and NIR-SWIR, respectively, to 100% accuracy for spectromics. However, recall for the positive OA class (sensitivity) showed mixed results with slightly lower rates for 3-fold SVM (Raman at 81.1%, NIR-SWIR at 85.0%, down to 80.0% for spectromics) and no difference under leave-one-out SVM observed.

Since the above evaluations were taken for each class in isolation, quality parameters were calculated from the accumulated hits to assess the classification model as a whole. Here the number of TP, TN, FP, and FN classified spectra was determined from the accumulated hits (summarised in Table 5.5).

Table 5.5 Quality Parameters based on accumulated hits of Support Vector Machine model "Control vs OA" to assess modelling performance. Ideal results are 100% for each.

	Accuracy	Sensitivity	Specificity	F-Score
3-fold Cross Validator				
Raman	77.8	76.9	78.6	77.7
NIR-SWIR	77.8	84.6	71.4	77.5
Concatenated	85.2	76.9	92.9	84.1
Leave-One-Out Cross Validator				
Raman	85.2	76.9	92.9	84.1
NIR-SWIR	81.5	76.9	85.7	81.1
Concatenated	88.9	76.9	100.0	87.0

Accuracy and F-Score of the whole model show marked improvement, considering the imbalanced classes, namely n = 14 control and n = 13 OA.[161] Under 3-fold cross validated training, accuracy improved from 77.8% for both Raman and NIR-SWIR, to 85.2% for spectromics; F-Score from 77.7% for Raman and 77.5% for NIR-SWIR, to 84.1% for spectromics. Similar improvements were seen under leave-one-out training, with accuracy improvement from 85.2% for Raman, 81.5% for NIR-SWIR, to 88.89% for spectromics; F-score from 84.1% for Raman, 81.1% for NIR-SWIR, to 87.0% for spectromics.

Although the reported improvements were relatively modest (~10% increase in specificity) this nonetheless highlights the rich chemometric information afforded by vibrational spectroscopy and the added benefit of employing the enhanced fingerprint, with specificity as high as 100%. This latter result suggests the control cartilage spectra contained greater inter-sample consistency, drawing attention perhaps to the disordering influence OA has on the tissue, resulting in relatively low sensitivity. Indeed, damage to the ECM, loss of vital PG and water, as the complex effects of the disease, would likely produce heterogeneity between patients.

Although the current data set clearly provide sufficient proof-of-concept, the work will require further validation, primarily through spatially correlated spectromics data (Raman and NIR-SWIR spectral data) and an increase in number of patient samples. An increase in number of spectra will improve the training and subsequently the accuracy of both the PCA-LDA and SVM models. Thus, considering the low number of samples in each class, for which only one spectrum (mean average) was used to represent each patient in each of the Raman, NIR-SWIR and Spectromics investigations, respectively, the proof-of-concept demonstrates high classification performance.

In future application it is also intended that Raman scattering and NIR-SWIR absorption spectra be spatially correlated such it would not be necessary to use the mean spectra for each patient

(Chapter 6). An increase in number of spectra, together with an increasing cohort of patients considered (spectral library), will most likely help improve the training and, subsequently, the accuracy of the PCA-LDA and SVM models.

5.4.4 Identifying spectral regions most pertinent to OA diagnosis

To determine which regions of the fingerprint were the most significant contributors to discerning inter-class variation, a series of independent statistical tests were performed on the concatenated spectra. The results from each test (Figure 5.8) were corroborated by identifying agreement between the highest scoring features (Figure 5.9) of each test. These corresponded to spectral regions most pertinent to tissue classification and in turn candidates for spectral biomarkers to distinguish control vs. OA AC tissue.

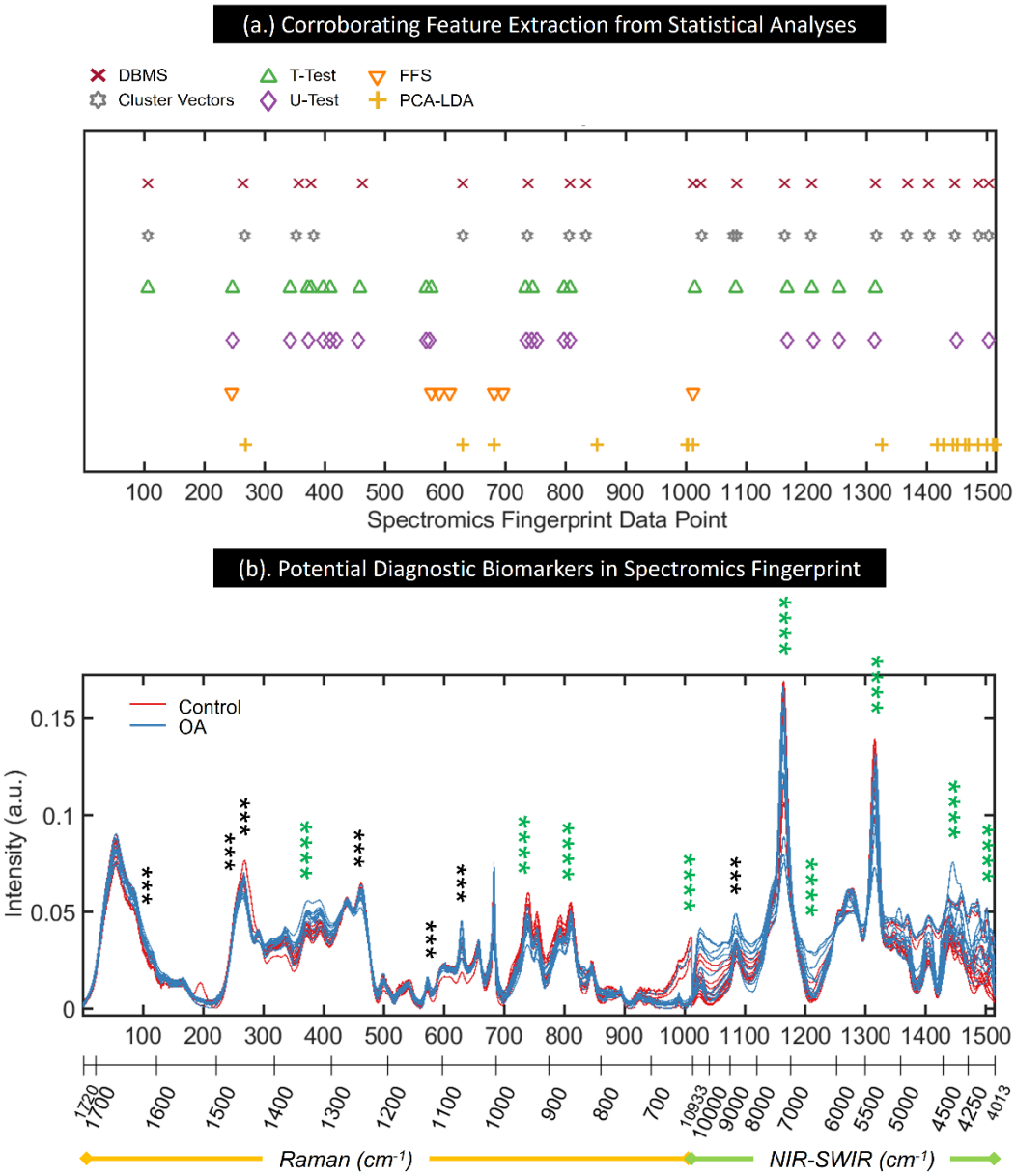

Figure 5.8 Candidate spectral biomarkers of OA were identified through corroboration between the highest scoring discriminative features in the spectra, identified through separate statistical tests. (a.) Highest scoring discriminating features identified in the spectromics fingerprint under Difference Between Mean Spectra (DBMS), Cluster Vector analysis, Student's T-test, Mann-Whitney U-Test, Feature Forward Selection (FFS) and PCA-LDA Loadings. (b.) Corroborating the statistical tests results saw certain spectral regions in agreement. The regions with agreement between four (green stars) and three (black stars) separate tests (test hits) highlight features with potential as diagnostic biomarkers.

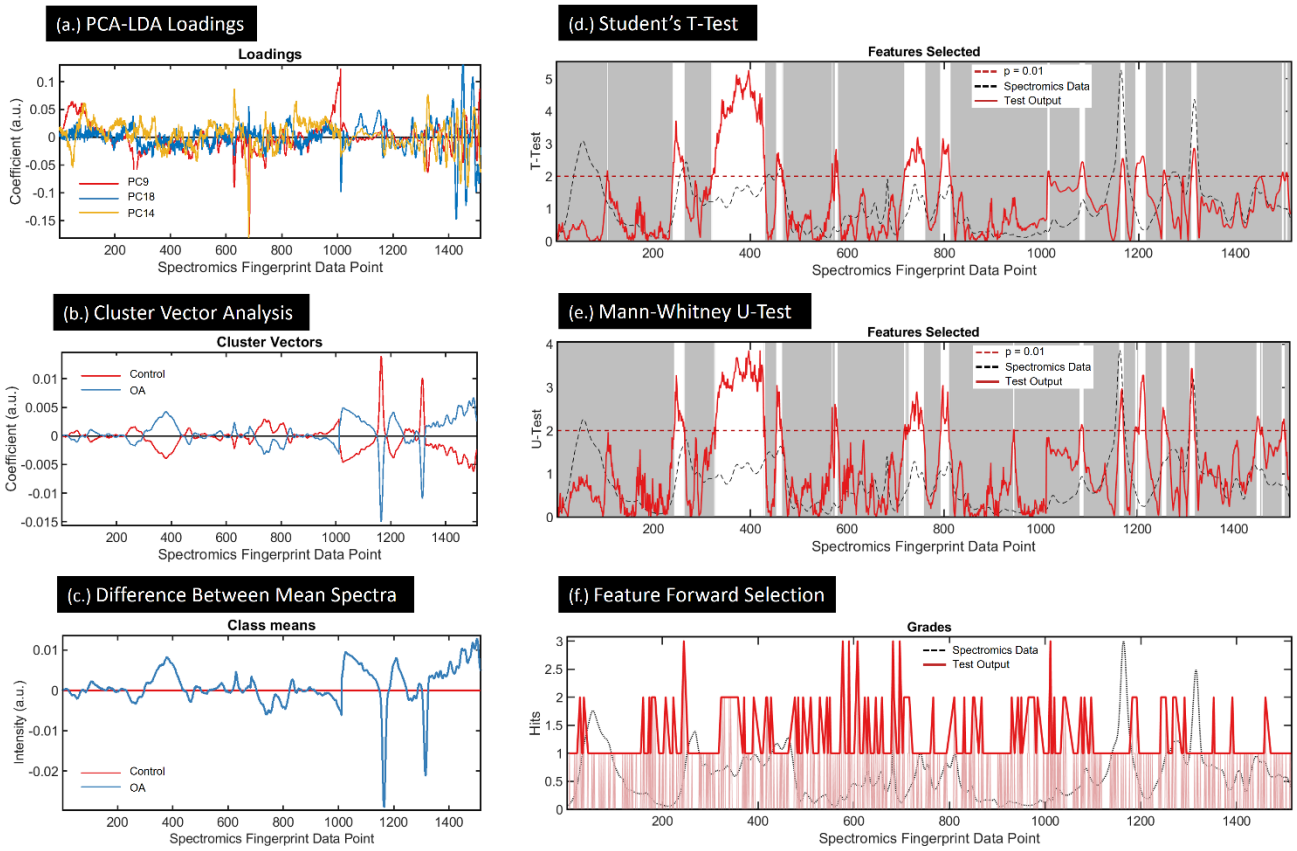

Figure 5.9 Results of separate statistical tests used to interrogate the Spectromics fingerprint to extract spectral features capable of distinguishing between Control and OA sample data. (a.) PCA-LDA Loadings of the most informative components (the top 3 PC's contributing to the first LD) detail the highest weighted wavenumbers which contributed to the PCA-LDA classification (positive and negative peaks). (b.) Cluster Vector analysis revealed the best interclass separation of spectral data in LDA space, and results back projected onto the original spectral variables show absolute peaks (positive and negative) at wavenumbers driving the separation. (c.) Difference Between Mean Spectra results show regions of absolute differences between Control and OA spectra, depicted as positive and negative peaks. (d.) Student's T-Test and (e.) Mann-Whitney U-Test results revealed at which wavenumbers the spectra from the OA and Control tissue samples showed statistically significant differences (p = 0.01) in signal intensity, depicted between the white bands. (f.) Finally, Feature Forward Selection results show an optimal subset of wavenumbers from which a LD classification model could be built, and the process repeated to identify the features most consistently improving the model, depicted as a peak positions on the feature histogram.

These were then assigned to the chemical vibration/AC tissue constituent (Table 5.6).

Table 5.6 Spectral Biomarkers identified by corroboration between independent statistical tests to identify discriminating spectral peaks between Osteoarthritis vs Control classed tissue. Features in agreement under four and three separate tests (no. of hits) are displayed alongside the corresponding Raman scattering and NIR-SWIR absorption wavenumber and attributed chemical vibration. [20,49,50,178]

Hits	Spectromics Data Point	Wavenumber (cm^{-1})	Modality	1st Deriv. Attrib.	2nd Deriv. Attrib.	Assignment
4*	373 – 381	1342.64 – 1334.18	Raman	-	-	CH, GAGs at 1342 cm^{-1}
4*	733 – 738	946.56 – 940.82	Raman	-	-	C–C deformation of aggrecan / C–O–C stretching of GAGs at 937 – 941 cm^{-1}
4*	806 – 808	862.16 – 859.83	Raman	-	-	C–C Stretching, Proline, Collagen at 856 – 859 cm^{-1}
4*	1011 / 1015	617.056 / 10819.9	Raman / NIR-SWIR	-	-	Spectromics Artefact: Raman to NIR-SWIR transition
4*	1164, 1168	7158.55, 7094.38	NIR-SWIR	7174.78	7062.73	O-H Stretching (1st Overtone) at 7280 - 6040, 7460 - 6780 cm^{-1}
4*	1207 – 1211	6524.79 – 6471.57	NIR-SWIR	-	6254.84	N-H stretch (-CONH, 1st overtone) at 6352 cm^{-1}
4*	1313 – 1316	5356.95 – 5333.09	NIR-SWIR	5342.02	5280.17	Bound & Free water at 5200 cm^{-1}
4*	1443 – 1449	4402.48 – 4366.62	NIR-SWIR	4408.17, 4420.64	4372.55, 4384.47	C–H bend (protein, 2nd overtone), at 4350 cm^{-1}
4*	1500 – 1503	4084.29 – 4068.83	NIR-SWIR	4073.97, 4058.60	4068.83, 4073.97	No precedent
3*	106, 107	1616.69, 1615.69	Raman	-	-	Amide I at 1612–1696 cm^{-1}
3*	245 – 247	1475.99 – 1473.94	Raman	-	-	CH_2 deformation/scissoring; protein & lipids at 1441 – 1460 cm^{-1}
3*	264 – 269	1456.43 – 1451.27	Raman	-	-	CH_2/CH_3 scissoring; collagen & other protein at 1451 cm^{-1}
3*	455 – 463	1255.22 – 1246.61	Raman	-	-	C-N stretching (Amide III) at 1230 – 1280 cm^{-1}
3*	575 – 577	1124.38 – 1122.17	Raman	-	-	Pyranose ring at 1127 – 1163 cm^{-1}
3*	629, 630	1064.33, 1063.21	Raman	-	-	SO_3^- stretching in sulphated GAGs, PGs at 1060 – 1064 cm^{-1}
3*	1083, 1084	8767.51, 8744.18	NIR-SWIR	8719.98	8577.59	C–H stretching (2nd overtone) at 8820 – 8060, 8695 - 8197 cm^{-1}

Relevant Raman spectral features included peaks at 1343 – 1334 cm^{-1} (CH wagging) indicative of presence of glycosaminoglycan (GAG) proteins, and the typically quoted amide III band around here at 1255 – 1246 cm^{-1} (C-N stretching), both shown to correlate with progression of OA. [20,21,49,102,104,151] The amide III band has been employed as a prominent spectral delineator between human healthy and OA knee AC, and its red shift as an indicator of mechanical impact compression in porcine AC. [21,103]

The peak at 1617 – 1616 cm^{-1} is representative of the amide I band (1612 – 1696 cm^{-1}), with magnitude shown to decrease consistently with increasing grade of OA in human knee chondrocytes. [178] Spectral markers identified at 1064 – 1063 cm^{-1} agree strongly with the symmetric SO_3^- stretching of sulphated-GAG (sGAG) protein, the quantification of which can determine the degeneration state of *ex vivo* human AC.[20,104,151]

Relevant NIR-SWIR spectral features included bands at 6543 – 6472 cm^{-1}, attributed to the N-H stretch (-CONH, 1st overtone) related to proteoglycan (PG) protein absorptions. This is regarded indicative of the ECM, and found to be the best spectral region for prediction of OA severity via Mankin scoring (6411 – 6496 cm^{-1}). [17] The 4402 – 4366 cm^{-1} band can be attributed to the 2nd overtone of the C-H bend, indicative of ECM protein content, pertinent since Partial Least Squares (PLS) modelling of the region of 4000 – 6000 cm^{-1} has predicted relative content of collagen and PG proteins in AC with error as low as 6%. [21]

The features at 7159 – 7094 cm^{-1} and 8767 – 8744 cm^{-1} describe O-H stretching (1st overtone) and C-H stretching (2nd overtone), respectively.[17,20] These have been attributed to water and collagen and PG proteins, their ratio forming a useful metric of relative water content (increasing during OA onset), Mankin score, and mechanical stiffness. The band centred about 5200 cm^{-1} has been used to accurately predict bound and free water through PLS regression modelling, represented by the spectromics biomarker found at 5357 – 5333 cm^{-1}. [20,50]

Interestingly, the fundamental vibrational modes of O-H and C-H stretching have been explicitly identified as Raman AC disease markers and shown to correlate with the increase in total cartilage hydration and loss of tissue constituents, respectively, as indicators of lesions. [151] This highlights the benefit of the complimentary and encompassing nature of the spectromics approach.

Also highlighted are potential “spectromics-specific” biomarkers, namely at the discontinuous transition from Raman to NIR-SWIR data and at around 4402-4367 cm^{-1} in NIR-SWIR absorbance. Though these cannot be attributed to pre-existing spectral markers of cartilage, these still offer a systematic feature unique to each spectra, and potentially a discriminatory

metric to aid tissue classification. Further implementation of the approach could elucidate such features.

5.5 Conclusions

This proof-of-concept study examined Raman scattering and NIR-SWIR absorption spectroscopy for chemometric assessment of articular cartilage tissue in an elegant low-level abstraction data fusion approach termed Spectromics. The improved classification potential of the enhanced spectromic fingerprint has been demonstrated and the potential for diagnosis of OA. This was proposed as method level innovation directly compatible with minimally invasive approaches with optical fibres and, conceivably, to enhance non-invasive deep NIR-SWIR approaches.

Binary classification models based on PCA-LDA and SVM have been assessed, which exhibited notable performance improvement when built upon the holistic Spectromics fingerprint over Raman or NIR-SWIR fingerprints alone.

PCA-LDA employing 20 PC's presented high performance accuracy (acting as a positive control) with complete class segregation. This was likely susceptible to overfitting artefacts but, nevertheless, showed a 5-6 fold improvement under Spectromics, valuable as an approach to maximize class differences, useful for disease stratification.

PCA-LDA employing 10 PC's showed an increase in accuracies of 77.8 % and 62.3 %, for Raman and NIR-SWIR, respectively, to 100 % for Spectromics. Only the Spectromics approach showed sufficient classification over Raman and NIR-SWIR for models using 5 PC's, showing robust performance when employing lower fidelity data, suitable also for reduced computational requirements.

SVM modelling similarly showed performance improvement ~10% for class prediction using Spectromics over Raman and NIR-SWIR alone. Performance was limited due to the small patient sample set and restrictions of one mean spectra per patient, but nonetheless demonstrated the beneficial contribution of the spectromics concept, even under such limitations. Spectral features most contributing to the classification elucidated clinically relevant tissue components, proposed as potential label-free, non-invasive OA biomarkers, and demonstrated interpretable feedback from the Spectromics approach.

Future work will seek to improve performance of the approach by adopting a spatially correlated spectromic fingerprinting strategy and increasing the number of patient samples to statistical powers appropriate for clinical trials. The lack of spatial correlation between Raman and SWIR

spectra of a given femoral head necessitated the data reduction to one mean spectra characteristic for each patient. Thus, there is rationale for developing a multimodal microscopectroscopy system on which concurrent, co-localised Raman and SWIR spectra may be collected from a sample. Here “real time” spectromics may be carried out that allows rapid detection, automatic preprocessing, and concatenation, and spatial correlation for sample mapping and imaging, detailed in Chapter 6. It is expected that performance for multivariate analysis and machine learning models will only benefit from larger number of spectral data used for training and validation.

In summary, the current proof-of-concept study demonstrates the potential of the spectromics approach for OA diagnosis with significant therapeutic diagnostic implications for an aging demographic.

Chapter 6 3D Microspectroscopy for “spectromics” mapping and correlative imaging of human femoral head cartilage

This chapter details results published in part as conference proceedings at SPIE Photonics Europe 2024, for which I was first author and primary contributor.

Hiroki Cook, Anna Crisford, Jitendra Nath Acharyya, Konstantinos Bourdakos, Janos Kanczler, Douglas Dunlop, Richard O. C. Oreffo, Sumeet Mahajan, *"Label-free 3D NIR-SWIR “Spectromics” mapping of human hip cartilage for diagnosis of osteoarthritis,"* Proc. SPIE PC13006, Biomedical Spectroscopy, Microscopy, and Imaging III, PC1300605 (2024) [2]

I would also like to acknowledge Dr Jacob Trend for training and input into the development of protocols for PolyCam scanning and Dragonfly software; Dr Simon Lane for early advice for software development in Python and tutorials in 3D CAD, printing, and laser cutting; Dr Niall Hanrahan for help in set up of the Raman microscope; and Ibrahim Abughazaleh for help in developing autofocusing software.

6.1 Abstract

Osteoarthritis (OA), a degenerative joint disease presented as degradation of articular cartilage, is a leading cause of disability worldwide, exacerbated with increasing aging populations. OA results in consistent pain and restricted mobility, and subsequently poses a serious burden on healthcare systems. Early detection and intervention (lifestyle, diet) is crucial in the absence of efficacious therapies, though current assessment techniques fall short and rely on heuristic markers (pain, inflammation), ionising radiation (CT), exogenous contrast (MRI), or invasive procedures.

Alternatively, vibrational spectroscopy utilising non-destructive near- and shortwave infrared (NIR, SWIR) light offers non-invasive, label-free assessment of cartilage, which is patient friendly and suitable for early detection of OA. Additionally, NIR-SWIR transparency windows facilitate deep penetration of optical light into tissue suitable for in vivo biochemical interrogation, potentially non-invasively. “Spectromics” describes an approach for low-level abstraction data fusion of non-destructive NIR Raman and NIR-SWIR absorption spectroscopy, providing an enhanced, interpretable “fingerprint” for diagnosis of OA in human cartilage. Discriminatory spectral features found through spectromics elucidated clinically relevant tissue components (OA biomarkers), allowing interpretable feedback from the enhanced fingerprint.

This study details the concept and development of an automated 3D goniometric multimodal hyperspectral mapping setup for characterisation of cartilage on human femoral head bone core samples and whole joint samples. This is presented as the first of its kind for non-contact NIR-SWIR vibrational spectroscopy measurements across intact human articular cartilage.

Facilitating hardware and developed software are reported which enabled automatic triggering of sample movement and spectroscopic capture. Custom sample mounting allowed handling and study of tissues with varying size and shape, and without sampling bias. The workflow for 3D spatially-resolved spectromics assessment of tissue surfaces is established and proof of principle demonstrated. These results provide the foundation for minimally invasive, deeply penetrating, label-free, chemometric diagnosis of the hip.

6.2 Introduction

Developing the "Spectromics" proof of concept established in Chapter 5, this work seeks to answer some of the limitations of the approach in moving towards clinical application. Primarily, the spectroscopic measurements of cartilage were averaged across the whole femoral head of a given patient. This was necessary given that measurements for Raman and NIR-SWIR spectroscopy were taken on separate systems on separate days, with no guarantee that spectra were captured from comparable tissue areas. A single concatenated, averaged spectrum was considered for each patient.

The motivation for the study detailed in this chapter was to develop spatially resolved spectromics assessment of OA in articular cartilage, wherein cartilage may be investigated *in situ,* and thus sensitive to tissue changes across the scale of the femoral head. Spatially resolved assessment would correlate morphologically relevant regions of tissue with their chemical fingerprint, for example investigating chemical fingerprints associated with weight bearing or damaged areas of cartilage.

Should such an approach be able to distinguish chemical changes within and between regions of thinned (diseased, OA pathology) and thick (healthy, unaffected) cartilage this would pave the way towards an objective spectroscopic grading of the whole cartilage tissue. To this end, an automated goniometric scanning system has been developed for mounting of whole tissue samples for multimodal, hyperspectral, 3D scanning of osteochondral tissue surfaces. A system capable of mapping of pathological and natural heterogeneities across whole joint tissues may be proffered as a platform for furthering biological and medical understanding of the complex effects of OA, in complex joint anatomies.

This study demonstrates Raman scattering and NIR-SWIR absorption hyperspectral mapping correlated with photogrammetry scans of whole and bone core samples of human femoral heads, post hip-arthroplasty. Here analysis was carried out with cartilage on a naturally occurring, diffusely reflecting substrate (subchondral bone) to emulate more closely the *in vivo* environment.

This approach resolves a key limitation of the preceding study, where cartilage slices were measured on a reflecting gold substrate which served to maximise the optical beam path. It is envisioned that an *ex vivo* ground truth would be of use to clinicians who may then use a library of spectral profiles to diagnose and grade OA severity in a routine arthroscopic procedure. As discussed previously, trends in the clinical literature point toward hip arthroplasty gaining popularity as a patient-friendly paradigm. In the interim, this scanning system would help maximise the use of each human tissue sample to aid with further preclinical research.

HYPOTHESIS 2: The spectromics approach can be translated to 3D and a multimodal microspectroscopy system for 3D mapping will allow for inherently correlative measurements of Raman scattering and NIR-SWIR absorption

Results described here relate to the construction and development of a multimodal microspectroscopy system for obtaining co-localised Raman and NIR-SWIR data from whole femoral heads tissue to map heterogeneity in 3D. This answers limitations of work reported in the preceding chapter which sought to prove the overarching hypothesis through spectromics, but analysed averaged and transreflected spectra.[1,156] The microspectroscopy system has allowed for 3D analysis of osteoarthritic human cartilage on the naturally occurring subchondral bone (diffuse reflecting substrate) and across bone cores representing the osteochondral junction of osteoarthritic and osteoporotic femoral heads.

6.3 Methodology Development

The results of this study are proposed as technology and methodology level development, namely in new integration for spectroscopic equipment and prototyped platform for 3D surface scanned spectromics assessment of osteoarthritic human tissue. The approach adopted for this platform is summarised in Figure 6.1.

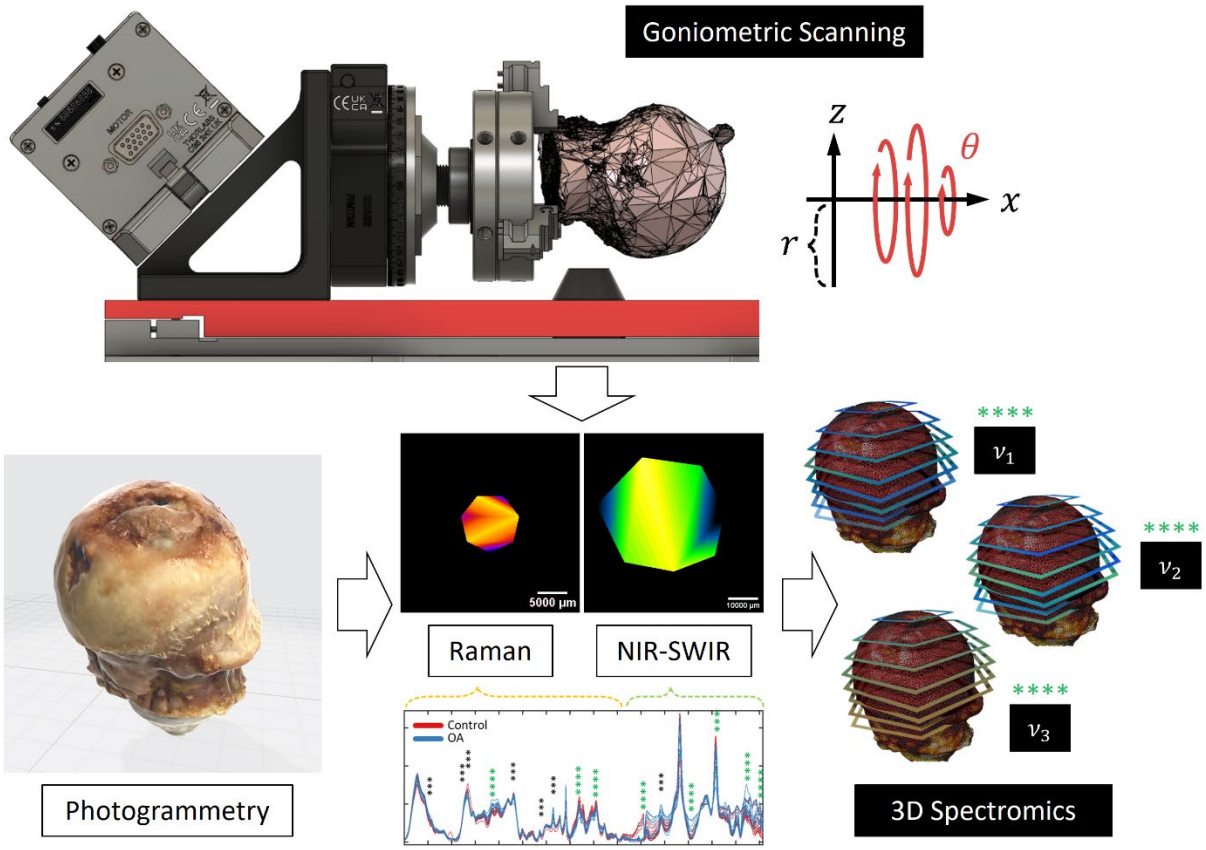

Figure 6.1 Concept for 3D microspectroscopy for Spectromics of human femoral heads: Sample scanned mapping of tissue is carried out on via motorised stages capable of moving the sample in polar degrees of freedom to build Raman scattering and NIR-SWIR absorption spectral images. Photogrammetry scans of tissue samples allow for 3D modelling with corresponding tissue features preserved. 3D spectral scans are constructed and spatially correlated with the photogrammetry models of each tissue to allow cross-referencing. Hyperspectral maps can then be investigated at specific wavelengths, such as at proposed spectromics biomarker wavelengths.

6.3.1 Sample Preparation

Human femoral head tissue collection and preparation was carried out by Dr Janos Kanczler of the University of Southampton.

Whole femoral head samples collected with full patient consent were fixed intact in 4% PFA for at least 72 hours, rinsed with water and stored in PBS to maintain osmotic pressure. This work was approved under the University of Southampton's local Ethics and Research Governance Office (ERGO 71875) and by the National Health Authority – North West – Greater Manchester East Research Ethics Committee (18/NW/0231) and conformed to the ethical guidelines of the Helsinki Declaration.

The use of whole femoral head samples preserves the naturally worn, degraded and healthy regions of articular cartilage in place across the femoral head. Present also are indentations and damage resulting from mechanical clamping during total hip arthroplasty procedure. Samples ranged in diameters of the order of 45 mm, largely spherical in shape, with a flat cut through the femoral neck acting as the base plane. There was a clear demarcation between cartilage tissue which would have been in contact with the hip within the acetabular cup and the femoral neck, typically with some soft tissue remaining. A sample from an OA (diseased) patient (female, aged 65) was selected for this study.

Bone core samples were also collected from similar femoral head samples and fixed using the same protocol. These were collected via a circular drill bit through the cartilage and into the subchondral bone, such that a cross section of the femoral head could be revealed along the long-axis of each cylindrical core. One end featured the cartilage layer and the other deep bone tissue. Samples from both OA (diseased, female, aged 57) and OP (control, female, aged 77) patients were selected for this study, and each had a uniform diameter of approximately 10 mm, long-axis length approximately 10 – 12 mm. The control samples typically showed a thick (up to 3 mm) layer of cartilage, diseased samples with considerably thinner (up to 1 mm) layer.[49,111,157,158] Bone appeared significantly rougher and more porous for the control (OP) samples.

The human osteochondral samples used in this study are displayed in Figure 6.2.

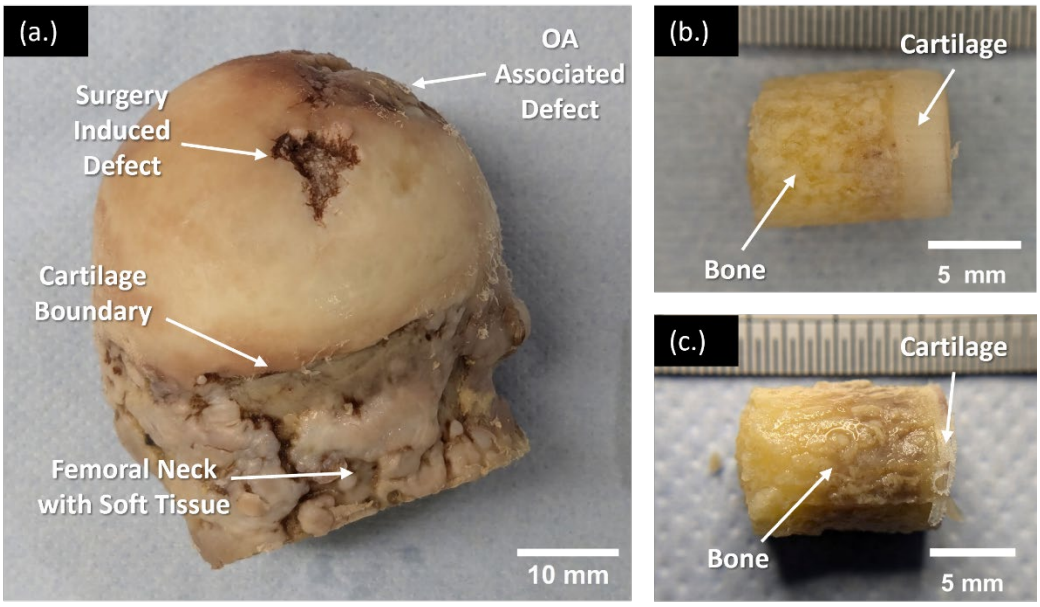

Figure 6.2 Samples prepared for analysis of whole human femoral head and bone core tissues: (a.) Whole human femoral head sample ("F65 OA") showing thick intact cartilage, OA damaged cartilage, and defects resulting from the arthroplasty surgery. The tissue can be divided into cartilage which would be in contact with the hip within the acetabular cup and the femoral neck which still holds some soft tissue. (b.) Core of femoral head tissue from a patient with osteoporosis, showing a thick layer of healthy cartilage ("F77 OP"). (c.) Core of femoral head tissue from a patient with osteoarthritis, showing thinned layer of cartilage ("F57 OA").

6.3.2 Systematic Mapping of Tissue Samples

The approach for multimodal mapping of the whole femoral heads for Spectromics analysis was established as follows. Herein, systematic sample mapping required the sample be moved relative to the objective lens for excitation and detection in discrete, small steps (high spatial resolution) across the surface of the largely spherical cartilage sample.

A predetermined set of (polar) coordinate positions across the tissue were iterated through for measurements under both Raman scattering and NIR-SWIR absorption spectroscopy. This would need to accommodate the contours of the sample whilst retaining the correct focus between the objective lens and sample surface. This required synchronised movement between the microscope stage (x, y), objective lens stage (z), and rotational stage (θ).

The axis of rotation was defined by the rotation stage and aligned as closely as possible with the long-axis of the whole femoral head. This was enabled by the centring action of a 3-jaw chuck holding the sample. The radius (r) values were defined by the position of the focal volume on the tissue surface. This was calculated from the position of the objective lens relative to the axis of

rotation. In practice, the femoral head tissue sample had some significant asymmetry in parts leading to a large variation in r, described in Figure 6.3 (a.) & (b.). This is in part due to the flat cut through the femoral neck performed by the surgeon that then acted as the tissue base plane, and needed to be in contact with the base of the 3-jaw chuck. The long axis of the femoral head (axis of rotation) was defined to follow the x axis.

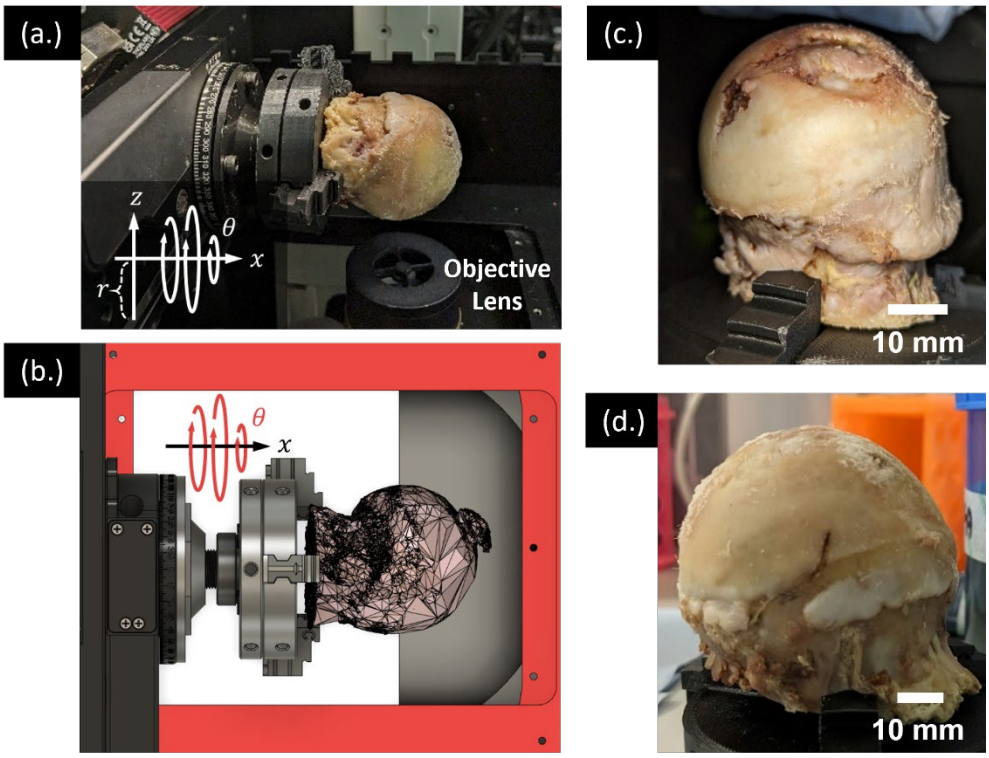

Figure 6.3 Mounting of asymmetric whole human femoral head samples on the goniometric scanning system: (a.) Human femoral head mounted in the 3-jaw chuck and suspended over the inverted objective lens. Scanning axes defined for translating the sample in 3D. (b.) Digital mock-up of another typical femoral head showing the flat base plane created by surgical severing of the femoral neck. The base plane is not aligned perpendicular with the central axis (x-axis) forming another source of asymmetry. (c.) The femoral head sample used in this investigation ("F65 OA") with diameter ~45 mm mounted in the chuck. (d.) Femoral head from a larger patient, rejected from this experiment due to too large diameter ~60 mm.

Accommodating the variation in z-position required refocusing of the objective lens. Strategies for autofocusing were developed but could only accommodate changes in r permitted by the z-translation stage of the Nikon Ti-E microscope, equivalent to approximately 10 mm total range. Thus, for the macroscale change in elevation required for the femoral head samples, at times with Δr > 25 mm, this was insufficient. Figure 6.3 (c.) shows the femoral head chosen for this study as compared to Figure 6.3 (d.) which shows that of a larger patient that could not be accommodated by the z-translation stage.

In such cases where range of z was insufficient, the lens position was set manually through a combination of inserting parfocal lens tube spacers between the objective lens and z-translation stage, adjustment of z-position, and insertion of spacers between the rotation stage and xy stage. Then distance from the axis of rotation r was recorded. For cylindrical osteochondral core samples of bone and cartilage, which required only a fixed r position (cylindrical surface scan), this was not required.

Hyperspectral data could then be captured at each polar coordinate position (r, θ, x). Data was stored as a multidimensional matrix, indexed with the polar coordinate values, containing the Raman and NIR-SWIR signals. Reconstruction of data was carried out in Cartesian coordinates, first as 2D tomographic slice, and then assembled into 3D volume for each wavelength. This then would allow for a heatmap of spectral peaks across the surface of the tissue, for both Raman and NIR-SWIR modes.

A custom 3-jaw chuck was 3D printed from a modified open-source model (see Appendix A) and mounted onto the rotation stage via a custom deigned and printed threaded connector, shown in Figure 6.4 (a.) & (b.). The 3-jaw chuck was chosen for its capacity to automatically centre samples to the central rotation axis and accommodate unusual shapes and sizes. This proved suitable for both (cylindrical) bone cores and (largely spherical) femoral head samples rotated about the objective lens, as shown in Figure 6.4 (c.). Additionally, the unreactive PLA plastic used in construction proved suitable for cleaning procedures required when handling human tissues.

Finally, in order to verify functionality of the goniometric system during development an open-source scale model of a human femoral head (see Appendix A) was 3D printed and tested. The PLA plastic models produced an appreciable Raman and NIR-SWIR spectral signature whilst also testing physical capacity to manipulate the sample adequately.

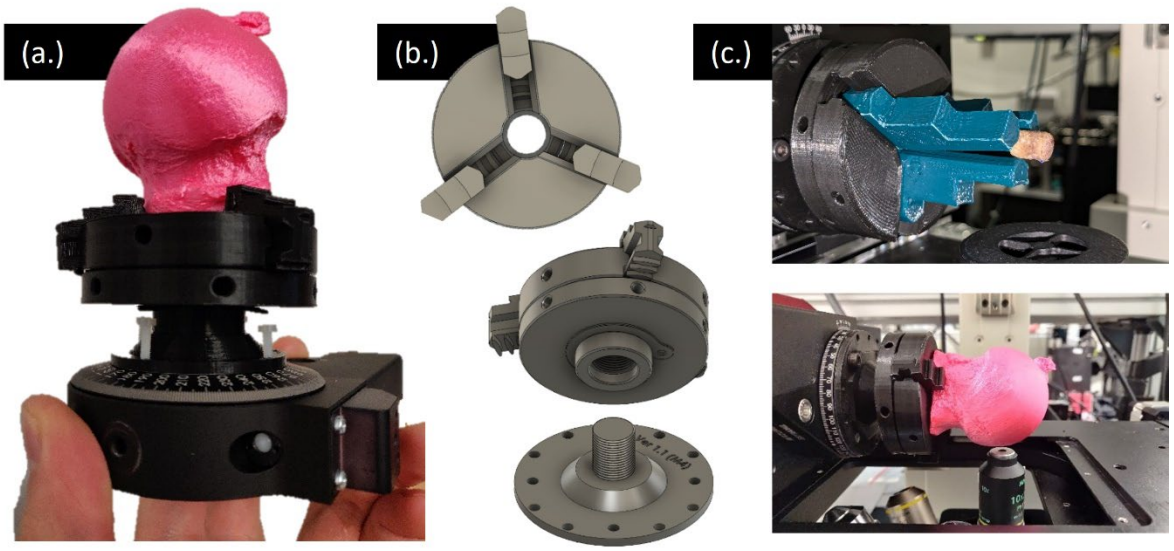

Figure 6.4 3D Printing for system prototyping and custom mounting of tissue samples (a.) Mock-up scale model of femoral head sample mounted via 3D printed chuck and screw plate onto the motorised rotation stage. (b.) 3-jaw chuck and base plate in CAD. (c.) Prototype versions of the tissue mounting rig with custom chuck jaws for holding cylindrical bone cores (~ 10 mm diameter) and the severed neck of femoral heads (~50 mm diameter).

6.3.3 Optics for the NIR-SWIR Regimes

To accommodate the wide NIR-SWIR spectral range, reflective optical components were preferred. Metal mirrored optics (planar and focusing components) displayed a high transmission efficiency across the NIR-SWIR wavelength range where refractive components performed poorly, particularly in long wavelengths up to 2.5 µm. This was attributed to interference from anti-reflective coatings with insufficient operating ranges and presence of chromatic aberration artefacts. Uncoated mirrored optics showed no aberration effects.

As such, a 15x reverse Cassegrain structure reflective objective (50105-02, Newport) was selected to ensure high transmission for signal delivery and collection, and metallic mirrors for free space manipulation of the beam for both Raman scattering and NIR-SWIR absorption spectroscopy. A common objective lens between modalities ensured localisation of signal collection to allow the multimodal mapping. Brightfield imaging could also be facilitated via this common objective lens given its broad wavelength compatibility, able to visualise the sample with no discernible chromatic aberration effects.

For the NIR-SWIR absorption spectroscopy setup, a bifurcated low-OH multimodal optical fibre (RC08SMA-P01, Thorlabs) delivered excitation light from the halogen source (left arm) and signal light (right arm) to the spectrometer. The fibre was connected to a silver mirrored off-axis

collimator to deliver the incoherent NIR-SWIR light to and from the objective. This was directed to and from the microscope back port via a silver and a gold mirror, with close to 100% transmittance across the wide NIR-SWIR range. For the Raman scattering spectroscopy set up, refractive optical components could be used without loss of performance through careful selection of the dichroic and anti-reflective coatings, since the detection pathway accommodated Stoke-shifted (>785 nm) wavelengths, with an optimised range only necessary up to around 1 μm.

A further consideration for the objective lens was relatively low NA (large depth of field) of 0.4, and a long working distance of 24 mm. The former ensured that small discrepancies for the relative positioning of the lens to the sample could be accounted for without affecting performance, useful for asymmetric/irregular sample shape and size. The latter allowed for ease of physical movement of the sample, since there would be enough clearance between samples and the lens. It is worth noting that this approach, as in the preceding study, sought to optimise back reflected spectroscopy to allow for in vivo detection in a future application.

6.3.4 Optics Improvements

The configuration described was subject to a number of iterations to maximise signal throughput for both Raman scattering and NIR-SWIR absorption signal, described in Figure 6.5.

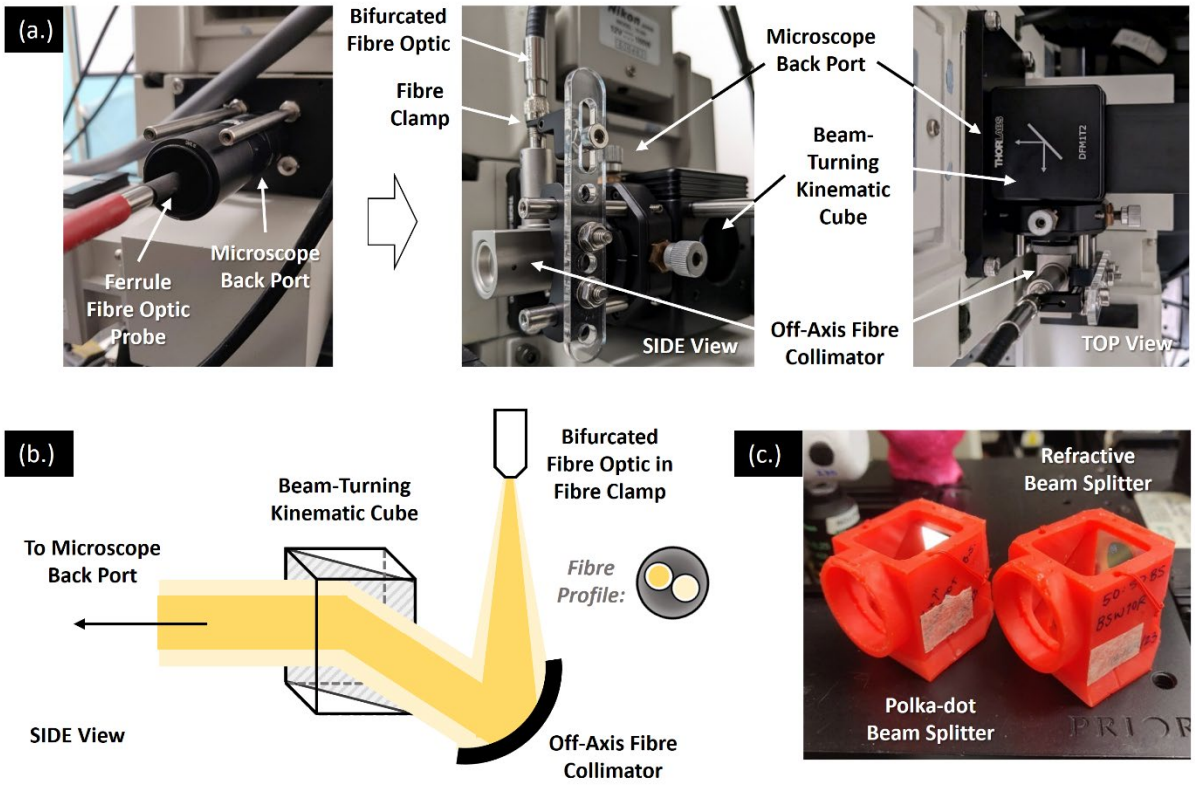

Figure 6.5 Development of optical system for multimodal Raman scattering and NIR-SWIR absorption measurements: (a.) Initial approach conducted NIR-SWIR spectral measurements via a ferrule fibre optic probe mounted to the microscope back port. This was replaced a bifurcated fibre optic probe clamped in an optimal position to deliver signal via off-axis fibre collimator, through beam-turning kinematic cube, then through microscope back port. (b.) Asymmetric profile of the bifurcated fibre optic required optimal positioning of the fibre end relative to the collimator. (c.) 3D printed filter cubes allowed customisable mounting of uncommon optics in the microscope, able to be rapidly constructed and implemented.

Initial approach saw NIR-SWIR excitation light (halogen lamp) introduced by the microscope back port, via a 50:50 refractive beam splitter (BS, BSW10R, Thorlabs), and to the sample via the reflective objective. Then back-reflected signal light was directed through the BS towards the output port of the microscope, collected via an uncoated planoconvex lens into a multimode optical fibre and onto the spectrometer. However, this suffered considerable losses in intensity as well as a transmission spectral profile artefact from the BS. The glass BS was changed for a 50:50 silver mirrored polka-dot BS (BPD2545-G, Thorlabs) which promised a flat reflection profile across the NIR-SWIR. However, this proved incompatible for imaging, producing a grid like pattern of illumination.

The next iteration saw use of the ferrule fibre probe R400-7-VIS-NIR, Ocean Insight), described in the preceding chapter, to deliver excitation light to and emitted light from the sample. This

was mounted simply to the microscope back port and light directed by a mirror to and from the sample via the reflective objective. Shortening the optical path length and removing intermediate optical components helped increase signal throughput. Yet this was still subject to significant signal losses due to lack of collimation of the incoherent broadband light and insecure mounting to the microscope.

Replacing the probe with the bifurcated optical fibre and off-axis collimator significantly improved signal throughput and mitigated effects of thermal noise (Figure 6.5 (a.)). However, this was subject to a ~500 µm discrepancy in focal position (*z*-direction) when comparing focus of the NIR-SWIR spectral system to the Raman and brightfield systems. This was attributed to the cross-section profile of the bifurcated fibre end being radially asymmetric (Figure 6.5 (b.)). This proved disruptive when measuring absorption of thin samples since short path length produced correspondingly low absorption resulting in low signal-to-noise. This was rectified by moving the terminal end of the bifurcated fibre cable away from the off-axis collimator and clamping in place both at specific height and radial orientation (Figure 6.5), which maximised the signal intensity from a gold mirror placed at the objective lens focus. With this mitigation, the system was able to detect appreciable signal from polymer standard films as thin as 50 µm in transreflectance geometry (100 µm path length). In practical terms this proved suitable for macroscale thicknesses of cartilage (1 – 3 mm), but assured reliability of results and maximized signal throughput to accommodate the low-intensity diffusely-reflected signals anticipated.

A beam turning kinematic cube (DFM1B & DFM1T2, Thorlabs) with right angle silver mirror insert, was included at the back port of the microscope to allow easy, precise, repeatable switching of the beam path between Raman and NIR-SWIR measuring modes. Removing the insert allowed the Raman laser to pass through; with the insert, NIR-SWIR light could be directed to and from the microscope, (Figure 6.5 (b.)). Finally, development of 3D printed microscope filter cubes allowed custom mounting for non-standard optical components such as the 1”x1” for the polka-dot BS (vs. standard 25 x 36 mm components), shown in (Figure 6.5 (c.)). Digital modelling and rapid construction allowed inexpensive iteration and fast deployment when prototyping the optical system.

6.3.5 Final Raman and NIR-SWIR Microspectroscopic System

The goniometric scanning technology demonstrated here was built upon a previously reported Raman microspectroscopy system.[179] This received NIR laser excitation from a 785 nm continuous wave laser (Laser 2000, UK), which was conveyed via a relay lens pair (both AC254-30-B-ML, Thorlabs) to the inverted microscope, then onto the objective lens via a 785 nm dichroic beamsplitter (Semrock). The back reflected Raman signal was then transmitted by the

dichroic filter, via a reflecting prism (left port), through a relay lens pair (both AC254-100-B-ML, Thorlabs), then via a further lens pair (AC254-100-B-ML and AC254-50-B-ML, Thorlabs) before light entered the spectrograph slit. The signal light was then analysed via a crossed Czerny-Turner spectrograph and CCD science camera (SR-303i-A-SIL and DU420A-BR-DD, Andor Technology, UK), referred to in the code as "Shamrock" and "iDus", respectively. The power of the 785 nm laser could be adjusted at its output via a selection of ND filters set into an automated filter wheel (FW212C, software ver. 3.2.0, Thorlabs).

A motorised inverted microscope base was installed (Eclipse Ti-E, Nikon, Japan) for its motorised focus capability, resolution in z (software limit) was ± 0.1 µm. A motorised XY stage (H117P1N4, Prior Scientific Instruments Ltd, UK) with proprietary controller (V31XYZE ProScan III, Prior Scientific Instruments Ltd, UK) was installed to allow precise planar positioning of the sample, resolution in xy (software limit) was 1 µm, metric accuracy was ± 0.17 µm/mm. Next a rotation stage (PRMTZ8-M, Thorlabs) was installed at 90 ° on the XY stage with its dedicated rotation motor control (KDC-101, software ver. 1.14.35, Thorlabs), referred to in the code as "KCube". Samples could then be mounted onto the rotation stage for precise angular positioning, resolution in θ (software limit) was ± 0.01°, percentage accuracy was 0.1%. A camera (ORCA-ER, C4742-80-12AG, Hamamatsu, Japan) was installed on the microscope (right port) for brightfield imaging of the sample.

The NIR-SWIR absorption spectroscopy beam path was integrated as follows. The broadband excitation light source (HL-2000-FHSA-LL, Ocean Insight) and spectrometer (NIRQuest2.5+, software ver. 2.0.16, Ocean Insight) utilised in the preceding chapter were coupled to a reflective off-axis collimator (RC08SMA-P01, Thorlabs) via a bifurcated fibre optic cable (BFY1000LS02, Thorlabs). The collimated excitation beam could then be directed to the inverted microscope via a kinematic cube (DFM1T2, Thorlabs) with gold prism mirror (MRA25-M01, Thorlabs). This beam turning cube could then be inserted for NIR-SWIR absorption mode or removed for Raman scattering mode spectroscopy. Finally, the NIR-SWIR excitation beam was directed to the objective lens via a mirror, and back reflected emission beam redirected by the same mirror to the collimator and onto the "NIRQuest" spectrometer.

Spectral acquisition parameters were as follows. Raman scattering signal intensity was recorded by the CCD in full vertical binning mode with an exposure time of 20s, calibrated with the 1004 cm^{-1} peak of a polystyrene standard sample. NIR-SWIR absorption signal was collected with 10 ms exposure time, averaged over 1000 acquisitions. Bright reference NIR-SWIR signal (I_0) was captured from a gold mirror slide mounted on the sample stage. Dark background reference spectra for both modalities were captured during the 3D scanning programme (785 nm laser / NIR-SWIR lamp off) and subtracted from the tissue sample signal.

The complete spectroscopic set up is shown in Figure 6.6.

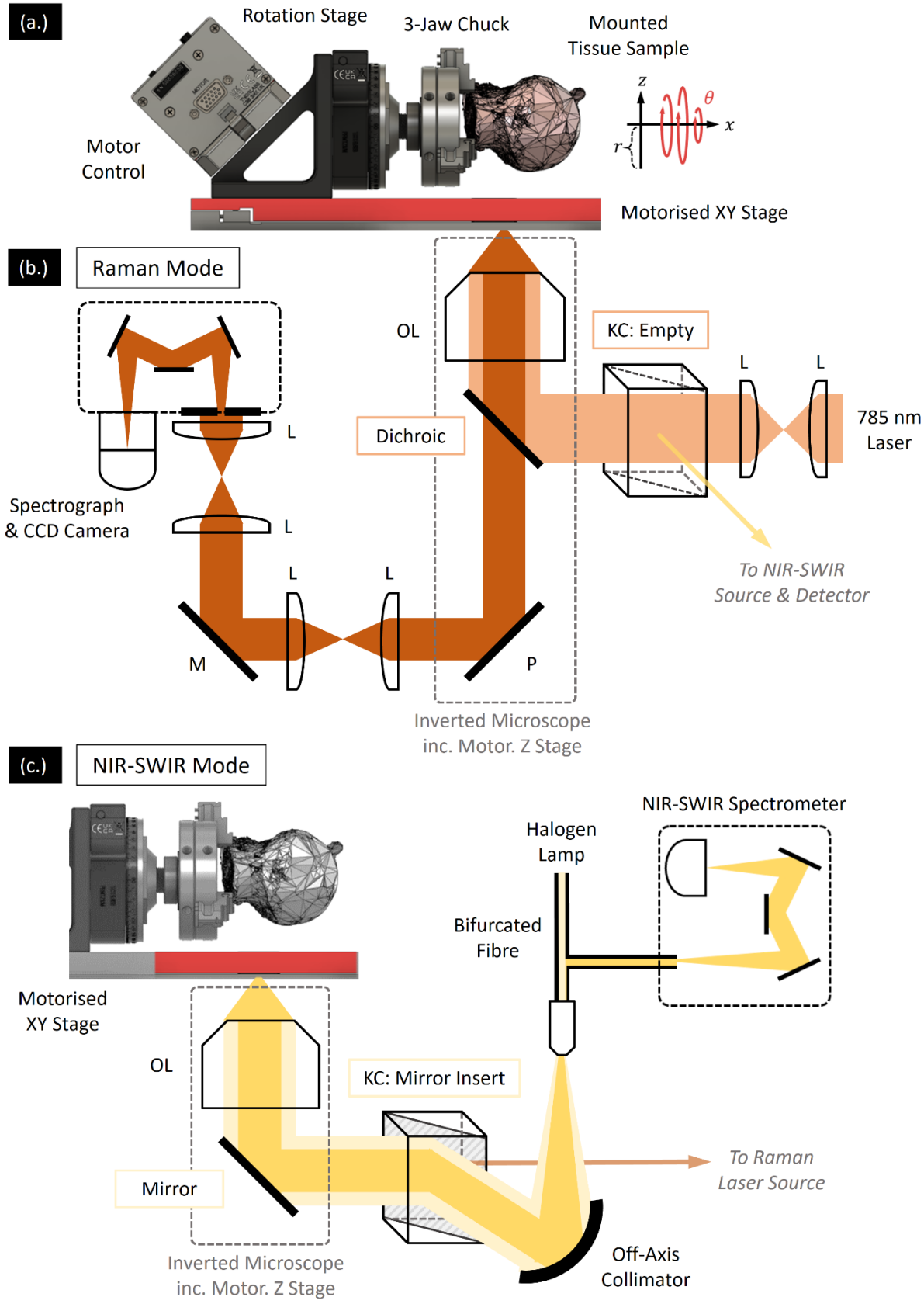

Figure 6.6 Raman scattering and NIR-SWIR absorption spectroscopy beam path for multimodal goniometric scanning system: (a.) Sample mounting of femoral heads allowed motorised translation (x, y, θ) about the (z-translated) reflective objective lens (OL).

(b.) Raman spectroscopic beam path where L are doublet lenses, P is a reflecting prism, M is a mirror. Switching to Raman mode is achieved with an empty kinematic cube (KC) allowing 785 nm excitation laser to pass through, via the dichroic filter, onto the sample. Back-reflected signal is directed through the dichroic and collected by a Czerny-Turner spectrograph and CCD camera. (c.) NIR-SWIR mode is enabled by a beam turning mirror insert in the KC directing excitation light via a mirror onto the sample. Excitation is provided by a broadband halogen lamp (left arm of bifurcated fibre) and back-reflected signal collected (right arm) onto a Czerny-Turner spectrometer. Both excitation and signal light are focused out of and into the fibre via an off-axis collimator.

6.3.6 Software Development for Equipment Control and Synchronisation

Python was chosen to develop the software for instrument control, synchronous capture of signals, handling hyperspectral data sets, and reconstruction of images. Python has wide compatibility with serial devices, software development kits (SDKs) from scientific instrument manufacturers, as well as intuitive numerical and data handling tools.

The following libraries were utilized from their respective manufacturers directly or through a third-party Python wrapper:

- **Raman spectrometer:** Andor SDK2 (Oxford Instruments, UK) was operated by its inbuilt Python wrapper, specifically “pyAndorSDK2” for frontend control of the iDus CCD camera (Raman spectral data) and “pyAndorSpectrograph” for the Shamrock spectrograph (grating position and slit width). Data from the CCD could be exported only in a proprietary Andor SIF format, requiring an open license Python software known as “sif-parser”. [180]
- **NIR-SWIR spectrometer:** SeaBreeze (Ocean Insight) software offered a C++ API, which was then harnessed with an open license Python wrapper known as “python-seabreeze” which offered both a C++ formatted backend and Python formatted frontend.[181]
- **Rotation stage:** Kinesis (Thorlabs) software offered .NET API controls, which were then harnessed with an open license Python wrapper known as “py_thorlabs_ctrl”, used as is and modified for frontend control of the stage.[182]

Other devices required an intermediate communication via Micro-Manager (ver. 2.0.2 20230815) , which received commands through Pycromanager.[183,184] The latter offered a Python library for control of hardware which proved incompatible for direct programming and instead could be configured through Micro-Manager, itself operating as a Java wrapper for the C++ backend device level commands.

Through Micro-Manager, the following devices were configured (see Appendix B) such that

- **Microscope stage** device “XYStage” was attributed to the Prior stage
- **Microscope focus** device “TIZDrive” to the Eclipse stage
- **Camera** device “HamamatsuHam_DCAM” to the ORCA-ER camera

Each instrument required initialisations (serial port connection, device identification, and device start up) and failsafes (soft- and hardware error monitoring, safe shutdown, and device disconnect) to ensure safe and repeatable operation.

Checks were performed at each stage in the script as appropriate for the specific requirements of the experiment and for optimal care of the device:

- **Raman spectrograph:** Shamrock required initialisation to open internal shutter, set diffraction grating position, and set entrance slit width. Should an error be detected during initialization and then in operation, the script implemented a safe shutdown and disconnect of this device and all other sensitive instruments.
- **Raman camera:** iDus required a cooling stage which triggered internal thermoelectric temperature control, polling ambient temperature until reaching the desired -80 °C at the CCD. An ongoing error detection protocol would implement safe shutdown and disconnect of this and all other instruments.
- **NIR-SWIR spectrometer:** NIRQuest required device search, serial connection, initialisation, shutdown and disconnect, as appropriate. Additionally, TEC was manually controlled at the device.
- **Rotation stage**: KCube required device initialisation, homing (aligning stage origin), velocity setting, disconnect and shutdown.
- **Microscope motion and camera:** Micro-Manager was required to be running with the Prior stage, Eclipse stage, and ORCA-ER camera configured and operable through the Micro-Manager GUI. Then the devices could receive commands through a Pycromanager “core” object, to then perform initialisation and shutdown as required.

Given Andor SDK 2 is minimally documented, with features not explicitly defined or described, the reader is directed to the README file and commentary noted throughout the final software (see Appendix D and Appendix E). Also important is ensuring ambient temperature is kept below 30 °C, otherwise this would trip the internal iDus temperature alarm, ceasing function of the camera until the CCD is cooled sufficiently. Additionally, due to an undetermined residual from the Kinesis API after shutdown and disconnect, a kernel restart was required through Python before the script could be run again. Implementing this step proved unobtrusive but the software bug prompts further investigation.

Finally, spectral data was recorded as a 1D matrix attributed to each position in 3D space (x, r, θ), producing the hyperspectral data set. This was handled through "pandas" functions in Python which allowed indexing and recall from multidimensional dataframes. [185]

A flowchart describing the software for the full Raman scattering and NIR-SWIR absorption experiment is illustrated in Figure 6.7, describing how the system may be operated for "cylindrical" scans iterating over (x, θ, fixed r), or for "spherical" scans which iterated over (x,θ) and require manual repositioning of r-position before capturing each Raman or NIR-SWIR spectra.

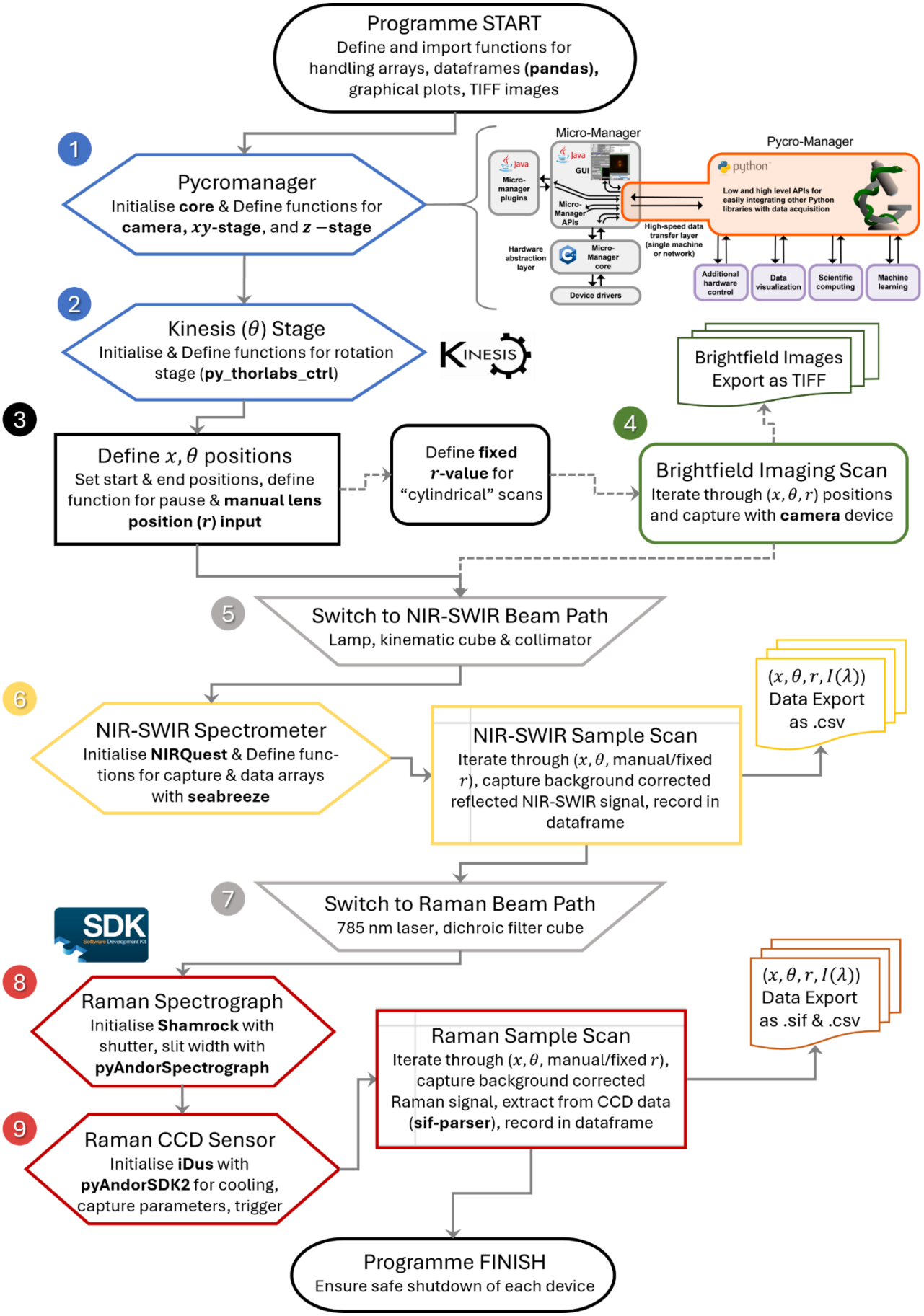

Figure 6.7 Flowchart for the 3D hyperspectral scanning programme written in Python: (1) The system preamble starts with preparation of general use functions, before initialising

the (1) pycromanager core devices [184] and (2) rotation stage devices. (3) Next, the (x, θ) coordinate positions are defined, and, should a "cylindrical" scan be carried out, a fixed r value is chosen for (4) brightfield images to be captured at each position. (5) The beam path is manually readied for NIR-SWIR absorption capture, followed by (6) initialisation of the NIR-SWIR spectrometer device for scanned capture and export of the hyperspectral dataframe. Readying for Raman scattering capture, includes (7) manual beam path switching, (8) start-up of the spectrograph, and (9) CCD sensor for scanned capture and export of the hyperspectral dataframe.

6.3.7 Spectral Data Processing

Hyperspectral dataframes were exported from the scanning script as CSV files with columns holding data associated with 3D position (x, r, θ) and spectral intensity at a given Raman and NIR-SWIR wavenumber $(I(\lambda_1), I(\lambda_2), \dots, I(\lambda_n))$. Specifically, background corrected Raman intensities as measured by the CCD, and background corrected raw reflected NIR-SWIR signal as measured by the NIRQuest spectrometer, was exported.

Raman signal was calibrated (pixel position and wavenumber) by measurement of pure polystyrene on the microscope stage using Andor SOLIS software (ver. 4.32.30065.0, Oxford Instruments, UK). Cosmic ray removal was performed by manually editing the dataframe. Data was then truncated to the range 1723.06 - 612.80 cm^{-1}.

NIR-SWIR absorbance values were calculated for the whole matrix by using the reflected signal from a mounted gold mirror slide as I_0, as previously described. Data was then truncated to the range 8257.28 - 4727.91 cm^{-1} to omit large magnitude noise readings at each extreme. The trimmed data sets sufficiently covered the spectromics biomarkers of cartilage identified in the preceding chapter.

Data matrices were then formatted for pre-processing steps carried out in irootlab.[160] Spectral pre-processing was carried following protocol from the preceding chapter:

Raman scattering spectra were treated with 5th-order polynomial baseline correction, wavelet de-noising via 6 level Haar thresholding, rubber-banding baseline correction, and vector normalisation. NIR-SWIR absorption spectra were treated with 1st-derivative transformation and 2nd order Savitsky-Golay smoothing filter (9 filter coefficients), rubber-banding baseline, correction, wavelet de-noising (6 level Haar thresholding), and finally vector normalisation.

Lastly, polar coordinates (x, r, θ) indices of the dataframes were transformed into Cartesian coordinates (x, y, z) for tomographic image reconstruction.

6.3.8 3D Data Reconstruction and Correlative Imaging

Hyperspectral mapping of the tissue surface at varying x-position along the length of each tissue sample traces out "rings" of spectral intensity centred about the axis of rotation. Each "ring" represented a tomographic slice at a given x-position that could then be reconstructed in 3D for correlative measurement of tissue heterogeneity across the sample surface, protocol laid out in Figure 6.8.

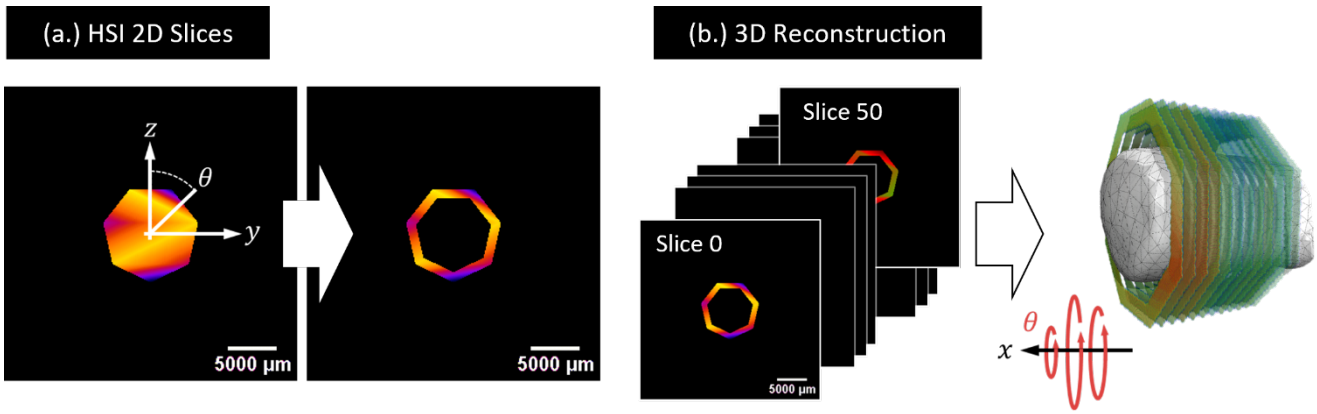

Figure 6.8 Spectral data slices to 3D mapping volume (a.) Spectral measurements at points around the sample circumference were interpolated into a heatmap and then cropped to produce a contour ring. (b.) Each tomographic ring slice could then be stacked appropriately in x direction and reconstructed into a volume map of surface spectra to be spatially correlated with the photogrammetry model.

Each slice was constructed as an interpolated heatmap with pixel value (8-bit) representing spectral intensity, before being cropped (distance mapping) to represent only surface measurements (contour ring) using FIJI, shown in Figure 6.8 (a.). [186] Then, slices were ordered within a stack, blank slices represented by images with zero intensities, shown in Figure 6.8 (b.). Pixel width in (x, y) was determined as 100 µm by the step size of the rotation and translation stages, in z determined as 10 µm by position in imaging stack.

Photogrammetry scans of the tissue samples were carried out via PolyCam mobile app software, which enabled automatic reconstruction, and exported a full colour model and surface mesh.[187] The full colour model allowed scrutiny of the sample for orientation and site specific tissue features. Hyperspectral image sequences were imported into 3D data handling software Dragonfly (Comet Technologies, Canada) for scaling and manual alignment with the photogrammetry mesh.[188] The 3D spectral images were then oversized slightly to allow cross reference between the tissue surface and its spectra, shown in Figure 6.8 (b.). One spectral image (representing intensity of a specific Raman or NIR-SWR wavenumber) was visualised at a time to assess spatial heterogeneity across each sample.

6.4 Results and Discussion

6.4.1 3D Hyperspectral Mapping of Human Bone Cores

Hyperspectral mapping was carried out for bone core samples under Raman scattering and NIR-SWIR absorption. Each cylindrically shaped sample was mounted in the 3-jaw chuck, suspended above the objective lens, with long-axis perpendicular to the lens defining the x-direction. Synchronised motion between the microscope stage (x, y), lens stage (z or r), and rotation stage (θ) allowed for sample mapping across the sample surface for coordinated (x, θ, r) measurements of Raman scattering and NIR-SWIR absorption.

Figure 6.9 describes the pre-processed diffusely reflected spectra under both modalities, averaged for each position in x along the length of each cylindrical sample, osteoarthritic and control. Bone core samples were rotated and translated about the objective lens (Figure 6.4 (c.)), such that sample scanning started at the "deep layer" representing just subchondral bone (stage at x = 1000 µm) and translated along the long-axis of the cylindrical core sample to the "shallow layer" of articular cartilage (stage at x = -4500 to -5500 µm).

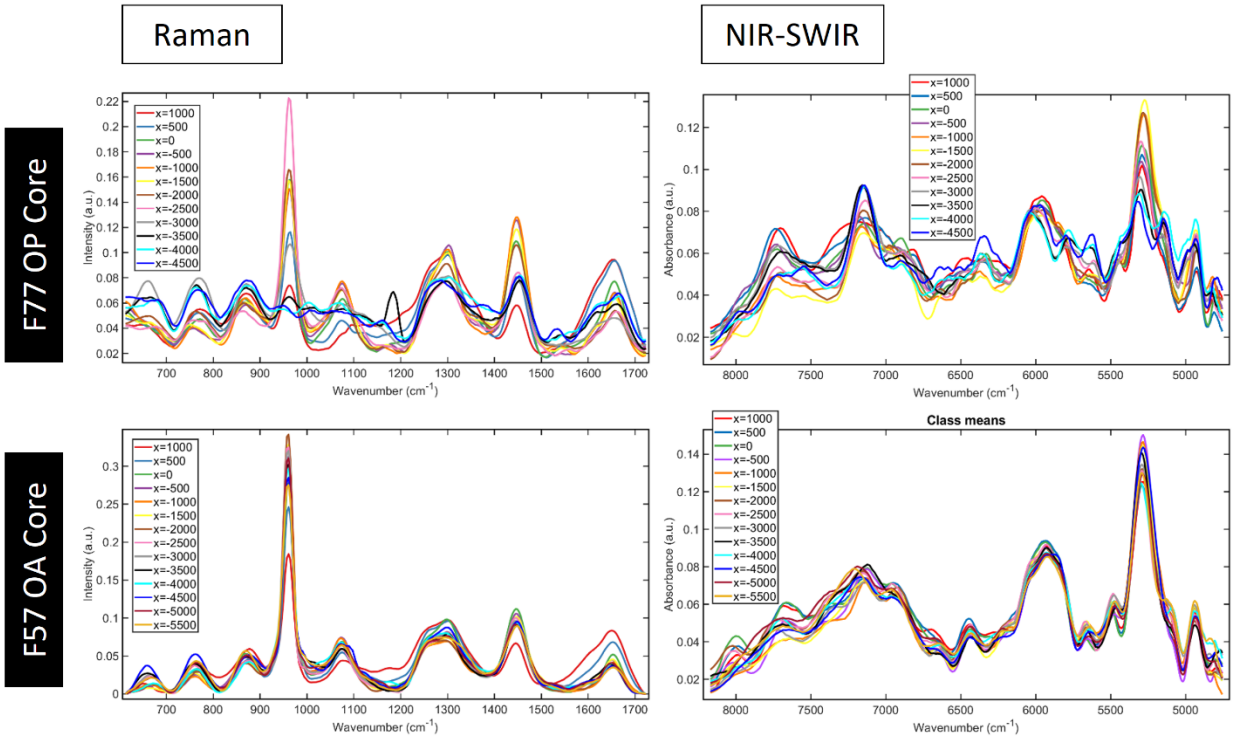

Figure 6.9 Vibrational spectroscopy of bone core samples at varying x positions. Spectra represented here were averaged for each x position along the length of the bone core, equivalent to layers of tissue deep within the femoral head (x = 1000 µm) and at the articular cartilage layer (x = -4500 to -5500). Raman scattering and NIR-SWIR

absorption spectra agree with that reported in literature for human subchondral bone.

Hyperspectral mapping images were evaluated at prominent Raman peaks associated with bone mineral/apatite (960 cm^{-1}), collagen matrix (1302 cm^{-1}), protein/lipid CH_2 deformation (1445 cm^{-1}), and collagen associated amide I (1649 cm^{-1}). Two prominent features from the NIR-SWIR spectrum were evaluated, attributed to the water peaks due to O-H stretching (7156 cm^{-1}, 1st order) and O-H stretching and bending (5283 cm^{-1}, 1st order). The spectral parameters chosen for this illustration and their significance in spectral assessment of osteochondral tissues recorded in literature, are detailed in Table 6.1.

Table 6.1 Raman and NIR-SWIR spectral markers used for bone core hyperspectral maps and respective osteochondral tissue assignments

Spectral Parameter	Osteochondral Tissue Property
Raman Scattering	
960 cm^{-1} (PO_4^{-3}, internal mode ν_1) [111,189]	FWHM at 960 cm^{-1} inversley proportional to mineral crystallinity [190] Mineral to matrix ratio (960 cm^{-1} / 1660 cm^{-1}) [190] Carbonate apatite to hydroxyapatite ratio: carbonate (1071 cm^{-1}) / phosphate (960 cm^{-1}) [111] for mineral crystallinity [189]
1302 cm^{-1} amide III (~1200 - 1320 cm^{-1}) [111]	Relative amount of PG: PG (1375 cm^{-1}) / amide III (1215 – 1300 cm^{-1}) [189] Collagen disorder: random coil (1268 cm^{-1}) / alpha helix confirmation (1244 cm^{-1}) [111]
1445 cm^{-1} (bending & stretching of C-H groups)	1450 cm^{-1} for collagen and proteins (CH_2 and CH_3)[52] CH_2 deformation/scissoring; collagen and lipids [20,49]
1649 cm^{-1} amide I (~1612–1696 cm^{-1}) [189]	Mineral to matrix ratio (960 cm^{-1} / 1660 cm^{-1}) [190] Collagen cross-link ratio (collagen maturity) (1660 cm^{-1} /1690 cm^{-1}) [190]
NIR-SWIR Absorption	
5283 cm^{-1} O-H stretching & bending (1st order)	Bound and free water [20,50]
7156 cm^{-1} O-H stretching (1st order)	Free water [20,50]

Figure 6.10 and Figure 6.11 show spatially correlated 3D data from photogrammetry scanning, Raman scattering and NIR-SWIR absorption hyperspectral mapping of a bone core from a control (“F77 OP”) and diseased (“F57 OA”) femoral head, respectively. Full colour scans show form and structure of the samples, particularly for layers corresponding to bone (darker colour,

rougher surface) and cartilage (lighter, smoother). Hyperspectral data shows variation in chemical composition at discrete steps along the length of each sample.

Results presented here do not yet go into depth for statistical or chemometric analysis of spectral responses but facilitate some macroscale observations indicative of 3D biochemical distributions. In addition, the scale and shape of the bone core samples are uniform, having been excised with a circular drill bit. As such the scanning system needed only consider variation in x and θ, with fixed objective lens position (fixed z and r), enabled in part by a relatively long depth of focus of the lens which helped ensure the sample was kept in focus whilst being rotated. The objective lens had a relatively small NA = 0.4, with depth of focus calculated as 2.35 μm for Raman spectroscopy (785 nm excitation) and 2.70 – 7.49 μm for NIR-SWIR spectroscopy (900 – 2500 nm excitation).[191]

This establishes a standard protocol that can be applied to future samples obtained by coring of the femoral head. Samples with significant asymmetry that require repositioning of the objective lens, e.g. the whole femoral head, add further complexity.

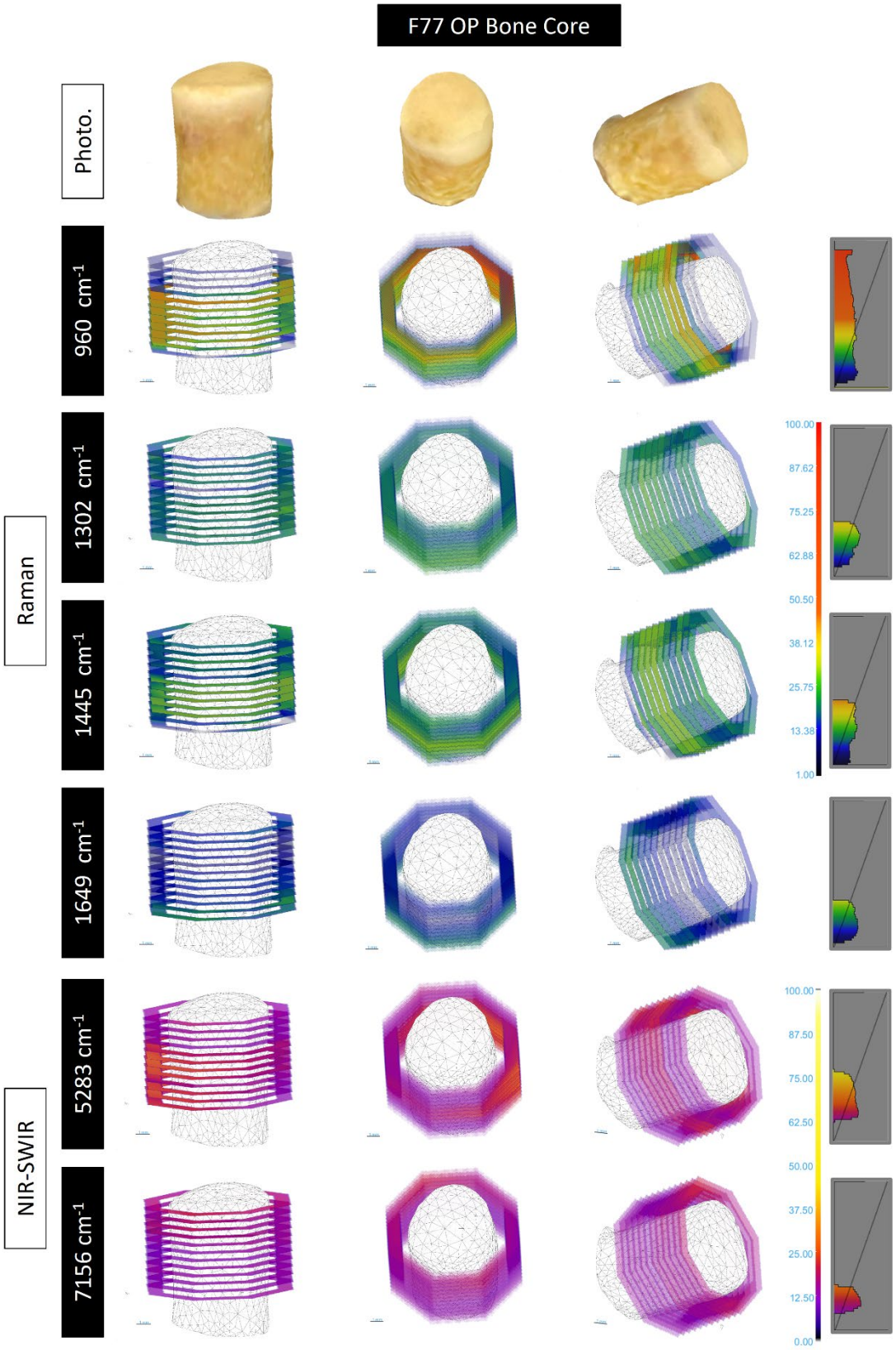

Figure 6.10 Correlated 3D hyperspectral Raman and NIR-SWIR mapping of OP bone core: Photogrammetry scans distinguish visible tissue features. Hyperspectral maps distinguish spectral response due to changing chemical composition across tissue. Colour bar legend shows normalised Raman scattering and NIR-SWIR absorption intensities (a.u.), histograms show intensity value distribution. Scale bar = 1 mm.

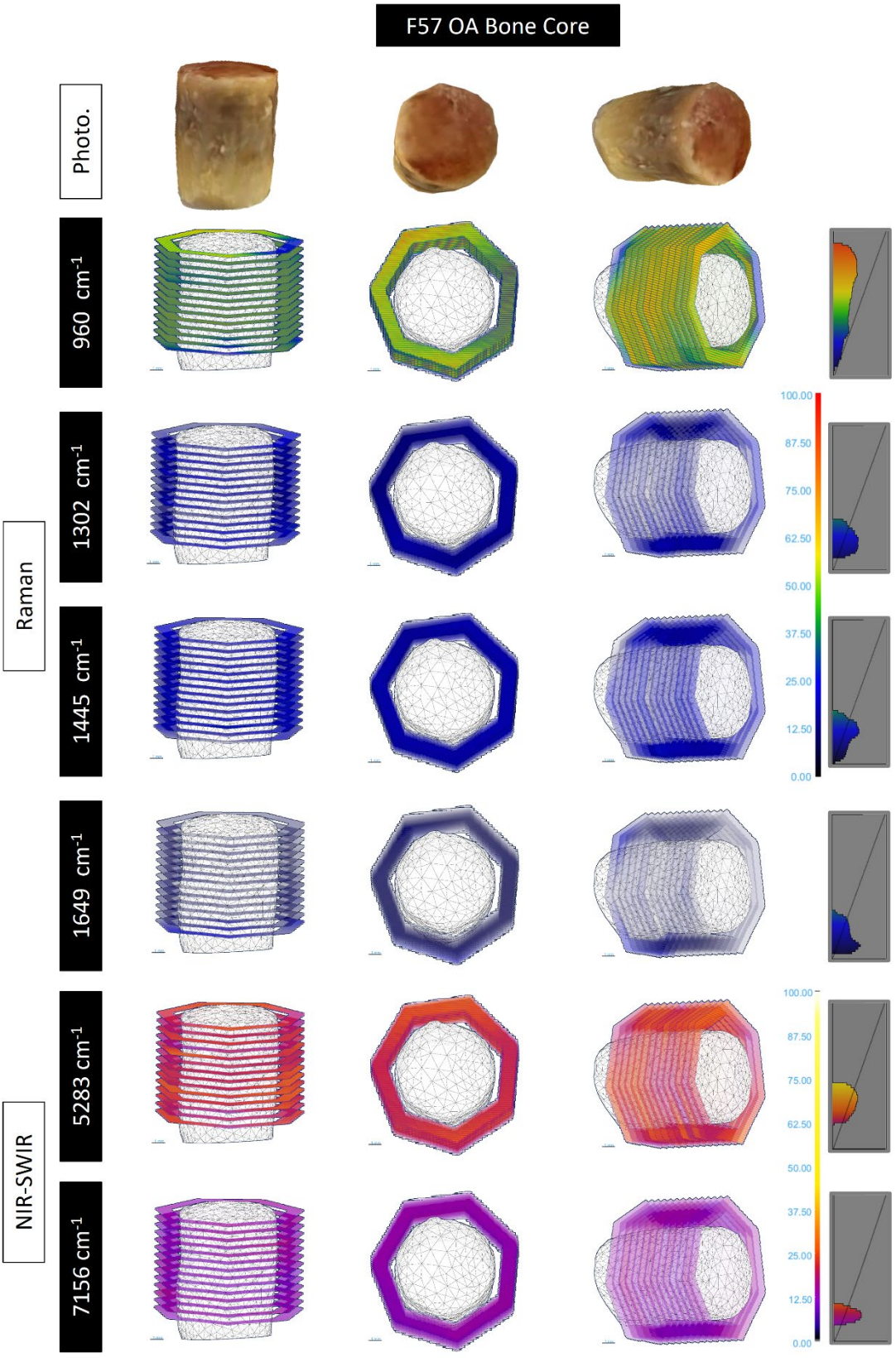

Figure 6.11 Correlated 3D hyperspectral Raman and NIR-SWIR mapping of OA bone core: Photogrammetry scans distinguish visible tissue features. Hyperspectral maps distinguish spectral response due to changing chemical composition across tissue. Colour bar legend shows normalised Raman scattering and NIR-SWIR absorption intensities (a.u.), histograms show intensity value distribution. Scale bar = 1 mm.

As discussed in Chapter 3, spectral discrimination of articular cartilage (collagen PG, GAG) from subchondral bone (mineral, hydroxyapatite) could be employed as a metric for surveying cartilage damage on the human joint. This is evident in the spatial distribution of spectral response in the F77 OP sample which sees a clear demarcation between cartilage and bone, since the sample possessed a thick layer of cartilage (photographed in Figure 6.2 (b.)) whereas F57 OA had little cartilage remaining (Figure 6.2 (c.)). With the current results, a change in the spectral response can be observed in 3D (Figure 6.10), most notably in the reduced intensity of the 960 cm^{-1} phosphate ν_1 mode, which is associated with mineral content (hydroxyapatite).

Figure 6.12 shows the averaged Raman scattering and NIR-SWIR absorption response for the OP bone core sample separated into layers of subchondral bone and cartilage. The cut off was determined by significant change in the Raman response from the phosphate ν_1 mode (960 cm^{-1}) and subduing of the broad feature between ~1000 – 1100 cm^{-1}.

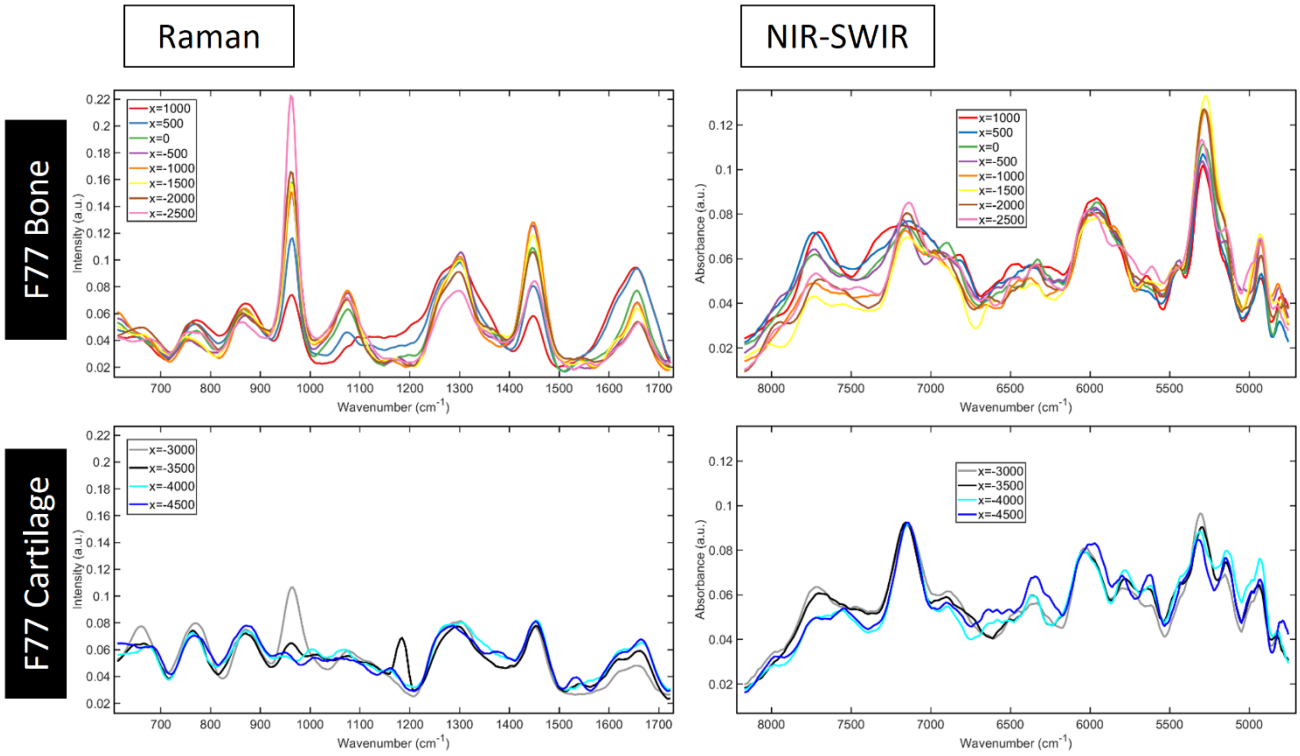

Figure 6.12 Vibrational spectroscopy of bone and cartilage layers in the osteoporotic bone core: Raman scattering and NIR-SWIR absorption spectra averaged for each "slice" along the length of the bone core, and divided between those corresponding to subchondral bone and to cartilage tissue.

The region ~1000 – 1100 cm^{-1} was not illustrated for hyperspectral mapping at a single wavelength given it may be convolution of a couple of indicative peaks across the osteochondral junction. As identified in the preceding chapter, in articular cartilage the ~1060 cm^{-1} band may be attributed to sGAG (symmetric SO_3^- stretching) shown to correlate with degeneration state in human *ex vivo* samples. [20,104,151] Within the more mineralised calcified

cartilage and subchondral bone layers, the ~1070 cm^{-1} band is associated with B-type carbonate which may be used to indicate subchondral bone remodelling. The carbonate is an imperfection in the apatite crystals of mineralised osteochondral tissue, which may be tracked by employ of 1070 cm^{-1} / 960 cm^{-1} ratio. [56,111,189] Carbonate substitution has been successfully monitored with this spectral ratio, found to be significantly higher in the subchondral bone of OA patients than control tissues, with overall reduced mineralisation, and slightly higher in the most-weight bearing region of femoral heads than least. This marker reflects the rate of bone remodelling and increased values may be indicative of early stage response to degenerative or trauma injury.[56,111]

For eroded tissues osteochondral tissues, spectral responses associated with GAG have been shown to decrease, marked by reduction in the 1063 cm^{-1} / 958 cm^{-1} (cartilage / bone) ratio [56] or 1375 cm^{-1} / 1215 – 1300 cm^{-1}(PG / amide III) ratio[189] intensity. However some scientists favour use of the 1375 cm^{-1} peak for assessing PG explicitly to avoid the strong overlap between the 1060 cm^{-1} PG peak with 1070 cm^{-1} carbonate peak.[189] The amide III envelope has been employed for measure of collagen disordering associated with tissue degeneration, particularly ratio between the maximum at 1244 cm^{-1} associated with random coil (damaged) and at 1268 cm^{-1} associated with α-helix (healthy) conformation.[111]

In general, NIR-SWIR absorption spectroscopy is not sensitive to phosphate from the apatite mineral in bone, but is particularly suited to the assessment of relative water content (free, bound), and for assessing PG, protein, collagen, and lipids.[190] NIR-SWIR mapping of the osteochondral junction has reportedly described distribution of water primarily in the MZ and DZ of cartilage, and at higher concentration than bone. [98] Results displayed here display a more distinct and marginally higher ~7000 cm^{-1} peak for the cartilage layer than for bone, but lower intensity for the ~5200 cm^{-1}, requiring further statistical analysis in order to make definitive claim of biochemical distribution.

Aside from the spectral bands associated with water, the hyperspectral scans also show prominent broad peaks about ~6000 cm^{-1} and ~6400 cm^{-1}. In articular cartilage, NIR-SWIR absorption at 6102 – 5446 cm^{-1} have been reported optimal for correlation with cartilage thickness, indicative of collagen and PGs (first overtone CH_n and SH absorptions). [16] Results of the spectromics study (Chapter 5) corroborated the importance of the band at 6543-6472 cm^{-1} (-CONH stretch, 1st overtone) indicative of PG and the ECM, and useful for prediction of Mankin score. [17]

The 3D scanning methodology and practical considerations for hardware reported here offer a potent platform for analysis under spectromics, that is, colocalised Raman scattering and NIR-SWIR hyperspectral data that may be used for accurate diagnosis of OA. Full integration of the

system would result in site-specific assessment of areas of cartilage to map out healthy vs diseased regions of cartilage. The next steps would see quantification of each site for its OA severity that is, areas of thick, healthy cartilage (verified grade 0) to eroded cartilage (verified grade 4-6) to correlate spectral response to clinical grading. Verification via gold standard clinical measure would offer more than the binary classification proven by spectromics thus far, but would require either graduated models for OA severity (enzymatic or mechanically degraded, animal or human tissue) or grading of site-specific wearing.

This system offers site-specific analysis for which a few promising quantitative approaches have been identified to supplement and/or be incorporated into the spectromics approach. Das Gupta et al. report use of k-means clustering (KMC) for spectral discrimination between human tibial calcified cartilage and the subchondral bone plate, and hierarchical cluster analysis (HCA) for identifying the tidemark.[189] The authors purport Raman sensitivity to mapping out "tidemark duplication" during OA wherein the calcified cartilage would advance into DZ articular cartilage and develop multiple mineralisation fronts, and offering another useful spectral biomarker for changing mineralisation.[189] Bergholt and colleagues report for similar samples, application of PCA and KMC, [192] and multivariate curve resolution (MCR) [153,154] for depth wise zonal characterisation of the osteochondral junction. MCR and conceptually similar direct classical least squares component analysis (DCLS) [109] employ reference spectra from pure analytes such as GAG, collagen, hydroxyapatite and water in order to produce concentration profiles of each subcomponent, and have proven sensitive to differentiation of natural and lesion tissues. [109,153,154]

Thus, results to date serve to prove Hypothesis 2, namely the system has proven sensitive to the key Raman scattering and NIR-SWIR absorption chromophores shown to correlate with OA for diagnostic assessment, and, crucially, can allow for mapping of heterogeneity across bone core samples. This is capable of mapping in 3D, spectral characteristics in tissue associated with natural and pathological heterogeneity, and at greater resolution than point measurements with a fibre optic probe or averaging of spectral measurements from cartilage across the joint. Further work is required to perform quantitative assessment of the human femoral head tissue through spectral features identified above and harnessing the diagnostic capability of the spectromics approach. For clinical feasibility, studies with significant statistical power (larger sample population) would need to be carried out. Protocols for sample preparation, mounting, automated scanning, and spectral acquisition have been established to allow a platform for such future studies.

6.4.2 3D Hyperspectral Mapping of Human Femoral Heads

The spectromics investigation in Chapter 5 was limited by reliance on transreflected absorption spectroscopy. Signals from cartilage were taken with the tissue on an unnatural or highly reflective substrate, and as such was not indicative of tissue *in situ* atop bone. Thus, spectral acquisitions and data pre-processing and analysis have since been optimised to accommodate signals from diffusely reflected light.

Hyperspectral mapping was carried out for whole femoral head samples under Raman scattering and NIR-SWIR absorption. Each largely spherically shaped sample was mounted in the 3-jaw chuck via gripping of the severed femoral neck, suspended above the objective lens, with long-axis perpendicular to the lens defining the x-direction. Synchronised motion between the microscope stage (x, y), lens stage (z or r), and rotation stage (θ) allowed for sample mapping across the sample surface for coordinated (x, θ, r) measurements of Raman scattering and NIR-SWIR absorption. For each (x, θ) position, the lens height was manually set by insertion or removal of spacer tubes in order to focus onto the sample surface, and each r position recorded in the hyperspectral dataframe.

Figure 6.13 describes NIR-SWIR absorption spectra from human femoral head articular cartilage on highly reflective and diffusely reflective substrates. Averaged spectra of cartilage samples measured following the protocol of the preceding chapter are shown in Figure 6.13 (a.). Cartilage slices were placed on a gold highly reflective slide (transreflectance) and suspended with significant air gap (~5 cm) between sample and benchtop (diffuse reflectance). In diffuse reflectance geometries there was significant broadband absorption without defined spectral peaks as compared to transreflected spectra, attributed to the low count of photons returning to the sensor without a reflective substrate.

Following the same pre-processing protocol detailed in Chapter 5, subtle peaks in the diffuse signal could still be elucidated, able to yield spectral features in the same wavenumber locations, albeit with reduced relative intensity in some peaks. For example, Figure 6.13 (a.) details reduced yet distinct peaks at around 5200 cm^{-1} (0^{th}-order), attributed to bound and free water, and O-H stretching 1^{st} overtone centred at 6900 cm^{-1} (0^{th}-order), also associated with water. Thus, diffuse absorption measurements of cartilage under suboptimal conditions may still allow for biochemical assessment of tissue, which may then be extended to map the heterogeneities across the joint tissue in vivo.

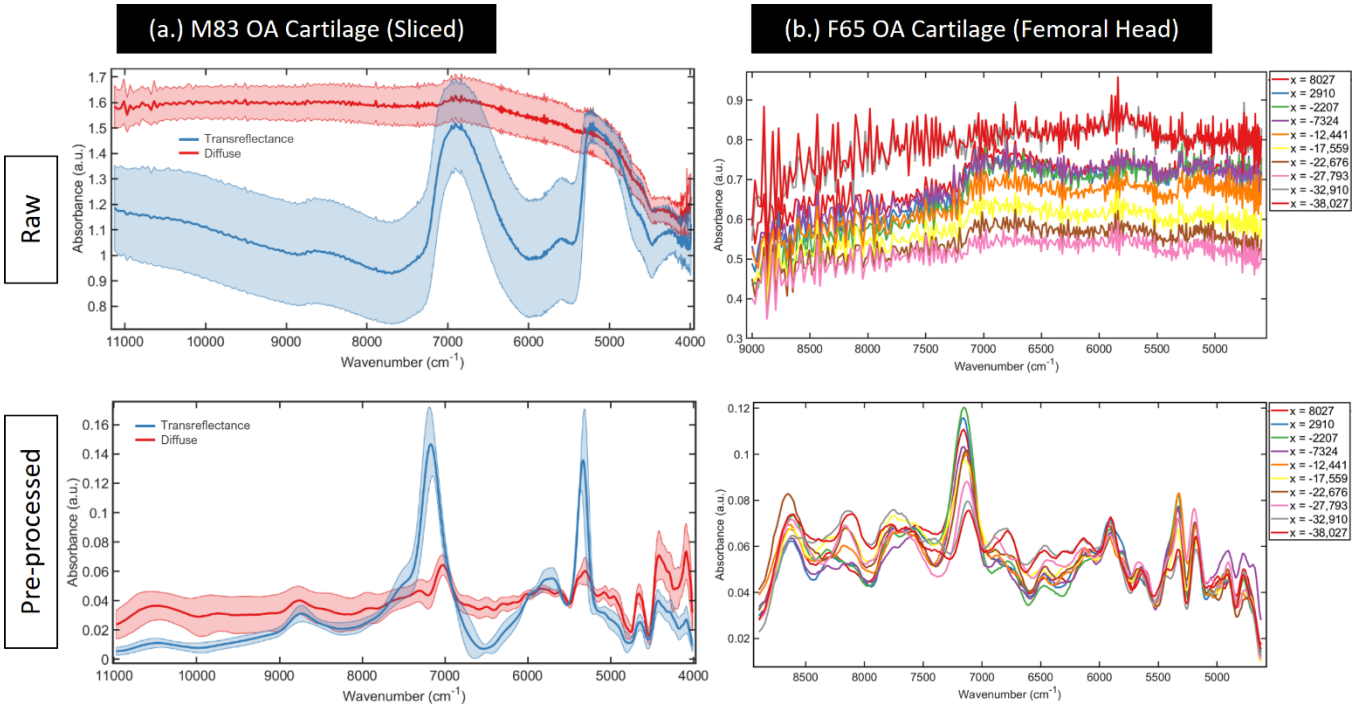

Figure 6.13 Comparing diffuse and transreflected NIR-SWIR absorption spectra of human cartilage, intact on the whole human femoral head (subchondral bone as substrate) and sliced (gold mirror as substrate), respectively. (a.) Averaged (mean and standard deviation) spectra from diffuse and transreflected NIR-SWIR absorptions for slices of osteoarthritic cartilage. "Raw" (0^{th} order) spectra show a broad absorption across the spectral range for diffuse captures compared to distinct peaks for transreflected captures. Pre-processed (1^{st} order) spectra show agreement in peak position between both modes of capture, demonstrate how subtle features may be extracted. (b.) "Raw" and pre-processed spectra from cartilage on a femoral head show the importance of pre-processing for retrieval of useful features for cartilage *in situ*, conducive to *in vivo* detection.

Figure 6.13 (b.) shows NIR-SWIR absorption spectra from articular cartilage *in situ* on the femoral head, displayed as average spectra for varying x positions along the long-axis of the tissue (average of each "ring"). It is anticipated that the spectral response here is confounded with some signal from the subchondral bone (mineralised tissue) which acted as the diffusely reflecting substrate. Nevertheless, this could provide a spectral biomarker of OA induced tissue wearing – should cartilage be sufficiently reduced, incident photons may interrogate deeper into the subchondral bone such that signal characteristic of mineralised tissue would appear more intensely. The substrate effect may be quantified by comparative measure of samples of only the subchondral bone, with cartilage layer naturally or surgically removed. This system is intended for such spatially resolved spectral mapping of tissue heterogeneity across the femoral head and so warrants further investigation.

Figure 6.14 shows correlated 3D data from photogrammetry scanning and NIR-SWIR absorption hyperspectral mapping of a whole human femoral head sample. Photogrammetry allowed scrutiny of the sample by observing visual changes in cartilage, including

- colour changes – healthy (pale) cartilage *vs*. damaged (red/dark) cartilage *vs*. subchondral bone (shiny)
- shape/texture changes – smooth, spherical surfaces *vs*. rough, thinned cartilage (inter-joint space narrowing) *vs*. smooth regions with subchondral bone exposed
- sample orientation – patient specific size and scale, allowing 3D correlation with spectral mapped volumes

Spectral heatmaps were evaluated at NIR-SWIR wavenumbers identified as potential spectromics biomarkers for OA in human cartilage, summarised in Table 6.2 and displayed in Figure 6.14.

Table 6.2 NIR-SWIR wavenumbers visualised for 3D scans of the femoral head, chosen from list of potential spectromics biomarkers of cartilage, with their attributed vibrational mode and significance for cartilage tissue.

1st Deriv. Peak	**Vibrational Mode**	**Assignment** [17,20,50]
5346 cm^{-1}	N-H Stretch (-CONH 1st Ov.)	Predict Bound & Free water
6435 cm^{-1}	O-H Stretch (1st Ov.)	PG (ECM), Predict Mankin score
7173 cm^{-1}	O-H Stretch (1st Ov.)	Water vs. collagen/PG, Ratio predicts relative water content
8649 cm^{-1}	C-H Stretch (2nd Ov.)	

As described above, application of chemometric analysis based on the relative absorption intensities, indicative of the relative tissue composition, will elucidate the heterogeneous tissue change associated with OA across the whole femoral head. The spectromics biomarkers of cartilage indicate regions with significant contribution to the diagnostic models built in the previous chapter and indicate potent spectral regions to map in 3D.

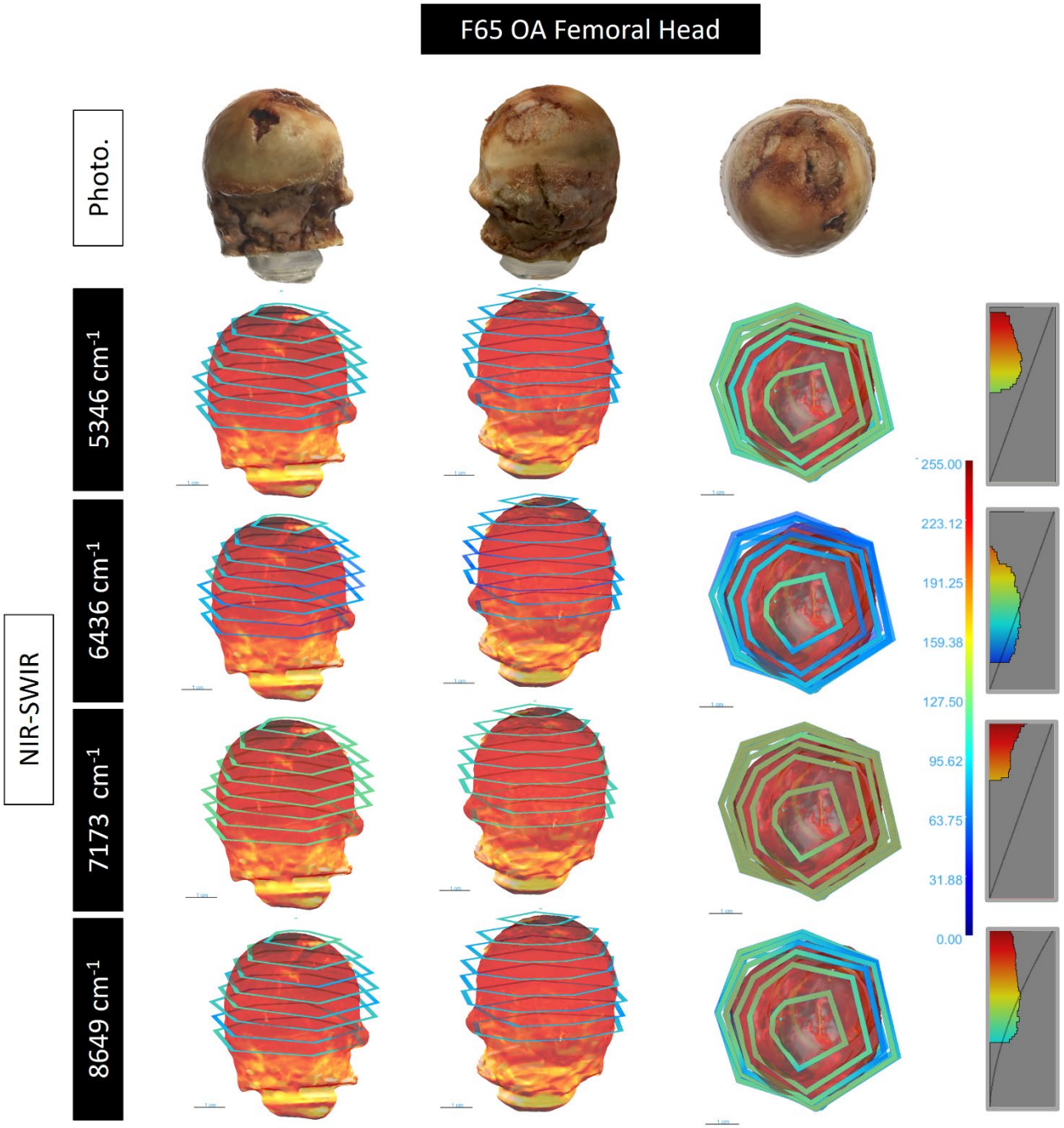

Figure 6.14 Correlated 3D hyperspectral NIR-SWIR mapping of cartilage across whole femoral head: Photogrammetry scans distinguish visible tissue features, allowing mapping of cartilage damage (surgically and naturally induced) by observing colour and texture changes. Hyperspectral maps evaluated at key spectromics wavelengths track spectral changes (chemical composition changes) which hold diagnostic potential across the tissue surface. Colour bar legend shows normalised NIR-SWIR absorption intensities (a.u.), histograms show intensity value distribution. Scale bar = 10 mm.

Thus NIR-SWIR hyperspectral images may indicate the distribution of major chromophores known to correlate with OA pathologies, such as water and PG, and attribute to site-specific composition and structure of articular cartilage. However, in order to make quantitative conclusion a multivariate model should be developed to calibrate spectral readings with histologically verified data, such as Safranin-O-stained sections for predictive modelling of PG content.[98] Nonetheless, data presented here shows proof-of-principle and indicative preliminary measurements, representing a step change from NIR-SWIR spectral mapping approaches to date, wherein bovine patella and osteochondral cross sections have been assessed by manual placement of a fibre optic probe in a macroscale grid pattern. [98]

Thus, results to date support Hypothesis 2 in part degree. Namely, capability has been demonstrated for the system to map heterogeneous NIR-SWIR absorption responses across the scale of the whole femoral head. Visible characteristics of cartilage including site-specific wear and damage can be correlated to its (diffuse) spectral response and therefore chemical composition. However, results have not directly cross-referenced spectral response to regions of thick and thinned cartilage, the tidemark between cartilage and the femoral neck, or defects induced by arthroscopy. Such results are anticipated and will likely show a quantifiable response in the spectral features identified above. Once acquired, comparison of the site specific spectral response to verifying data of chemical changes (histology) and clinical grading (Mankin, KL) could assist in fully demonstrating clinical functionality.

It is important to note that results for spectral mapping of the femoral head have only been carried out thus far under NIR-SWIR absorption spectroscopy. Future work will require application of Raman next for mapping the site-specific tissue changes across the tissue, proven to be sensitive to OA induced composition changes of spongy and subchondral bone on human femoral heads.[111]

As described in 6.3.6 Software Development for Equipment Control and Synchronisation, scans with varying (r) value required manual positioning of the objective lens. This was due to the mechanical limitation of the Nikon Eclipse motorised stage which could only accommodate a range of 10 mm. As such the hyperspectral scan illustrated in Figure 6.14 was carried out over the course of approximately 3 hours. Long acquisition times also holds risk of samples drying out.

Thus, further development of the system necessitates both an improved z-stage (greater range of motion) and an autofocusing function for fully automated scans of spherical objects, be that larger femoral head samples or other macroscale asymmetric samples. Raman spectroscopy with the current CCD camera was sensitive to ambient temperature (sensor saturation, triggering device soft-lock), and as such could not be operated on warm summer days.

Additional equipment for active cooling of the camera, such as fans or Peltier cooler, and increased ventilation, would help keep internal temperatures below threshold to extend the operable ambient temperature range of the system.

In summary, the system is sensitive to the diffusely reflecting spectral signal obtained from human subchondral bone and articular cartilage from intact tissue samples. Again, this demonstrated the capacity for 3D mapping of spectral features associated with natural and pathological heterogeneity, and at greater spatial resolution than point measurements with a fibre optic probe. Heterogeneity may be mapped in both spectral modes and cross-referenced to visual features, though results presented here demonstrate only the capacity of NIR-SWIR and argue the potential for Raman mapping of the whole femoral head.

This system has the potential as a platform for studies into further understanding the mechanism of OA and associated degradation of tissue. Understanding biochemical changes of soft tissues across the whole joint could give insight into how OA may differentially affect specific patients (age, sex), at specific times (OA grade), and at specific positions (weight bearing, comorbidities) within the joint. It is anticipated that the results presented here offer a tool for furthering biological and medical understanding of this complex disease.

6.4.3 Improvements to Correlative Imaging

The protocol laid out above involved manual alignment of the surface mesh (photogrammetry) of the whole femoral head to the relatively low-resolution spectral map. This was prone to ambiguity since the Dragonfly software could not display the full colour photo model, and instead relied on topographical features such as macro-scale form and texture changes.

Preliminary work has been carried out in the use of fiducial markers to aid alignment of photogrammetry and hyperspectral maps. Polystyrene pellets were chosen for their strong and distinct signal in both Raman and NIR-SWIR modalities, displayed in Figure 6.15.

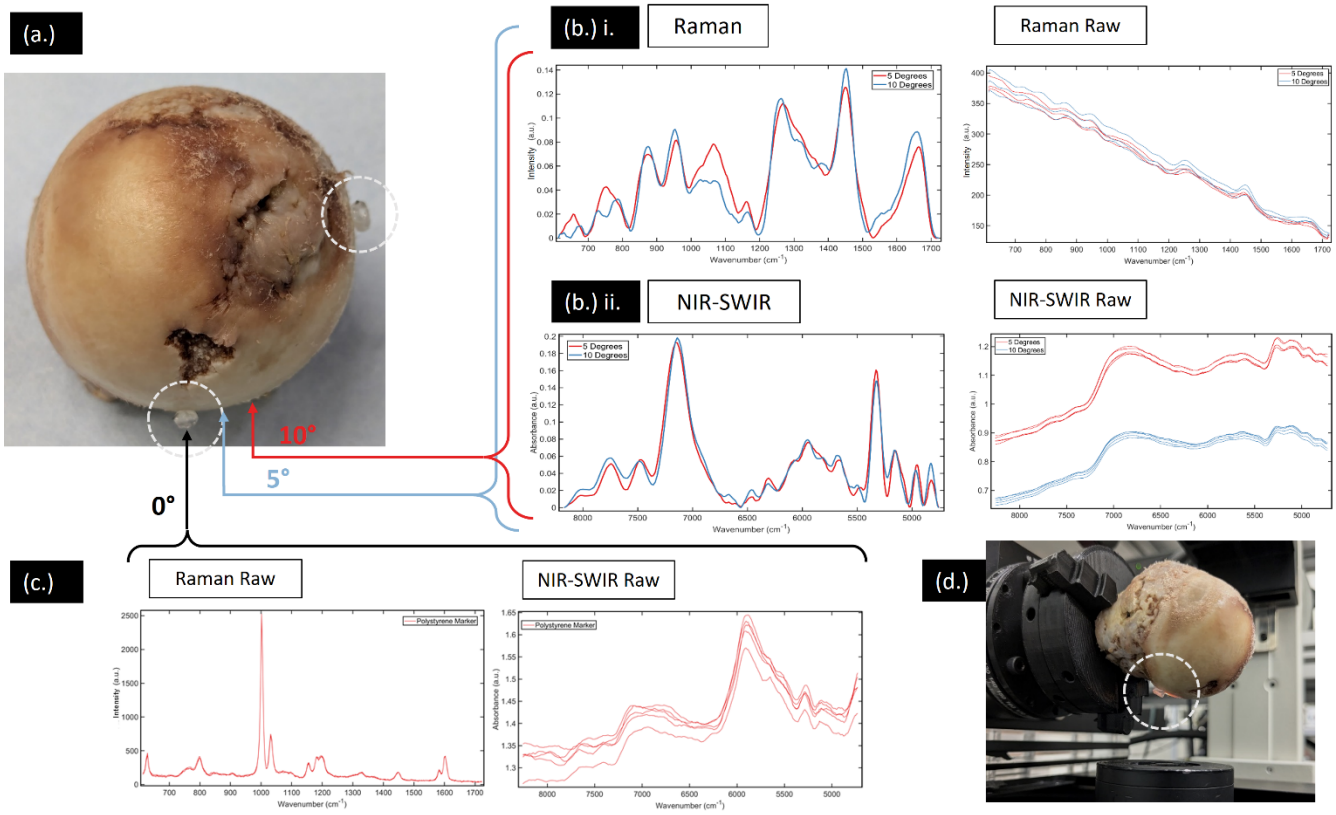

Figure 6.15 Fiducial markers to aid alignment of spectral data from the whole human femoral head. (a.) Femoral head with attached polystyrene bead fiducial markers. (b.)i. Pre-processed (left) and "raw" (0^{th} order) (right) Raman spectra of cartilage adjacent to the polystyrene marker. (b.)ii. Pre-processed (left) and "raw" (0^{th} order) (right) NIR-SWIR spectra of cartilage adjacent to polystyrene marker. (c.) "Raw" (0^{th} order) spectra for Raman and NIR-SWIR Polystyrene bead showing clear discernible spectral shape. (d.) Femoral head with fiducial markers mounted onto goniometric scanning system.

Polystyrene pellets (approx. 2 x 3 mm) where attached to the femoral head sample at points orthogonal to each other ($\Delta\theta$ = 90°) and offset in height (Δx = 15 mm), shown in Figure 6.15 (a.). This would allow triangulation for each of the 3D data sets to aid in manual alignment, thanks to distinct difference in spectral response between the adjacent cartilage (Figure 6.15 (b.)) and the pellet (Figure 6.15 (c.)). Future work would see alignment carried out via an automated peak detection programme, sensitive for example to the narrow and intense 1004 cm^{-1} Raman peak from polystyrene.

6.5 Conclusions and Future Work

This study constructed and developed an automated 3D goniometric multimodal hyperspectral mapping system capable of co-localised Raman scattering and NIR-SWIR absorption mapping across bone cores and whole human femoral head samples. This was motivated by the need for "real time" spectromics assessment of cartilage *in situ* on subchondral bone, rather than spectral measurements on separate spectroscopic systems with tissue samples placed on a reflective surface.

The diffusely reflected NIR excited Raman scattering and NIR-SWIR absorption response of diseased (osteoarthritic) and control (osteoporotic) osteochondral tissues was investigated. The approach for optimal pre-processing of diffuse spectra was investigated to translate the spectromics approach established in the preceding chapter (reflective substrate) to a technique conducive to *in vivo* measurements (natural substrates). This has been proposed for arthroscopic clinical application. Pre-processing steps including 1st derivative transformation and noise reduction elucidated the same spectral features proposed as biomarkers through the spectromics study.

The full workflow has been established for automated goniometric surface scanning, including mounting of intact tissues, optimal choice for NIR-SWIR optics and hardware, spectral acquisition software development, and 3D reconstruction of processed spectral data. Results to date have demonstrated capacity to map spectral response across the surface of bone cores representing the osteochondral junction of diseased and control femoral heads, and across the surface of diseased whole femoral head tissues.

The system was demonstrated as the first of its kind for non-contact Raman scattering and NIR-SWIR absorption hyperspectral mapping of whole human osteochondral tissues. Measurements without the need for placement of optical fibre probes in contact with the tissue could accommodate a range of tissue samples without sampling bias and high spatial resolution (small stage movement steps). Varying sample geometries have been accommodated so far in cylindrically symmetric bone cores with diameter ~10 mm, and asymmetric, largely spherical whole femoral head with diameter ~45 mm. Uniquely shaped surface scans of each sample were then cross referenced with full colour photogrammetry scans.

The system was developed with the vision of integrated multimodal scanning capable of collecting a library of spectra as *ex vivo* ground truth from which a clinician may assess cartilage tissue arthroscopically under spectromics. Results to date show proof of the capability for detailed insight into site-specific biochemical composition across the surface of tissue

samples, referenced against visible changes in photogrammetry scans. Hyperspectral mapping shows suitable sensitivity to Raman and NIR-SWIR spectral features known to correlate with OA progression, capable of detecting spatial pathological heterogeneities across whole femoral head samples.

This included peaks attributed to tissue mineralization (Raman ~960 cm^{-1}) able to distinguish the thicker cartilage layer of the control bone core sample, compared to the severely thinned cartilage in the diseased sample, and attributed to amide I (Raman ~1649 cm^{-1}) and carbonate (Raman ~1070 cm^{-1}), which in ratio with the hydroxyapatite peak could track early OA degradation across the surface of intact cartilage and subchondral bone. Other spectral peaks with proven correlation with OA were evaluated across each 3D surface including those attributed to water (NIR-SWIR ~5283 cm^{-1} and ~7156 cm^{-1}) and PG (amide III, Raman ~1302 cm^{-1}).

For the scanning of whole human femoral head tissue surface, hyperspectral maps were evaluated at NIR-SWIR peaks identified as potential spectromics biomarkers, features most contributing to accurate detection of OA in human cartilage. The utility of these features has precedent in the literature for the prediction of water content, PG content, and Mankin score. Results to date showcase the capacity of NIR-SWIR mapping and argue the potential for Raman mapping of the whole femoral head.

Thus, these results are proposed to inform a paradigm shift in arthroscopic assessment of intact cartilage under label free vibrational spectroscopy. Leveraging the accuracy of the spectromics approach may mean a reduced number of spectral features (biomarkers) need be considered when assessing tissue, reducing computational expense. Utilising a library of site-specific spectral measurements across exemplar human femoral heads may mean only a few sites need be targeted when carrying out arthroscopic measurements, reducing healthcare system expense. This provides the foundation for increased accuracy and improved patient quality of life in the early detection of OA.

Quantitative analysis approaches have been discussed for gaining understanding of the biochemical composition (e.g. peak ratios) and heterogeneous distribution across the scale of the femoral head (PCA, HCA, MCR etc.) resulting from OA. Further investigation into inter-sample classifications under spectromics now requires more samples to be mapped, and in order to build the envisioned spectral library. Quantitative conclusions about the varying degrees of OA severity across the tissue (intra-sample classification) now require verification through a gold standard (Mankin, KL score), adding further proof for clinical viability.

In summary, the overall scanning approach is offered as a platform for further understanding the complex mechanism of OA, and across complex joints such as the hip. Hyperspectral assessment of soft tissues across the whole joint could give further insight into the effect of patient parameters such as age and sex, which may have differential effect on the wearing of joints, due to comorbidities, lifestyle choices, etc. It is hoped that results presented here offer methodology and tool-level development for furthering biological and medical understanding.

Finally, further strategies for system and protocol improvements are identified below.

6.5.1 Autofocus Strategies

As identified above, this system would benefit greatly from the implementation of autofocusing for spectral measurements across the varying surface contours of each macroscale sample. One strategy explored involved spatial frequency analysis of brightfield images of the sample surface. This assumed that high spatial frequencies corresponded to finer details resolved in the image, indicating the objective lens has been brought to focus on the tissue sample surface. An algorithmic approach was developed to iterate through varying z-positions of the microscope focusing stage, capture a brightfield image, evaluate the spatial frequencies (focus metric), and return the z position with the highest frequency. This was also carried out by using standard deviation of the pixel values as the focus metric, where higher contrast in a focused image would show greater distribution of pixel intensities, as compared to a blurred out-of-focus image. This would then be incorporated as an additional step in the scanning programme, wherein the sample could be mapped first for its height (z) at each cylindrical position (x, θ), coordinate positions recorded, and then revisited for a scan of NIR-SWIR absorption and Raman scattering signals.

However, this could not be implemented due to the limited range of the Eclipse Ti-E z-stage of only 10 mm. As such, the system may be improved by replacement with an alternative objective lens mounting stage with greater range of motion or construction of a linearly translating stage with closed-loop servo control, allowing precise and repeatable positioning. This would be implemented in a similar way for control via Python in the scanning programme.

6.5.2 Spherical Parallel Manipulator

An alternative approach for sample scanning of the femoral head would be through mounting on a spherical parallel manipulator (SPM), capable of rotating a sample in 3 rotational degrees of freedom to prescribe a spherical workspace.[193–195] The 3RRR SPM is composed of three identical articulated curved limbs sharing a common base platform (BP) and common mobile platform (MP). The MP may be rotated about a common point in the centre of the mechanism, defined by

intersection of the axes of all joints, depicted in Figure 6.16. Should the femoral head be mounted onto the MP the sample may be rotationally translated about the focus point of the objective lens, tracing across the largely spherical surface.

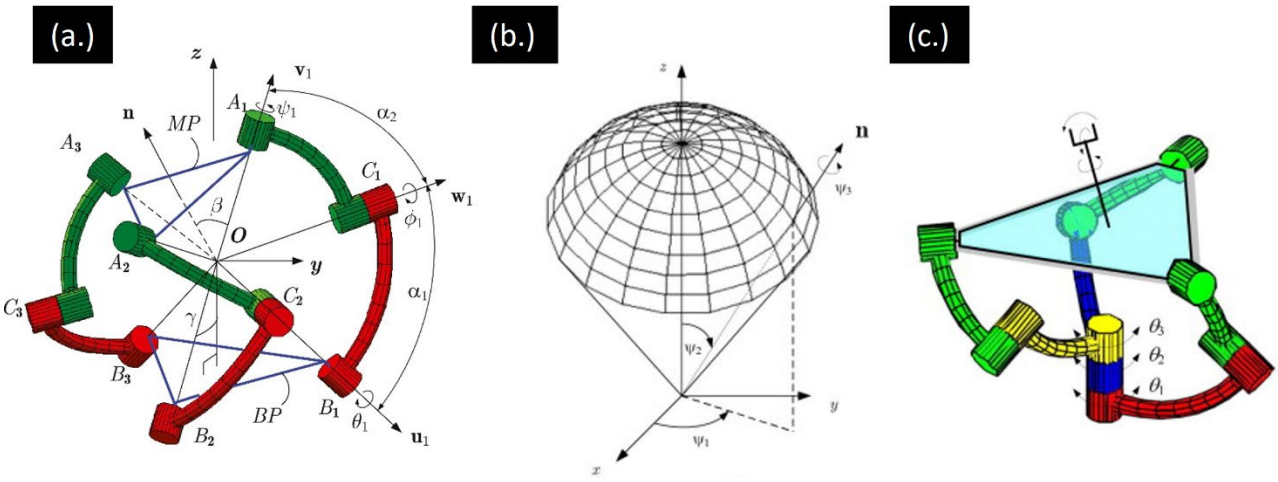

Figure 6.16 (a.) Schematic of a general 3RRR spherical parallel manipulator (SPM) made up of three identical articulated limbs, sharing a common base plate (BP), common mobile platform (MP) on which the sample may be mounted, capable of rotations about a common point (O) at the centre. From Bai et al.[193] (b.) Prescribed workspace of the 3RRR SPM. (c.) A special case SPM where $\gamma = 0$, referred to as an active ball joint. From Bai et al.[195] Reproduced with permission from Elsevier.

Such a scanning system would allow for larger freedom to manipulate the sample for scanning across asymmetric and largely varying topographies on the femoral head. Should the SPM be mounted on a z-translating stage (with suitable range of motion) this could accommodate a greater range of femoral head sample sizes (diameters). Custom construction of the SPM limbs, most likely through 3D-printing, could accommodate ranges of sample sizes (small, medium, large etc.) as well as for other tissue geometries (cylindrical etc.), shown in Figure 6.16 (c.).

Chapter 7 Single-Cell Resolved Precise Ablation of Tissue for NIR-SWIR Therapeutics

This chapter describes results published in part as a research article with Journal of Biomedical Optics for which I was joint first author along with Matthew Gerard (Optoelectronics Research Centre, University of Southampton) and a primary contributor. Reproduced below with permission from SPIE.

Matthew D. Gerard [†], Hiroki Cook [†], James A. Read, Ibrahim H. Abughazaleh, Panuwat Srisamran, Siddhi Chugh, Sijing Liang, Qiang Fu, Richard O. C. Oreffo, David J. Richardson, Sumeet Mahajan, Lin Xu, *"Single-cell high-precision ablation using nanosecond-pulsed thulium-doped fiber laser,"* Opt. Eng. 63(8) 086102 (2024), [†] Joint First Authors [3]

Design and in-house manufacture of the TDFA and MOPA system was carried out principally by Matthew Gerard of the Optoelectronics Research Centre (ORC, University of Southampton). The laser system was delivered to the Institute for Life Sciences (IfLS, University of Southampton) and then implementation into the microscope system (imaging, sample manipulation) was carried out principally by Hiroki Cook. Development and optimisation of the overall ablation system and each ablation experiment was carried out in close collaboration, reflected in status of joint first authorship of the published results. This included optimising for sample preparation and handling, optical components for ablation and imaging, instrument programming, and processing and interpretation of results.

7.1 Abstract

This study demonstrates pulsed laser ablation at single-cell level precision on onion epidermal and human neuroblastoma samples, reported for the first time using an advanced 1.95 µm nanosecond-pulsed thulium-doped fibre laser (TDFL) with high degree of pulse control. This configuration allowed targeting of the highest water absorption peak in the NIR-SWIR regime that can be accommodated by conventional silica optics. Coupling to a custom configured microscope with motorised stage allowed precise sample positioning and utilising reflective optics allowed efficient transmission of the ablation beam without chromatic aberration.

Individual cells were accurately destroyed whilst minimising collateral damage to neighbouring cells through systematic tuning of overall ablation outcome by varying pulse parameters, namely average power, exposure time, pulse duration, and repetition rate. Single-cell ablation was achieved with a precision of 31.3 ± 0.1 µm for the onion epidermal cells and 19.9 ± 0.1 µm for fixed human neuroblastoma cells, the latter capable of targeting individual cells in a sample of up to 250,000 cells, showing high precision suitable for selective ablation without affecting

the overall sample. Careful control of the pulse parameters produced ablation without carbonisation and cavitation bubbles.

The TDFL, with an easily accessible range of wavelengths, provides significant opportunities in the field of biology and medicine for stimulation and dissection. High-precision laser ablation with minimal collateral damage demonstrated here paves the way for micro- surgery in clinical applications.

7.2 Introduction

Laser ablation is a top-down process through which material is removed from a substrate following irradiation with a focused laser beam and occurs once the targeted volume has absorbed sufficient energy to result in degradation and destruction. Ever since the invention of the first laser in 1960 by Maiman,[196] there has been considerable anticipation toward the application of lasers to medicine and the potential therein to selectively destroy tissue; however, the first clinically viable techniques were not demonstrated until the 1980s.[197] As laser technology has progressed, applied systems have gradually permeated into a greater number of clinical settings such as ophthalmology [136–138,198] and lithotripsy, removal of kidney stones and other hardened masses.[119,131–133] Regarding the latter, holmium-doped yttrium aluminum garnet (Ho:YAG) lasers have been the accepted gold standard for the last two decades; however, in recent years, a new challenger has emerged in the form of the thulium (Tm)-fibre laser. Tm fibre lasers target peaks within the water absorption spectrum, taking advantage of the high percentage of water in the human body. The advantage the thulium-doped fibre laser (TDFL) brings is a more than four-fold increase in the water absorption coefficient, from 30 to 140 cm^{-1} as shown in Figure 7.1.

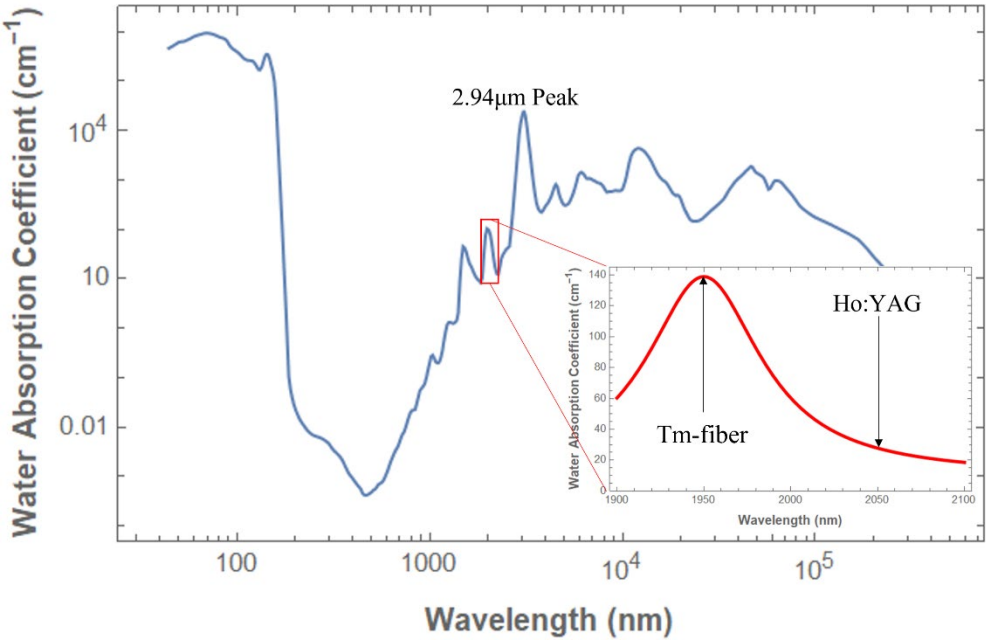

Figure 7.1 Broadband water absorption spectrum ranging from the UV to the far IR with the 2.94 µm peak identified. The inset highlights the 1.95 µm peak and the difference in absorption coefficient between the Tm-fibre laser used in this investigation and a typical Ho:YAG laser

A higher coefficient of water absorption results in a greater ablation efficiency and lowers the ablation threshold, leading to an enhanced safety profile, and improved outcome for patients in higher surgery success rate and reduced collateral damage. Considering biological tissue as turbid, scattering media,[64] lasers operating in the near and shortwave infrared (NIR, SWIR) benefit from deep penetration as compared to visible radiation [4] due to a decrease in the scattering coefficient with increasing wavelength.[12,67,68] Reduced attenuation thus would aid ablation efficiency by minimizing collateral heating and damage to surrounding, healthy tissues as a greater proportion of photons reach the intended target. In comparison to bulky solid-state lasers, Tm-fibre lasers offer a number of advantages including compactness, robustness, and reliability. The large surface-area-to-volume ratio of fibres ensures simple and effective heat dissipation, and their high degree of flexibility allows application in otherwise awkward procedures such as ureteroscopy and intraoral surgery.[129]

The highest infrared (IR) water absorption peak is centred at 2.94 µm, [135] which is therefore the most efficient ablating wavelength. However, considering water absorption alone does not give the full picture for optical design choices in instrumentation and further adoption of this technology. Low-loss transmission of 2.94 µm radiation is currently only readily possible in soft-glass-based fibres, such as fluoride and sapphire fibres that display poor physical and chemical qualities compared to their silica-glass counterparts.[199,200] Maintaining a fused silica fibre design supports a commercially more affordable end-product which in the long-term would improve

global user accessibility. Consequently, the 1.9 μm absorption peak has been targeted for the highest water absorption peak transmissible through silica fibres.

In the quest towards highly precise surgery, for example in cornea trephination or in retinal surgery where preservation of healthy photoreceptor cells is paramount, scientists have generally focused on systems targeting the highest peak of water absorption at 2.94 μm.[138–140,201] Utilising 300 ps pulses at 2.95 μm, Miller and colleagues showed that incisions in murine skin models were achievable with a precision of 8 μm, smaller than the diameter of a single skin fibroblast, resulting in minimised scarring compared to conventional surgical laser (Er:YAG) or a scalpel. [139] Achieving a similar level of precision at 1.9 μm would be a significant step forward with an alternative and more economically viable system.

A key flaw suffered by many commercial laser ablation products is their lack of control over fundamental pulse parameters. They are designed only to generate pulses with specific pulse durations and at specific repetition rates, with limited or negligible user control to customise the end result. This is a non-issue should the systems only target one type of tissue since these will be configured for a set of agreed optimum parameters from which any deviation would be damaging or dangerous.[130,202,203] Building a system for a more extensive application not only requires the targeting of a common absorption band (water) but also comprehensive control of the pulse parameters to facilitate high-quality ablation across a wide variety of tissues.

The interaction between light and biological tissue is complex, [94] sensitive to both composition and morphology, and thus, any broadly applied laser ablation tool must be able to adapt to these changes to prove its effectiveness. This chapter details the development for microsurgery of a single-mode TDFL with a pulsed output and configured as a master oscillator power amplifier (MOPA) system. The laser output has a central wavelength of 1.95 μm, with a spectral linewidth of ≤0.3 nm, and provided a near-diffraction-limited output with a beam quality of $M^2 \leq 1.2$. The pulses were generated from a diode laser directly modulated by an arbitrary function generator.

To further understand the effects of pulsed laser emission on ablation outcome, four fundamental parameters, average power (P_{avg}), pulse duration (τ), repetition rate (R), and exposure time (t_{exp}), were individually varied using the AFG3102 and the subsequent effects on both cell types were examined.

HYPOTHESIS 3: Targeting the NIR-SWIR water absorption peak with 1950 nm laser pulses through a novel ns-pulsed Th-doped laser can allow for precise single-cell scale ablation for clinical application

7.3 Methodology

The underlying aims for developing a system for precise laser ablation are as follows:

1. Focused laser beam with spot size as small as possible
2. Laser coincides with sample at surface
3. Sample mounted securely and precisely adjustable
4. Viewing and imaging of the sample during ablation

This was to enable investigation into four fundamental laser pulse parameters and accurately measure its effect on ablation of cell samples, namely:

1. Average power, P_{avg}
2. Pulse duration, τ
3. Repetition rate, R
4. Exposure time, t_{exp}

Fine control of the laser pulse parameters was investigated to produce accurate cutting of cell samples whilst keeping collateral damage to a minimum. Here cell fate was used as a metric for ablation precision, quantified following criteria laid out in 7.3.6 Quantifying Ablation.

7.3.1 TDFL Development

The thulium-doped fibre laser (TDFL) was configured as a MOPA, wherein a low power, spectrally narrow signal is employed to "seed" the system with a specific wavelength, before passing through three successive amplifier stages to reach the desired level of output power. The TDFL system is described in Figure 7.2, each amplifier stage demarcated within the dashed line.

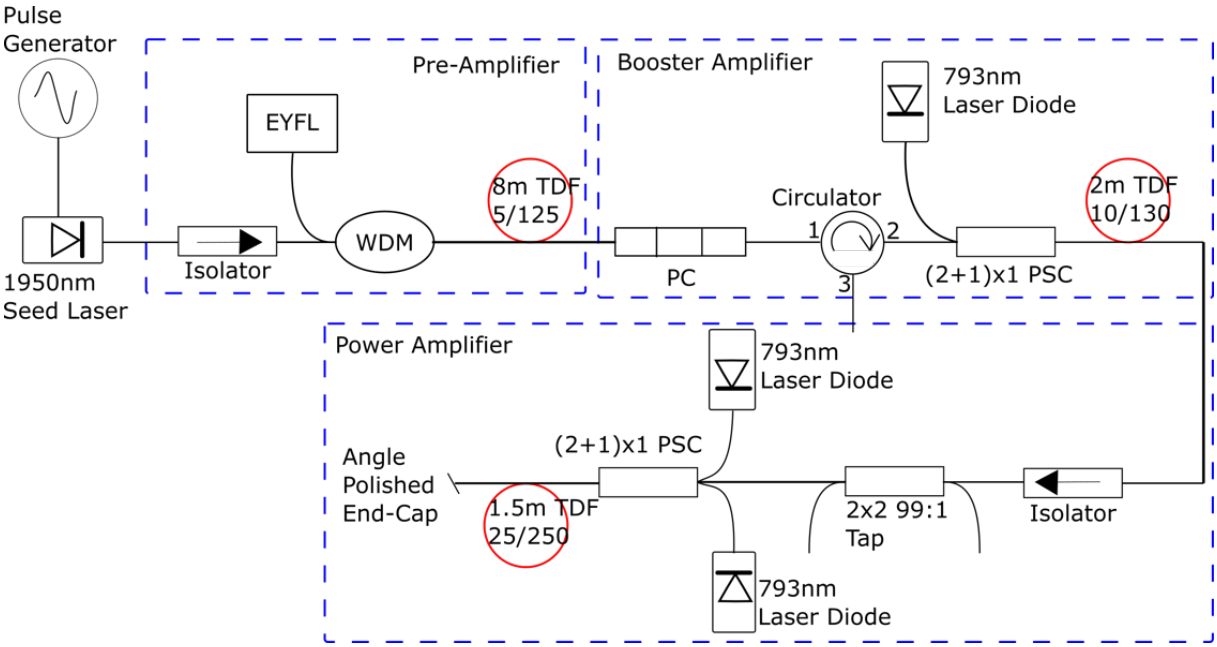

Figure 7.2 Full system schematic of the TDFL with each amplifier stage contained within a dashed line. The 1.95 µm laser diode acts as seed for the signal 1950 nm wavelength and the pulse generator controls pulsed operation. The pre-amplifier stage consists of an isolator, a wavelength division multiplier (WDM), and an 8 m thulium-doped fibre (TDF) with core/cladding specifications of 5/125 µm pumped by a 1565 nm Er-Yb fibre laser (EYFL). The booster amplifier consists of a polarization controller, a circulator, and 2 m TDF with core/cladding specifications of 10/130 µm pumped by a 793 nm laser diode. The power amplifier consists of an isolator, a 2 × 2 99:1 tap, a 1.5 m TDF pumped by a pair of 793 nm laser diodes, and an angle-polished endcap. TDFL designed and constructed by Matthew Gerard (ORC).

Laser pulses were generated from the diode laser (InGaAs/InP multiple quantum well discrete-mode, Eblana Photonics, Dublin, Ireland) [204], biased below threshold, and directly modulated by an arbitrary funciton generator (AFG3102, Tektronix, Beaverton, Oregon, United States). This allowed control over the four fundamental pulse parameters described above for the 1950 nm signal by tuning of the AFG3102. The seed laser was actively cooled by thermoelectric cooler (TEC) during operation, ensuring stable emission wavelength. Output power of the seed laser was recorded at ~1 mW.

The pre-amplifier stage consisted of an 8 m length of thulium-doped fibre (TDF, TmDF200, OFS) which was forward core-pumped by an Er-Yb fibre laser (EYFL, in-house manufactured at the ORC), operating at 1564 nm through a wavelength division multiplexer (WDM). An isolator placed after the seed laser prevented back reflection from the amplifier. Average output power after the pre-amplifier was measured at 265 mW.

The booster amplifier stage consisted of a double-clad TDF (PM-TDF-10P/130-HE, Coherent, East Granby, Connecticut, United States) cladding pumped by a 793 nm laser diode (I5F-HS1, DILAS, Tucson, Arizona, United States) at 9 W. The double-clad TDF had core/cladding diameter of10/130 μm, cladding absorption of 9.6 dB/m at 793 nm, and length of 2 m to ensure sufficient pump absorption.

A polarisation dependent circulator acted as an isolator and port to monitor background travelling signal for signs of stimulated Brillouin scattering (SBS) during power amplification. Average output power of 1.25 W was obtained from the booster amplifier without any observable SBS. SBS is a nonlinear scattering effect capable of generating backward-traveling pulses with the potential to damage components within the TDFL when the optical power becomes too high. Due to the narrow spectrum generated by the seed laser (<0.3 nm) and the length of pulses used (>10 ns), preventing SBS is of the utmost importance. [205–207]

The power amplifier stage consisted of a large-mode area (LMA) TDF (LMA-TDF-25P/250-M, Coherent) with core/cladding diameter of 25/250 μm with a cladding absorption of 11.4 dB/m at 793 nm, and a short length of 1.5 m to provide sufficient pump absorption whilst eliminating the likelihood of SBS occurring. Two 793 nm laser diodes (MTAB00107 and MTAB00114, BWT, Beijing, China), each with 30 W maximum power, pumped the LMA TDF via a (2+1)×1 pump/signal combiner.

The TDF was wired on a racetrack mount to exclude high-order modes and ensure fundamental-mode operation, and water cooling at 12°C was applied to the mount to improve and maintain the slope efficiency. An angle-polished endcap made from a 1 mm length of coreless fibre was spliced to the end of the TDF to prevent back reflection. A 2 × 2 coupler with a 99 : 1 ratio was placed behind the TDF to provide a 1% coupling port for monitoring both the forward and backward signal powers within the amplifier.

The MOPA system was characterised for output power, spectrum, pulse shape, and beam quality of the 1950 nm signal, described in Figure 7.3. Under 50 ns pulses at 250 kHz, the signal power from the power amplifier showed a linear increase with pump power with slope efficiency of 40% and maximum output power of 11W (Figure 7.3 (a)). The signal had a central wavelength at 1951.5 nm with narrow linewidth of ≤0.3 nm and optical signal to noise measured at 22 dB relative to the spontaneous emission background (Figure 7.3 (b)). Pulse width and repetition rate could be tuned via the AFG3102 to produce for example laser pulses with 7 ns, 40 ns, 350 ns, and 680 ns duration, corresponding to 10 ns, 50 ns, 500 ns, and 1 μs electrical pulse duration, respectively (Figure 7.3 (c)). The 20-30% shortening of pulse duration is caused by the spiking inherent to the gain modulation of the setup.[208,209]

Beam quality was near diffraction-limited with an average M^2 value <1.2, shown in Figure 7.3 (d).

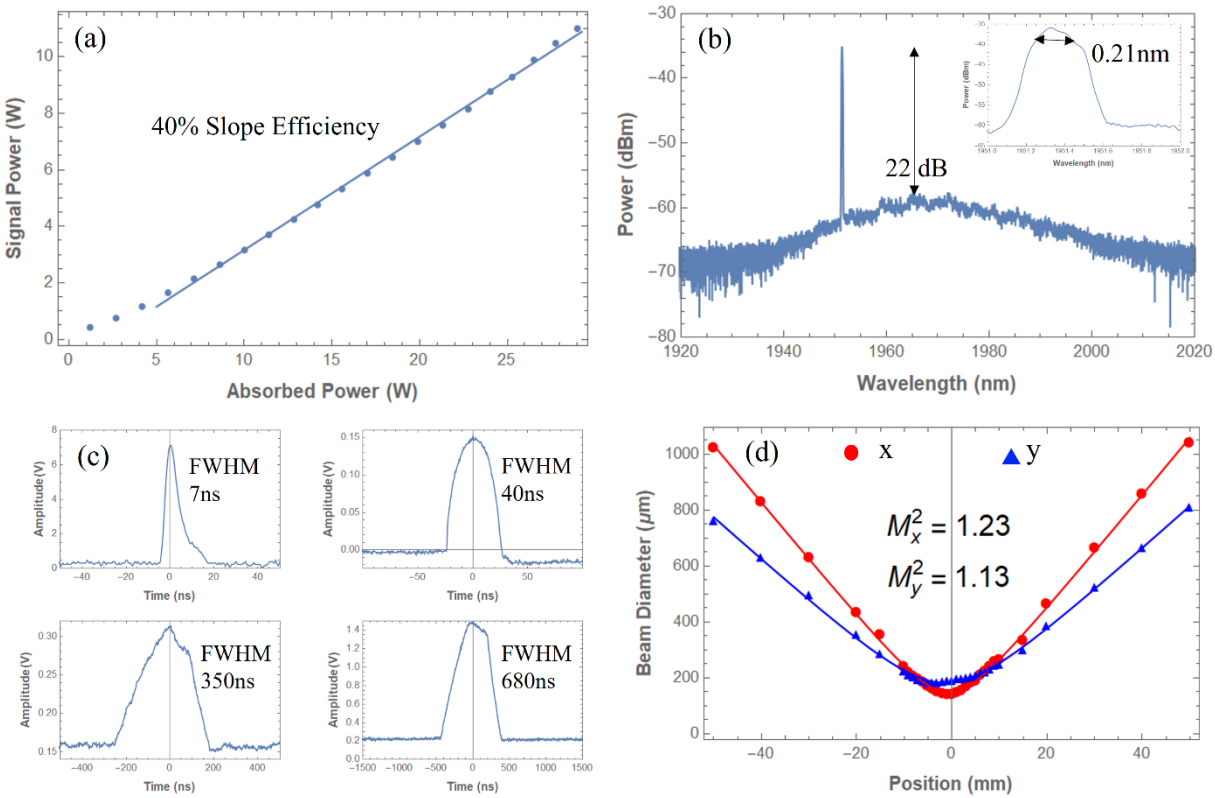

Figure 7.3 Characterisation of the master oscillator power amplifier (MOPA) (a) The thulium-doped fibre laser (TDFL), showed power slope efficiency of 40%. (b) Signal spectrum centred at 1951.5 nm with narrow linewidth ≤ 0.3 nm (inset) and 22 dB optical signal-to-noise ratio (0.05 nm resolution). (c) The optical pulse shape and full-width half maximum (FWHM) of 10 ns (top left), 50 ns (top right), 500 ns (bottom left), and 1 μs (bottom right) electrical pulse, as measured with a photodiode. (d) Beam quality of the signal along the x-axis (red) and y-axis (blue), with average beam quality M^2 = 1.18. MOPA and TDFL output characterised by Matthew Gerard (ORC).

Individual pulse energy, E_p, is given by

$$E_p = \frac{P_{avg}}{R} \quad (1)$$

where P_{avg} is the average power of the laser pulse, and R is its repetition rate. The peak pulse power is given by

$$P_p = \frac{P_{avg}}{R\tau} \quad (2)$$

where τ is laser pulse duration. The corresponding pulse energy (E_p) and peak pulse power (P_p) for the 40 ns pulse in Figure 7.3 (c) are 43 µJ and 457 W, respectively.

7.3.2 Laser Ablation Delivery and Optimisation

Schematic of the beam delivery system developed in-house is described in Figure 7.4.

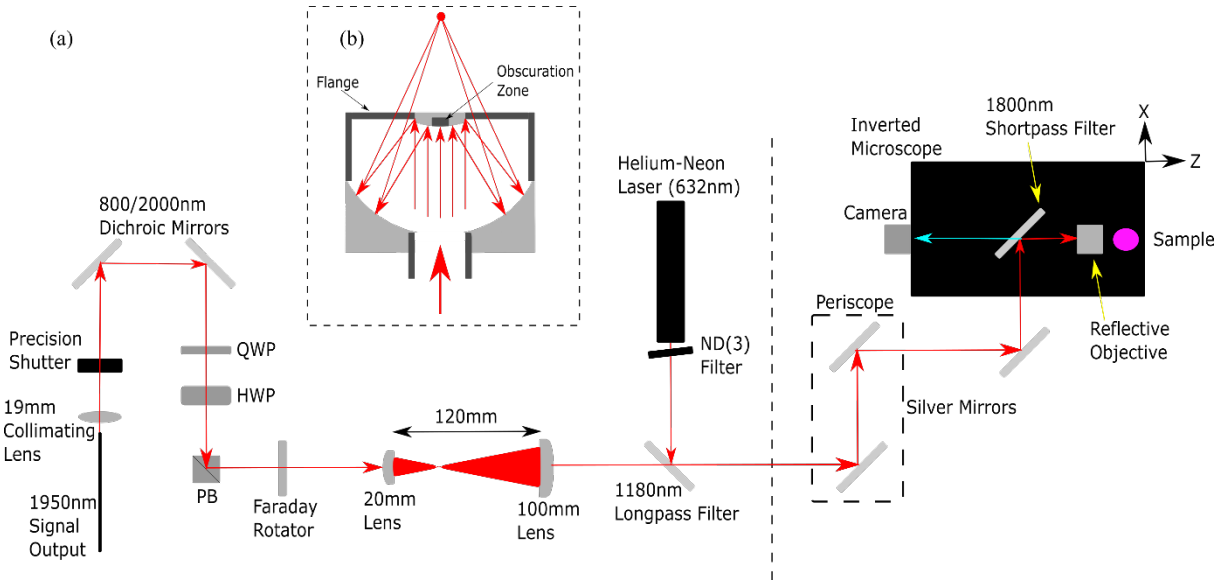

Figure 7.4 Schematic of the beam delivery setup coupling 1.95 µm signal from the thulium-doped fibre laser (TDFL) into the microscope for laser ablation. (a) The signal passes through a 19 mm collimating lens and time-controlled shutter, before reflecting off a pair of 800/2000 nm dichroic mirrors. A combination of quarter-wave plate (QWP) and a half-wave plate (HWP) selected the appropriate polarisation for transmission through a polarization beam splitter (PB). After passing through a Faraday rotator, the beam is expanded by a telescope made up of a 20 mm and 100 mm lens. An 1180 nm long pass filter combines the signal with a He-Ne guidance beam into a periscope comprised of two silver mirrors. A third silver mirror reflects the light into the microscope (black box, top right) where an 1800 nm short pass filter directs the beam through a reflective objective lens, onto the sample. The camera can visualise the sample during ablation by virtue of the 1800 nm short pass. (b) Beam diagram of the reflective objective lens (NA = 0.52), with obscuration of 17% reported by the manufacturer.

The output beam from the TDFL was collimated with a 19 mm lens before passing through a programmable mechanical shutter (SH1, via SC10 benchtop controller, ThorLabs). A pair of 800 nm / 2000 nm dichroic mirrors filtered any remaining residual from the 793 nm pump laser. Then a combination of a quarter-wave plate (QWP), half-wave plate (HWP), and polarising beam splitter (PB) allowed adjustment of the 1950 nm beam polarisation. The beam next encountered

a Faraday rotator which served to prevent any back reflections of light with the same polarisation, thus protecting the amplifier from possible damage.

A system for precise laser ablation would facilitate the following:

a) Focused laser beam with spot size as small as possible
b) Laser coincides with sample at surface
c) Sample mounted securely and precisely adjustable
d) Viewing and imaging of the sample during ablation

These aims were answered through integration of the TDFL MOPA into an inverted microscope system (Eclipse Ti-U, Nikon, Tokyo Japan) with precise motorised stage (MIV-2000 TE2000HE, coupled to MS 2000 control unit, Applied Scientific Instrumentation), coordinate positions programmed with MicroManager 1.4 software (μManager). The SH1 programmable mechanical shutter was used to control the exposure time of the laser beam on the sample. The opening time of the shutter could be controlled with millisecond precision.

Following transmission through the Faraday rotator, the 1950 nm beam was expanded by a telescope comprising of a 100 mm and 20 mm lens in order to match the back aperture of the reflective objective lens. The focal length ratio meant for a beam diameter expansion by factor of 5. A periscope comprised of silver coated mirrors and mechanical circular iris apertures diverted and aligned the laser beam into the back port of the microscope. A mounted 1180 nm long pass (LP) filter (DMLP1180R, Thorlabs) on the benchtop allowed overlap between a 632 nm (visible) He-Ne guidance laser and the1950 nm TDFL beam to aid optimisation of laser system alignment, and alignment between field of view of the microscope eyepiece and brightfield camera.

7.3.3 Optimising Optical Components

Microscopic imaging was developed to allow precise visualisation of the effects of ablation on each sample. To enhance imaging contrast of the largely translucent cell samples, differential interference contrast (DIC) and phase contrast paradigms were investigated. These allowed capture of subtle changes in the unlabelled cell samples. Images were captured before the ablation event, optics changed to allow simple beam path for ablation, and then optics reverted for imaging after the ablation event.

However, this proved impractical both for time required for the complete process and for poor performance characteristic of the refractive objective lenses. The former meant ablation could not be observed in real time, and the latter resulted in low output power at the sample and chromatic aberration issues (incompatible optical coatings at 1950 nm). Indeed, of the

refractive lenses investigated, the most promising had transmission about 40% (Nikon, CFI Plan Apochromat Lambda D 10X, 0.45 NA). This power loss was compounded by other losses in the system such that maximal transmission when the laser reached the sample was predicted to be 11.8%, found experimentally to be 6.5%. This further loss was attributed to optics within the microscope stand (inaccessible optics) and some absorption by water vapour between free space coupled optics.

Instead, a reflective objective lens was preferred for high transmission efficiency and lack of chromatic aberration. Here a 36x reverse Cassegrain structure objective lens (Newport, 50102-02) was employed, with infinite back focal length (suitable for collimated laser input) and 0.52 NA. This was composed of Al(MgF_2) coated mirrors affording a broad operating wavelength range with 94% reflectance at 1.95 µm. This also ensured spatial coincidence between the 1950 nm and 632 nm guidance laser focal spots on the sample. Overall laser power transmission from fibre output to sample was measured as 33.0%, attributed in part to absorption from ambient air humidity between free space coupled optics. Theoretical diffraction-limited spot size was calculated as 3.32 µm. Physical spot size was obtained with knife-edge method and measured to be 3.61 ± 0.22 µm, close to the theoretical calculation and deemed sufficient for single-cell precision. [210]

During ablation, the laser beam is delivered through the back port of the microscope, directed by an internal filter cube to the objective lens and onto the sample. An 1800 nm short pass (SP) filter (DMSP1800R, Thorlabs) in the filter cube reflected the 1950 nm ablating beam towards the sample whilst allowing shorter visible light to a mounted camera to observe ablation in real time. This SP filter had 99.0% reflectance at 1950 nm, 84.5% at 632 nm, and several transmission peaks of 30-40% in the visible region, reported by the manufacturer. Practically, this transmission favoured blue wavelengths in the visible allowing brightfield images illuminated by a white lamp to see the sample. An additional 750 nm SP filter (Thorlabs) was attached to the microscope eyepiece to ensure neither pump nor signal beam could leak through for safe operation of the ablation system.

Brightfield images (transmission geometry) were captured using a scientific camera (Digital Sight DS-Fi1c, Nikon) mounted to the microscope side port, with proprietary software (NIS Elements F, Nikon). Video frames capturing the ablation event were analysed to accurately track cell fate under laser exposure. Video-rate footage was captured at 12 fps using screen capture software (Bandicam, Irvine, California, United States), with individual frames exported and timestamped. Measurement and calculation of each metric was carried out using the widely used open-source image analysis software ImageJ (FIJI [186]), on images scaled using microscopy standards.

Finally, some practicalities in a shared lab space meant a significant 1950 nm leak was discovered from the bare TDF which overlapped with the Stokes-shifted Raman signals measured by the adjacent 3D spectromics setup (Chapter 6), displayed in the figure below. As such, metallic shielding was required to cover both the TDFL and the Raman spectrograph and CCD sensor, whilst maintaining sufficient air flow for cooling fans in both setups.

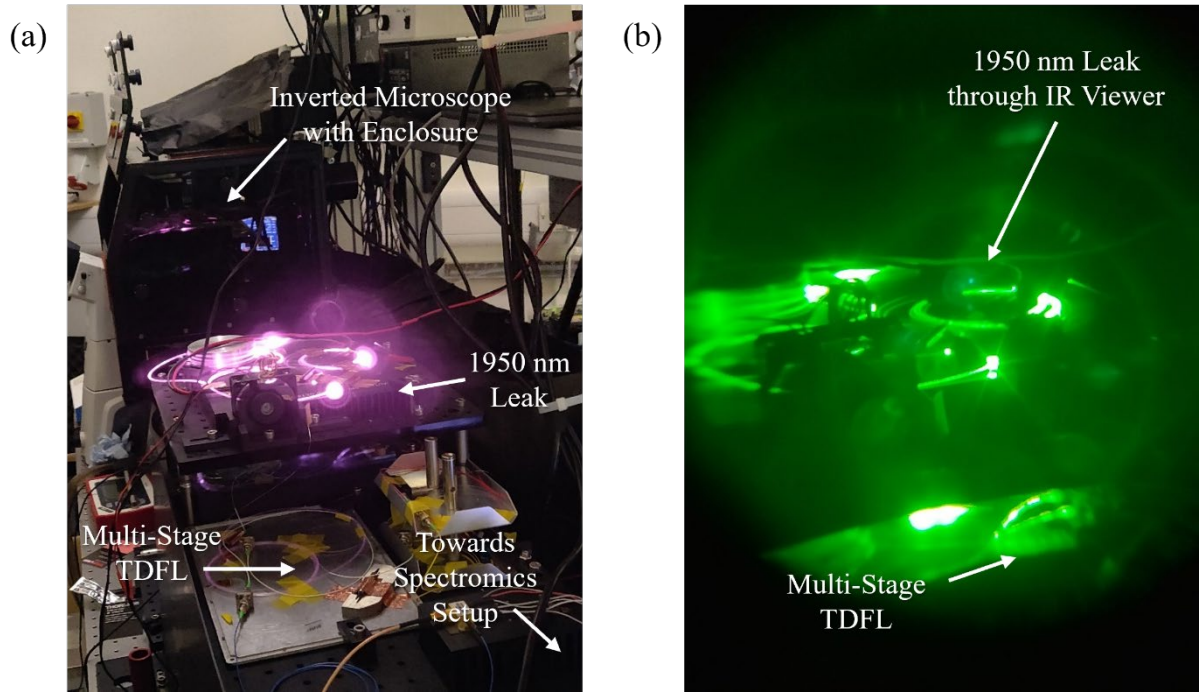

Figure 7.5 1950 nm leak from the Tm-doped fibres visible through a CMOS camera sensor through (a) inbuilt IR SP filter and (b) IR alignment viewer tool. To prevent signal interference into the adjacent 3D spectromics scanning system both TDFL and Raman spectrograph and camera were adequately shielded with metallic covers.

7.3.4 Preliminary Measurements

Some preliminary ablation tests were carried out to confirm initial operation of the full microsurgical system and establish the "ball-park" values for pulse parameters to further investigate.

Porcine muscle and fat tissue (bacon rasher) was obtained from the supermarket, requiring no ethical approval. A small section was cut from the rasher which included both muscle and fat exposed bare to the unfocussed beam on the benchtop, and then placed on a microscope slide (1 mm thick), sealed with paraffin wax. Samples had an average thickness of 2.9 mm.

Samples were exposure to the "raw" laser beam by suspending in the beam path after 19 mm lens to see whether the 1950 nm could indeed cut into mature water rich tissues. Penetration of the beam through the tissue was observed with clean edges under t_{exp} = 1 s (τ = 100 ns, R = 125

kHz, with P_{avg} = 11 W, P_p = 555 W, E_p = 88 uJ), cutting holes with ~200 µm diameter. For samples mounted on the microscope stage resulted in marking with significant carbonisation (and audible "cooking" of tissue) under t_{exp} = 60 s, τ = 100 ns, R = 125kHz, and P_{avg} = 11W. The longer exposure times required were attributed to losses due to the refractive lens, motivating the choices made above.

Optimisation of onion cell ablation approach involved systematic testing of pulse parameters in a grided pattern across the sample under a pulse regime of t_{exp} = 0.5 s τ = 50 ns, R = 250 kHz, P_{avg} varied between 0.42 W – 11 W. Qualitative assessment showed blistering of targeted cells with surrounding cells unscathed, thus identifying the "ball-park" values. The regular arrangement of the cells also facilitated alignment of the system to ensure ablation occurred in an expected and reproducible location on the target sample. Optimisation of the SH-SY5Y sample preparation approach involved culturing of cells to high confluence in order to provide a regular arrangement of cells, emulating structured tissue.

7.3.5 Sample Preparation

Onion Epidermal Cells

Water-rich epidermal cells within the interfacial layer between fleshy leaves of red onions were prepared to produce water-rich cell samples with high regularity. Here samples took the form of intact and hydrated skin leaves (membranous layer) which contain a natural cell monolayer with grid-like structure, which proved helpful to elucidate ablation efficiency and visualise collateral damage.

Fresh onion skin leaves were mounted between two coverslips (Agar Scientific, ø24 mm, thickness 0.13-0.16 mm) in a screw fit metal sample holder (Attofluor™ Cell Chamber for Microscopy, A7816). Onions were stored at room temperature, the cell samples mounted on the inverted microscope stage for ablation and discarded after each experiment.

Human Neuroblastoma Cells

Human cell samples were cultured from the SH-SY5Y neuroblastoma cloned cell line for samples with both photomechanical and clinical relevancy. The SH-SY5Y cells were cultured in Dulbecco's modified Eagle's medium (DMEM), supplemented with 10% fetal bovine serum (FBS) and 1% penicillin and streptomycin (pen-strep) antibiotic mixture. Cells were incubated under standard atmospheric conditions (37 °C, 5% CO_2), monitored for mycoplasma and passaged as required. Cells were cultured onto coverslips (Agar Scientific, ø20 mm, thickness

0.13-0.16 mm) to high confluence, around 90%, equivalent to approx. 250,000 cells per well. Culturing of cells was undertaken by Dr James Read, University of Southampton.

This produced cell monolayers, which were subsequently fixed in 4% paraformaldehyde (PFA), before being washed twice with phosphate buffer solution (PBS). Samples were stored refrigerated and immersed in PBS. These provided a regularly arranged grid of cells across a large field-of-view which allowed accurate readout of ablation position and efficacy.

Coverslips holding the cell monolayers were removed from the PBS ahead of ablation experiments, sandwiched face down between two ø24 mm coverslips within a metal sample holder. After addition of PBS, the sample was sealed within the holder. Practically, this geometry ensured the laser was incident on the cell sample having only passed through one thin coverslip, cells remained hydrated with membranes intact and stable at room temperature, and in a fixed focal plane comparable to the rigid positioning of structured cells in a mature tissue sample.

7.3.6 Quantifying Ablation

To facilitate consistent methodology for quantifying the effect of laser ablation, with varying pulse parameters and on different tissue types, the following ablation metrics were defined:

1. Ablation area (AA), fully denatured/vaporized region of tissue
2. Thermally altered area (TAA), total area of thermally irreversible damage
3. Mechanically altered area (MAA), translated/perturbed area of tissue
4. Ablation efficiency (AE) in percent, ratio of AA/TAA multiplied by 100

For onion epidermal cells, AA described regions fully vaporized, and TAA described regions discoloured due to thermal damage (translucent to brown/black). MAA was not calculated for the onion epidermal cells as their morphology (rigid cell walls) rendered such effects negligible.

For neuroblastoma cells, where thermal damage (TAA evidenced by carbonisation) was not observed, AA described affected regions of cells resulting in full or partial cell bursting, evidenced by cell debris or malformation. Methodology for AA is detailed in Figure 7.6, detailing how indicative ablation area was determined through observing cell fate before, during, and after laser exposure.

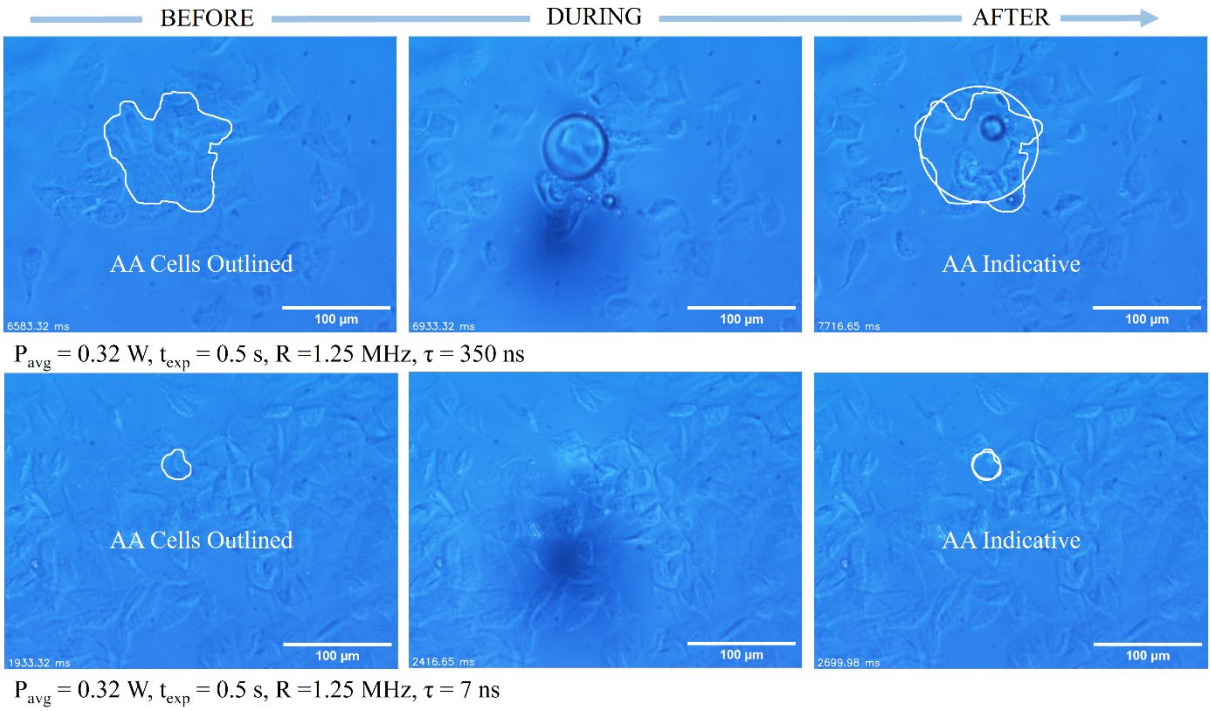

Figure 7.6 Methodology for quantifying ablated area (AA) from live imaging during ablation: from left to right shows brightfield images captured from video footage of the cell sample immediately before, during, and after ablation. Region of the sample considered for AA is highlighted (right) by the selection brush tool to accurately measure which cells were directly affected, as "AA Cells Outlined". Indicative total area under influence of the symmetric beam spot is highlighted (left) as "AA Indicative". Shortening of pulse duration from τ = 350 ns (top) to τ = 7 ns (bottom) shows reduced AA and no formation of cavitation bubbles during and none remaining after ablation event.

The MAA described the area over which the laser exerted a significant mechanical influence, measured as the maximal radial movement or disturbance of cells centred at the point of ablation. The MAA was mitigated by mounting the cells between cover slips to ensure cells were not displaced by the pressure wave imparted by an incident laser pulse before experiencing thermal influence of the pulse. This was favoured also to enable a model conducive to ablation of cells in a mature, structured tissue. Subsequently, AE was not calculated for ablation of the human cell samples.

7.3.7 Cell Staining for Membrane Integrity

Cell membrane integrity was examined as a proxy for viability as preserved, fixed cells were examined that offer a thermomechanical model of human tissue. Trypan Blue staining was carried out to highlight cells with damaged membranes which could verify ablation effects. Cells were stained in well plates (250,000 cells in 1 ml media) before mounting for ablation, then

observed (video capture) for up to 5 min following ablation to allow the stain to enter any compromised membrane. Full colour brightfield images before, immediately post-ablation, and 5 min after ablation were analysed to observe any physical changes and any colour changes due to the stain penetrating damaged cells over time.

7.4 Results

Experiments on various tissue samples were carried out to investigate the influence of the four fundamental pulse parameters (P_{avg}, t_{exp}, τ, R) on ablation, quantified by the AA, TAA, MAA, and AE. This took the form of some preliminary measurements on porcine tissue in order to outline the approach, before developing for precise and efficient ablation for onion epidermal and human neuroblastoma cells.

7.4.1 Ablation of Onion Epidermal Cells

Onion epidermal cells were chosen for their natural water content and due to their repetitive grid-like nature, allowing straightforward identification of which cells were ablated, thermally altered, and unaffected. This simple morphology also helped to optimise the alignment of the beam delivery system, ensuring effective and precise ablation. For each test, optimal values for the remaining pulse parameters were determined by those which gave the highest precision and kept constant for subsequent tests.

Figure 7.7 shows the effect of laser irradiation of onion epidermal cells when P_{avg} was increased from 0.85 W (a), to 1.7 W (b), and 3.7 W (c) while the other parameters remained unchanged, fixed at t_{exp} = 5 s, τ = 40 ns, R = 250 kHz. The respective ablation efficiencies were 0.0%, 26.6% ± 1.4%, and 27.3% ± 1.4%. The final value is, arguably, a clear overestimation as the TAA shows no visible boundary within the field of view, but illustrates the undesirable effect of overexposure.

Figure 7.7 also shows the results after laser irradiation of onion epidermal cells when t_{exp} was decreased, from 1 s (d), to 0.75 s (e), and 0.5 s (f) with other parameters unchanged, fixed at P_{avg} = 3.7 W, τ = 40 ns, R = 250 kHz. The respective ablation efficiencies were 33.2% ± 1.5%, 22.1% ± 1.6%, and 46.9% ± 3.9%, where error quoted here throughout is standard deviation.

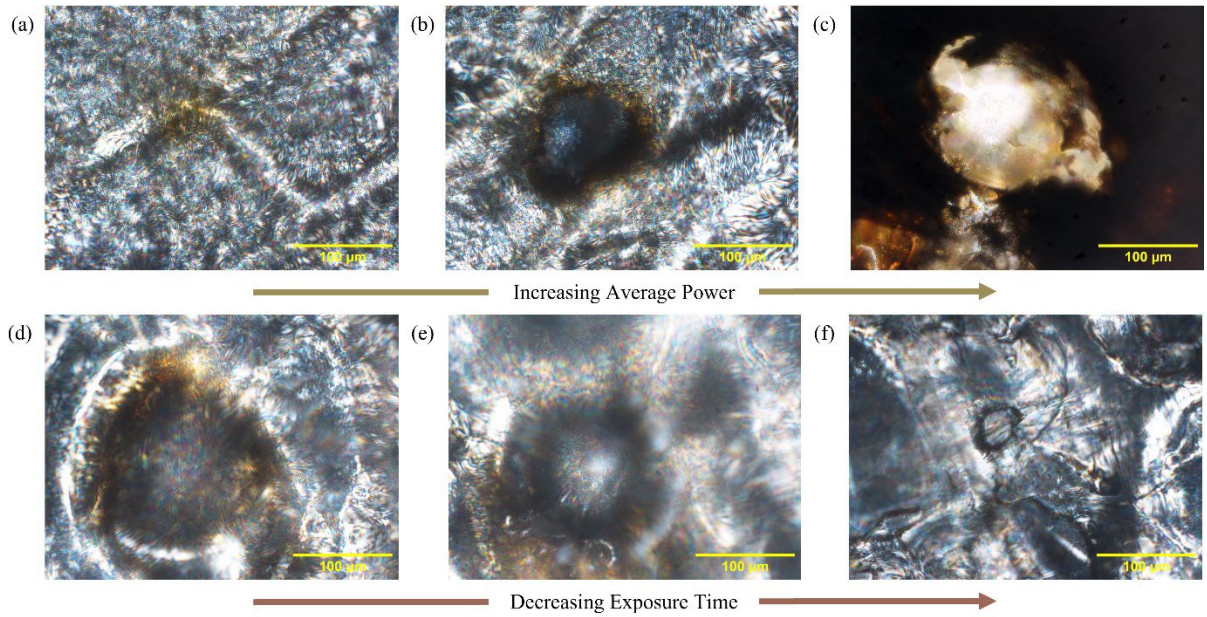

Figure 7.7 Establishing ablation efficiencies (AE) with increasing average power (P_{avg}) and decreasing exposure time (t_{exp}) on onion epidermal cells. Top row describes ablation under (a) P_{avg} = 0.85 W, (b) P_{avg} = 1.7 W, and (c) P_{avg} = 3.7 W pulses. Respective AE was recorded as 0.0%, 26.6% ± 1.4%, and 27.3% ± 1.4%. Remaining pulse parameters were fixed at t_{exp} = 5 s, τ = 40 ns, R = 250 kHz. Bottom row describes ablation under (d) t_{exp} = 1 s, (e) t_{exp} = 0.75 s, and (f) t_{exp} = 0.5 s pulses. Respective AE was recorded as 33.2% ± 1.5%, 22.1% ± 1.6%, and 46.9% ± 3.9%. Remaining pulse parameters were fixed at P_{avg} = 3.7 W, τ = 40 ns, R = 250 kHz. Scale bar = 100 µm.

Figure 7.8 shows the effect of laser irradiation on onion epidermal cells when τ was increased from 40 ns (a), to 350 ns (b), and 680 ns (c) while the other parameters remained unchanged, fixed at P_{avg} = 3.7 W, t_{exp} = 0.5 s, R =250 kHz. The respective ablation efficiencies were 46.9% ± 3.9%, 25.7% ± 1.0%, and 18.0% ± 0.9%. Figure 7.8(c) again depicts widespread damage that extends beyond the field of view, affecting the calculated AE value, but suffices to describe an undesirable outcome.

Figure 7.8 also shows the results after laser irradiation of onion epidermal cells when R was increased from 1.25 MHz (d), to 2.5 MHz (e), and 5 MHz (f) while the other parameters remained unchanged, fixed at P_{avg} = 3.7 W, t_{exp} = 0.5 s, τ = 7 ns. The respective ablation efficiencies were 45.3% ± 3.9%, 0.0%, and 0.0% (practically no ablation effect).

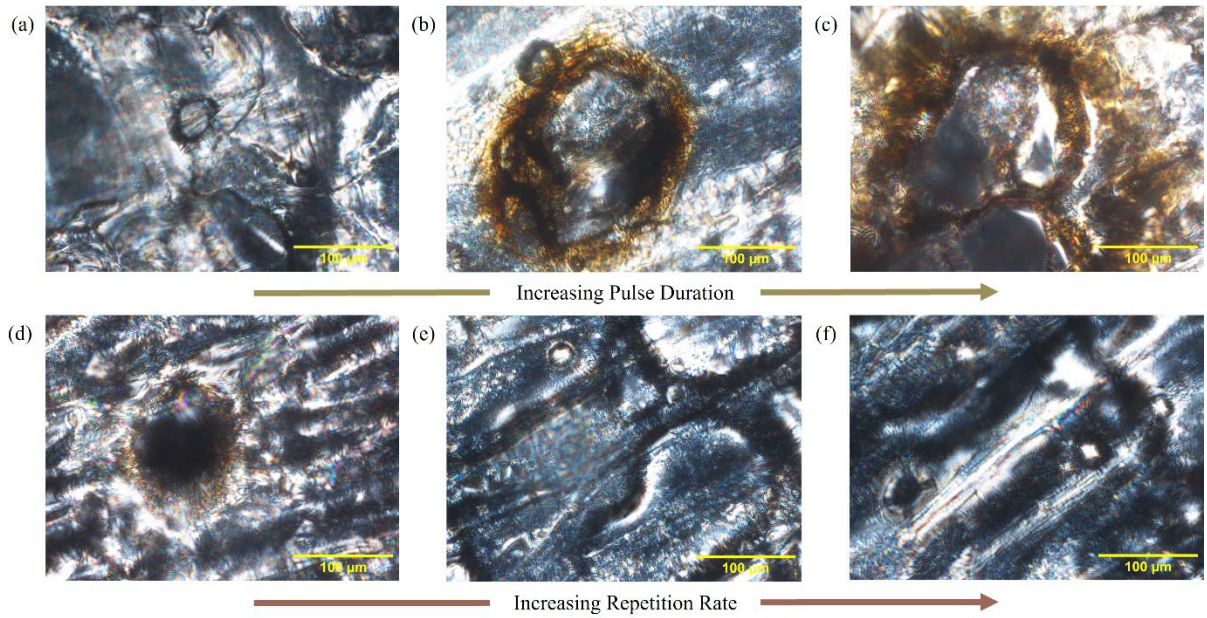

Figure 7.8 Establishing ablation efficiencies (AE) with increasing pulse duration (τ) and repetition rate (R) on onion epidermal cells. Top row describes affected area under (a) τ = 40 ns, (b) τ = 350 ns, and (c) τ = 680 ns pulses. Respective AE was recorded as 46.9% ± 3.9%, 25.7% ± 1.0%, and 18.0% ± 0.9%. Remaining pulse parameters were fixed at P_{avg} = 3.7 W, t_{exp} = 0.5 s, R =250 kHz. Bottom row describes affected area under (d) R = 1.25 MHz, (e) R = 2.5 MHz, and (f) R = 5.0 MHz pulses. Respective AE was recorded as 45.3% ± 3.9%, 0.0% and 0.0%. Remaining pulse parameters were fixed at P_{avg} = 3.7 W, t_{exp} = 0.5 s, τ = 7 ns. Scale bar = 100 µm.

Finally, Figure 7.9 depicts graphically the relationship between AE and each of the four fundamental pulse parameters for onion epidermal cells.

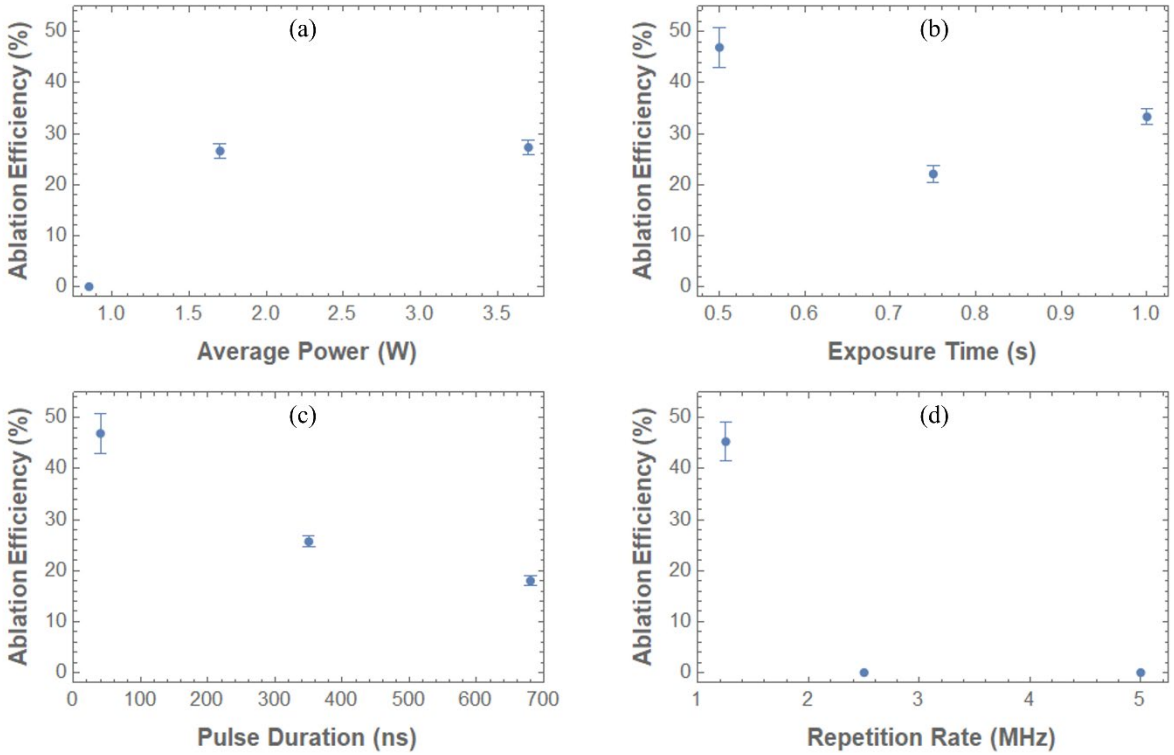

Figure 7.9 Influence of each pulse parameter in isolation on ablation efficiency (AE) on onion epidermal cells. The relationship between AE and (a) P_{avg}, (b) t_{exp}, (c) τ, and (d) R, is shown with respective error (standard deviation). For each test, optimal values for the remaining pulse parameters were determined by those which gave the highest precision and kept constant for subsequent tests.

7.4.2 Ablation of Human Neuroblastoma Cells

Fixed human neuroblastoma cells were examined to show viability of precisely ablating cancer cells using a laboratory based pre-clinically relevant model. Once cultured the cells exist in a highly confluent monolayer, suitably emulating cells that would be arranged closely together in vivo, upon which to demonstrate high selectivity and precision ablation. Careful selection of pulse parameters enabled targeting of individual cells in samples containing up to 250,000 cells, depicted in the figure below. The white circles drawn in the following figures represent the indicative AA for each different pulse modality.

Figure 7.10 shows the SH-SY5Y cells before and after laser irradiation when t_{exp} was decreased, from 0.5 s (a-b), to 0.3 s (c-d), and to 0.1 s (e-f) while the other parameters remained unchanged, fixed at P_{avg} = 0.87 W, τ = 7 ns, R =1.25 MHz. The respective AA values were 33895 ± 98 μm^2, 26733 ± 256 μm^2, and 6783 ± 23 μm^2.

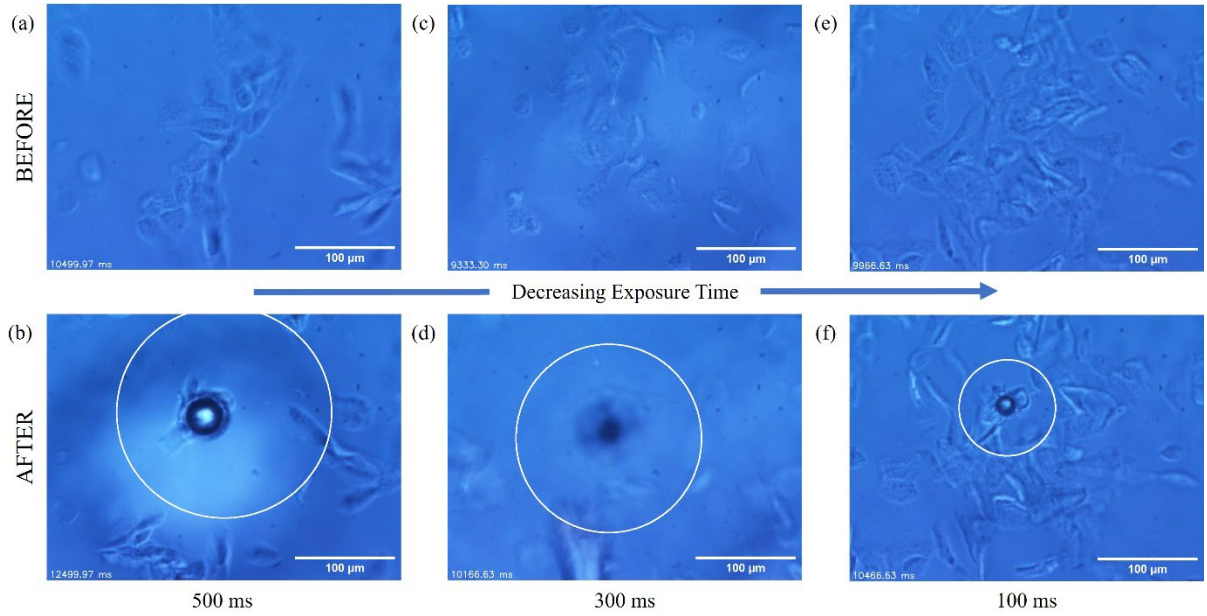

Figure 7.10 Increasing ablation precision with decreasing exposure time (t_{exp}) on SH-SY5Y cells. Image (a) shows before and (b) after ablation with t_{exp} = 500 ms; (c) shows before and (d) after ablation with t_{exp} = 300 ms; (e) shows before and (f) after ablation with t_{exp} = 100 ms. Remaining pulse parameters were fixed at P_{avg} = 0.87 W, τ = 7 ns, R =1.25 MHz. Scale bar = 100 μm.

Figure 7.11 shows the SH-SY5Y cells before and after laser irradiation when P_{avg} was increased, from 0.39 W (a-b), to 1.7 W (c-d), and to 3.7 W (e-f) while the other parameters remained unchanged, fixed at t_{exp} = 0.1 s, τ = 7 ns, R =1.25 MHz. The respective AA values were 435 ± 16 μm^2, 10904 ± 89 μm^2, and 31553 ± 236 μm^2.

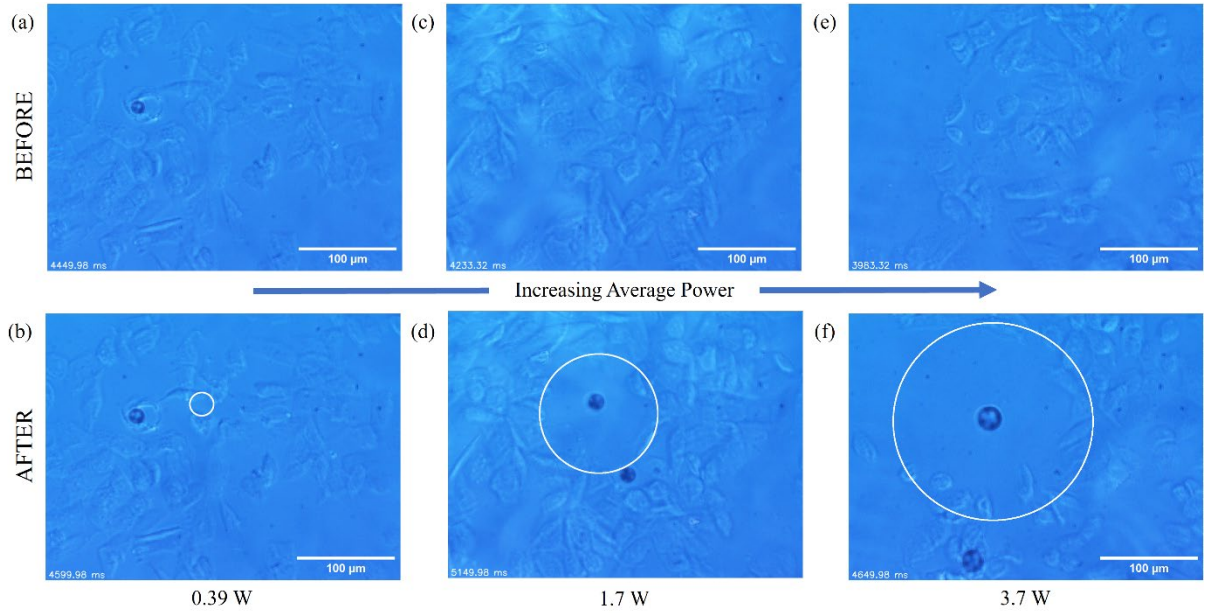

Figure 7.11 Decreasing ablation precision with increasing average power (P_{avg}) on SH-SY5Y cells. Image (a) shows before and (b) after ablation with P_{avg} = 0.39 W; (c) shows before and (d) after ablation with P_{avg} = 1.7 W; (e) shows before and (f) after ablation with P_{avg} = 3.7 W. Remaining pulse parameters were fixed at t_{exp} = 0.1 s, τ = 7 ns, R =1.25 MHz. Scale bar = 100 µm.

Figure 7.12 shows the SH-SY5Y cells before and after laser irradiation when τ was increased from 7 ns (a-b), to 40 ns (c-d), and to 350 ns (e-f) while the other parameters remained unchanged, fixed at P_{avg} = 0.32 W, t_{exp} = 0.5 s, R =1.25 MHz. The respective AA values were 512 ± 10 μm^2, 2833 ± 21 μm^2, and 9099 ± 69 μm^2.

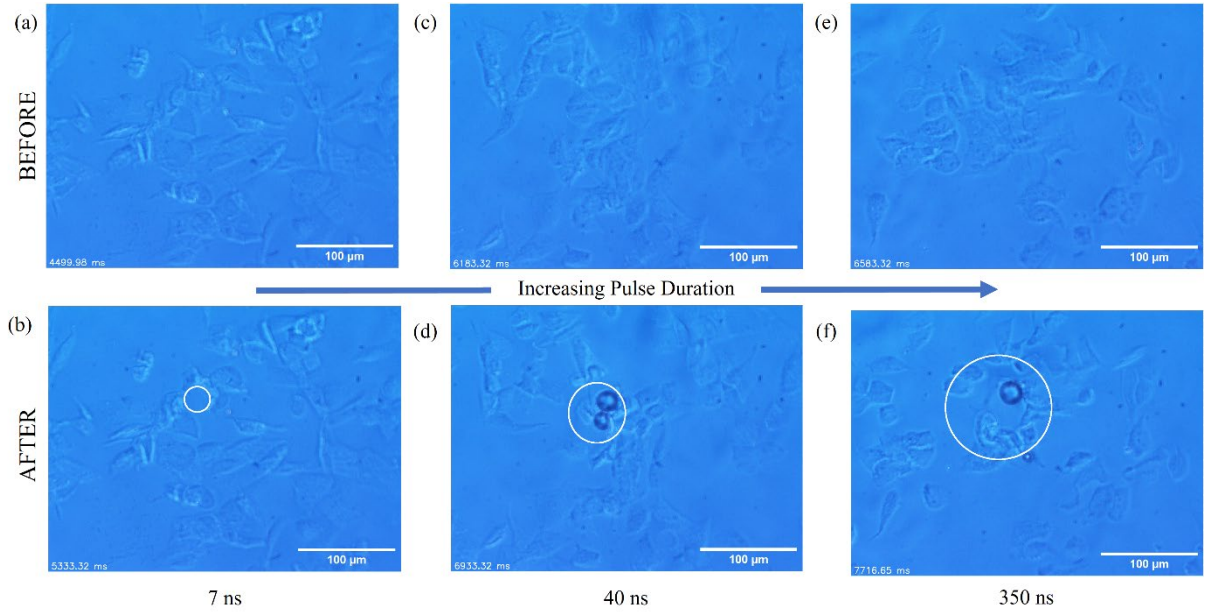

Figure 7.12 Decreasing ablation precision with increasing pulse duration (τ) on SH-SY5Y cells. Image (a) shows before and (b) after ablation with τ = 7 ns; (c) shows before and (d) after ablation with τ = 40 ns; (e) shows before and (f) after ablation with τ = 350 ns. Remaining pulse parameters were fixed: P_{avg} = 0.32 W, t_{exp} = 0.5 s, R =1.25 MHz. Scale bar = 100 μm.

Figure 7.13 shows the SH-SY5Y cells before and after laser irradiation when R was increased from 1.25 MHz (a-b), to 5.0 MHz (c-d), and 20.0 MHz (e-f) while the other parameters remained unchanged, fixed at P_{avg} = 0.32 W, t_{exp} = 0.5 s, τ = 7 ns. The respective AA values were 517 ± 13 μm^2, 1167 ± 18 μm^2, and 19153 ± 191 μm^2.

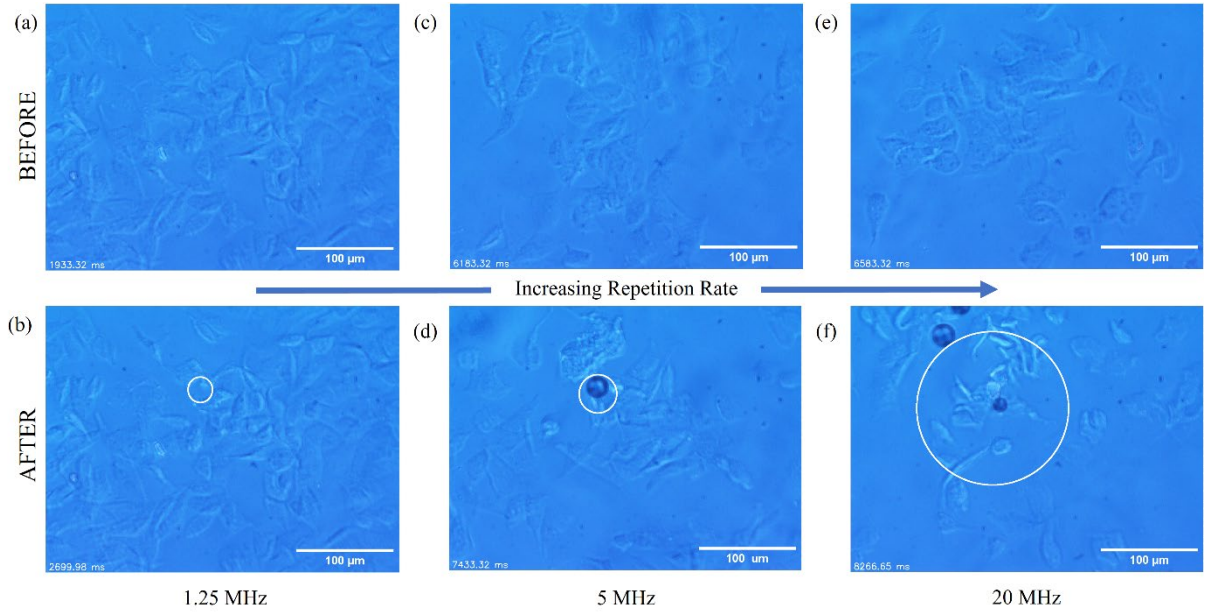

Figure 7.13 Decreasing ablation precision with increasing repetition rate (R) on SH-SY5Y human neuroblastoma cells. Image (a) shows before and (b) after ablation with R = 1.25 MHz; (c) shows before and (d) after ablation with R = 5.0 MHz.; (e) shows before and (f) after ablation with R = 20.0 MHz. Remaining pulse parameters were fixed: P_{avg} = 0.32 W, t_{exp} = 0.5 s, τ = 7 ns. Scale bar = 100 μm.

Finally, Figure 7.14 displays the quantitative trends for AA relative to each of the pulse parameters. Optimal values for a given parameter were determined by that which gave the highest precision (smallest AA) and kept constant for subsequent tests.

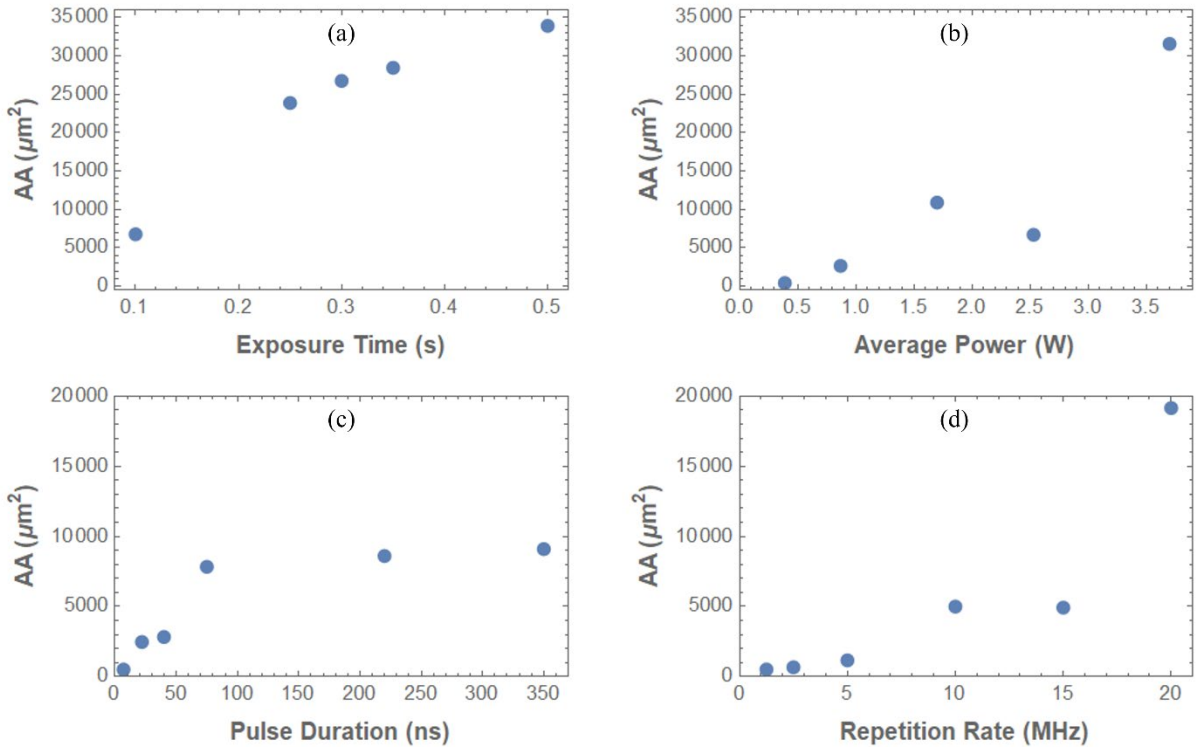

Figure 7.14 Influence of each pulse parameter in isolation on AA for the SH-SY5Y cells. The relationship between ablation area and (a) t_{exp}, (b) P_{avg}, (c) τ, and (d) R, is shown with respective error (standard deviation). For each test, optimal values for the remaining pulse parameters were determined by those which gave the highest precision and kept constant for subsequent tests.

The ideal parameters for precise ablation of the SH-SY5Y samples were determined to be P_{avg} = 0.25- 0.32 W, t_{exp} = 0.5 s, τ = 7 ns, and R = 1.25 MHz. This allowed accurate ablation of a single cell, which was verified with a cell viability assay (Trypan Blue).

7.4.3 Single Cell Precision

Ablation of a single isolated human neuroblastoma cell is described in Figure 7.15, wherein the targeted cell has undergone significant mechanical damage, while surrounding cells remain unaffected. Ablation was carried out with parameters of P_{avg} = 0.25 W, t_{exp} = 0.5 s, τ = 7 ns, R = 1.25 MHz. AA was quantified as 405 ± 12μm^2 (Figure 7.15 (a-b)) and 311 ± 3 μm^2 (Figure 7.15 (c-d)), and as a result the respective ablation precision (AA diameter) demonstrated is 22.7 ± 0.1 μm and 19.9 ± 0.1 μm. “Debris” of the ablated cell is visible, showing that ablation power is sufficient to damage (beyond the ablation threshold) but not vaporize the tissue unduly,

indicating pulse parameters have been tailored for accurate ablation with negligible collateral effect.

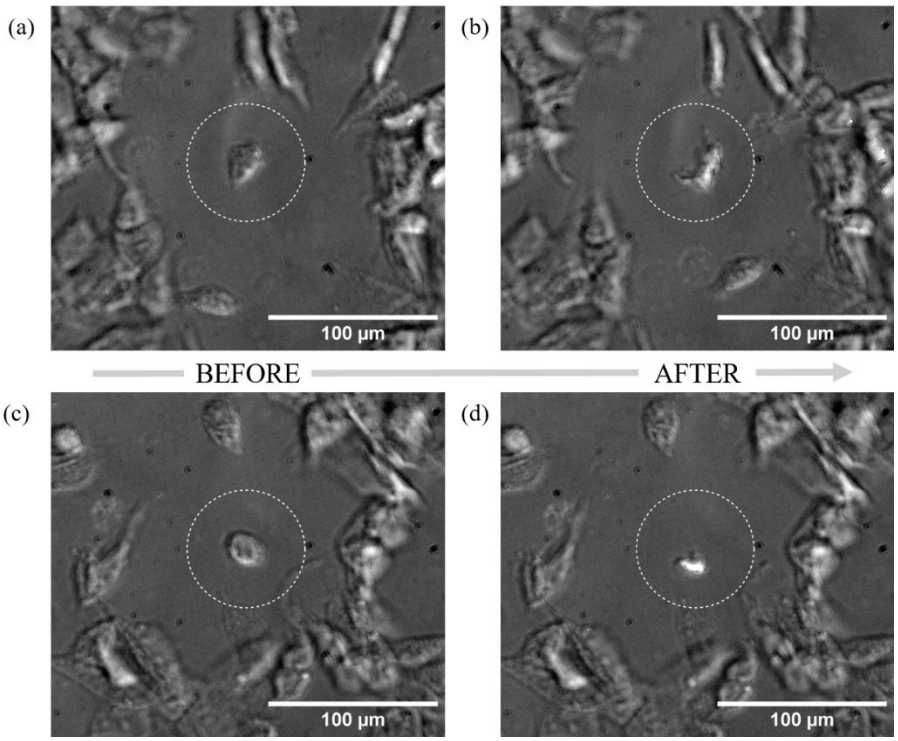

Figure 7.15 Single isolated human neuroblastoma cells ablated whilst surrounding cells remain unperturbed. Results shows the "debris" of the cell after undergoing significant mechanical damage. Ablation was carried out with parameters P_{avg} = 0.25 W, t_{exp} = 0.5 s, τ = 10 ns, and R = 1.25 MHz on two occasions, (a-b), and (c-d). The dashed circle here indicates which cell was targeted and is not representative of the AA value.

Cell membrane integrity was considered as proxy for cell damage when regarding ablation of the preserved (dead) cell modes. Figure 7.16 describes single-cell scale ablation (average short axis diameter of 28.4 ± 0.1 µm) under ideal pulse parameters, employing a cell viability assay (Trypan Blue dye staining) to verify which cells are significantly damaged. A decrease in the cell membrane integrity and thus increased permeability was used as a marker for cell damage following ablation. Since fixing using PFA (protein crosslinking to stabilise the cells) does not significantly perforate the cell membranes (absence of large pore perforation), dye uptake could indicate cells sufficiently damaged upon laser irradiation. In practical terms, the cell membranes may be affected to a limited degree and allow minimal dye uptake hence some light staining before ablation in Figure 7.16 (a). [211]

In comparing the cells immediately post ablation (Figure 7.16 (b)) and 300 s after ablation Figure 7.16 (c)), there is increased saturation of the dye in the ablated cell tissues, indicating uptake through significantly mechanically compromised cell membranes (marker for cell viability).

Crucially the surrounding unaffected cells show no change in morphology or dye uptake from before ablation, indicating the high rate of cell survival and validation of the accuracy of our ablation.

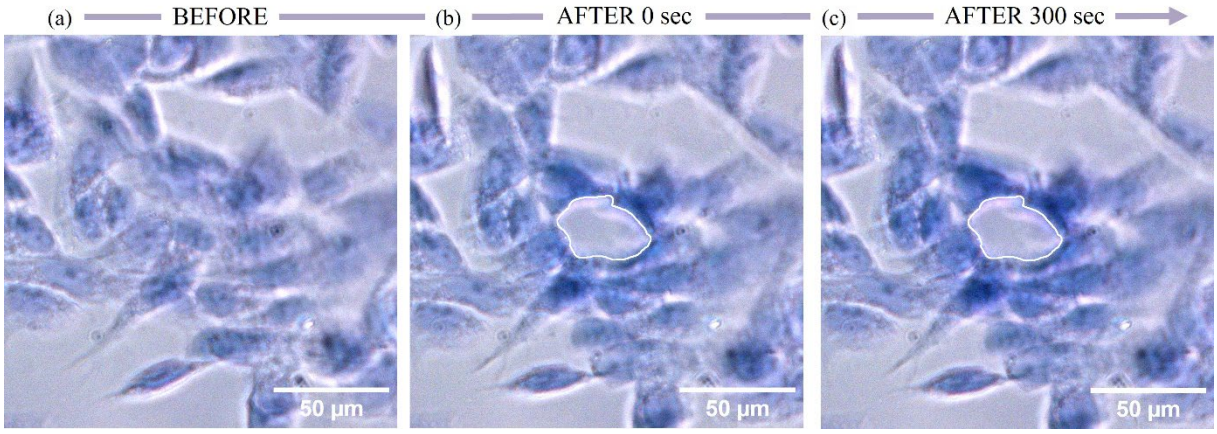

Figure 7.16 Cell viability assay for single human neuroblastoma cell ablation, full colour brightfield images taken (a) before, (b) immediately after, and (c) 5 mins after ablation. Cells stained with Trypan Blue before mounting onto microscope to carry out ablation. Ablated area boundary marked, short axis with average diameter of 28.4 ± 0.1 µm, of the scale of a single cell. Compromised cell membrane indicating significant damage shown by increased blue colour saturation (Trypan Blue stain) in ablated cell tissue after 5 minutes. Ablation was carried out with parameters P_{avg} = 0.32 W, t_{exp} = 0.5 s, τ = 7 ns, and R = 1.25 MHz

7.5 Discussion

7.5.1 Ablation Outcomes for Onion Epidermal Cells

Analysis of ablation outcomes on onion epidermal cells was carried out qualitatively (visible effects such as colour) and quantitatively (calculating AE) to assess the influence of the pulse parameters.

Figure 7.7 depicts the outcome when P_{avg} or t_{exp} were varied in ablation of onion epidermal cells, observing the cell fate when changing the total energy deposited onto the samples. Figure 7.7 (a). shows a degree of visible carbonisation (colour change for the translucent cells to brown/black) but no ablation. Biological tissue has a threshold of radiant exposure (ablation threshold) and so this is an example of insufficient energy delivery. Increasing P_{avg} further increased the total energy deposited, crossing the ablation threshold for ablation to occur. However, also evident is an upper energy limit, since an excessive P_{avg} value led to widespread

carbonization, shown in Figure 7.7 (c) which is undesirable. Figure 7.7 (b) described an optimal average power leading to refining next the exposure time.

Decreasing the t_{exp} lowered the total energy deposited onto the sample (P_p was kept constant). Decreasing t_{exp} reduced both the AA and TAA, until ablation was achieved with a precision (AA diameter) of 31.3 ± 0.1 µm and an AE of 46.9% ± 3.9%, under pulse parameters of P_{avg} = 3.7 W, t_{exp} = 0.5 s, τ = 40 ns, R = 250 kHz. The precisely ablated area was sufficiently small to ablate a single onion cell without visibly affecting neighbouring cells (minimal visible carbonization) as depicted in Figure 7.7 (f).

Trend analysis proved inconclusive for AE with respect to solely P_{avg} and t_{exp}, primarily due to a small sample set for this study. In establishing an ablation power threshold for this sample, this also proved more complex since depositing 4.25 J of total energy resulted in no ablation (Figure 7.7 (a)) whereas 1.85 J of total energy could achieve single cell ablation (Figure 7.7 (f)). As such total power is not the whole story, rather the time resolved manner of deposition is crucial. A higher pulse energy and power (E_p and P_p) for in Figure 7.7 (f) compared to Figure 7.7 (a) suggest that delivery of the laser energy over a shorter time-scale (lower exposure time for same average power) improved the ablation outcome (above threshold with low collateral). This approach will increase the temperature in the targeted tissue increasing likelihood of ablation and vaporisation. [94]

Figure 7.8 depicts outcome when τ or R were varied in ablation of onion epidermal cells, here observing the cell fate where total energy deposited remained constant but the manner of deposition was varied. Here, for set P_{avg} and t_{exp}, short 40 ns pulses resulted in precision (AA diameter) of 31.3 ± 0.1 µm ablating only a single cell (Figure 7.8 (a)), whereas longer 680 ns pulses of caused widespread ablation and carbonisation of the order of hundreds of microns (Figure 7.8 (c)). There was a clear trend for larger AA and TAA under longer pulse durations and a decrease in AE, indicative of a lack of thermal confinement. [94] Such confinement can be understood by the characteristic thermal diffusion time (t_d) of the biological tissue type, wherein should $\tau \leq td$ then the energy of the pulse would not be able to diffuse into the cells neighbouring the target. [94,212] Thus shorter pulses for a given total power (P_{avg} and t_{exp}) affords high precision and efficiency with reduced collateral, favoured for microsurgery.

Next, increasing R would maintain total energy deposited on the sample whilst reducing the energy and power of each pulse, for a given P_{avg} and t_{exp}, transferring from fewer high-energy pulses to many low-energy pulses. Here, efficacy of ablation dropped rapidly with increasing R such that there was little discolouration (Figure 7.8 (e)) or no visible change (Figure 7.8 (f)), suggesting the sample could not surpass the ablation threshold. Higher temperatures and

pressures in tissue are expected under shorter and higher intensity pulses, necessary to bring the tissue up to suitable ablation conditions. [94]

7.5.2 Ablation Outcomes for Human Neuroblastoma Cells

Analysis of ablation outcomes on onion epidermal cells was carried out qualitatively (observed mechanical effects) and quantitatively (calculating AA) to assess the influence of the pulse parameters. No thermal damage (discolouration, carbonisation) was visible for the SH-SY5Y cells, instead mechanical effects such as cell structure damage and displacement could be assessed.

Figure 7.10 and Figure 7.14 (a) describe the influence of t_{exp} on ablation of SH-SY5Y cells. Here a clear trend was recognised for increase in AA with increasing t_{exp}. MAA increased with increasing t_{exp} evidenced by large empty areas where cells had been pushed outward from the center of the incident beam spot. As with the onion epidermal cells, a shorter t_{exp} is preferred when aiming to confine the thermomechanical effects and achieve precise ablation.

Figure 7.11 and Figure 7.14 (b) describe the effect of varying P_{avg} during ablation of SH-SY5Y cells. Here an overall increase in AA with increasing P_{avg} was observed, though a slight decrease in AA is observed between 1.7 W to 2.5 W average power. Also observed was an increase in MAA, regarded as collateral damage and representing a negative outcome. Under a P_{avg} of 0.39 W, ablation was achieved with a precision of 23.5 ± 0.1 μm (Figure 7.11 (b)), sufficiently small to ablate a single cell. It is also worth noting a dark circle present in the before and after images of this ablation event (Figure 7.11 (a) and (b)) which was identified as a cavitation bubble from the previous experiment. The fact that this bubble remained stationary through a subsequent burst of radiation adds further credence to the precision of this system.

Figure 7.12 and Figure 7.14 (c) describe the influence of τ on ablation of SH-SY5Y cells. Here AA increased directly with increasing τ, similar to the onion epidermal cells, again suggesting thermomechanical confinement would worsen with longer duration pulses. The trend displayed a shape that levelled off after 75 ns, with reduced rate of AA increase beyond this point. This suggests the thermal diffusion time for SH-SY5Y cells is close to this value, allowing heat to dissipate to the cells surrounding the target. Under a τ value of 7 ns, ablation was achieved with single cell scale precision of 25.5 ± 0.1 μm.

Figure 7.13 and Figure 7.14 (d) describe the effect of varying R during ablation of SH-SY5Y cells. Here increasing AA was observed with increasing R, differing from the results from the onion epidermal cells most likely due to the differing cell morphology (rigid plant cell walls). It can be said that as R is increased, the duty cycle of the beam would become larger, so that the laser

beam may become closer in behaviour to a continuous wave (CW). Under quasi-CW conditions, thermomechanical confinement would reduce, consistent with the results observed. Under an R value of 1.25 MHz, ablation was achieved with precision of 25.6 ± 0.1 μm (Figure 7.13 (b)).

The creation of cavitation bubbles observed in some ablation experiments are a marker of suboptimal pulse parameters. These bubbles would expand under radiant exposure, before collapsing inwards, applying further pressure on the cells, likely inducing mechanical damage, and adding to collateral. These cavitation bubbles are visible as small black circles throughout the Figures in Section 7.4.2, which often coincided with the beam focal spot, though occasionally would be found nearby but having moved away from the centre of ablation (Figure 7.11 (d), Figure 7.13(d) and (f)). Video footage of the ablation events displayed this with some regularity, which prompts further investigation.

SH-SY5Y cell samples employed in this investigation were essentially monolayers, on which has been demonstrated effective ablation with precise lateral resolution. To ascertain the resolution along the beam propagation (z-axis), the depth of focus of the reflective objective can be calculated (assuming no chromatic aberration, justified above) using

$$\Delta z = \frac{\lambda}{4n\left(1 - \sqrt{1 - \left(\frac{NA}{n}\right)^2}\right)} \quad (3)$$

where Δz is depth of field, λ is the signal wavelength (1950 nm), NA is numerical aperture, and n the refractive index (air). [191] Depth of focus was calculated as 3.34 μm, and outside this range, quality of ablation will decrease since the larger spot size may affect a larger area. However, as the spot size increases radiant exposure should also decrease, such that below the ablation threshold only carbonisation may occur. The exact spot size and position in z for this threshold limit, particularly in consideration for future ablation in 3D tissue structures, will depend on the interplay between the pulse parameters identified above.

7.6 Conclusions and Future Work

This work detailed the development and execution of a laser ablation system based around a 1950 nm TDFL, capable of single-cell scale precision as demonstrated on onion epidermal cell and fixed SH-SY5Y human neuroblastoma cells as tissue models. The four fundamental pulse parameters were systematically tuned in order to confine ablation damage to within the bounds of a single target cell.

The results indicate precise ablation at the cellular scale is best achieved with short pulse durations (high peak pulse power) with low repetition rates (low average power, but above tissue threshold). Conversely, long pulse duration (relative to t_d), or high repetition rate (with P_{avg} above tissue threshold) may deposit an excess amount of energy or reduce thermomechanical confinement, lowering ablation efficiency and risking collateral damage. In micro-surgical applications it would be imperative to preserve as much surrounding tissue as possible, e.g. healthy tissue surrounding a malignant tumour, whilst ensuring precision cutting for the surgeon operating.

Optimising these parameters achieved ablation with precision (AA diameter) of 31.3 ± 0.1 μm on onion epidermal cells and down to 19.9 ± 0.1 μm on single SH-SY5Y cells. The capacity to target and destroy human tissue with single-cell precision on a coverslip containing in excess of 250,000 cells is attractive. Through developing precise and selective ablation of two structurally distinct samples (plant and animal), this work demonstrates the broad tuneability and capability of this system, through targeting the common and efficient NIR-SWIR water absorption.

Further work looks to broaden the flexibility of the system to allow cutting through thicker, mature tissue with similar precision to prove efficacy as a tool for micro-surgery. Revision of the sample mounting and manipulation system, i.e. moving away from the microscope stand and stage, should allow for more efficient beam delivery since losses due to any internal optics of the microscope stand may be eliminated. To this end the next version of the system sees optics mounted on a vertical breadboard to allow upright microscopy and beam delivery, focusing lens positioned above the sample mounted on a motorised stage. Preliminary results for precise cutting of cartilage slices show promise for this approach.

Chapter 8 From Mars to Humans: Demonstrating Raman Spectroscopy to the Public

8.1 Abstract

Public communication and outreach form a vital component of scientific research. There is an obligation to disseminate knowledge of new discovery and in so doing a chance to promote the discipline to wide range of audiences. Outreach activities that bring science, technology, engineering, and mathematics (STEM) to young and old alike can have direct influence on education development and career trajectory.[213]

This chapter details some of the successes enjoyed in public engagement during my candidature with the Molecular Biophotonics and Imaging group of the University of Southampton, as a key developer of the "From Mars to Humans" activity as part of the Royal Society Summer Science Exhibition (SSE) 2023. The exhibit was delivered to over 10,000 visitors over the course of six days. With a clear message of the benefit of interdisciplinary research, this interactive exhibit sought to convey the wide applicability of Raman spectroscopy technologies for advances in both interplanetary discovery and diagnostic approaches. Two flagship activities were developed to showcase these messages: the "Raman 4 Life" model Mars rover and the "Dr. Raman" model microspectroscopy system, covering "Mars" to "Humans" respectively.

Such approaches sought to translate the concepts of Raman spectroscopy from fundamental phenomena through to state-of-the-art remote and domestic application for various audiences. This captured the zeitgeist by focusing on popular topics of public health and interplanetary discovery, intending to relate to and inspire a new generation of scientists. This work also offered the opportunity for raising the public profile for the research conducted at the University of Southampton and within the EPSRC Transformative Healthcare "InLightenUs" project. The elements of the interactive stand will be detailed and some of the gathered public response data described to lay out a blueprint for novel STEM teaching tools.

8.2 Introduction

The "From Mars to Humans" outreach exhibit incorporated a number of hands-on activities in which a range of audiences could participate in demonstrations of Raman spectroscopy, from fundamental physical concepts through to applications at the cutting-edge of science. This work sought to demonstrate the endeavours of biophotonics research for the achievement of fast and accurate detection and monitoring of tissue. In particular this allowed a showcase of the interdisciplinary work carried out at the University of Southampton, within EPSRC Transformative Healthcare "InLightenUs" project, to develop deeply penetrating non-invasive, non-destructive, label-free multiscale (nm to cm) and multimodal imaging-based diagnostics.

Raman spectroscopy forms the core of our research and represents one of the fastest growing spectroscopic techniques today, benefitting from no requirement for sample preparation, quantitative readout and insensitivity to water. Given its potency, we sought to convey the science surrounding its applications in diagnostic applications by highlighting two high profile use cases within the public conscience. Namely, as part of the NASA Perseverance mission seeking out alien life and as a valuable tool for public health, capable of detecting bone and cartilage pathologies, or applications of Raman spectroscopy from “Mars to Humans”.

The approaches for effective and engaging public outreach were developed with training from the public communications team at the Science Museum Group (SMG, London, UK) ahead of the delivering the full activity at the Royal Society Summer Science Exhibition (SSE) in 2023. This I attended with Yong En (Janet) Kok of the University of Nottingham, also a member of the InLightenUs team.

The exhibit was designed with the intent to improve science capital in audiences, to shape their attitude and relationship with science, technology, engineering, and mathematics (STEM). This required reflection on the needs and motivation of the audience. Employ of challenges and arranging light competition was encouraged, though too easy and audiences may feel patronised, too difficult and they may be made to feel at fault, that they are “bad at science”. Play and gamification also helped to counter the stereotype that science existed only in serious tones and confined to labs. Novelty and curiosity, personal relevance and positive reinforcement of STEM skills were all vital to effective public engagement. Success in this venture would see an activity facilitate:

- Two-way open conversation between demonstrator and participant
- Participants coming to their own understanding of a topic; discovering something themselves

To this end, the “From Mars to Humans” exhibit at SSE 2023 was bult as a cohesive interactive stand, incorporating a range of custom activities detailed in the following sections. This included concepts taught by scientists with expertise and practice in the areas of physical science, biochemistry, biomedical spectroscopy, adaptive optics, and machine learning.

The overarching learning objectives were identified as follows:

1. **Diagnostic power of Raman Spectroscopy**
    a. A technique central to the medical technologies developed by the interdisciplinary InLightenUs research programme
    b. How Raman spectroscopy uses the “tiny” vibrations of molecules to give insight into life

2. **The need for and benefits of interdisciplinary research**
    a. Visitors would be able to appreciate that the spectroscopic techniques, artificial intelligence, optical physics and light-shaping technologies being developed within the InLightenUs programme work together for transforming the diagnosis of musculoskeletal diseases
    b. We would demonstrate how NASA Perseverance also uses Raman spectroscopy to detect life on Mars
    c. Interdisciplinary research is intrinsically inclusive as it appreciates and utilises diverse skills within multifunctional teams
3. **Medical innovations go hand-in-hand with amazing discoveries in space**
    a. Visitors would thus journey from "Mars to Humans" to experience how fundamental scientific research, development, and innovations can have diverse applications ranging from diagnostics on Earth to finding life on Mars
    b. Experience how powerful innovations in medical technologies on earth go hand in hand with amazing discoveries in space

Scripts were prepared for our demonstrators at each activity to facilitate open invitations to visitors; with inclusive explanations (avoiding jargon) suitable for audiences with different age and STEM capital; to showcase the relevance of STEM in "everyday life"; and to empower participants in confidence and ownership of their STEM skills.

Figure 8.1 Proud exhibitors showcasing science to any and all audiences! From (a.) the Royal Society fellows' soirée during the public Summer Science Exhibition to (b.) local audiences at the Pint of Science lay lecture events.

8.3 General Report of the Exhibits

8.3.1 Description of the Full Exhibit

The floor plan and general layout of the “From Mars to Humans” stand presented at the Royal Society Summer Science Exhibition 2023 is described in Figure 8.2. This was constructed as an interactive space in which participants may be involved in control of the model rover on a simulated Mars terrain or in spectral assessment of “tissues” against a clinical green backdrop.

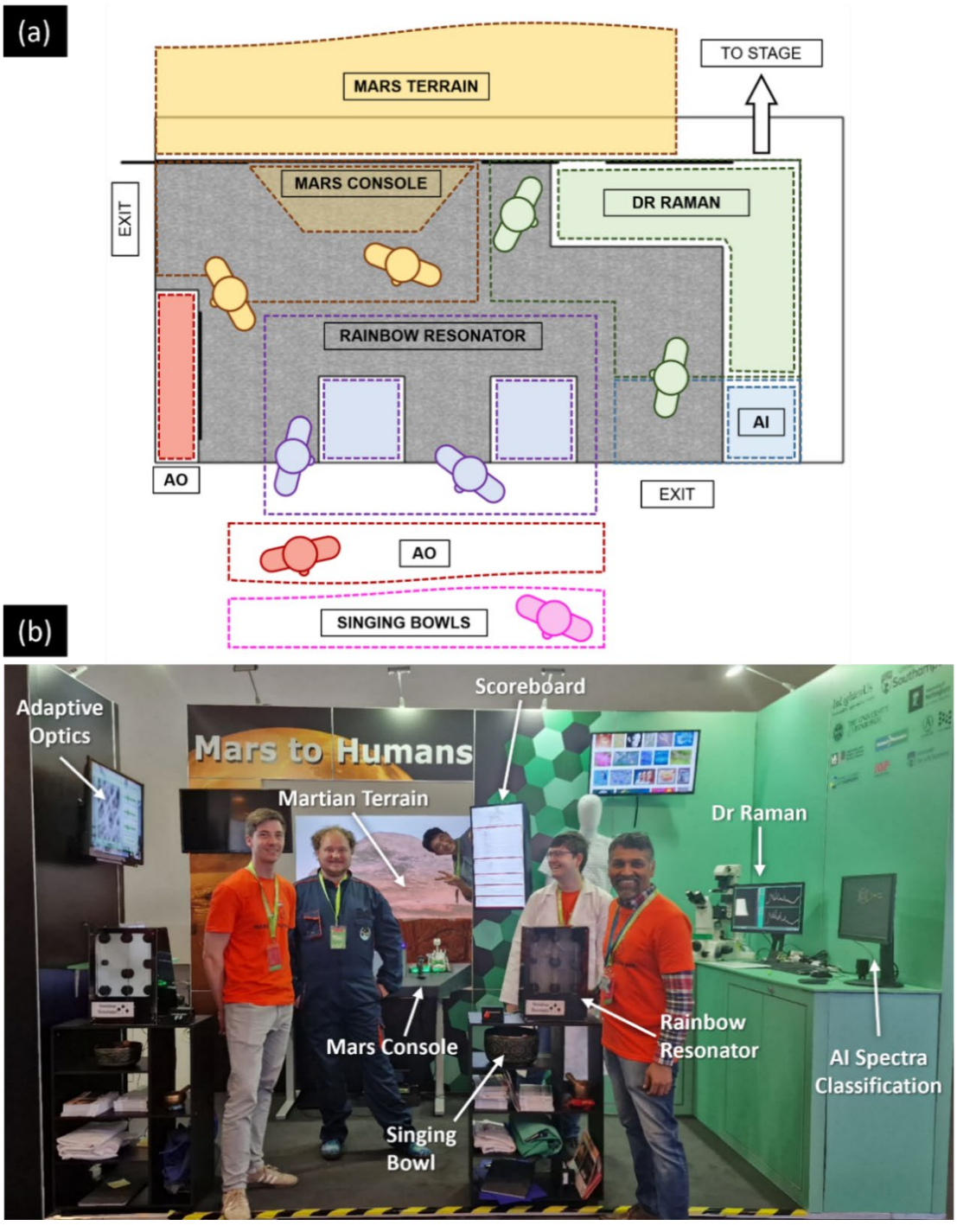

Figure 8.2 The “From Mars to Humans” exhibit at the Royal Society Summer Science Exhibition 2023. (a.) The floorplan of the exhibit stand, designed to engage crowds and queuing

visitors with “singing bowls”, adaptive optics (AO) demonstrations, and the “Rainbow Resonator”. Then participants were directed to either control of the “Raman 4 Life” rover or towards “Dr. Raman” to showcase Raman along with artificial intelligence (AI) in clinical application. (b.) The complete exhibit with demonstrators in uniform, conveying the interdisciplinary research involved with such research, carried out by space (jumpsuits) and biomedical (white lab coat) scientists, and beyond.

“Acoustic Raman” and the “Rainbow Resonator”

Activities at the front of the exhibit aimed to draw the public in, enthuse and direct members to the main stand. This allowed an introduction to the concept of vibrational resonances through an analogue of sound vibrations through use of “singing bowls”, shown in Figure 8.3 (a.). Here intended teaching points were to convey how resonance is characteristic of a particular molecule (natural frequency), as pitch is characteristic of the sound from bowls of different sizes. This could be related to light (like the mallet) supplying energy to molecules (like the bowls) to give rise to different colours (frequency or wavelengths) that are measured in Raman spectroscopy. Success in this activity would see the audience learning about vibrational resonances and excited to learn more about what measuring vibrations could do for us. The portable bowls have proven useful for engaging groups (arriving families or school groups) crowd control, and guiding people to queuing for the main activities.

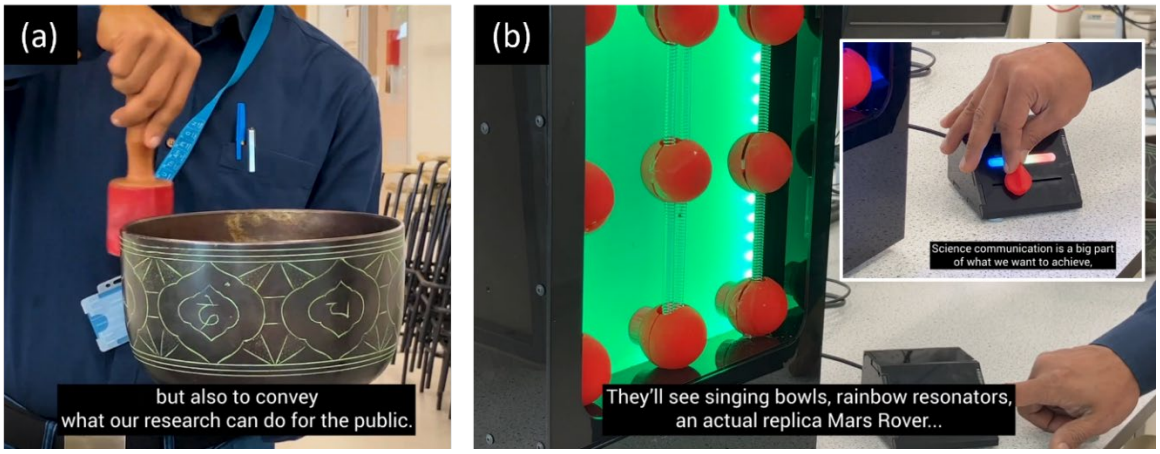

Figure 8.3 Introductory activities to demonstrate fundamental Raman phenomena.

(a.) A “singing bowl” which may be induced into resonance by excitation with a wooden mallet (b.) One of two “Rainbow Resonator” devices, with vibrating models of visually similar triatomic molecules that resonate at a specific frequency and emit light (LED). The frequency is varied by a physical slider (inset).

Video frames captured from “University of Southampton, “Revolutionary healthcare technology selected for prestigious science show””

https://www.youtube.com/watch?v=PHdp5DGNoLM (accessed September 11, 2024)

"Shaking boxes" have been used previously to great effect.[213] Here audiences were invited to tell the difference between the hidden contents of boxes solely by the sound produced when each is shaken. This was achieved by recognising pitch difference between dried rice (high pitched), coffee beans (mid frequency), and pasta (low frequency). Teaching points centred on how this was analogous to how Raman scattering elucidates the vibrations of hidden molecules.

The "Rainbow Resonator" device (Figure 8.3 (b.)) consisted of models of three triatomic molecules, visually similar, which were driven by a common linear motor. Under a specific vibration each would resonate illuminated by a corresponding light (red, green, and blue), set by a user operated slider. This aimed to convey the physical mechanism of Raman spectroscopy wherein the laser light would induce vibrational resonances to scatter light at characteristic wavelengths. The pattern of colours scattered by a material (Raman spectrum) is characteristic of its constituent molecules, and hence, whether they correspond to a diseased state or the presence of alien life. Success in this activity would see audiences understand how lasers and could identity molecules and excited to learn more about how this is utilised in studies of space environments and to understand disease on Earth.

Adaptive Optics Web App

An interactive adaptive optics (AO) web app aimed to demonstrate how optical corrections could counter distortion of signals and images when passing through material, such as through the human body or space/atmosphere particulates. Demonstrated on roaming tablets, this also served to draw and manage the visiting crowds. At quieter times, for particularly interested visitors, or when explaining to a group, visitors could be guided to the big screen to see a larger version of the demonstration, shown in Figure 8.2. Visitors would be presented with 3 – 4 images of the human body or stars/planets which, through an interactive slider, would transform from a blurred/unrecognisable image to clear. Three optical corrections presented to the participant were combinations of defocus, astigmatism (related to eyeglasses), and coma (related to light entering at an angle). Success in this activity would see an audience understand the distortion of light through a medium, adaptive optics correction, and the role of AI in optimising these parameters.

Audiences were then directed to either one of the flagship activities, namely the "Raman 4 Life" model Mars rover demonstration or the "Dr. Raman" model microspectroscopy and spectral analysis system.

“Raman 4 Life”

The “Raman 4 Life” activity aimed to demonstrate how Raman spectroscopy is playing a key role in the NASA Perseverance mission to find signs of past and potential life on the surface of Mars. The exhibit made use of an elevated stage with a simulated Martian terrain upon which a model of the Mars rover could be driven from a console with joystick and buttons to trigger measurements from an onboard miniature 785 nm Raman spectroscope, described in Figure 8.4 (a.). A custom remote-controlled rover model was constructed in our lab capable of 6-wheel rocker-bogie motion and with a motorised arm holding the small Raman spectroscope, emulating the NASA rover for its all-terrain driving system and sensors, displayed in Figure 8.4 (b.). This evolved from a previously reported model rover, and sought to draw attention to the SHERLOC (Scanning Habitable Environments with Raman and Luminescence for Organics and Chemicals) arm mounted sensor and SuperCam (for laser induced breakdown spectroscopy) body mounted camera on the real rover.[213]

A table-top mounted interface (“Mission Control” console) housed a display for the live feed of the rover mounted camera, and joystick and large buttons used to control the rover. Participants manoeuvred the rover to target spots on the model terrain and could control acquisition of a live (or simulated) Raman signal to see whether the target contained a “fingerprint” of alien life. Some control was reserved for the demonstrator to ensure laser safety and allow for an emergency shut down.

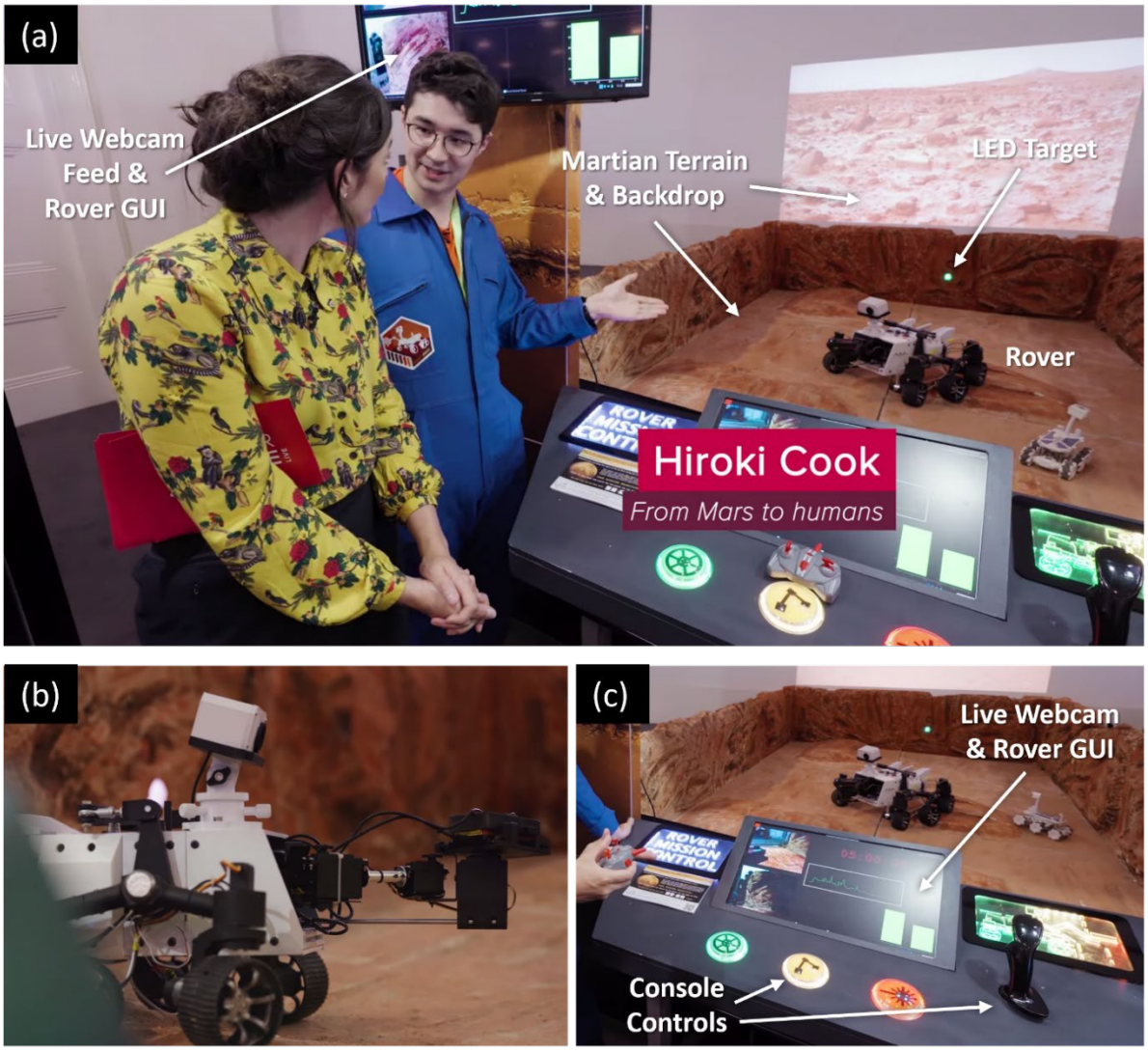

Figure 8.4 The "Raman 4 Life" Mars rover activity, a flagship of the "From Mars to Humans" exhibit. (a.) Participants were guided through the concepts of Raman spectroscopy employed on the Martian surface to seek out "signs of life" through measuring laser induced vibrations from molecules (b.) The "Raman 4 Life" rover which closely emulated NASA Perseverance including remote motion control and miniature Raman spectroscope in the articulated arm (c.) The console interface from which participants could control the rover remotely and activate capture of the Raman signal from LED targets embedded in the terrain model.
Video frames captured from "The Royal Society, "From Mars to bone disease | The Royal Society"", https://youtu.be/GckG59CUNAI?si=0jCHQ_jaxO2azlxq , (accessed September 11, 2024)

Learning outcomes were achieved by demonstrators following a dedicated script, reproduced in the "Demonstrator Handbook" in Appendix F. This aimed to guide participants through the concepts for Raman lasers producing a "chemical fingerprint" for identifying molecules, and that since life depends on certain molecules (amino acids, organic carbon, aromatics), one may

identify molecular “signs of life” through remote Raman spectroscopy. Raman technology was chosen specifically for this end within NASA Perseverance and required an interdisciplinary approach to build and operate. The research of the University of Southampton and EPSRC Transformative Healthcare “InLightenUs” venture depended on collaboration between scientists of different disciplines, including physicists, chemists, biologists, computer scientists, geologists etc. Thus, audiences were invited to engage in career envisioning, and to recognize the range of tools used to build the set and rover, including CAD and 3D printing, involved in many school curriculums.

Operation of the rover was gamified to encourage a rapid turnover, with participants competing for a record time to drive to and measure each target around the set, top scores displayed on an overhead screen. Success for this activity saw audiences excited to learn more about how discoveries in space are facilitated by technologies used on Earth for biomedical applications, and aware that this work requires close collaboration between various scientists and engineers, with school children encouraged to consider such careers.

Visitors would then be invited to consider use of Raman spectroscopy for human (clinical) applications and directed to attend the “Dr. Raman” exhibit, if not already seen.

“Dr Raman”

The “Dr. Raman” activity aimed to demonstrate how Raman spectroscopy is playing a key role at the cutting edge of biomedical research and in particular for assessing bone and cartilage diseases at the University of Southampton and within the InLightenUs team. The exhibit recruited a mannequin dressed in surgical gown with an exposed 3D printed pelvis to represent a patient undergoing hip arthroplasty or arthroscopy surgery, shown in Figure 8.5 (a.). From here a demonstrator dressed in scrubs (clinical surgeon) or white lab coat (biomedical scientist) would select a soft silicon “biopsy” sample and place onto the light sealed stage of the microscope (Figure 8.5 (b.)) in order to capture a Raman signal (Figure 8.5 (c.)). Raman microspectroscopy was also mediated by a miniaturised 785 nm spectrometer within the body of the microscope, which captured signals from hidden polymer disks attached to the bottom of the sample holder. The plastic discs ensured strong and repeatable Raman signal, and displayed a “healthy” (plastic 1 e.g. PMMA) or “diseased” (plastic 2 e.g. PC) spectral fingerprint. The “biopsy” samples were visually identical so the demonstrator could assert that, while indistinguishable to the eye, Raman spectroscopy-based analysis could pick up differences.

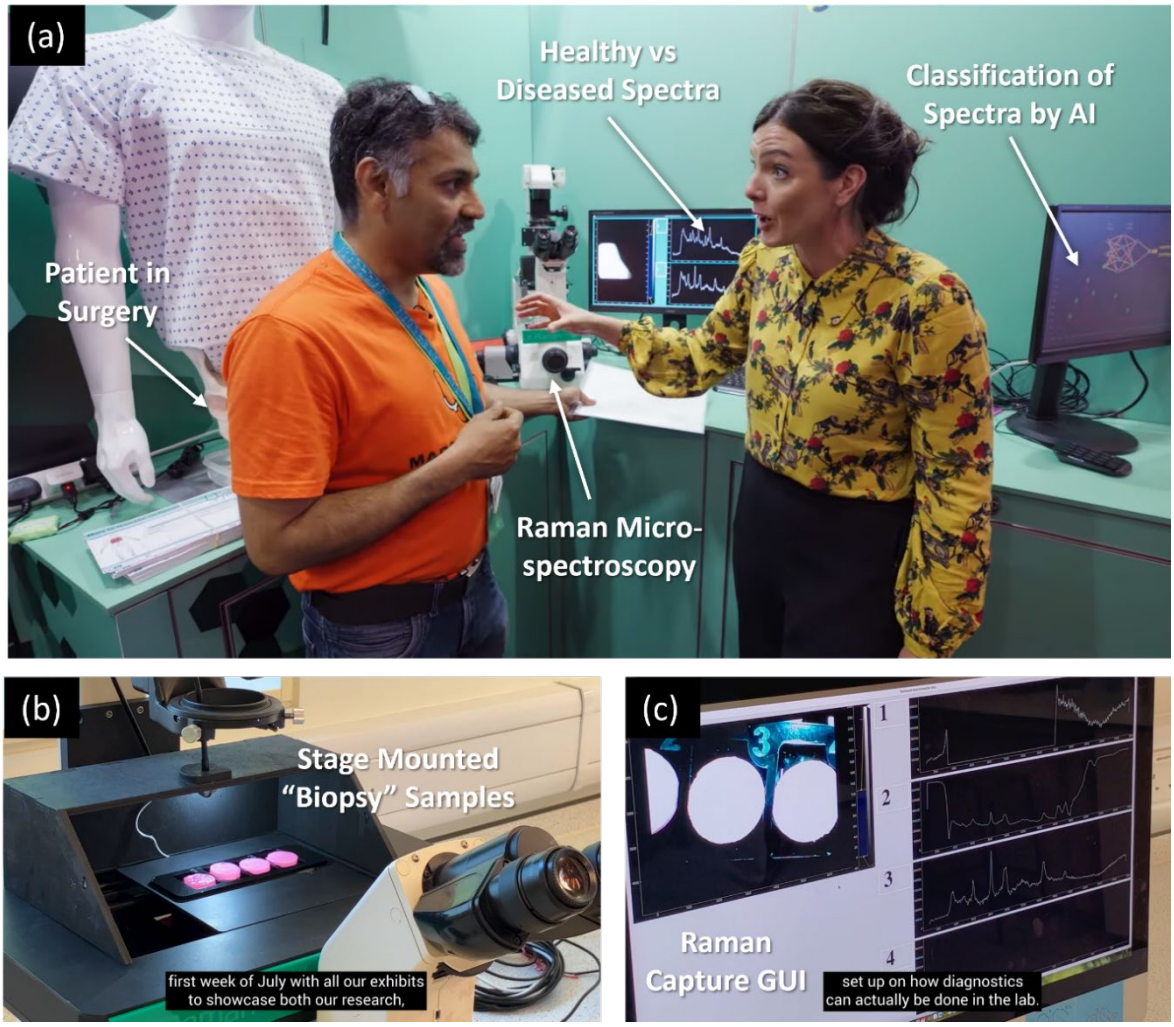

Figure 8.5 The "Raman 4 Life" Mars rover activity, a flagship of the "From Mars to Humans" exhibit. (a.) Participants were guided through the concepts for surgical retrieval of a cartilage and bone biopsy, measurements via Raman microspectroscopy, and then analysis of the spectral data (including AI) in order to detect diseases.
Video frame captured from "The Royal Society, "From Mars to bone disease | The Royal Society"", https://youtu.be/GckG59CUNAI?si=0jCHQ_jaxO2azlxq , (accessed September 11, 2024)
(b.) The faux "biopsy" samples would be placed on the microscope stage and (c.) spectra captured capable of determining signals from plastic disks corresponding to a "healthy" or "diseased" sample. The use of AI could then be demonstrated by a dedicated web app to teach the principles of neural networks for spectral analysis.
Video frames captured from "University of Southampton, "Revolutionary healthcare technology selected for prestigious science show""
https://www.youtube.com/watch?v=PHdp5DGNoLM (accessed September 11, 2024)

Learning outcomes were achieved by demonstrators following a dedicated script, reproduced in the "Demonstrator Handbook" in Appendix F. This aimed to guide participants through the

concepts for Raman “chemical fingerprinting” as label free and non-destructive biological tissue assessment. Combined with the cutting edge in optical physics (light shaping AO) and in AI, this could allow for accurate detection of bone and joint diseases, ideally at an early stage. Researchers at the University of Southampton and within the InLightenUs programme are developing technologies that can improve healthcare for older individuals - clinical applications of Raman on Earth. The message relayed also described how results today would rely on biopsies and future evolution of the technology will see in vivo assessment minimally- or entirely non-invasively.

Demonstrators guided participants through the process of “reading” the spectral signal to determine indicative “healthy” or “diseased” peaks. Manual human interpretation could then be augmented by powerful AI interpretation, demonstrated with the follow-on diagnostic web app, in Figure 8.2. The interdisciplinary collaboration between the clinician and biomedical surgeon was also conveyed in the role play of the demonstrators. Thus, success in this activity saw participants able to understand Raman spectroscopy applied “to Humans” for disease diagnosis, the specific aims of research at the University of Southampton and InLightenUs team, and how this was reliant on close collaboration between scientists (physicists, biochemists) and clinicians.

AI Diagnosis Web App

Finally, the AI web app was employed as direct continuation from the signal acquisition on “Dr. Raman”, which aimed to show how AI technology may be used to speed up the process of disease detection in Raman spectral data. The web app would display an animation describing how important features from the spectra are propagated through a deep neural network. The app could be triggered via key presses corresponding to a “healthy” or “diseased” verdict, operated by the demonstrator. Teaching points included how a neural network could be applied to raw spectra and trained to determine the most biologically relevant wavelengths decision making in disease diagnosis. This was shown analogous to the human brain, learning from past experience to make a decision.

The work at the University of Southampton and the InLightenUs team was promoted, describing to the public how AI was being implemented in the classification of spectra from osteoporosis and osteoarthritis patients, work that resulted in recent publication from Kok and colleagues from the InLightenUs team. [158] Success in this activity saw participants excited to learn more about what neural networks could do to solve various tasks, particularly when applied in the medical field.

8.3.2 Produced Handbook as Teaching Resource

A key resource developed for this work was a "Demonstrator Handbook" produced by myself and Yong En (Janet) Kok of the University of Nottingham, and with input from some members of the EPSRC Transformative Healthcare "InLightenUs" project cohort. The handbook is reproduced in the Appendix F detailing scripts and prompts for teaching points for each of the activities detailed above. The scripts were developed following training from the public engagement team at the Science Museum Group, aspiring with each activity to:

- "Hook": to capture attention and spark interest
- "Inform": sharing STEM knowledge
- "Enable": providing the opportunity for visitors to do something with such knowledge
- "Extend": empowering visitors to make the experience last longer

Finally, demonstrators were encouraged to continually "Reflect" on audiences' needs and experiences in order make appropriate changes before, during & after the event. This proved to be of considerable help in navigating a diverse audience of visitors during the Summer Science Exhibition and has served to inform successful outreach activities beyond, described below.

8.3.3 Local Outreach Activities

Other public science communication activities have been held at local events including the University of Southampton (UoS) Science and Engineering Festival (SOTSEF), with the UoS Roadshow at the New Forest & Hampshire County Show (ASAO, UK), at the Somerscience Festival (Somerscience Trust, UK), and with the Pint of Science Festival (Pint of Science, UK). Each garnered a wide audience of school children, families, and adults. A pared down version of the activities would be delivered usually limited to the "singing bowls" and "shaking boxes" to convey the physical fundamentals, before showcasing the model rover and miniature Raman spectrometer in live demonstrations.

For example, recent demonstrations with Pint of Science saw interactive lay lecture presentations within a relaxed environment in a bar to local families, adults, and off-duty university academics, shown in Figure 8.6. A live demonstration of Raman analysis of common drinks was demonstrated showing the sensitivity of the technique in detecting samples of pure (ethanol), high-proof (gin) and low-proof (beer) alcohol. Showcasing the model rover prompted questions from school age children on its construction (acknowledging STEM skills in practice) and about interdisciplinary collaborations (career envisioning).

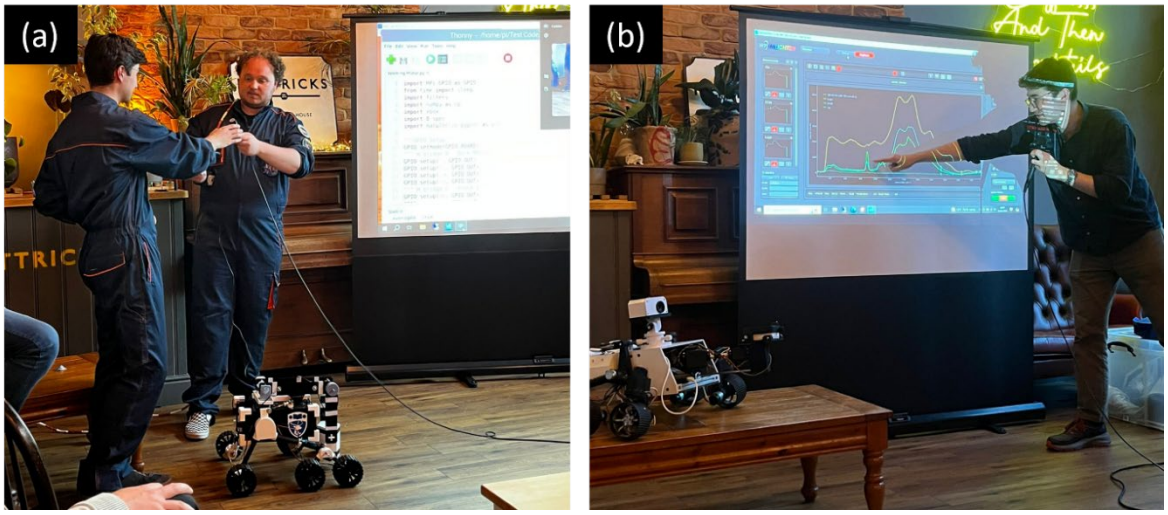

Figure 8.6 Demonstrating Raman phenomena with the “Raman 4 Life” rover to a lay audience in a local bar as part of Pint of Science in (a.) 2023 and (b.) 2024. This involved guiding audiences through the search for alien life facilitated by the efficacy of Raman spectroscopy for distinguishing samples, here between samples of pure (ethanol), high-proof (gin) and low-proof (beer) alcohol.

8.4 General Feedback and Concluding Remarks

Some quantifiable successes have been recorded for these activities, most notable through primary participant feedback gathered at SOTSEF 2022, reported by Kleboe et al.[213] The most important metrics were those indicating positive change in attitude towards STEM (increasing science capital) and understanding of scientific concepts demonstrated.

Questions pertaining to the clarity and engaging delivery of the presenters and how well scientific ideas were described were met with vast majority votes of “Very Good”, some “Good”, and no “Neutral” votes. This was reflected across the range of interactive demonstrations. When asked “Has the Mars to Humans activity inspired you to attend another Science Festival?” over 80% of participants answered “Yes”, indicating a clear positive effect on attitude towards STEM.[213] Also the “Dr. Raman” and “Raman 4 Life” activities were overwhelmingly voted as “Essential” and “Very Relevant” to participants’ everyday life.

A general report from the production team of the Somerscience Festival 2024 described how 47% of attendees said the festival made them feel more likely to consider studying or working in STEM. The report also described how awareness of STEM careers reportedly increased from 78% positive in 2023 to 83% in 2024, commenting that this suggests demonstrators may have geared public messaging more toward destination and careers, [214] thanks perhaps in part to the “From Mars to Humans” activities.

Overall, the public engagement activities described here have been a labour of love and have been delivered by an incredible team from the University of Southampton and InLightenUs project in the hope of enthusing and empowering future scientists.

Chapter 9 General Conclusions

The research presented in this thesis focuses on new methodologies for the diagnostic assessment and therapeutic treatment of tissues exploiting the optical biological transparency windows in the NIR-SWIR. Each approach offers the means for potential paradigm shift away from clinical practice, specifically departure from the radiographic assessment of osteoarthritis and use of CO_2 and Ho:YAG clinical lasers.

The background and theory for this thesis was presented in Chapter 2. This included discussion of the shortcomings of current clinical paradigms for diagnosis of OA and how vibrational spectroscopy through arthroscopy may offer a suitable alternative, benefiting from the biological transparency windows. Strategies to target the high absorption cross section of water in the NIR-SWIR under pulsed lasers were then explored for photoablation applications. A comprehensive review of the literature followed in Chapter 3, considering the state-of-the-art in NIR-SWIR optical tissue assessments for insight into OA and in NIR-SWIR clinical photoablation, laying out the foundation and need for the advances delivered in this project.

In Chapter 5 a proof-of-concept was delivered for a novel approach termed “spectromics”, where low abstraction data fusion between Raman scattering and NIR-SWIR absorption spectra allowed for an enhanced chemical fingerprinting technique. This allowed for a holistic assessment of vibrational bonds (Raman and IR active) for enhanced biochemical information about the state of analysed tissues. This study presented the first instance of spectromics applied in the detection of OA in human cartilage samples representing n = 13 diseased (osteoarthritic) and n = 14 control (osteoporotic) tissues, with spectra of cartilage slices measured under transreflectance. Classification performance under PCA-LDA and SVM models was interrogated, wherein the spectromics analysis consistently outperformed analysis under Raman or NIR-SWIR data alone. Under 10 PC’s, spectromics allowed for 100% segregation of tissue classes, compared to 77.8 % and 62.3 %, for Raman and NIR-SWIR, respectively. Under 20 PC’s spectromics accounted for a 5 – 6 fold improvement, under 5 PC’s only spectromics could segregate tissue, thus showing admirable performance even under data limit constraint. SVM achieved high classification accuracy of 95% (control) and 80% (OA), using the combined vibrational data. Performance was limited due to small patient sample set and restrictions of one mean spectrum per patient, but nonetheless showcases the benefits of the spectromics approach and offers an advance in spectroscopic assessment of OA.

The spectromics approach is proffered as a technique level innovation compatible with arthroscopic measurements within minimally invasive procedures. This can be adopted into

established clinical practice for arthroscopic assessment and treatment of the hip, offering a patient friendly paradigm (less surgical trauma). The enhanced spectromics fingerprint was then probed through a series of statistical tests (interpretable feedback) to identify the spectral regions most indicative of OA state, verified against those derived in the literature, and proposed as label free OA biomarkers. This could be adopted for efficient clinical assessment since only a few indicative spectral features need be considered. Further proof of clinical viability would see spectromics applied to a larger number of patient samples.

Chapter 6 detailed the construction and development of an automated 3D goniometric hyperspectral mapping system of co-localised Raman scattering and NIR-SWIR absorption measurements, the first of its kind for non-contact 3D spectral assessment of human osteochondral tissues. This investigated the translation of the spectromics approach to 3D mapping across the surface of bone cores and whole samples of human femoral heads, and mapped site-specific distribution of spectromics biomarkers and other indicative spectral features relating to OA pathologies. This resolved limitations of the preceding spectromics study that relied on transreflected spectra, averaged per patient: the reported system now allows for unbiased and site-specific mapping across the whole joint tissue with cartilage and subchondral bone *in situ*, thus closer to the *in vivo* environment. The ultimate aspiration for this system is its utility in developing a library of spectral data of human OA and control tissues as an *ex vivo* ground truth for future arthroscopic approaches. With such a library only a few sites may need to be targeted with an arthroscope probe, reducing time for procedure, reducing healthcare system expense, and improving patient quality of life

The full workflow was established for automated surface scanning including mounting of various tissues, optimal hardware, development of spectral acquisition software, and 3D reconstruction of data. Hyperspectral maps were cross referenced against full-colour photogrammetry scans of the tissue samples, showing visual changes to the tissue associated with natural, surgical and disease effects. The multimodal system proved suitably sensitive for mapping of natural and pathological heterogeneities across whole joint tissues, and is proffered as a platform for furthering biological and medical understanding of the complex effects of OA, in complex joints like the hip. This leverages the sensitivity of the spectromics approach to OA associated changes invisible to conventional radiography, including soft tissue changes undetected by x-ray, and label free biochemical composition analysis impossible through MRI. Results to date have shown fully correlated 3D Raman scattering and NIR-SWIR absorption scans of bone core samples representing the osteochondral junction of OA and control femoral heads, and 3D NIR-SWIR absorption scans of a whole OA femoral head. Future work was identified in the evolution of the scanning system to allow for improvements in the z-stage range and autofocusing, and in improved correlation strategies such as use of fiducial markers.

Considering next the therapeutic techniques of the NIR-SWIR optical regime, Chapter 7 presented work carried out to establish efficient and precise photoablation through targeting of the 1.95 μm water absorption peak in cell samples. This detailed the construction of a micro-surgical photoablation system enabled by a custom ns-pulsed thulium-doped fibre laser capable of producing a high-quality beam with precise control of fundamental pulse parameters. Fine tuning of pulse duration, repetition rate, exposure time and average power facilitated the first demonstration of single-cell scale ablation on plant samples (onion epidermal cells) and human neuroblastoma sampled (SH-SY5Y cells) with such a laser.

This achieved precision of 31.3 ± 0.1 μm on onion epidermal cells and 19.9 ± 0.1 μm on single SH-SY5Y cells. The capacity to target and destroy human tissue with single-cell precision on a coverslip containing in excess of 250,000 cells proves a very promising tool for microsurgical applications. Results indicated that ablation at the cellular scale is best with short pulse durations with low repetition rates, delivering energy just above tissue threshold. Conversely, long pulse duration relative to the thermal diffusion time of the sample, or high repetition rate may reduce thermomechanical confinement, lowering ablation efficiency and risking collateral damage. Demonstrations on two structurally distinct samples (plant and animal) indicates the broad tuneability and capability of this system. In microsurgical applications it would be imperative to preserve as much surrounding tissue as possible, e.g. healthy tissue surrounding a malignant tumour, whilst ensuring precision cutting for the surgeon operating. Since these were fixed (dead) cell samples, cell membrane integrity was employed as a mechanical analogue for tissue viability and investigated under Trypan Blue staining. These results corroborated the ability of the system for precise ablation with minimal collateral. The success in delivering single-cell scale photoablation through targeting the high absorption coefficient of water common to all *in vivo* tissues is very promising, and developments to the microsurgery system for incisions into thicker, mature tissue are now being explored.

Finally, Chapter 8 presented a general report of the public engagement and science communication activities carried out over the course of my candidature with the Molecular Biophotonics and Imaging group. In particular, the concepts and delivery of the “From Mars to Humans” activity for which I was a key developer and its delivery to the public as part of the Royal Society Summer Science Exhibition in 2023. The two flagship activities were described, namely the “Raman 4 Life” model Mars rover and the “Dr. Raman” model microspectroscopy system, covering applications of Raman spectroscopy from “Mars” to “Humans” respectively. The elements of the interactive stand, attitudes for public engagement, and quantified successes in audience response data were described.

The developments and results presented in this thesis contribute to the overall goal of exploiting the NIR-SWIR optical regime for development of new approaches to diagnosis and therapy, contributing advances in techniques for the clinical assessment of OA and for precise and efficient photoablation. These findings exhibit high clinical relevance and are proffered to ultimately serve patients undergoing such care.

Bibliography

(1) Cook, H.; Crisford, A.; Bourdakos, K.; Dunlop, D.; Oreffo, R. O.; Mahajan, S. Holistic Vibrational Spectromics Assessment of Human Cartilage for Osteoarthritis Diagnosis. *Biomed. Opt. Express* **2024**, *15* (7), 4264. https://doi.org/10.1364/boe.520171.

(2) Cook, H.; Crisford, A.; Acharyya, J. N.; Bourdakos, K. N.; Kanczler, J.; Dunlop, D.; Oreffo, R. O. C.; Mahajan, S. Label-Free 3D NIR-SWIR "Spectromics" Mapping of Human Hip Cartilage for Diagnosis of Osteoarthritis. In *Biomedical Spectroscopy, Microscopy, and Imaging III*; Popp, J., Gergely, C., Eds.; SPIE, 2024; p 13. https://doi.org/10.1117/12.3022003.

(3) Gerard, M. D.; Cook, H.; Read, J. A. Single-Cell High-Precision Ablation Using Nanosecond-Pulsed Thulium-Doped Fiber Laser. **2024**, *63* (August), 1–20. https://doi.org/10.1117/1.OE.63.8.086102.

(4) *Deep Imaging in Tissue and Biomedical Materials*; Shi, L., Alfano, R. R., Eds.; Jenny Stanford Publishing, 2017. https://doi.org/10.1201/9781315206554.

(5) Gupta, A.; Obmann, V. C.; Jordan, M.; Lennartz, S.; Obmann, M. M.; Hokamp, N. G.; Zopfs, D.; Pennig, L.; Fürtjes, G.; Ramaiya, N.; Gilkeson, R.; Laukamp, K. R. CT Artifacts after Contrast Media Injection in Chest Imaging: Evaluation of Post-Processing Algorithms, Virtual Monoenergetic Images and Their Combination for Artifact Reduction. *Quant. Imaging Med. Surg.* **2021**, *11* (1), 226–239. https://doi.org/10.21037/QIMS-20-435.

(6) Guo, B. J.; Yang, Z. L.; Zhang, L. J. Gadolinium Deposition in Brain: Current Scientific Evidence and Future Perspectives. *Front. Mol. Neurosci.* **2018**, *11* (September), 1–12. https://doi.org/10.3389/fnmol.2018.00335.

(7) Lassailly, F.; Griessinger, E.; Bonnet, D. "Microenvironmental Contaminations" Induced by Fluorescent Lipophilic Dyes Used for Noninvasive in Vitro and in Vivo Cell Tracking. *Blood* **2010**, *115* (26), 5347–5354. https://doi.org/10.1182/blood-2009-05-224030.

(8) Jensen, E. C. Use of Fluorescent Probes: Their Effect on Cell Biology and Limitations. *Anat. Rec.* **2012**, *295* (12), 2031–2036. https://doi.org/10.1002/ar.22602.

(9) Mohammed, N. A.; Rafie, I.; Mahfouz, A.; Achkar, K.; Hajar, R. Contrast-Induced

Nephropathy. *Hear. Views* **2013**, *14* (3), 106. https://doi.org/10.4103/1995-705X.125926.

(10) Swain, S.; Sarmanova, A.; Mallen, C.; Kuo, C. F.; Coupland, C.; Doherty, M.; Zhang, W. Trends in Incidence and Prevalence of Osteoarthritis in the United Kingdom: Findings from the Clinical Practice Research Datalink (CPRD). *Osteoarthr. Cartil.* **2020**, *28* (6), 792–801. https://doi.org/10.1016/j.joca.2020.03.004.

(11) Safiri, S.; Kolahi, A. A.; Smith, E.; Hill, C.; Bettampadi, D.; Mansournia, M. A.; Hoy, D.; Ashrafi-Asgarabad, A.; Sepidarkish, M.; Almasi-Hashiani, A.; Collins, G.; Kaufman, J.; Qorbani, M.; Moradi-Lakeh, M.; Woolf, A. D.; Guillemin, F.; March, L.; Cross, M. Global, Regional and National Burden of Osteoarthritis 1990-2017: A Systematic Analysis of the Global Burden of Disease Study 2017. *Ann. Rheum. Dis.* **2020**, 819–828. https://doi.org/10.1136/annrheumdis-2019-216515.

(12) Golovynskyi, S.; Golovynska, I.; Stepanova, L. I.; Datsenko, O. I.; Liu, L.; Qu, J.; Ohulchanskyy, T. Y. Optical Windows for Head Tissues in Near-Infrared and Short-Wave Infrared Regions: Approaching Transcranial Light Applications. *J. Biophotonics* **2018**, *11* (12), 1–12. https://doi.org/10.1002/jbio.201800141.

(13) Sordillo, L. A.; Sordillo, D. C.; Shi, L.; Sordillo, P. P.; Alfano, R. R. SWIR Windows as an Adjunctive to Biopsy for Distinguishing and Monitoring Benign and Malignant Tissues. **2020**, No. February, 50. https://doi.org/10.1117/12.2550311.

(14) Feng, Z.; Tang, T.; Wu, T.; Yu, X.; Zhang, Y.; Wang, M.; Zheng, J.; Ying, Y.; Chen, S.; Zhou, J.; Fan, X.; Zhang, D.; Li, S.; Zhang, M.; Qian, J. Perfecting and Extending the Near-Infrared Imaging Window. *Light Sci. Appl.* **2021**, *10* (1). https://doi.org/10.1038/s41377-021-00628-0.

(15) Kafan Attari, I.; Semenov, D. V.; Nippolainen, E.; Hauta-Kasari, M.; Töyräs, J.; Afara, I. O. Optical Properties of Articular Cartilage in the Near-Infrared Spectral Range Are Related to Its Proteoglycan Content. **2020**, No. May 2020, 33. https://doi.org/10.1117/12.2555291.

(16) Afara, I.; Prasadam, I.; Crawford, R.; Xiao, Y.; Oloyede, A. Non-Destructive Evaluation of Articular Cartilage Defects Using near-Infrared (NIR) Spectroscopy in Osteoarthritic Rat Models and Its Direct Relation to Mankin Score. *Osteoarthr. Cartil.* **2012**, *20* (11), 1367–1373. https://doi.org/10.1016/j.joca.2012.07.007.

(17) Afara, I. O.; Prasadam, I.; Arabshahi, Z.; Xiao, Y.; Oloyede, A. Monitoring Osteoarthritis

Progression Using near Infrared (NIR) Spectroscopy. *Sci. Rep.* **2017**, *7* (1), 1–9. https://doi.org/10.1038/s41598-017-11844-3.

(18) Padalkar, M. V.; Pleshko, N. Wavelength-Dependent Penetration Depth of near Infrared Radiation into Cartilage. *Analyst* **2015**, *140* (7), 2093–2100. https://doi.org/10.1039/c4an01987c.

(19) Poole, A. R.; Kobayashi, M.; Yasuda, T.; Laverty, S.; Mwale, F.; Kojima, T.; Sakai, T.; Wahl, C.; El-Maadawy, S.; Webb, G.; Tchetina, E.; Wu, W. Type II Collagen Degradation and Its Regulation in Articular Cartilage in Osteoarthritis. *Ann. Rheum. Dis.* **2002**, *61* (SUPPL. 2), 78–81. https://doi.org/10.1136/ard.61.suppl_2.ii78.

(20) Rieppo, L.; Töyräs, J.; Saarakkala, S. Vibrational Spectroscopy of Articular Cartilage. *Appl. Spectrosc. Rev.* **2017**, *52* (3), 249–266. https://doi.org/10.1080/05704928.2016.1226182.

(21) Yu, C.; Zhao, B.; Li, Y.; Zang, H.; Li, L. Vibrational Spectroscopy in Assessment of Early Osteoarthritis—a Narrative Review. *Int. J. Mol. Sci.* **2021**, *22* (10). https://doi.org/10.3390/ijms22105235.

(22) Ryd, L.; Brittberg, M.; Eriksson, K.; Jurvelin, J. S.; Lindahl, A.; Marlovits, S.; Möller, P.; Richardson, J. B.; Steinwachs, M.; Zenobi-Wong, M. Pre-Osteoarthritis. *Cartilage* **2015**, *6* (3), 156–165. https://doi.org/10.1177/1947603515586048.

(23) Novakofski, K. D.; Pownder, S. L.; Koff, M. F.; Williams, R. M.; Potter, H. G.; Fortier, L. A. High-Resolution Methods for Diagnosing Cartilage Damage In Vivo. **2016**. https://doi.org/10.1177/1947603515602307.

(24) Baer, K.; Kieser, S.; Schon, B.; Rajendran, K.; Ten Harkel, T.; Ramyar, M.; Löbker, C.; Bateman, C.; Butler, A.; Raja, A.; Hooper, G.; Anderson, N.; Woodfield, T. Spectral CT Imaging of Human Osteoarthritic Cartilage via Quantitative Assessment of Glycosaminoglycan Content Using Multiple Contrast Agents. *APL Bioeng.* **2021**, *5* (2). https://doi.org/10.1063/5.0035312.

(25) Faulkner, K. Introduction to Physics in Modern Medicine (Second Edition) KaneSuzanne Amador Boca Raton, FL, USA CRC Presspp. 422 + Xviii 2009£38:99ISBN: 978-1-58488-943-4. *Br. J. Radiol.* **2010**, *83* (987), 271–271. https://doi.org/10.1259/bjr-83-987-271.

(26) Roemer, F. W.; Demehri, S.; Omoumi, P.; Link, T. M.; Kijowski, R.; Saarakkala, S.; Crema,

M. D.; Guermazi, A. State of the Art: Imaging of Osteoarthritis—Revisited 2020. *Radiology* **2020**, *296* (1), 5–21. https://doi.org/10.1148/radiol.2020192498.

(27) Messina, C.; Maffi, G.; Vitale, J. A.; Ulivieri, F. M.; Guglielmi, G.; Sconfenza, L. M. Diagnostic Imaging of Osteoporosis and Sarcopenia: A Narrative Review. *Quant. Imaging Med. Surg.* **2018**, *8* (1), 86–99. https://doi.org/10.21037/qims.2018.01.01.

(28) Adams, J. E. Advances in Bone Imaging for Osteoporosis. *Nat. Rev. Endocrinol.* **2013**, *9* (1), 28–42. https://doi.org/10.1038/nrendo.2012.217.

(29) Li, X.; Majumdar, S. Quantitative MRI of Articular Cartilage and Its Clinical Applications. *J. Magn. Reson. Imaging* **2013**, *38* (5), 991–1008. https://doi.org/10.1002/jmri.24313.

(30) Aguilar, H. N.; Battié, M. C.; Jaremko, J. L. MRI-Based Hip Cartilage Measures in Osteoarthritic and Non-Osteoarthritic Individuals: A Systematic Review. *RMD Open* **2017**, *3* (1), e000358. https://doi.org/10.1136/rmdopen-2016-000358.

(31) Mourad, C.; Vande Berg, B. Osteoarthritis of the Hip: Is Radiography Still Needed? *Skeletal Radiol.* **2023**, *52* (11), 2259–2270. https://doi.org/10.1007/s00256-022-04270-8.

(32) Hunter, D. J.; Guermazi, A.; Lo, G. H.; Grainger, A. J.; Conaghan, P. G.; Boudreau, R. M.; Roemer, F. W. MOAKS (MRI Osteoarthritis Knee Score). *Osteoarthr. Cartil.* **2011**, *19* (8), 990–1002. https://doi.org/10.1016/j.joca.2011.05.004.Evolution.

(33) Peterfy, C. G.; Guermazi, A.; Zaim, S.; Tirman, P. F. J.; Miaux, Y.; White, D.; Kothari, M.; Lu, Y.; Fye, K.; Zhao, S.; Genant, H. K. Whole-Organ Magnetic Resonance Imaging Score (WORMS) of the Knee in Osteoarthritis. *Osteoarthr. Cartil.* **2004**, *12* (3), 177–190. https://doi.org/10.1016/j.joca.2003.11.003.

(34) Vomer, R. P.; Boggess, S.; Boggess, B. Ultrasound Evaluation of Knee Osteoarthritis. *Cureus* **2023**, *15* (5), 1–12. https://doi.org/10.7759/cureus.39188.

(35) Braun, H. J.; Gold, G. E. Diagnosis of Osteoarthritis: Imaging. *Bone* **2012**, *51* (2), 278–288. https://doi.org/10.1016/j.bone.2011.11.019.

(36) Singh, A. P.; Saran, S.; Thukral, B. B.; Kaushik, R. Ultrasonographic Evaluation of Osteoarthritis-Affected Knee Joints. *J. Med. Ultrasound* **2021**, *29* (1), 39–45. https://doi.org/10.4103/JMU.JMU_45_20.

(37) Jahr, H.; Brill, N.; Nebelung, S. Detecting Early Stage Osteoarthritis by Optical Coherence

Tomography? *Biomarkers* **2015**, *20* (8), 590–596. https://doi.org/10.3109/1354750X.2015.1130190.

(38) Chu, C. R.; Williams, A.; Tolliver, D.; Kwoh, C. K.; Bruno, S.; Irrgang, J. J. Clinical Optical Coherence Tomography of Early Articular Cartilage Degeneration in Patients with Degenerative Meniscal Tears. *Arthritis Rheum.* **2010**, *62* (5), 1412–1420. https://doi.org/10.1002/art.27378.

(39) Huang, D.; Swanson, E. A.; Lin, C. P.; Schuman, J. S.; Stinson, W. G.; Chang, W.; Hee, M. R.; Flotte, T.; Gregory, K.; Puliafito, C. A.; Fujimoto, J. G. Optical Coherence Tomography. *Science (80-.).* **1991**, *254* (5035), 1178–1181. https://doi.org/10.1126/science.1957169.

(40) Wang, Y.; Liu, S.; Lou, S.; Zhang, W.; Cai, H.; Chen, X. Application of Optical Coherence Tomography in Clinical Diagnosis. *J. X-Ray Sci. Technol. Clin. Appl. Diagnosis Ther.* **2019**, *27* (6), 995–1006. https://doi.org/10.3233/XST-190559.

(41) Li, X.; Martin, S.; Pitris, C.; Ghanta, R.; Stamper, D. L.; Harman, M.; Fujimoto, J. G.; Brezinski, M. E. High-Resolution Optical Coherence Tomographic Imaging of Osteoarthritic Cartilage during Open Knee Surgery. *Arthritis Res Ther* **2005**, *7* (2), R318. https://doi.org/10.1186/ar1491.

(42) Rashidifard, C.; Vercollone, C.; Martin, S.; Liu, B.; Brezinski, M. E. The Application of Optical Coherence Tomography in Musculoskeletal Disease. *Arthritis* **2013**, *2013*, 1–13. https://doi.org/10.1155/2013/563268.

(43) Martin, S.; Rashidifard, C.; Norris, D.; Goncalves, A.; Vercollone, C.; Brezinski, M. E. Minimally Invasive Polarization Sensitive Optical Coherence Tomography (PS-OCT) for Assessing Pre-OA, a Pilot Study on Technical Feasibility. *Osteoarthr. Cartil. Open* **2022**, *4* (4), 100313. https://doi.org/10.1016/j.ocarto.2022.100313.

(44) Nam, H. S.; Yoo, H. Spectroscopic Optical Coherence Tomography: A Review of Concepts and Biomedical Applications. *Appl. Spectrosc. Rev.* **2018**, *53* (2–4), 91–111. https://doi.org/10.1080/05704928.2017.1324876.

(45) Carlos Cuartas-Vélez. *Visible-Light Spectroscopic Optical Coherence Tomography: Applications and Technology.*; 2023.

(46) An, R.; Gu, H.; Guo, Z.; Zhong, H.; Wei, H.; Wu, G.; He, Y.; Xie, S.; Yang, H. Diagnosis of Knee Osteoarthritis by OCT and Surface-Enhanced Raman Spectroscopy. *J. Innov. Opt.*

Health Sci. **2022**, *15* (05). https://doi.org/10.1142/S1793545822500274.

(47) Fitzgerald, S.; Akhtar, J.; Schartner, E.; Ebendorff-Heidepriem, H.; Mahadevan-Jansen, A.; Li, J. Multimodal Raman Spectroscopy and Optical Coherence Tomography for Biomedical Analysis. *J. Biophotonics* **2023**, *16* (3). https://doi.org/10.1002/jbio.202200231.

(48) Afara, I. O.; Hauta-Kasari, M.; Jurvelin, J. S.; Oloyede, A.; Töyräs, J. Optical Absorption Spectra of Human Articular Cartilage Correlate with Biomechanical Properties, Histological Score and Biochemical Composition. *Physiol. Meas.* **2015**, *36* (9), 1913–1928. https://doi.org/10.1088/0967-3334/36/9/1913.

(49) Casal-Beiroa, P.; Balboa-Barreiro, V.; Oreiro, N.; Pértega-Díaz, S.; Blanco, F. J.; Magalhães, J. Optical Biomarkers for the Diagnosis of Osteoarthritis through Raman Spectroscopy: Radiological and Biochemical Validation Using Ex Vivo Human Cartilage Samples. *Diagnostics* **2021**, *11* (3). https://doi.org/10.3390/diagnostics11030546.

(50) Afara, I. O.; Oloyede, A. Resolving the Near-Infrared Spectrum of Articular Cartilage. *Cartilage* **2021**, *13* (1_suppl), 729S-737S. https://doi.org/10.1177/19476035211035417.

(51) Afara, I. O.; Shaikh, R.; Nippolainen, E.; Querido, W.; Torniainen, J.; Sarin, J. K.; Kandel, S.; Pleshko, N.; Töyräs, J. Characterization of Connective Tissues Using Near-Infrared Spectroscopy and Imaging. *Nat. Protoc.* **2021**, *16* (2), 1297–1329. https://doi.org/10.1038/s41596-020-00468-z.

(52) Moura, C. C.; Bourdakos, K. N.; Tare, R. S.; Oreffo, R. O. C.; Mahajan, S. Live-Imaging of Bioengineered Cartilage Tissue Using Multimodal Non-Linear Molecular Imaging. *Sci. Rep.* **2019**, *9* (1), 1–9. https://doi.org/10.1038/s41598-019-41466-w.

(53) Bhosale, A. M.; Richardson, J. B. Articular Cartilage: Structure, Injuries and Review of Management. *Br. Med. Bull.* **2008**, *87* (1), 77–95. https://doi.org/10.1093/bmb/ldn025.

(54) Buckwalter, J. A.; Mow, V. C.; Ratcliffe, A. Restoration of Injured or Degenerated Articular Cartilage. *J. Am. Acad. Orthop. Surg.* **1994**, *2* (4), 192–201. https://doi.org/10.5435/00124635-199407000-00002.

(55) Olumegbon, I. A.; Oloyede, A.; Afara, I. O. Near-Infrared (NIR) Spectroscopic Evaluation of Articular Cartilage: A Review of Current and Future Trends. *Appl. Spectrosc. Rev.* **2017**, *52* (6), 541–559. https://doi.org/10.1080/05704928.2016.1250010.

(56) Esmonde-White, K. A.; Esmonde-White, F. W. L.; Morris, M. D.; Roessler, B. J. Fiber-Optic Raman Spectroscopy of Joint Tissues. *Analyst* **2011**, *136* (8), 1675–1685. https://doi.org/10.1039/c0an00824a.

(57) Quaresima, V.; Ferrari, M.; Scholkmann, F. Ninety Years of Pulse Oximetry : History , Current Status , and Outlook. **2024**, *29*, 1–34. https://doi.org/10.1117/1.JBO.29.S3.S33307.

(58) Kim, J. A.; Wales, D. J.; Yang, G. Z. Optical Spectroscopy for in Vivo Medical Diagnosis — A Review of the State of the Art and Future Perspectives. *Prog. Biomed. Eng.* **2020**, *2* (4), 0–28. https://doi.org/10.1088/2516-1091/abaaa3.

(59) Pozzi, P.; Gandolfi, D.; Porro, C. A.; Bigiani, A.; Mapelli, J. Scattering Compensation for Deep Brain Microscopy: The Long Road to Get Proper Images. *Front. Phys.* **2020**, *8* (February), 1–6. https://doi.org/10.3389/fphy.2020.00026.

(60) Cramer, S. W.; Carter, R. E.; Aronson, J. D.; Kodandaramaiah, S. B.; Ebner, T. J.; Chen, C. C. Through the Looking Glass: A Review of Cranial Window Technology for Optical Access to the Brain. *Journal of Neuroscience Methods*. Elsevier B.V. April 15, 2021, p 109100. https://doi.org/10.1016/j.jneumeth.2021.109100.

(61) Parodi, V.; Jacchetti, E.; Osellame, R.; Cerullo, G.; Polli, D.; Raimondi, M. T. Nonlinear Optical Microscopy: From Fundamentals to Applications in Live Bioimaging. *Front. Bioeng. Biotechnol.* **2020**, *8* (October), 1–18. https://doi.org/10.3389/fbioe.2020.585363.

(62) Wilson, R. H.; Nadeau, K. P.; Jaworski, F. B.; Tromberg, B. J.; Durkin, A. J. Review of Short-Wave Infrared Spectroscopy and Imaging Methods for Biological Tissue Characterization. *J. Biomed. Opt.* **2015**, *20* (3), 030901. https://doi.org/10.1117/1.jbo.20.3.030901.

(63) Filatova, S. A.; Shcherbakov, I. A.; Tsvetkov, V. B. Optical Properties of Animal Tissues in the Wavelength Range from 350 to 2600 Nm. *J. Biomed. Opt.* **2017**, *22* (3), 035009. https://doi.org/10.1117/1.jbo.22.3.035009.

(64) Sordillo, L. A.; Pu, Y.; Pratavieira, S.; Budansky, Y.; Alfano, R. R. Deep Optical Imaging of Tissue Using the Second and Third Near-Infrared Spectral Windows. *J. Biomed. Opt.* **2014**, *19* (5), 056004. https://doi.org/10.1117/1.jbo.19.5.056004.

(65) Shi, L.; Sordillo, L. A.; Rodríguez-Contreras, A.; Alfano, R. Transmission in Near-Infrared

Optical Windows for Deep Brain Imaging. *J. Biophotonics* **2016**, *9* (1–2), 38–43. https://doi.org/10.1002/jbio.201500192.

(66) Sordillo, L. A.; Shi, L.; Sordillo, D.; Sordillo, P.; Alfano, R. R. Advances in Medical Applications Using SWIR Light in the Wavelength Range from 1000 to 2500 Nm. **2019**, No. March 2019, 28. https://doi.org/10.1117/12.2513382.

(67) Bhandari, A.; Hamre, B.; Frette, Ø.; Stamnes, K.; Stamnes, J. J. Modeling Optical Properties of Human Skin Using Mie Theory for Particles with Different Size Distributions and Refractive Indices. *Opt. Express* **2011**, *19* (15), 14549. https://doi.org/10.1364/oe.19.014549.

(68) Xu, M.; Alfano, R. R. *Plum Pudding Random Medium Model of Biological Tissue and Optical Biomedical Imaging in Nir and Swir Spectral Windows*; Elsevier Ltd, 2018. https://doi.org/10.1016/B978-0-323-48067-3.00020-2.

(69) Sordillo, D. C.; Sordillo, L. A.; Sordillo, P. P.; Shi, L.; Alfano, R. R. Short Wavelength Infrared Optical Windows for Evaluation of Benign and Malignant Tissues. *J. Biomed. Opt.* **2017**, *22* (4), 045002. https://doi.org/10.1117/1.jbo.22.4.045002.

(70) Butler, H. J.; Ashton, L.; Bird, B.; Cinque, G.; Curtis, K.; Dorney, J.; Esmonde-White, K.; Fullwood, N. J.; Gardner, B.; Martin-Hirsch, P. L.; Walsh, M. J.; McAinsh, M. R.; Stone, N.; Martin, F. L. Using Raman Spectroscopy to Characterize Biological Materials. *Nat. Protoc.* **2016**, *11* (4), 664–687. https://doi.org/10.1038/nprot.2016.036.

(71) Nicolson, F.; Kircher, M. F.; Stone, N.; Matousek, P. Spatially Offset Raman Spectroscopy for Biomedical Applications. *Chem. Soc. Rev.* **2021**, *50* (1), 556–568. https://doi.org/10.1039/d0cs00855a.

(72) Dooley, M.; Prasopthum, A.; Liao, Z.; Sinjab, F.; McLaren, J.; Rose, F. R. A. J.; Yang, J.; Notingher, I. Spatially-Offset Raman Spectroscopy for Monitoring Mineralization of Bone Tissue Engineering Scaffolds: Feasibility Study Based on Phantom Samples. *Biomed. Opt. Express* **2019**, *10* (4), 1678. https://doi.org/10.1364/boe.10.001678.

(73) Dooley, M.; McLaren, J.; Rose, F. R. A. J.; Notingher, I. Investigating the Feasibility of Spatially Offset Raman Spectroscopy for In-Vivo Monitoring of Bone Healing in Rat Calvarial Defect Models. *J. Biophotonics* **2020**, *13* (10), 1–10. https://doi.org/10.1002/jbio.202000190.

(74) Mazumder, N.; Balla, N. K.; Zhuo, G. Y.; Kistenev, Y. V.; Kumar, R.; Kao, F. J.; Brasselet, S.; Nikolaev, V. V.; Krivova, N. A. Label-Free Non-Linear Multimodal Optical Microscopy—Basics, Development, and Applications. *Front. Phys.* **2019**, *7* (October), 1–26. https://doi.org/10.3389/fphy.2019.00170.

(75) Cheng, J. X.; Xie, X. S. Coherent Anti-Stokes Raman Scattering Microscopy: Instrumentation, Theory, and Applications. *J. Phys. Chem. B* **2004**, *108* (3), 827–840. https://doi.org/10.1021/jp035693v.

(76) Adur, J.; Carvalho, H. F.; Cesar, C. L.; Casco, V. H. Nonlinear Microscopy Techniques: Principles and Biomedical Applications. In *Microscopy and Analysis*; InTech, 2016. https://doi.org/10.5772/63451.

(77) Moura, C. C.; Tare, R. S.; Oreffo, R. O. C.; Mahajan, S. Raman Spectroscopy and Coherent Anti-Stokes Raman Scattering Imaging: Prospective Tools for Monitoring Skeletal Cells and Skeletal Regeneration. *J. R. Soc. Interface* **2016**, *13* (118), 9–11. https://doi.org/10.1098/rsif.2016.0182.

(78) Costa Moura, C.; Lanham, S. A.; Monfort, T.; Bourdakos, K. N.; Tare, R. S.; Oreffo, R. O. C.; Mahajan, S. Quantitative Temporal Interrogation in 3D of Bioengineered Human Cartilage Using Multimodal Label-Free Imaging. *Integr. Biol. (United Kingdom)* **2018**, *10* (10), 635–645. https://doi.org/10.1039/c8ib00050f.

(79) Ferraro, J. R.; Nakamoto, K.; Brown, C. W. Basic Theory. In *Introductory Raman Spectroscopy*; Elsevier, 2003; pp 1–94. https://doi.org/10.1016/B978-012254105-6/50004-4.

(80) Khan, B.; Kafian-Attari, I.; Nippolainen, E.; Shaikh, R.; Semenov, D.; Hauta-Kasari, M.; Töyräs, J.; Afara, I. O. Articular Cartilage Optical Properties in the Near-Infrared (NIR) Spectral Range Vary with Depth and Tissue Integrity. *Biomed. Opt. Express* **2021**, *12* (10), 6066. https://doi.org/10.1364/boe.430053.

(81) Larkin, P. Basic Principles. In *Infrared and Raman Spectroscopy*; Elsevier, 2011; pp 7–25. https://doi.org/10.1016/B978-0-12-386984-5.10002-3.

(82) Pasquini, C. Near Infrared Spectroscopy: A Mature Analytical Technique with New Perspectives – A Review. *Anal. Chim. Acta* **2018**, *1026*, 8–36. https://doi.org/10.1016/j.aca.2018.04.004.

(83) *Combination Bands, Overtones and Fermi Resonances - Chemistry LibreTexts*. https://chem.libretexts.org/Bookshelves/Physical_and_Theoretical_Chemistry_Textbook_Maps/Supplemental_Modules_(Physical_and_Theoretical_Chemistry)/Spectroscopy/Vibrational_Spectroscopy/Vibrational_Modes/Combination_Bands%2C_Overtones_and_Fermi_Resonances (accessed 2021-06-21).

(84) Banwell, C. N. *Fundamentals of Molecular Spectroscopy, Edisi Kedua, McGRAW-Hill Book Company Limited, London.*; 1983.

(85) Smith, E.; Dent, G. *Modern Raman Spectroscopy*; Wiley, 2019. https://doi.org/10.1002/9781119440598.

(86) Tuschel, D. Selecting an Excitation Wavelength for Raman Spectroscopy. *Spectrosc. (Santa Monica)* **2016**, *31* (3).

(87) Hudak, S. J.; Haber, K.; Sando, G.; Kidder, L. H.; Lewis, E. N. Practical Limits of Spatial Resolution in Diffuse Reflectance NIR Chemical Imaging. *NIR news* **2007**, *18* (6), 6–8. https://doi.org/10.1255/nirn.1038.

(88) Sinefeld, D.; Paudel, H. P.; Ouzounov, D. G.; Bifano, T. G.; Xu, C. Adaptive Optics in Multiphoton Microscopy: Comparison of Two, Three and Four Photon Fluorescence. *Opt. Express* **2015**, *23* (24), 31472. https://doi.org/10.1364/oe.23.031472.

(89) Wright, A. J.; Poland, S. P.; Girkin, J. M.; Freudiger, C. W.; Evans, C. L.; Xie, X. S. Adaptive Optics for Enhanced Signal in CARS Microscopy. *Opt. Express* **2007**, *15* (26), 18209. https://doi.org/10.1364/OE.15.018209.

(90) Booth, M. J. Adaptive Optical Microscopy: The Ongoing Quest for a Perfect Image. *Light Sci. Appl.* **2014**, *3* (January), 1–7. https://doi.org/10.1038/lsa.2014.46.

(91) Sahu, P.; Mazumder, N. Improving the Way We See: Adaptive Optics Based Optical Microscopy for Deep-Tissue Imaging. *Front. Phys.* **2021**, *9* (March), 1–8. https://doi.org/10.3389/fphy.2021.654868.

(92) Khalkhal, E.; Rezaei-Tavirani, M.; Zali, M. R.; Akbari, Z. The Evaluation of Laser Application in Surgery: A Review Article. *J. Lasers Med. Sci.* **2019**, *10* (5), S104–S111. https://doi.org/10.15171/jlms.2019.S18.

(93) Schena, E.; Saccomandi, P.; Fong, Y. Laser Ablation for Cancer: Past, Present and Future. *J. Funct. Biomater.* **2017**, *8* (2), 19. https://doi.org/10.3390/jfb8020019.

(94) Vogel, A.; Venugopalan, V. Mechanisms of Pulsed Laser Ablation of Biological Tissues. *Chem. Rev.* **2003**, *103* (2), 577–644. https://doi.org/10.1021/cr010379n.

(95) Hale, G. M.; Querry, M. R. Optical Constants of Water in the 200-Nm to 200-Mm Wavelength Region. *Appl. Opt.* **1973**, *12* (3), 555. https://doi.org/10.1364/AO.12.000555.

(96) Murphy, M. J.; Torstensson, P. A. Thermal Relaxation Times : An Outdated Concept in Photothermal Treatments. **2014**, 973–978. https://doi.org/10.1007/s10103-013-1445-8.

(97) Ravi-Kumar, S.; Lies, B.; Lyu, H.; Qin, H. Laser Ablation of Polymers: A Review. *Procedia Manuf.* **2019**, *34*, 316–327. https://doi.org/10.1016/j.promfg.2019.06.155.

(98) Afara, I. O.; Shaikh, R.; Nippolainen, E.; Querido, W.; Torniainen, J.; Sarin, J. K.; Kandel, S.; Pleshko, N.; Töyräs, J. Characterization of Connective Tissues Using Near-Infrared Spectroscopy and Imaging. *Nat. Protoc.* **2021**, *16* (2), 1297–1329. https://doi.org/10.1038/s41596-020-00468-z.

(99) Prakash, M.; Joukainen, A.; Torniainen, J.; Honkanen, M. K. M.; Rieppo, L.; Afara, I. O.; Kröger, H.; Töyräs, J.; Sarin, J. K. Near-Infrared Spectroscopy Enables Quantitative Evaluation of Human Cartilage Biomechanical Properties during Arthroscopy. *Osteoarthr. Cartil.* **2019**, *27* (8), 1235–1243. https://doi.org/10.1016/j.joca.2019.04.008.

(100) Afara, I. O.; Sarin, J. K.; Ojanen, S.; Finnilä, M. A. J.; Herzog, W.; Saarakkala, S.; Korhonen, R. K.; Töyräs, J. Machine Learning Classification of Articular Cartilage Integrity Using Near Infrared Spectroscopy. *Cell. Mol. Bioeng.* **2020**, *13* (3), 219–228. https://doi.org/10.1007/s12195-020-00612-5.

(101) Unal, M.; Akkus, O. Shortwave-Infrared Raman Spectroscopic Classification of Water Fractions in Articular Cartilage Ex Vivo. *J. Biomed. Opt.* **2018**, *23* (01), 1. https://doi.org/10.1117/1.jbo.23.1.015008.

(102) Lim, N. S. J.; Hamed, Z.; Yeow, C. H.; Chan, C.; Huang, Z. Early Detection of Biomolecular Changes in Disrupted Porcine Cartilage Using Polarized Raman Spectroscopy. *J. Biomed. Opt.* **2011**, *16* (1), 017003. https://doi.org/10.1117/1.3528006.

(103) Oshima, Y.; Kiyomatsu, H.; Miura, H.; Ishimaru, Y.; Hino, K. Evaluation of Degenerative Changes in Articular Cartilage of Osteoarthritis by Raman Spectroscopy. In *Imaging, Manipulation, and Analysis of Biomolecules, Cells, and Tissues XVI*; Farkas, D. L., Nicolau, D. V., Leif, R. C., Eds.; SPIE, 2018; p 45. https://doi.org/10.1117/12.2291383.

(104) Richardson, W.; Wilkinson, D.; Wu, L.; Petrigliano, F.; Dunn, B.; Evseenko, D. Ensemble Multivariate Analysis to Improve Identification of Articular Cartilage Disease in Noisy Raman Spectra. *J. Biophotonics* **2015**, *8* (7), 555–566. https://doi.org/10.1002/jbio.201300200.

(105) Jamil, M.; Dandachli, W.; Noordin, S.; Witt, J. Hip Arthroscopy : Indications , Outcomes and Complications. *Int. J. Surg.* **2018**, *54*, 341–344. https://doi.org/10.1016/j.ijsu.2017.08.557.

(106) Cross, G. W. V.; Sobti, A. S.; Khan, T. Hip Arthroscopy in Osteoarthritis: Is It an Option? *J. Clin. Orthop. Trauma* **2021**, *22*, 101617. https://doi.org/10.1016/j.jcot.2021.101617.

(107) Stone, A. V; Ph, D.; Stubbs, A. J. Arthroscopic Management of Hip Chondral Defects : A Systematic Review of the Literature. *Arthrosc. J. Arthrosc. Relat. Surg.* **2016**, 1–9. https://doi.org/10.1016/j.arthro.2016.01.058.

(108) Sarin, J. K.; te Moller, N. C. R.; Mancini, I. A. D.; Brommer, H.; Visser, J.; Malda, J.; van Weeren, P. R.; Afara, I. O.; Töyräs, J. Arthroscopic near Infrared Spectroscopy Enables Simultaneous Quantitative Evaluation of Articular Cartilage and Subchondral Bone in Vivo. *Sci. Rep.* **2018**, *8* (1), 1–10. https://doi.org/10.1038/s41598-018-31670-5.

(109) Gaifulina, R.; Nunn, A. D. G.; Draper, E. R. C.; Strachan, R. K.; Blake, N.; Firth, S.; Thomas, G. M. H.; McMillan, P. F.; Dudhia, J. Intra-Operative Raman Spectroscopy and Ex Vivo Raman Mapping for Assessment of Cartilage Degradation. *Clin. Spectrosc.* **2021**, *3* (June), 100012. https://doi.org/10.1016/j.clispe.2021.100012.

(110) Esmonde-White, K. Raman Spectroscopy Detection of Molecular Changes Associated with Osteoarthritis. *PhD Thesis, Univ. Michigan.* **2009**, No. June.

(111) Buchwald, T.; Niciejewski, K.; Kozielski, M.; Szybowicz, M.; Siatkowski, M.; Krauss, H. Identifying Compositional and Structural Changes in Spongy and Subchondral Bone from the Hip Joints of Patients with Osteoarthritis Using Raman Spectroscopy. *J. Biomed. Opt.* **2012**, *17* (1), 017007. https://doi.org/10.1117/1.jbo.17.1.017007.

(112) Huang, X.; Teye, E.; Sam-Amoah, L. K.; Han, F.; Yao, L.; Tchabo, W. Rapid Measurement of Total Polyphenols Content in Cocoa Beans by Data Fusion of NIR Spectroscopy and Electronic Tongue. *Anal. Methods* **2014**, *6* (14), 5008–5015. https://doi.org/10.1039/c4ay00223g.

(113) Li, M.; Xue, J.; Du, Y.; Zhang, T.; Li, H. Data Fusion of Raman and Near-Infrared Spectroscopies for the Rapid Quantitative Analysis of Methanol Content in Methanol-Gasoline. *Energy and Fuels* **2019**, *33* (12), 12286–12294. https://doi.org/10.1021/acs.energyfuels.9b03021.

(114) Zhu, S.; Song, Z.; Shi, S.; Wang, M.; Jin, G. Fusion of Near-Infrared and Raman Spectroscopy for in-Line Measurement of Component Content of Molten Polymer Blends. *Sensors (Switzerland)* **2019**, *19* (16). https://doi.org/10.3390/s19163463.

(115) Zhao, Q.; Yu, Y.; Hao, N.; Miao, P.; Li, X.; Liu, C.; Li, Z. Data Fusion of Laser-Induced Breakdown Spectroscopy and Near-Infrared Spectroscopy to Quantitatively Detect Heavy Metals in Lily. *Microchem. J.* **2023**, *190*. https://doi.org/10.1016/j.microc.2023.108670.

(116) Shaikh, R.; Tafintseva, V.; Nippolainen, E.; Virtanen, V.; Solheim, J.; Zimmermann, B.; Saarakkala, S.; Töyräs, J.; Kohler, A.; Afara, I. O. Characterisation of Cartilage Damage via Fusing Mid-Infrared, Near-Infrared, and Raman Spectroscopic Data. *J. Pers. Med.* **2023**, *13* (7), 1–12. https://doi.org/10.3390/jpm13071036.

(117) Huang, Y.; Yang, Y.; Sun, Y.; Zhou, H.; Chen, K. Identification of Apple Varieties Using a Multichannel Hyperspectral Imaging System. *Sensors* **2020**, *20* (18), 5120. https://doi.org/10.3390/s20185120.

(118) Novakovic, D.; Rickert, S.; Blitzer, A. Office-Based Laser Treatment of Oral Premalignant Lesions. *Oper. Tech. Otolaryngol. - Head Neck Surg.* **2011**, *22* (2), 159–164. https://doi.org/10.1016/j.otot.2011.04.002.

(119) Traxer, O.; Keller, E. X. Thulium Fiber Laser: The New Player for Kidney Stone Treatment? A Comparison with Holmium:YAG Laser. *World J. Urol.* **2020**, *38* (8), 1883–1894. https://doi.org/10.1007/s00345-019-02654-5.

(120) Resch, H. M.; Körber, N.; Niehren, S. Next Generation Laser Microdissection : Whole Slide Imaging Meets Laser Microdissection. **2020**, No. September, 1–4.

(121) Jékely, G.; Colombelli, J.; Hausen, H.; Guy, K.; Stelzer, E.; Nédélec, F.; Arendt, D. Mechanism of Phototaxis in Marine Zooplankton. *Nature* **2008**, *456* (7220), 395–399. https://doi.org/10.1038/nature07590.

(122) Colombelli, J.; Reynaud, E. G.; Stelzer, E. H. K. Investigating Relaxation Processes in

Cells and Developing Organisms: From Cell Ablation to Cytoskeleton Nanosurgery; 2007; pp 267–291. https://doi.org/10.1016/S0091-679X(06)82008-X.

(123) Colombelli, J.; Grill, S. W.; Stelzer, E. H. K. Ultraviolet Diffraction Limited Nanosurgery of Live Biological Tissues. *Rev. Sci. Instrum.* **2004**, *75* (2), 472–478. https://doi.org/10.1063/1.1641163.

(124) Van Acker, T.; Buckle, T.; Van Malderen, S. J. M.; van Willigen, D. M.; van Unen, V.; van Leeuwen, F. W. B.; Vanhaecke, F. High-Resolution Imaging and Single-Cell Analysis via Laser Ablation-Inductively Coupled Plasma-Mass Spectrometry for the Determination of Membranous Receptor Expression Levels in Breast Cancer Cell Lines Using Receptor-Specific Hybrid Tracers. *Anal. Chim. Acta* **2019**, *1074*, 43–53. https://doi.org/10.1016/j.aca.2019.04.064.

(125) Malskat, W. S. J.; Stokbroekx, M. A. L.; Van Der Geld, C. W. M.; Nijsten, T. E. C.; Van Den Bos, R. R. Temperature Profiles of 980- and 1,470-Nm Endovenous Laser Ablation, Endovenous Radiofrequency Ablation and Endovenous Steam Ablation. *Lasers Med. Sci.* **2014**, *29* (2), 423–429. https://doi.org/10.1007/s10103-013-1449-4.

(126) Setia, A.; Schmedt, C.-G.; Sroka, R. Endovenous Laser Ablation Using Laser Systems Emitting at Wavelengths > 1900 Nm: A Systematic Review. *Lasers Med. Sci.* **2022**, *37* (9), 3473–3483. https://doi.org/10.1007/s10103-022-03609-w.

(127) Palombi, L.; Morelli, M.; Bruzzese, D.; Martinelli, F.; Quarto, G.; Bianchi, P. G. Endovenous Laser Ablation (EVLA) for Vein Insufficiency: Two-Year Results of a Multicenter Experience with 1940-Nm Laser Diode and a Novel Optical Fiber. *Lasers Med. Sci.* **2024**, *39* (1). https://doi.org/10.1007/s10103-024-04000-7.

(128) Whiteley, M. S.; Cross, A. C.; Whiteley, V. C. No Significant Difference between 1940 and 1470 Nm in Endovenous Laser Ablation Using an in Vitro Porcine Liver Model. *Lasers Med. Sci.* **2022**, *37* (3), 1899–1906. https://doi.org/10.1007/s10103-021-03449-0.

(129) Guney, M.; Tunc, B.; Gulsoy, M. Investigating the Ablation Efficiency of a 1940-Nm Thulium Fibre Laser for Intraoral Surgery. *Int. J. Oral Maxillofac. Surg.* **2014**, *43* (8), 1015–1021. https://doi.org/10.1016/j.ijom.2014.02.010.

(130) Alagha, H. Z.; Gülsoy, M. Photothermal Ablation of Liver Tissue with 1940-Nm Thulium Fiber Laser: An Ex Vivo Study on Lamb Liver . *J. Biomed. Opt.* **2016**, *21* (1), 015007. https://doi.org/10.1117/1.jbo.21.1.015007.

(131) Pal, D.; Paul, A.; Shekhar, N. K.; Chowdhury, S. Das; Sen, R.; Chatterjee, K.; Pal, A. COM Stone Dusting and Soft Tissue Ablation With Q-Switched Thulium Fiber Laser. *IEEE J. Sel. Top. Quantum Electron.* **2019**, *25* (1), 1–8. https://doi.org/10.1109/JSTQE.2018.2854538.

(132) Blackmon, R. L.; Irby, P. B.; Fried, N. M. Comparison of Holmium:YAG and Thulium Fiber Laser Lithotripsy: Ablation Thresholds, Ablation Rates, and Retropulsion Effects. *J. Biomed. Opt.* **2011**, *16* (7), 071403. https://doi.org/10.1117/1.3564884.

(133) Taratkin, M.; Laukhtina, E.; Singla, N.; Tarasov, A.; Alekseeva, T.; Enikeev, M.; Enikeev, D. How Lasers Ablate Stones: In Vitro Study of Laser Lithotripsy (Ho:YAG and Tm-Fiber Lasers) in Different Environments. *J. Endourol.* **2021**, *35* (6), 931–936. https://doi.org/10.1089/end.2019.0441.

(134) Pal, D.; Paul, A.; Shekhar, N. K.; Chowdhury, S. Das; Sen, R.; Chatterjee, K.; Pal, A. COM Stone Dusting and Soft Tissue Ablation with Q-Switched Thulium Fiber Laser. *IEEE J. Sel. Top. Quantum Electron.* **2019**, *25* (1), 1–8. https://doi.org/10.1109/JSTQE.2018.2854538.

(135) Downing, H. D.; Williams, D. Optical Constants of Water in the Infrared. *J. Geophys. Res.* **1975**, *80* (12), 1656–1661. https://doi.org/10.1029/JC080i012p01656.

(136) Serafetinides, A. A.; Makropoulou, M.; Spyratou, E.; Bacharis, C. Alternatives to Excimer Laser Refractive Surgery : UV and Mid-Infrared Laser Ablation of Intraocular Lenses and Porcine Cornea. **2007**, *6604*, 1–13. https://doi.org/https://doi.org/10.1117/12.727214.

(137) Ren, Q.; Venugopalan, V.; Schomacker, K. Mid-Infrared Laser Ablation of the Cornea : A Comparative Study. **1992**, *281*.

(138) Linke, S. J.; Frings, A.; Ren, L.; Gomolka, A.; Schumacher, U.; Reimer, R.; Hansen, N. O.; Jowett, N.; Richard, G.; Miller, R. J. D. A New Technology for Applanation Free Corneal Trephination: The Picosecond Infrared Laser (PIRL). *PLoS One* **2015**, *10* (3), 1–12. https://doi.org/10.1371/journal.pone.0120944.

(139) Amini-Nik, S.; Kraemer, D.; Cowan, M. L.; Gunaratne, K.; Nadesan, P.; Alman, B. A.; Miller, R. J. D. Ultrafast Mid-IR Laser Scalpel: Protein Signals of the Fundamental Limits to Minimally Invasive Surgery. *PLoS One* **2010**, *5* (9), e13053. https://doi.org/10.1371/journal.pone.0013053.

(140) FRIEDRICH, R. E.; QUADE, M.; JOWETT, N.; KROETZ, P.; AMLING, M.; KOHLRUSCH, F. K.; ZUSTIN, J.; GOSAU, M.; SCHLÜTER, H.; MILLER, R. J. D. Ablation Precision and Thermal

Effects of a Picosecond Infrared Laser (PIRL) on Roots of Human Teeth: A Pilot Study Ex Vivo. *In Vivo (Brooklyn)*. **2020**, *34* (5), 2325–2336. https://doi.org/10.21873/invivo.12045.

(141) Zhao, P.; Mondal, S.; Martin, C.; DuPlissis, A.; Chizari, S.; Ma, K.-Y.; Maiya, R.; Messing, R. O.; Jiang, N.; Ben-Yakar, A. Femtosecond Laser Microdissection for Isolation of Regenerating C. Elegans Neurons for Single-Cell RNA Sequencing. *Nat. Methods* **2023**, *20* (4), 590–599. https://doi.org/10.1038/s41592-023-01804-3.

(142) Mangione, F.; D'Antuono, R.; Tapon, N. Photoablation at Single Cell Resolution and Its Application in the Drosophila Epidermis and Peripheral Nervous System. *Front. Physiol.* **2023**, *13*. https://doi.org/10.3389/fphys.2022.1093303.

(143) Zhang, W.; Doherty, M.; Peat, G.; Bierma-Zeinstra, S. M. A.; Arden, N. K.; Bresnihan, B.; Herrero-Beaumont, G.; Kirschner, S.; Leeb, B. F.; Lohmander, L. S.; Mazières, B.; Pavelka, K.; Punzi, L.; So, A. K.; Tuncer, T.; Watt, I.; Bijlsma, J. W. EULAR Evidence-Based Recommendations for the Diagnosis of Knee Osteoarthritis. *Ann. Rheum. Dis.* **2010**, *69* (3), 483–489. https://doi.org/10.1136/ard.2009.113100.

(144) Ryd, L.; Brittberg, M.; Eriksson, K.; Jurvelin, J. S.; Lindahl, A.; Marlovits, S.; Möller, P.; Richardson, J. B.; Steinwachs, M.; Zenobi-Wong, M. Pre-Osteoarthritis. *Cartilage* **2015**, *6* (3), 156–165. https://doi.org/10.1177/1947603515586048.

(145) Sinusas, K. Osteoarthritis: Diagnosis and Treatment. *Am. Fam. Physician* **2012**, *85* (1), 49–56. https://doi.org/10.1136/bmj.1.5222.355-a.

(146) Michael, J. W. P.; Schlüter-Brust, K. U.; Eysel, P. Epidemiologie, Ätiologie, Diagnostik Und Therapie Der Gonarthrose. *Dtsch. Arztebl.* **2010**, *107* (9), 152–162. https://doi.org/10.3238/arztebl.2010.0152.

(147) Gademan, M. G. J.; Hofstede, S. N.; Vliet Vlieland, T. P. M.; Nelissen, R. G. H. H.; Marang-Van de Mheen, P. J. Indication Criteria for Total Hip or Knee Arthroplasty in Osteoarthritis: A State-of-the-Science Overview. *BMC Musculoskelet. Disord.* **2016**, *17* (1), 1–11. https://doi.org/10.1186/s12891-016-1325-z.

(148) Chu, C. R.; Williams, A. A.; Coyle, C. H.; Bowers, M. E. Early Diagnosis to Enable Early Treatment of Pre-Osteoarthritis. *Arthritis Res. Ther.* **2012**, *14* (3), 212. https://doi.org/10.1186/ar3845.

(149) Li, X.; Wang, S.; Liu, W.; Wu, H.; Zhu, Y. Causal Effect of Physical Activity and Sedentary

Behaviors on the Risk of Osteoarthritis : A Univariate and Multivariate Mendelian Randomization Study. *Sci. Rep.* **2023**, 1–10. https://doi.org/10.1038/s41598-023-46984-2.

(150) ElMasry, G.; Nakauchi, S. Prediction of Meat Spectral Patterns Based on Optical Properties and Concentrations of the Major Constituents. *Food Sci. Nutr.* **2016**, *4* (2), 269–283. https://doi.org/10.1002/fsn3.286.

(151) Gaifulina, R.; Nunn, A. D. G.; Draper, E. R. C.; Strachan, R. K.; Blake, N.; Firth, S.; Thomas, G. M. H.; McMillan, P. F.; Dudhia, J. Intra-Operative Raman Spectroscopy and Ex Vivo Raman Mapping for Assessment of Cartilage Degradation. *Clin. Spectrosc.* **2021**, *3* (March), 100012. https://doi.org/10.1016/j.clispe.2021.100012.

(152) Mason, D.; Murugkar, S.; Speirs, A. D. Measurement of Cartilage Sub-component Distributions through the Surface by Raman Spectroscopy-based Multivariate Analysis. *J. Biophotonics* **2021**, *14* (1). https://doi.org/10.1002/jbio.202000289.

(153) Albro, M. B.; Bergholt, M. S.; St-Pierre, J. P.; Vinals Guitart, A.; Zlotnick, H. M.; Evita, E. G.; Stevens, M. M. Raman Spectroscopic Imaging for Quantification of Depth-Dependent and Local Heterogeneities in Native and Engineered Cartilage. *npj Regen. Med.* **2018**, *3* (1), 1–11. https://doi.org/10.1038/s41536-018-0042-7.

(154) Bergholt, M. S.; St-Pierre, J. P.; Offeddu, G. S.; Parmar, P. A.; Albro, M. B.; Puetzer, J. L.; Oyen, M. L.; Stevens, M. M. Raman Spectroscopy Reveals New Insights into the Zonal Organization of Native and Tissue-Engineered Articular Cartilage. *ACS Cent. Sci.* **2016**, *2* (12), 885–895. https://doi.org/10.1021/acscentsci.6b00222.

(155) Raj, P.; Wu, L.; Almeida, C.; Conway, L.; Tanwar, S.; Middendorf, J.; Barman, I. Shining Light on Osteoarthritis: Spatially Offset Raman Spectroscopy as a Window into Cartilage Health. *bioRxiv* **2023**, 2023.08.14.553328. https://doi.org/10.1101/2023.08.14.553328.

(156) Crisford, A.; Cook, H.; Bourdakos, K.; Venkateswaran, S.; Dunlop, D.; Oreffo, R. O. C.; Mahajan, S. Harnessing Raman Spectroscopy and Multimodal Imaging of Cartilage for Osteoarthritis Diagnosis. *medRxiv* **2023**, 2023.09.05.23294936. https://doi.org/10.1101/2023.09.05.23294936.

(157) Crisford, A.; Cook, H.; Bourdakos, K.; Venkateswaran, S.; Dunlop, D.; Oreffo, R. O. C.; Mahajan, S. Harnessing Raman Spectroscopy and Multimodal Imaging of Cartilage for

Osteoarthritis Diagnosis. *Sci. Rep.* **2024**, *14* (1), 31466. https://doi.org/10.1038/s41598-024-83155-3.

(158) Kok, Y. E.; Crisford, A.; Parkes, A.; Venkateswaran, S.; Oreffo, R.; Mahajan, S.; Pound, M. Classification of Osteoarthritic and Healthy Cartilage Using Deep Learning with Raman Spectra. *Sci. Rep.* **2024**, *14* (1), 15902. https://doi.org/10.1038/s41598-024-66857-6.

(159) Houtman, E.; van Hoolwerff, M.; Lakenberg, N.; Suchiman, E. H. D.; van der Linden-van der Zwaag, E.; Nelissen, R. G. H. H.; Ramos, Y. F. M.; Meulenbelt, I. Human Osteochondral Explants: Reliable Biomimetic Models to Investigate Disease Mechanisms and Develop Personalized Treatments for Osteoarthritis. *Rheumatol. Ther.* **2021**, *8* (1), 499–515. https://doi.org/10.1007/s40744-021-00287-y.

(160) Trevisan, J.; Angelov, P. P.; Scott, A. D.; Carmichael, P. L.; Martin, F. L. IRootLab: A Free and Open-Source MATLAB Toolbox for Vibrational Biospectroscopy Data Analysis. *Bioinformatics* **2013**, *29* (8), 1095–1097. https://doi.org/10.1093/bioinformatics/btt084.

(161) Morais, C. L. M.; Lima, K. M. G.; Singh, M.; Martin, F. L. Tutorial: Multivariate Classification for Vibrational Spectroscopy in Biological Samples. *Nat. Protoc.* **2020**, *15* (7), 2143–2162. https://doi.org/10.1038/s41596-020-0322-8.

(162) Devitt, G.; Howard, K.; Mudher, A.; Mahajan, S. Raman Spectroscopy: An Emerging Tool in Neurodegenerative Disease Research and Diagnosis. *ACS Chem. Neurosci.* **2018**, *9* (3), 404–420. https://doi.org/10.1021/acschemneuro.7b00413.

(163) Devitt, G.; Crisford, A.; Rice, W.; Weismiller, H. A.; Fan, Z.; Commins, C.; Hyman, B. T.; Margittai, M.; Mahajan, S.; Mudher, A. Conformational Fingerprinting of Tau Variants and Strains by Raman Spectroscopy. *RSC Adv.* **2021**, *11* (15), 8899–8915. https://doi.org/10.1039/d1ra00870f.

(164) Lister, A. P.; Highmore, C. J.; Hanrahan, N.; Read, J.; Munro, A. P. S.; Tan, S.; Allan, R. N.; Faust, S. N.; Webb, J. S.; Mahajan, S. Multi-Excitation Raman Spectroscopy for Label-Free, Strain-Level Characterization of Bacterial Pathogens in Artificial Sputum Media. *Anal. Chem.* **2022**, *94* (2), 669–677. https://doi.org/10.1021/acs.analchem.1c02501.

(165) Shen, X.; Ye, S.; Xu, L.; Hu, R.; Jin, L.; Xu, H.; Liu, J.; Liu, W. Study on Baseline Correction Methods for the Fourier Transform Infrared Spectra with Different Signal-to-Noise Ratios. *Appl. Opt.* **2018**, *57* (20), 5794. https://doi.org/10.1364/ao.57.005794.

(166) Martyna, A.; Menżyk, A.; Damin, A.; Michalska, A.; Martra, G.; Alladio, E.; Zadora, G. Improving Discrimination of Raman Spectra by Optimising Preprocessing Strategies on the Basis of the Ability to Refine the Relationship between Variance Components. *Chemom. Intell. Lab. Syst.* **2020**, *202* (April). https://doi.org/10.1016/j.chemolab.2020.104029.

(167) Lister, A.; Avershina, E.; Ali, J.; Devitt, G.; Hanrahan, N.; Highmore, C.; Webb, J.; Muller, F.; Mahajan, S.; Ahmad, R. Multi-Excitation Raman Spectroscopy Complements Whole Genome Sequencing for Rapid Detection of Bacterial Infection and Resistance in WHO Priority Pathogens. *bioRxiv* **2022**, 2022.02.08.479540. https://doi.org/10.1101/2022.02.08.479540.

(168) Torniainen, J.; Afara, I. O.; Prakash, M.; Sarin, J. K.; Stenroth, L.; Töyräs, J. Open-Source Python Module for Automated Preprocessing of near Infrared Spectroscopic Data. *Anal. Chim. Acta* **2020**, *1108*, 1–9. https://doi.org/10.1016/j.aca.2020.02.030.

(169) Georgiev, D.; Pedersen, S. V.; Xie, R.; Fernández-Galiana, Á.; Stevens, M. M.; Barahona, M. RamanSPy: An Open-Source Python Package for Integrative Raman Spectroscopy Data Analysis. *Anal. Chem.* **2024**, *96* (21), 8492–8500. https://doi.org/10.1021/acs.analchem.4c00383.

(170) Martin, F. L.; German, M. J.; Wit, E.; Fearn, T.; Ragavan, N.; Pollock, H. M. Identifying Variables Responsible for Clustering in Discriminant Analysis of Data from Infrared Microspectroscopy of a Biological Sample. *J. Comput. Biol.* **2007**, *14* (9), 1176–1184. https://doi.org/10.1089/cmb.2007.0057.

(171) Camilo; Medeiros De Morais, L. Novel Chemometric Approaches towards Handling Biospectroscopy Datasets. **2020**, No. June.

(172) Callery, E. L.; Morais, C. L. M.; Paraskevaidi, M.; Brusic, V.; Vijayadurai, P.; Anantharachagan, A.; Martin, F. L.; Rowbottom, A. W. New Approach to Investigate Common Variable Immunodeficiency Patients Using Spectrochemical Analysis of Blood. *Sci. Rep.* **2019**, *9* (1), 1–15. https://doi.org/10.1038/s41598-019-43196-5.

(173) Owen, A. J. Uses of Derivative Spectroscopy. *Spectroscopy* **1995**, 8.

(174) Liu, C.; Liu, C.; Ren, X.; Si, L.; Shen, H.; Wang, Q.; Yao, W. Quantitative Evaluation of Subchondral Bone Microarchitecture in Knee Osteoarthritis Using 3T MRI. *BMC Musculoskelet. Disord.* **2017**, *18* (1), 496. https://doi.org/10.1186/s12891-017-1865-x.

(175) Nippolainen, E.; Shaikh, R.; Virtanen, V.; Rieppo, L.; Saarakkala, S.; Töyräs, J.; Afara, I. O. Near Infrared Spectroscopy Enables Differentiation of Mechanically and Enzymatically Induced Cartilage Injuries. *Ann. Biomed. Eng.* **2020**, *48* (9), 2343–2353. https://doi.org/10.1007/s10439-020-02506-z.

(176) Sarin, J. K.; Nykänen, O.; Tiitu, V.; Mancini, I. A. D.; Brommer, H.; Visser, J.; Malda, J.; van Weeren, P. R.; Afara, I. O.; Töyräs, J. Arthroscopic Determination of Cartilage Proteoglycan Content and Collagen Network Structure with Near-Infrared Spectroscopy. *Ann. Biomed. Eng.* **2019**, *47* (8), 1815–1826. https://doi.org/10.1007/s10439-019-02280-7.

(177) Linus, A.; Tanska, P.; Sarin, J. K.; Nippolainen, E.; Tiitu, V.; Mäkelä, J. T. A.; Töyräs, J.; Korhonen, R. K.; Mononen, M. E.; Afara, I. O. Visible and Near-Infrared Spectroscopy Enables Differentiation of Normal and Early Osteoarthritic Human Knee Joint Articular Cartilage. *Ann. Biomed. Eng.* **2023**, *51* (10), 2245–2257. https://doi.org/10.1007/s10439-023-03261-7.

(178) Kumar, R.; Singh, G.; Grønhaug, K.; Afseth, N.; de Lange Davies, C.; Drogset, J.; Lilledahl, M. Single Cell Confocal Raman Spectroscopy of Human Osteoarthritic Chondrocytes: A Preliminary Study. *Int. J. Mol. Sci.* **2015**, *16* (12), 9341–9353. https://doi.org/10.3390/ijms16059341.

(179) Hanrahan, N. Label-Free Light Sheet Microscopy for 3D Imaging of Biological Specimens, 2021.

(180) *sif-parser Software*. https://pypi.org/project/sif-parser/.

(181) *python-seabreeze Software*. https://pypi.org/project/sif-parser/.

(182) *py_thorlabs_ctrl Software*. https://github.com/rwalle/py_thorlabs_ctrl.

(183) Edelstein, A. D.; Tsuchida, M. A.; Amodaj, N.; Pinkard, H.; Vale, R. D.; Stuurman, N. Advanced Methods of Microscope Control Using MManager Software. *J. Biol. Methods* **2014**, *1* (2), e10. https://doi.org/10.14440/jbm.2014.36.

(184) Pinkard, H.; Stuurman, N.; Ivanov, I. E.; Anthony, N. M.; Ouyang, W.; Li, B.; Yang, B.; Tsuchida, M. A.; Chhun, B.; Zhang, G.; Mei, R.; Anderson, M.; Shepherd, D. P.; Hunt-Isaak, I.; Dunn, R. L.; Jahr, W.; Kato, S.; Royer, L. A.; Thiagarajah, J. R.; Eliceiri, K. W.; Lundberg, E.; Mehta, S. B.; Waller, L. Pycro-Manager: Open-Source Software for

Customized and Reproducible Microscope Control. *Nat. Methods* **2021**, *18* (3), 226–228. https://doi.org/10.1038/s41592-021-01087-6.

(185) McKinney, W. Data Structures for Statistical Computing in Python; 2010; pp 56–61. https://doi.org/10.25080/Majora-92bf1922-00a.

(186) Schindelin, J.; Arganda-Carreras, I.; Frise, E.; Kaynig, V.; Longair, M.; Pietzsch, T.; Preibisch, S.; Rueden, C.; Saalfeld, S.; Schmid, B.; Tinevez, J.-Y.; White, D. J.; Hartenstein, V.; Eliceiri, K.; Tomancak, P.; Cardona, A. Fiji: An Open-Source Platform for Biological-Image Analysis. *Nat. Methods* **2012**, *9* (7), 676–682. https://doi.org/10.1038/nmeth.2019.

(187) *PolyCam 3D Scanning*. https://poly.cam/.

(188) *Dragonfly Comet Technologies Canada*. https://www.theobjects.com/dragonfly.

(189) Das Gupta, S.; Finnilä, M. A. J.; Karhula, S. S.; Kauppinen, S.; Joukainen, A.; Kröger, H.; Korhonen, R. K.; Thambyah, A.; Rieppo, L.; Saarakkala, S. Raman Microspectroscopic Analysis of the Tissue-Specific Composition of the Human Osteochondral Junction in Osteoarthritis: A Pilot Study. *Acta Biomater.* **2020**, *106*, 145–155. https://doi.org/10.1016/j.actbio.2020.02.020.

(190) Querido, W.; Kandel, S.; Pleshko, N. Applications of Vibrational Spectroscopy for Analysis of Connective Tissues. *Molecules* **2021**, *26* (4), 1–31. https://doi.org/10.3390/molecules26040922.

(191) Young, I.; Zagers, R.; Van Vliet, L.; Mullikin, J.; Boddeke, F.; Netten, H. Depth-of-Focus in Microscopy. *8th Scand. Conf. Image Anal. Tromso, Norw.* **1993**.

(192) Bergholt, M. S.; St-Pierre, J.-P.; Offeddu, G. S.; Parmar, P. A.; Albro, M. B.; Puetzer, J. L.; Oyen, M. L.; Stevens, M. M. Raman Spectroscopy Reveals New Insights into the Zonal Organization of Native and Tissue-Engineered Articular Cartilage. *ACS Cent. Sci.* **2016**, *2* (12), 885–895. https://doi.org/10.1021/acscentsci.6b00222.

(193) Bai, S.; Li, X.; Angeles, J. A Review of Spherical Motion Generation Using Either Spherical Parallel Manipulators or Spherical Motors. *Mech. Mach. Theory* **2019**, *140*, 377–388. https://doi.org/10.1016/j.mechmachtheory.2019.06.012.

(194) Bai, S.; Hansen, M. R.; Andersen, T. O. Modelling of a Special Class of Spherical Parallel Manipulators with Euler Parameters. *Robotica* **2009**, *27* (2), 161–170.

https://doi.org/10.1017/S0263574708004402.

(195) Bai, S. Optimum Design of Spherical Parallel Manipulators for a Prescribed Workspace. *Mech. Mach. Theory* **2010**, *45* (2), 200–211. https://doi.org/10.1016/j.mechmachtheory.2009.06.007.

(196) MAIMAN, T. H. Stimulated Optical Radiation in Ruby. *Nature* **1960**, *187* (4736), 493–494. https://doi.org/10.1038/187493a0.

(197) Krauss, J. M.; Puliafito, C. A.; Steinert, R. F. Laser Interactions with the Cornea. *Surv. Ophthalmol.* **1986**, *31* (1), 37–53. https://doi.org/10.1016/0039-6257(86)90050-0.

(198) Deshmukh, R.; Stevenson, L. J.; Vajpayee, R. B. Laser-Assisted Corneal Transplantation Surgery. *Surv. Ophthalmol.* **2021**, *66* (5), 826–837. https://doi.org/10.1016/j.survophthal.2021.01.009.

(199) Harrington, J. A. *Infrared Fibers and Their Applications*; SPIE, 2004. https://doi.org/10.1117/3.540899.

(200) *Optical-Thermal Response of Laser-Irradiated Tissue*; Welch, A. J., Van Gemert, M. J. C., Eds.; Springer US: Boston, MA, 1995. https://doi.org/10.1007/978-1-4757-6092-7.

(201) Wesendahl, T.; Janknecht, P.; Ott, B.; Frenz, M. Erbium:YAG Laser Ablation of Retinal Tissue under Perfluorodecaline: Determination of Laser-Tissue Interaction in Pig Eyes. *Investig. Ophthalmol. Vis. Sci.* **2000**, *41* (2), 505–512.

(202) Blackmon, R. L.; Irby, P. B.; Fried, N. M. Comparison of Holmium:YAG and Thulium Fiber Laser Lithotripsy: Ablation Thresholds, Ablation Rates, and Retropulsion Effects. *J. Biomed. Opt.* **2011**, *16* (7), 071403. https://doi.org/10.1117/1.3564884.

(203) Blackmon, R. L.; Irby, P. B.; Fried, N. M. Enhanced Thulium Fiber Laser Lithotripsy Using Micro-Pulse Train Modulation. *J. Biomed. Opt.* **2012**, *17* (2), 028002. https://doi.org/10.1117/1.JBO.17.2.028002.

(204) Phelan, R.; O'Carroll, J.; Byrne, D.; Herbert, C.; Somers, J.; Kelly, B. In0.75Ga0.25As/InP Multiple Quantum-Well Discrete-Mode Laser Diode Emitting at 2 Um. *IEEE Photonics Technol. Lett.* **2012**, *24* (8), 652–654. https://doi.org/10.1109/LPT.2012.2185689.

(205) Kobyakov, A.; Sauer, M.; Chowdhury, D. Stimulated Brillouin Scattering in Optical Fibers. *Adv. Opt. Photonics* **2010**, *2* (1), 1. https://doi.org/10.1364/AOP.2.000001.

(206) Keaton, G. L.; Leonardo, M. J.; Byer, M. W.; Richard, D. J. Stimulated Brillouin Scattering of Pulses in Optical Fibers. *Opt. Express* **2014**, *22* (11), 13351. https://doi.org/10.1364/OE.22.013351.

(207) Sincore, A.; Bodnar, N.; Bradford, J.; Abdulfattah, A.; Shah, L.; Richardson, M. C. SBS Threshold Dependence on Pulse Duration in a 2053 Nm Single-Mode Fiber Amplifier. *J. Light. Technol.* **2017**, *35* (18), 4000–4003. https://doi.org/10.1109/JLT.2017.2729508.

(208) Paschotta, R. Gain Switching - an Encyclopedia Article. In *RP Photonics Encyclopedia*; RP Photonics AG, 2007. https://doi.org/10.61835/va1.

(209) Paschotta, R. Spiking - an Encyclopedia Article. In *RP Photonics Encyclopedia*; RP Photonics AG, 2007. https://doi.org/10.61835/cv6.

(210) TRÄGÅRDH, J.; MACRAE, K.; TRAVIS, C.; AMOR, R.; NORRIS, G.; WILSON, S. H.; OPPO, G. -L.; MCCONNELL, G. A Simple but Precise Method for Quantitative Measurement of the Quality of the Laser Focus in a Scanning Optical Microscope. *J. Microsc.* **2015**, *259* (1), 66–73. https://doi.org/10.1111/jmi.12249.

(211) Cheng, R.; Zhang, F.; Li, M.; Wo, X.; Su, Y.-W.; Wang, W. Influence of Fixation and Permeabilization on the Mass Density of Single Cells: A Surface Plasmon Resonance Imaging Study. *Front. Chem.* **2019**, *7*. https://doi.org/10.3389/fchem.2019.00588.

(212) Anderson, R. R.; Parrish, J. A. Selective Photothermolysis: Precise Microsurgery by Selective Absorption of Pulsed Radiation. *Science (80-.).* **1983**, *220* (4596), 524–527. https://doi.org/10.1126/science.6836297.

(213) Kleboe, J.; Szoor-Mcelhinney, H.; Cook, H.; Lane, S.; Hanrahan, N.; Read, J.; Loan, T.; Mahajan, S. From Mars to Humans: Interactive Raman Spectroscopy-Based Outreach Activities. In *Optics Education and Outreach VII*; Gregory, G. G., Poulin-Girard, A.-S., Eds.; SPIE, 2022; p 41. https://doi.org/10.1117/12.2646462.

(214) Bower, C. 2024 Somerscience Festival Evaluation Report. **2024**.

Appendix A Open Licence 3D Models

Femoral Head Model:

"Arthritic femoral head (left), hip capsule and tendon, removed during my total joint replacement by doctorow on Thingiverse: https://www.thingiverse.com/thing:5231333"

"This thing was created by Thingiverse user mdkendall, and is licensed under cc-sa."

Three-Jaw Chuck:

"2.5inch Three Jaw Chuck by mdkendall on Thingiverse: https://www.thingiverse.com/thing:2670620"

"This thing was created by Thingiverse user mdkendall, and is licensed under cc-sa."

Appendix B Micromanager Configuration

“20231002_mm20nightly_goniometer_nikonz_hamm_prior.cfg”

```
# Generated by Configurator on Wed Aug 16 17:57:14 BST 2023

# Reset
Property,Core,Initialize,0

# Devices
Device,COM3,SerialManager,COM3
Device,TIScope,NikonTI,TIScope
Device,TIAnalyzer,NikonTI,TIAnalyzer
Device,TINosePiece,NikonTI,TINosePiece
Device,TIFilterBlock1,NikonTI,TIFilterBlock1
Device,TILightPath,NikonTI,TILightPath
Device,TIZDrive,NikonTI,TIZDrive
Device,TIPFSOffset,NikonTI,TIPFSOffset
Device,TIPFSStatus,NikonTI,TIPFSStatus
Device,HamamatsuHam_DCAM,HamamatsuHam,HamamatsuHam_DCAM
Device,XYStage,Prior,XYStage

# Pre-init settings for devices
Property,COM3,AnswerTimeout,500.0000
Property,COM3,BaudRate,9600
Property,COM3,DTR,Disable
Property,COM3,DataBits,8
Property,COM3,DelayBetweenCharsMs,0.0000
Property,COM3,Fast USB to Serial,Disable
Property,COM3,Handshaking,Off
Property,COM3,Parity,None
Property,COM3,StopBits,1
Property,COM3,Verbose,1
Property,XYStage,Port,COM3

# Pre-init settings for COM ports

# Hub (parent) references
Parent,TIAnalyzer,TIScope
Parent,TINosePiece,TIScope
Parent,TIFilterBlock1,TIScope
Parent,TILightPath,TIScope
Parent,TIZDrive,TIScope
Parent,TIPFSOffset,TIScope
Parent,TIPFSStatus,TIScope

# Initialize
Property,Core,Initialize,1

# Delays

# Focus directions
FocusDirection,TIZDrive,0
```

```
FocusDirection,TIPFSOffset,0

# Roles
Property,Core,Camera,HamamatsuHam_DCAM
Property,Core,Focus,TIZDrive
Property,Core,AutoShutter,1

# Camera-synchronized devices

# Labels
# TINosePiece
Label,TINosePiece,5,6
Label,TINosePiece,4,5
Label,TINosePiece,3,4
Label,TINosePiece,2,3
Label,TINosePiece,1,2
Label,TINosePiece,0,1
# TIFilterBlock1
Label,TIFilterBlock1,5,6
Label,TIFilterBlock1,4,5
Label,TIFilterBlock1,3,4
Label,TIFilterBlock1,2,3
Label,TIFilterBlock1,1,2
Label,TIFilterBlock1,0,1
# TILightPath
Label,TILightPath,3,4-Left80
Label,TILightPath,2,3-Right100
Label,TILightPath,1,2-Left100
Label,TILightPath,0,1-Eye100

# Configuration presets

# PixelSize settings
# Resolution preset: Res0
ConfigPixelSize,Res0,Core,XYStage,XYStage
PixelSize_um,Res0,1.0
PixelSizeAffine,Res0,1.0,0.0,0.0,0.0,1.0,0.0
```

Appendix C Anaconda Environment

“Anaconda Env Backup Goniometer 2.yaml”

```
name: Goniometer2
channels:
 - defaults
dependencies:
 - alabaster=0.7.12=pyhd3eb1b0_0
 - arrow=1.2.3=py311haa95532_1
 - astroid=2.14.2=py311haa95532_0
 - asttokens=2.0.5=pyhd3eb1b0_0
 - atomicwrites=1.4.0=py_0
 - autopep8=1.6.0=pyhd3eb1b0_1
 - babel=2.11.0=py311haa95532_0
 - backcall=0.2.0=pyhd3eb1b0_0
 - bcrypt=3.2.0=py311h2bbff1b_1
 - beautifulsoup4=4.12.2=py311haa95532_0
 - binaryornot=0.4.4=pyhd3eb1b0_1
 - black=23.3.0=py311haa95532_0
 - blas=1.0=mkl
 - bleach=4.1.0=pyhd3eb1b0_0
 - boltons=23.0.0=py311haa95532_0
 - brotli=1.0.9=h2bbff1b_7
 - brotli-bin=1.0.9=h2bbff1b_7
 - brotlipy=0.7.0=py311h2bbff1b_1002
 - bzip2=1.0.8=he774522_0
 - ca-certificates=2023.05.30=haa95532_0
 - certifi=2023.7.22=py311haa95532_0
 - cffi=1.15.1=py311h2bbff1b_3
 - chardet=4.0.0=py311haa95532_1003
 - charset-normalizer=2.0.4=pyhd3eb1b0_0
 - click=8.0.4=py311haa95532_0
 - cloudpickle=2.2.1=py311haa95532_0
 - colorama=0.4.6=py311haa95532_0
 - conda-package-handling=2.2.0=py311haa95532_0
 - conda-package-streaming=0.9.0=py311haa95532_0
 - console_shortcut=0.1.1=4
 - contourpy=1.0.5=py311h59b6b97_0
 - cookiecutter=1.7.3=pyhd3eb1b0_0
 - cryptography=41.0.2=py311h31511bf_0
 - cycler=0.11.0=pyhd3eb1b0_0
 - debugpy=1.6.7=py311hd77b12b_0
 - decorator=5.1.1=pyhd3eb1b0_0
 - defusedxml=0.7.1=pyhd3eb1b0_0
 - diff-match-patch=20200713=pyhd3eb1b0_0
 - dill=0.3.6=py311haa95532_0
 - docstring-to-markdown=0.11=py311haa95532_0
 - docutils=0.18.1=py311haa95532_3
 - entrypoints=0.4=py311haa95532_0
 - executing=0.8.3=pyhd3eb1b0_0
 - flake8=6.0.0=py311haa95532_0
 - fonttools=4.25.0=pyhd3eb1b0_0
```

```
- freetype=2.12.1=ha860e81_0
- giflib=5.2.1=h8cc25b3_3
- glib=2.69.1=h5dc1a3c_2
- gst-plugins-base=1.18.5=h9e645db_0
- gstreamer=1.18.5=hd78058f_0
- icu=58.2=ha925a31_3
- idna=3.4=py311haa95532_0
- imagesize=1.4.1=py311haa95532_0
- importlib-metadata=6.0.0=py311haa95532_0
- importlib_metadata=6.0.0=hd3eb1b0_0
- inflection=0.5.1=py311haa95532_0
- intel-openmp=2023.1.0=h59b6b97_46319
- intervaltree=3.1.0=pyhd3eb1b0_0
- ipykernel=6.25.0=py311h746a85d_0
- ipython=8.12.2=py311haa95532_0
- ipython_genutils=0.2.0=pyhd3eb1b0_1
- isort=5.9.3=pyhd3eb1b0_0
- jaraco.classes=3.2.1=pyhd3eb1b0_0
- jedi=0.18.1=py311haa95532_1
- jellyfish=0.9.0=py311h2bbff1b_0
- jinja2=3.1.2=py311haa95532_0
- jinja2-time=0.2.0=pyhd3eb1b0_3
- jpeg=9e=h2bbff1b_1
- jsonpatch=1.32=pyhd3eb1b0_0
- jsonpointer=2.1=pyhd3eb1b0_0
- jupyter_client=8.1.0=py311haa95532_0
- jupyter_core=5.3.0=py311haa95532_0
```

```
- jupyterlab_pygments=0.1.2=py_0
- keyring=23.13.1=py311haa95532_0
- kiwisolver=1.4.4=py311hd77b12b_0
- krb5=1.19.4=h5b6d351_0
- lazy-object-proxy=1.6.0=py311h2bbff1b_0
- lerc=3.0=hd77b12b_0
- libbrotlicommon=1.0.9=h2bbff1b_7
- libbrotlidec=1.0.9=h2bbff1b_7
- libbrotlienc=1.0.9=h2bbff1b_7
- libclang=14.0.6=default_hb5a9fac_1
- libclang13=14.0.6=default_h8e68704_1
- libdeflate=1.17=h2bbff1b_0
- libffi=3.4.4=hd77b12b_0
- libiconv=1.16=h2bbff1b_2
- libogg=1.3.5=h2bbff1b_1
- libpng=1.6.39=h8cc25b3_0
- libsodium=1.0.18=h62dcd97_0
- libspatialindex=1.9.3=h6c2663c_0
- libtiff=4.5.0=h6c2663c_2
- libvorbis=1.3.7=he774522_0
- libwebp=1.2.4=hbc33d0d_1
- libwebp-base=1.2.4=h2bbff1b_1
- libxml2=2.10.3=h0ad7f3c_0
- libxslt=1.1.37=h2bbff1b_0
- lxml=4.9.2=py311h2bbff1b_0
- lz4-c=1.9.4=h2bbff1b_0
- markupsafe=2.1.1=py311h2bbff1b_0
```

```
- matplotlib=3.7.1=py311haa95532_1
- matplotlib-base=3.7.1=py311hf62ec03_1
- matplotlib-inline=0.1.6=py311haa95532_0
- mccabe=0.7.0=pyhd3eb1b0_0
- menuinst=1.4.19=py311h59b6b97_1
- mistune=0.8.4=py311h2bbff1b_1000
- mkl=2023.1.0=h6b88ed4_46357
- mkl-service=2.4.0=py311h2bbff1b_1
- mkl_fft=1.3.6=py311hf62ec03_1
- mkl_random=1.2.2=py311hf62ec03_1
- more-itertools=8.12.0=pyhd3eb1b0_0
- munkres=1.1.4=py_0
- mypy_extensions=0.4.3=py311haa95532_1
- nbclient=0.5.13=py311haa95532_0
- nbconvert=6.5.4=py311haa95532_0
- nbformat=5.7.0=py311haa95532_0
- nest-asyncio=1.5.6=py311haa95532_0
- numpy-base=1.25.2=py311hd01c5d8_0
- numpydoc=1.5.0=py311haa95532_0
- openssl=1.1.1v=h2bbff1b_0
- packaging=23.0=py311haa95532_0
- pandocfilters=1.5.0=pyhd3eb1b0_0
- paramiko=2.8.1=pyhd3eb1b0_0
- parso=0.8.3=pyhd3eb1b0_0
- pathspec=0.10.3=py311haa95532_0
- pcre=8.45=hd77b12b_0
- pexpect=4.8.0=pyhd3eb1b0_3
```

```
- pickleshare=0.7.5=pyhd3eb1b0_1003
- pillow=9.4.0=py311hd77b12b_0
- pip=23.2.1=py311haa95532_0
- platformdirs=2.5.2=py311haa95532_0
- pluggy=1.0.0=py311haa95532_1
- ply=3.11=py311haa95532_0
- poyo=0.5.0=pyhd3eb1b0_0
- prompt-toolkit=3.0.36=py311haa95532_0
- psutil=5.9.0=py311h2bbff1b_0
- ptyprocess=0.7.0=pyhd3eb1b0_2
- pure_eval=0.2.2=pyhd3eb1b0_0
- pycodestyle=2.10.0=py311haa95532_0
- pycosat=0.6.4=py311h2bbff1b_0
- pycparser=2.21=pyhd3eb1b0_0
- pydocstyle=6.3.0=py311haa95532_0
- pyflakes=3.0.1=py311haa95532_0
- pygments=2.15.1=py311haa95532_1
- pylint=2.16.2=py311haa95532_0
- pylint-venv=2.3.0=py311haa95532_0
- pyls-spyder=0.4.0=pyhd3eb1b0_0
- pynacl=1.5.0=py311h8cc25b3_0
- pyopenssl=23.2.0=py311haa95532_0
- pyparsing=3.0.9=py311haa95532_0
- pyqt=5.15.7=py311hd77b12b_0
- pyqt5-sip=12.11.0=py311hd77b12b_0
- pyqtwebengine=5.15.7=py311hd77b12b_0
- pyrsistent=0.18.0=py311h2bbff1b_0
```

```
- pysocks=1.7.1=py311haa95532_0
- python=3.11.4=h966fe2a_0
- python-dateutil=2.8.2=pyhd3eb1b0_0
- python-fastjsonschema=2.16.2=py311haa95532_0
- python-lsp-black=1.2.1=py311haa95532_0
- python-lsp-jsonrpc=1.0.0=pyhd3eb1b0_0
- python-lsp-server=1.7.2=py311haa95532_0
- python-slugify=5.0.2=pyhd3eb1b0_0
- pytoolconfig=1.2.5=py311haa95532_1
- pytz=2022.7=py311haa95532_0
- pywin32=305=py311h2bbff1b_0
- pywin32-ctypes=0.2.0=py311haa95532_1000
- pyyaml=6.0=py311h2bbff1b_1
- pyzmq=25.1.0=py311hd77b12b_0
- qdarkstyle=3.0.2=pyhd3eb1b0_0
- qstylizer=0.2.2=py311haa95532_0
- qt-main=5.15.2=he8e5bd7_8
- qt-webengine=5.15.9=hb9a9bb5_5
- qtawesome=1.2.2=py311haa95532_0
- qtconsole=5.4.2=py311haa95532_0
- qtpy=2.2.0=py311haa95532_0
- qtwebkit=5.212=h2bbfb41_5
- requests=2.31.0=py311haa95532_0
- rope=1.7.0=py311haa95532_0
- rtree=1.0.1=py311h2eaa2aa_0
- ruamel.yaml=0.17.21=py311h2bbff1b_0
- setuptools=68.0.0=py311haa95532_0
```

```
- sip=6.6.2=py311hd77b12b_0
- six=1.16.0=pyhd3eb1b0_1
- snowballstemmer=2.2.0=pyhd3eb1b0_0
- sortedcontainers=2.4.0=pyhd3eb1b0_0
- soupsieve=2.4=py311haa95532_0
- sphinx=5.0.2=py311haa95532_0
- sphinxcontrib-applehelp=1.0.2=pyhd3eb1b0_0
- sphinxcontrib-devhelp=1.0.2=pyhd3eb1b0_0
- sphinxcontrib-htmlhelp=2.0.0=pyhd3eb1b0_0
- sphinxcontrib-jsmath=1.0.1=pyhd3eb1b0_0
- sphinxcontrib-qthelp=1.0.3=pyhd3eb1b0_0
- sphinxcontrib-serializinghtml=1.1.5=pyhd3eb1b0_0
- spyder=5.4.3=py311haa95532_1
- spyder-kernels=2.4.4=py311haa95532_0
- sqlite=3.41.2=h2bbff1b_0
- stack_data=0.2.0=pyhd3eb1b0_0
- tbb=2021.8.0=h59b6b97_0
- text-unidecode=1.3=pyhd3eb1b0_0
- textdistance=4.2.1=pyhd3eb1b0_0
- three-merge=0.1.1=pyhd3eb1b0_0
- tinycss2=1.2.1=py311haa95532_0
- tk=8.6.12=h2bbff1b_0
- toml=0.10.2=pyhd3eb1b0_0
- tomlkit=0.11.1=py311haa95532_0
- toolz=0.12.0=py311haa95532_0
- tornado=6.3.2=py311h2bbff1b_0
- tqdm=4.65.0=py311h746a85d_0
```

```
- traitlets=5.7.1=py311haa95532_0
- ujson=5.4.0=py311hd77b12b_0
- unidecode=1.2.0=pyhd3eb1b0_0
- urllib3=1.26.16=py311haa95532_0
- vc=14.2=h21ff451_1
- vs2015_runtime=14.27.29016=h5e58377_2
- watchdog=2.1.6=py311haa95532_0
- wcwidth=0.2.5=pyhd3eb1b0_0
- webencodings=0.5.1=py311haa95532_1
- whatthepatch=1.0.2=py311haa95532_0
- wheel=0.38.4=py311haa95532_0
- win_inet_pton=1.1.0=py311haa95532_0
- wrapt=1.14.1=py311h2bbff1b_0
- xz=5.4.2=h8cc25b3_0
- yaml=0.2.5=he774522_0
- yapf=0.31.0=pyhd3eb1b0_0
- zeromq=4.3.4=hd77b12b_0
- zipp=3.11.0=py311haa95532_0
- zlib=1.2.13=h8cc25b3_0
- zstandard=0.19.0=py311h2bbff1b_0
- zstd=1.5.5=hd43e919_0
- pip:
  - anyio==3.7.1
  - argon2-cffi==23.1.0
  - argon2-cffi-bindings==21.2.0
  - async-lru==2.0.4
  - attrs==23.1.0
```

```
  - clr-loader==0.2.5
  - comm==0.1.4
  - dask==2023.8.0
  - docstring-inheritance==2.0.0
  - et-xmlfile==1.1.0
  - fqdn==1.5.1
  - fsspec==2023.6.0
  - ipywidgets==8.1.0
  - isoduration==20.11.0
  - json5==0.9.14
  - jsonschema==4.19.0
  - jsonschema-specifications==2023.7.1
  - jupyter==1.0.0
  - jupyter-console==6.6.3
  - jupyter-events==0.7.0
  - jupyter-lsp==2.2.0
  - jupyter-server==2.7.1
  - jupyter-server-terminals==0.4.4
  - jupyterlab==4.0.5
  - jupyterlab-server==2.24.0
  - jupyterlab-widgets==3.0.8
  - locket==1.0.0
  - ndtiff==2.2.1
  - notebook==7.0.2
  - notebook-shim==0.2.3
  - numpy==1.25.1
  - opencv-python==4.8.0.76
```

```
- openpyxl==3.1.2
- overrides==7.4.0
- pandas==2.0.3
- partd==1.4.0
- prometheus-client==0.17.1
- pyandorsdk2==1.2.0
- pyandorspectrograph==1.2.0
- pycromanager==0.28.1
- python-json-logger==2.0.7
- pythonnet==3.0.1
- pyusb==1.2.1
- pywinpty==2.0.11
- referencing==0.30.2
- rfc3339-validator==0.1.4
- rfc3986-validator==0.1.1
- rpds-py==0.9.2
- seabreeze==2.4.0
- send2trash==1.8.2
- sif-parser==0.3.0
- sniffio==1.3.0
- terminado==0.17.1
- tifffile==2023.12.9
- tzdata==2023.3
- uri-template==1.3.0
- webcolors==1.13
- websocket-client==1.6.1
- widgetsnbextension==4.0.8
```

Appendix D Python Code for 3D Cylindrical HSI

```
# -*- coding: utf-8 -*-
"""
3D Hyperspectral Cylindrical Scan: SWIR and Raman

1. Initialise pycromanager camera, xy-stage
2. Initialise Kinesis (theta)
3. Initialise radius r (z-position and lens height)

4. Define x, theta position list

5. Brightfield scan of sample at fixed radius (z) position

6. SWIR Scan: Background (take gold reference separately)
6.1. Scan through positions (x, theta) list
6.2. Save SWIR with (x, theta, r) position
6.3. Save Hyperspectral Dataframe

7. Switch Modalities

8. Initialise Andor Spectrograph (shutter, slit, grating position)

9. Raman Scan: Background (take standard spectrum for manual x calibration separately)
9.1. Scan through positions (x, theta) list
9.2. Save Raman with (x, theta, r) position
9.3. Save Hyperspectral Dataframe

Once established want each numbered section as a separate python file with functions that
can be called in the main script

@author: Hiro
"""

# ---------- OS and Standard Functions ----------

import os
from datetime import date
import time
from tqdm import tqdm
import numpy as np
import matplotlib.pyplot as plt
import tifffile as tf

def create_subfolder(exp_name):
    """
    Creates subfolder in existing directory where current .py file is

    Parameters
    ----------
    exp_name : str
```

```
    Verbose name of experiment - adds the current date

  Returns
  -------
  subfolder : str
    Subfolder named with current date and experiment name

  """
  subfolder = f"./{date.today()}_{exp_name}"
  if not os.path.exists(subfolder):
    os.makedirs(subfolder)
  print ("Subfolder ready!")
  return subfolder

def wait_for_keyword(keyword):
  """
  Makes a pause in the script for a manual action, requires keyword input

  Parameters
  ----------
  keyword : str
    Case sensitive custom keyword

  Returns
  -------
  None.
```

```
  """
  def get_input():
    """
    Takes use input via keyboard

    Returns
    -------
    None.

    """
    return input(f"Type '{keyword}' and press Enter to continue:")
  # Keep prompting until desired input is received
  while True:
    user_input = get_input()
    if user_input.lower() == keyword.lower():
      break
    else:
      print(f"Invalid input! Please type '{keyword}'")
  # Continue with rest of programme
  print("Continuing with the programme...")
  time.sleep(1.0)

def dance_function():
  """
  Test function, prints some boogie fever

  Returns
```

```
    -------
    None.

    """
    print("\o "); print(" |\\"); print("/ \\"); time.sleep(0.5)
    print(" o "); print("<|>"); print("/ \\"); time.sleep(0.5)
    print(" o/"); print("/| "); print("/ \\"); time.sleep(0.5)
    print(" o "); print("<|>"); print("/ \\"); time.sleep(0.5)

# ---------- Pandas Dataframe Functions ----------
import pandas as pd

# ---------- Pandas Dataframe Functions ----------
# Create pandas data frame to wrangle hyperspectral data

def convert_spectrum_to_dataframe(wvlgth, intnsty, y_pos):
    """
    Want wavelengths as column headings, intensities as row entries, position as index

    Parameters
    ----------
    wvlgth : array
        Wavelengths from spectrometer
    intnsty : array
        Signal valeues from spectrometer
    y_pos : float
        Coordinate value to save as data label

    Returns
    -------
    df_converted : float
        Pandas datafranme with index label from y_pos coordinate value

    """
    # column_string_list = [str(item for item in [x])]
    # print("columns =", column_string_list)
    # df_converted = pd.DataFrame([y], index=[f"{theta}"], columns=column_string_list)
    df_converted = pd.DataFrame([intnsty], index=[f"{y_pos}"], columns=[wvlgth])
    return df_converted

def save_spectrum_to_dataframe(main_df, spectrum_entry):
    """
    Save latest spectrum to main dataframe, append rows with common column headings

    Parameters
    ----------
    main_df : dataframe
        Take in current state of main dataframe
    spectrum_entry : float
        Take in latest spectrum to append to dataframe

    Returns
    -------
    main_df : dataframe
```

```
    Updated main dataframe

    """
    print("Saving Spectrum to Database...")
    # Want to append rows to dataframe with common column headings
    main_df = pd.concat([main_df, spectrum_entry])
    print("Spectrum Saved to Database!")
    return main_df

def save_dataframe_to_csv(df, df_name, folder):
    """
    Save main dataframe as .csv

    Parameters
    ----------
    df : dataframe
        Take in final main dataframe
    df_name : str
        Define name for final .csv containing main data
    folder : str
        Takes in designated folder for saving the data

    Returns
    -------
    None.

    """
    file_path = os.path.join(folder, df_name)
    # Save the DataFrame to a CSV file
    df.to_csv(file_path, index=True)

# ========== 1. INITIALISE PYCROMANAGER ==========
# Micromanager running simultaneously with correct config file
from pycromanager import Core

# ---------- Pycromanager Functions ----------

def initialise_pycromanager(core):
    """
    Start up pycromanager; requires micromanager to be running in background

    Parameters
    ----------
    core : function-like
        Core imported from pycromanager module

    Returns
    -------
    core : function-like
        Renamed micromanager core object MMCore
    xy_device : function-like
        Renamed micromanager stage object XY_stage
    camera_device : function-like
        Renamed micromanager stage object Camera
```

```
    """
    print("========== Initialising PycroManager ==========")
    print("MicroManager Core =", core)
    # Retrieve name for pycro_xy_device
    xy_device = core.get_xy_stage_device()
    print(f"Stage Device = {xy_device}")
    # Retrieve name for pycro_cam_device
    camera_device = core.get_camera_device()
    print(f"Camera Device = {core.get_camera_device()}")
    print("========== PycroManager Ready! ==========")
    return core, xy_device, camera_device

def wait_for_xy_stage(core):
    """
    (Doesn't seem to work) Wait for XY Stage to stop moving

    Parameters
    ----------
    core : function-like
        Core imported from pycromanager module

    Returns
    -------
    None.

    """
    print("Waiting for XY Stage Motion Complete...")
    # core.waitForDeviceType('XYStageDevice')
    time.sleep(2.0)
    print("XY Stage Ready!")

def xy_check_position(core):
    """
    Get current XY position from Prior stage

    Parameters
    ----------
    core : function-like
        Core imported from pycromanager module

    Returns
    -------
    current_x : float
        Absolute X position in um
    current_y : float
        Absolute Y position in um

    """
    print("Getting Current XY Position...")
    current_x = core.get_x_position()
    current_y = core.get_y_position()
    print(f"Current X is = {current_x} um")
    print(f"Current Y is = {current_y} um")
```

```
    return current_x, current_y

def z_check_position(core):
    """
    Get current Z position from Nikon Ti

    Parameters
    ----------
    core : function-like
        Core imported from pycromanager module

    Returns
    -------
    current_z : float
        Absolute Z position in um

    """
    print("Getting Current Z Position...")
    current_z = core.get_position()
    print(f"Current Z is = {current_z} um")
    return current_z

def xy_absolute_move(core, x_abs, y_abs):
    """
    Move to absolute XY position on Prior stage

    Parameters
    ----------
    core : function-like
        Core imported from pycromanager module
    x_abs : float
        Absolute X position coordinate in um
    y_abs : float
        Absolute Y position coordinate in um

    Returns
    -------
    None.

    """
    current_x = core.get_x_position()
    current_y = core.get_y_position()
    print(f"Starting at ({current_x},{current_y})")
    print(f"Aiming for ({x_abs},{y_abs})")
    core.set_xy_position(x_abs,y_abs) # Important for positions to be int()
    # May need to add wait function, or wait for motion finishing etc.
    time.sleep(1.0)
    check_x = core.get_x_position()
    check_y = core.get_y_position()
    print(f"Finishing at ({check_x},{check_y})")

def z_absolute_move(core, z_abs):
    """
    Move to absolute Z position on Nikon Ti
```

```
    Parameters
    ----------
    core : function-like
        Core imported from pycromanager module
    z_abs : float
        Absolute Z position coordinate in um

    Returns
    -------
    None.

    """
    current_z = core.get_position()
    print(f"Starting at ({current_z})")
    print(f"Aiming for ({z_abs})")
    core.set_position(z_abs)
    # May need to add wait function, or wait for motion finishing etc.
    check_z = core.get_position()
    print(f"Finishing at ({check_z})")

def xy_relative_move(core, x_jog, y_jog):
    """
    Relative XY move on Prior stage

    Parameters
    ----------
```

```
    core : function-like
        Core imported from pycromanager module
    x_jog : float
        Relative X move coordinate in um
    y_jog : float
        Relative Y move coordinate in um

    Returns
    -------
    None.
    """
    current_x = core.get_x_position()
    current_y = core.get_y_position()
    print(f"Starting at ({current_x},{current_y})")
    print(f"Moving xy step ({x_jog},{y_jog})")
    core.set_relative_xy_position(x_jog,y_jog)
    # May need to add wait function, or wait for motion finishing etc.
    check_x = core.get_x_position()
    check_y = core.get_y_position()
    print(f"Finishing at ({check_x},{check_y})")

def z_relative_move(core, z_jog):
    """
    Relative Z move on Nikon Ti

    Parameters
    ----------
```

```
    core : function-like
        Core imported from pycromanager module
    z_jog : float
        Relative Z move coordinate in um

    Returns
    -------
    None.

    """
    current_z = core.get_position()
    print(f"Starting at ({current_z})")
    print(f"Moving z step ({z_jog})")
    core.set_relative_position(z_jog)
    # May need to add wait function, or wait for motion finishing etc.
    check_z = core.get_position()
    print(f"Finishing at ({check_z})")

def brightfield_initialise(core):
    """
    Initialise Hamamatsu Camera via pycromanager

    Parameters
    ----------
    core : function-like
        Core imported from pycromanager module
```

```
    Returns
    -------
    None.

    """
    core.initialize_device("HamamatsuHam_DCAM")
    print ("Hamamatsu Camera Initialised")

def brightfield_snap(core):
    """
    Snaps image data with Hamamatsu, retrieves image tags and reshapes into image

    Parameters
    ----------
    core : function
        Core imported from pycromanager module

    Returns
    -------
    pixels : array
        2D Array of image data from Hamamatsu camera
    tagged_image_height : int
        Image height in pixels
    tagged_image_width : int
        Image width in pixels

    """
```

```
    print("Snapping Image with Hamamatsu...")
    core.snap_image()
    # Produce numpy array of camera image
    tagged_image = core.get_tagged_image()
    tagged_image_height = tagged_image.tags['Height']
    tagged_image_width = tagged_image.tags['Width']
    # Must import numpy as np
    pixels = np.reshape(tagged_image.pix,
newshape=[tagged_image_height,tagged_image_width])
    print ("Image Captured, Exported as Array!")
    # Return numpy array of pixel values
    return pixels, tagged_image_height, tagged_image_width

def brightfield_view_save(image_array, exp_name, image_name, x_pos, theta_pos,
view_bool, tiff_bool):
    """
    Take image data array (Hamamatsu) and saves with position metadata in title

    Parameters
    ----------
    image_array : array
        Take in image data from camera (Hamamatsu)
    exp_name : str
        Defines subfolder from overall experiment name - keep the same
    image_name : str
        Name to save image file under
    x_pos : float
        X position to name image file (metadata in title)
    y_pos : float
        Y position to name image file (metadata in title)
    view_bool : bool
        True = view in terminal; False = don't view - may be necessary for saving as employs
imshow (possible bug, keep as True)
    tiff_bool : bool
        True = save as TIFF file; False = don't save as TIFF

    Returns
    -------
    None.

    """
    folder = create_subfolder(exp_name)
    file_path = os.path.join(folder, image_name)
    # Take brightfield image as numpy array
    # Must import matplotlib.pyplot as plt
    if view_bool:

        plt.title(f"{exp_name}_{image_name}: x={x_pos} um theta={theta_pos} um")
        plt.imshow(image_array)
    print("Saving as .png ...")
    plt.imsave(f'{file_path}_x_{int(x_pos)}um_{int(theta_pos)}deg.png', image_array)
    if tiff_bool:
        # Must import tifffile as tf
        print("Saving as .tif ...")
```

```
    tf.imwrite(f"{file_path}_x_{int(x_pos)}um_{int(theta_pos)}deg.tif", image_array)
    print ("Hamamatsu Images Saved!")



# ---------- Pycromanager Initialise ----------
# Get object representing micro-manager core
# Also define pycromanager device labels for Prior Stage and Hamamatsu Camera
MM_Core, XY_Stage, Camera = initialise_pycromanager(Core())

# ========== 2. INITIALISE KINESIS ==========
# ---------- Kinesis Modules ----------

import py_thorlabs_ctrl.kinesis # Import rwalle's frontend module
# init function automatically determines if the installation path is valid
# This must contain Thorlabs.MotionControl.Controls.dll
py_thorlabs_ctrl.kinesis.init(r'C:\Program Files\Thorlabs\Kinesis')
# Import module from downloaded github folders
# Seems to have nested classes: KCubeDCServo(KCubeMotor(Motor)))
from py_thorlabs_ctrl.kinesis.motor import KCubeDCServo

# ---------- Rotation Stage Functions ----------
def initialise_rotation_stage(ser_no):
    """
    Initialise Kinesis KCube and create stage object

    Parameters
    ----------
```

```
    ser_no : int
        Serial no. of KCube

    Returns
    -------
    stage : object
        KCube object with functions such as home etc.

    """
    print( "========== Initialising Kinesis ==========")
    stage = KCubeDCServo(ser_no)
    print("Kinesis Initialised!")
    return stage

def enable_rotation_stage(rot_device):
    """
    Create and Enable KCube (Initialise, Start Polling, Enable, Load Motor Config)

    Parameters
    ----------
    rot_device : function-like
        Callable KCube object

    Returns
    -------
    None.
```

```
    """
    print("Creating KCube Controller...")
    rot_device.create()
    print("Controller Created!")
    print("Enabling KCube Controller...")
    rot_device.enable()
    print(f"Enabled K-Cube Named {rot_device.get_name()}, Serial
No.{rot_device.get_serial_number()}")

def home_rotation_stage(rot_device):
    """
    Home KCube: Check if homed, visualise homing, and confirm

    Parameters
    ----------
    rot_device : function-like
        Callable KCube object

    Returns
    -------
    None.

    """
    # Check whether the rotation stage is homed: True/False?
    print(f"Homed? {rot_device.is_homed()}")
    if not rot_device.is_homed():
        print("Start Homing")
        rot_device.home()
        #  Visualise as rotation stage is homing
        while not rot_device.is_homed():
            # Check if rotation stage is busy / still moving
            print (f"Homing... Moving? {rot_device.is_moving()}; Position =
{rot_device.get_position()}")
            time.sleep(0.5)

    time.sleep(1.0)
    print(f"========== Now Homed! Position = {rot_device.get_position()} ==========")

def disable_rotation_stage(rot_device):
    """
    Disable KCube Controller before turning off

    Parameters
    ----------
    rot_device : function-like
        Callable KCube object

    Returns
    -------
    None.

    """
    # Disable Device
    print ("Disabling KCube Controller...")
```

```
    rot_device.disable()
    print("Disabled KCube Controller!")
    time.sleep(1.0)

def disconnect_rotation_stage(rot_device):
    """
    Disconnect KCube from PC

    Parameters
    ----------
    rot_device : funciton-like
        Callable KCube object

    Returns
    -------
    None.

    """
    # Disconnect Device
    print("Disconnecting KCube Controller...")
    rot_device.disconnect()
    print("Disconnected KCube Controller!")
    time.sleep(1.0)

def set_vel_accel_rotation_stage(rot_device, max_velocity, acceleration):
    """
    Set max velocity and acceleration parameters for rotation stage

    Parameters
    ----------
    rot_device : function-like
        Callable KCube object
    max_velocity : float
        Define max velocity in degrees/sec
    acceleration : float
        Define acceleration in degrees/sec/sec

    Returns
    -------
    current_velo : float
        Newly defined velocity value
    current_accel : float
        Newly defined acceleration value

    """
    # Backend: set_velocity function seems to have bug with undefined "params" - replaced
with velocity_params
    print(f"Setting max velocity to {max_velocity}, acceleration to {acceleration}")
    rot_device.set_velocity(max_velocity, acceleration)
    # Confirm whether velocity parameters set properly
    current_velo = rot_device.get_velocity()
    current_accel = rot_device.get_accelaration()
    print(f"Velocity set to {current_velo}, Accel set to {current_accel}")
    time.sleep(1.0)
```

```
    return current_velo, current_accel

def theta_check_position(rot_device):
    """
    Check current theta position from KCube

    Parameters
    ----------
    rot_device : funciton-like
        Callable KCube object

    Returns
    -------
    current_pos : float
        Current theta position (degrees)

    """
    current_pos = rot_device.get_position()
    return current_pos

def wait_for_theta_stage(rot_device):
    """
    Wait for KCube to stop moving; if true wait 0.1 sec

    Parameters
    ----------
    rot_device : function-like
        Callable KCube object

    Returns
    -------
    None.

    """
    while rot_device.is_moving():
        print(f"Still Moving; now at {rot_device.get_position()}")
        time.sleep(0.1)

def theta_absolute_move(theta_position, rot_device):
    """
    Move to absolute theta position on KCube; wait for stage to start moving before polling position

    Parameters
    ----------
    theta_position : float
        Theta value (degrees) to move round to
    rot_device : function-like
        Callable KCube object

    Returns
    -------
    None.
```

```
    """
    rot_device.move_absolute(theta_position)
    # Important to let stage start moving before polling whether it is moving
    time.sleep(2.0)

# ---------- Kinesis Rotation Stage Initialise----------
try:
    # Serial number of KCube
    kcube_serial = 27264246
    KCube = initialise_rotation_stage(kcube_serial)
    # Create K-Cube controller instance
    enable_rotation_stage(KCube)
    # Set max velocity and acceleration parameters for rotation stage
    velocity = 20.0
    acceleration = 10.0
    set_velocity, set_acceleration = set_vel_accel_rotation_stage(KCube, velocity,
acceleration)

    # Kinesis Stage Homing
    # Check position - seems to return the value in degrees
    check_theta_once = theta_check_position(KCube)
    print(f"What's the position? At {check_theta_once}")
    #  Home Rotation Stage
    home_rotation_stage(KCube)

    # Wait a bit
    print("Waiting for 2 seconds...")
    time.sleep(2.0)

except Exception as e:
    print(f"UH OH! An error occurred in KCube: {e}")

    print ("Shutting Down KCube...")
    # Disable Rotation Stage
    disable_rotation_stage(KCube)

    # Disconnect Rotation Stage
    disconnect_rotation_stage(KCube)

print("========== Kinesis Rotation Stage Ready! ==========")


# ========== 3. INITIALISE RADIUS r VALUE ==========

# ---------- Radius value functions ----------
def get_radius_value(spacer_height_c, z_position, origin_f):
    """
    Get radius position (distance of focal volume from axis of rotation)

    Parameters
    ----------
    spacer_height_c : float
        Lens tube height (cm) to raise objective lens
    z_position : float
        Z position of Nikon Ti
```

```
    origin_f : float
        Default = 136.9 cm; Total distance between bottom of Nikon Ti to axis of rotation

    Returns
    -------
    r_position : float
        Radius value from axis of rotation (cm)

    """
    while True:
        try:
            c_value = float(input(spacer_height_c))
            print(f"You entered: c= {c_value} mm")
            lens_height = z_position*0.001 + c_value + 24.0 + 38.6
            print(f"So lens height: h = {lens_height} mm")
            r_position = origin_f - lens_height
            print(f"So r position value: r = {r_position} mm")

            return r_position
        except ValueError:
            print("Invalid input. Please enter a valid float value.")

def manual_focus_pause(core, get_z_keyword, dance_keyword, continue_keyword):
    """
    Pause script to allow manual focusing using camera feed in micromanager

    Parameters
    ----------
    core : function-like
        Core imported from pycromanager module
    get_z_keyword : str
        Custom keyword to trigger reading of Z position on Nikon Ti
    dance_keyword : str
        Custom keyword to initiate boogie time
    continue_keyword : str
        Custom keyword to allow rest of script to run

    Returns
    -------
    optimal_z : float
        Record Z position as recorded from camera - use to calculate radius r

    """
    optimal_z = None
    print("Manually focus camera to acheive optimal z position!")
    while True:
        user_input = input(f"Enter '{get_z_keyword}' to capture focused z position,
'{dance_keyword}' to perform a dance, or '{continue_keyword}' to carry on script:
").strip().lower()
        if user_input == get_z_keyword.lower():
            print("Capturing z position...")
            optimal_z = z_check_position(core)
            print(f"Optimal z position saved as {optimal_z}. Happy?")
```

```
    elif user_input == dance_keyword.lower():
        # Perform operation 2 (displaying a little dance)
        print("Performing a little dance for you...")
        dance_function()
        print("Dance completed!")
    elif user_input == continue_keyword.lower():
        # Continue script
        print("Continuing script...")
        break
    else:
        print(f"Invalid input. Enter '{get_z_keyword}' to capture focused z position,
'{dance_keyword}' to perform a dance, or '{continue_keyword}' to carry on script: ")

  return optimal_z

origin_f = 136.9 # mm

current_z_position = z_check_position(MM_Core)
cylinder_radius_global = get_radius_value("Enter the spacer height (c) mm: ",
current_z_position, origin_f)

# ========== 4. DEFINE X, THETA POSITIONS ==========

# ---------- EXPERIMENT NAME ----------
# Global experiment name without date
experiment_name_global = "F57_OA_5"
```

```
# ---------- Cylinder Acquisition Parameters ----------
number_of_theta_steps = 8
starting_x_position = 1000
finishing_x_position = -6000
number_of_x_steps = 15
check_x, starting_y_position = xy_check_position(MM_Core)
# Move Prior stage back to first position
print("Move to first position (x, fixed y)")
xy_absolute_move(MM_Core, int(starting_x_position), int(starting_y_position))

def make_cylindrical_position_list(th_step_no, x_start, x_finish, x_step_no):
  """
  Make list of theta and x positions to iterate through for cylindrical scan

  Parameters
  ----------
  th_step_no : int
    Total number of positions for rotation in theta
  x_start : float
    Starting stage position (um)
  x_finish : float
    Sinishing stage position (um)
  x_step_no : int
    Total number of positions for x translation

  Returns
  -------
```

```
    th_pos_list : float
        Array of absolute theta positions (degrees)
    x_pos_list : float
        Array of absolute x positions (um)

    """
    # Define theta position list
    th_pos_list = np.linspace(0, 360, th_step_no)
    # Define x position list
    x_pos_list = np.linspace(x_start, x_finish, x_step_no)

    return th_pos_list, x_pos_list


THETA_POSITIONS_LIST, X_POSITIONS_LIST =
make_cylindrical_position_list(number_of_theta_steps, starting_x_position,
finishing_x_position, number_of_x_steps)

# ========== 5. CYLINDRICAL BRIGHTFIELD IMAGE SCAN ==========
# Iterate through x and theta positions for brightfield tile scan
# ---------- CYLINDRICAL BRIGHTFIELD FUNCTION ----------
def BRIGHTFIELD_3D_CYLINDER_SCAN(pycro_core, rot_device, x_coords, theta_coords,
r_value):
    """
    Iterate through x, theta position lists and snap an image with Hamamatsu, image file
named with coordinates x, theta, r

    Parameters
```

```
    ----------
    pycro_core : function-like
        Core imported from pycromanager module
    rot_device : function-like
        Callable KCube object
    x_coords : float
        Array of x positions defined previously from make_cylindrical_position_list() function
    theta_coords : float
        Array of theta positions defined previously from make_cylindrical_position_list() function
    r_value : float
        Radius value calculated from previous get_radius_value() function

    Returns
    -------
    ORIGIN_X : float
        Starting x position
    FIXED_Y : TYPE
        Starting y position, fixed for cyliindrical scan

    """
    # Snap and save image at starting x, theta position (origin)
    origin_image_data, full_height, full_width = brightfield_snap(pycro_core)
    ORIGIN_X, FIXED_Y = xy_check_position(pycro_core)
    current_theta = theta_check_position(rot_device)
    brightfield_view_save(origin_image_data, experiment_name_global, "Origin_FOV",
ORIGIN_X, current_theta, True, True)
```

```
  # For each x position
  for X_POSITION in tqdm(x_coords, desc='Total X Positions', unit='x'):
    print(f"\rWorking on X: {X_POSITION} um ", flush=True)
    time.sleep(1.0)  # Wait for Stage Movement

    for THETA_POSITION in tqdm(theta_coords, desc='Total Theta Positions', unit='theta'):
      print(f"\rCapturing X: {X_POSITION} um; Theta Position: {THETA_POSITION} º",
flush=True)
      # Check current theta position
      current_theta = theta_check_position(rot_device)
      # Check current x position
      current_x, current_y = xy_check_position(pycro_core)
      print(f"Currently at theta={current_theta}º, x={current_x}")

      each_position_image_data, full_height, full_width = brightfield_snap(pycro_core)
      brightfield_view_save(each_position_image_data, experiment_name_global,
f"Brightfield_R={r_value}", X_POSITION, current_theta, True, False)

      # Move to next theta position
      print("Move to next theta position...")
      theta_absolute_move(THETA_POSITION, rot_device)
      wait_for_theta_stage(rot_device)
      print(f"Now at position: {theta_check_position(rot_device)}º")

    # Move to next x
    print("Move to next x position...")
    xy_absolute_move(pycro_core, X_POSITION, FIXED_Y)
    wait_for_xy_stage(pycro_core)
    x_check, y_check = xy_check_position(pycro_core)
    print(f"Now at position: {x_check} x position")

  print ("All positions reached!")
  return ORIGIN_X, FIXED_Y

# ---------- CARRY OUT BRIGHTFIELD SCAN ----------
print("========== STARTING UP BRIGHTFIELD SCAN ==========")
ORIGIN_X, ORIGIN_Y = BRIGHTFIELD_3D_CYLINDER_SCAN(MM_Core, KCube,
X_POSITIONS_LIST, THETA_POSITIONS_LIST, cylinder_radius_global)

# Move Prior stage back to first position
print("Moving back to first position (x, fixed y)")
xy_absolute_move(MM_Core, int(ORIGIN_X), int(ORIGIN_Y))

print("========== FINISHED BRIGHTFIELD SCAN ==========")
plt.close()    # Ctch and close any remaining graphs


# ========== 6. CYLINDRICAL SWIR SCAN ==========
print("GET READY for SWIR spectral capture...")
print("Switch kinematic cube for SWIR beampath...")
wait_for_keyword("swir")   # Wait for "swir" keyword before continuing
#  Initialise SWIR Spectrometer
# ---------- Ocean Optics Modules ----------
import seabreeze.spectrometers as sb
```

```
# Can call dictionary of supported features via
sb.Spectrometer.from_serial_number(spectrometer_serial).features

# ---------- SWIR Ocean Optics Spectrometer Functioncs ----------
# Initialise: Look for devices, Connect, Define spectrometer to use

def look_for_spectrometers():
    """
    Searches for spectrometer and prints as list, raised error if none connected

    Raises
    ------
    ValueError
        DESCRIPTION.

    Returns
    -------
    None.

    """
    print("Looking for Ocean Optics spectrometers...")
    devices_list = sb.list_devices()
    if not devices_list:
        raise ValueError("No Ocean Optics spectrometer found!")
    print(f"Devices List = {devices_list}")

def initialise_spectrometer(ser_no):
    """
    Initialise specific OO spectrometer via serial number: NIRQuest = "NQ25B0171", USB2K =
"USB2+R00019"

    Parameters
    ----------
    ser_no : str
        Serial no. NIRQuest = "NQ25B0171", USB2K = "USB2+R00019"

    Returns
    -------
    spectrometer : function-like
        Callable Ocean Optics spectrometer object

    """
    spectrometer = sb.Spectrometer.from_serial_number(ser_no)
    print(f"Chosen spectrometer {spectrometer}")

    return spectrometer

def close_spectrometer(spec_device):
    """
    Disconnect and close spectrometer

    Parameters
    ----------
    spec_device : funciton-like
```

```
    Callable Ocean Optics spectrometer object

  Returns
  -------
  None.

  """
  print("Closing Spectrometer...")
  spec_device.close()
  time.sleep(1.0)
  print ("Spectrometer Closed!")

# Set integration time in milliseconds
def set_integration_time(spec_device, milsec):
  """
  Set integration time of Ocean Optics spectrometer (ms)

  Parameters
  ----------
  spec_device : object
    Callable Ocean Optics spectrometer object
  milsec : int
    Integration time in ms

  Returns
  -------
  None.
  """
  spec_device.integration_time_micros(milsec * 1000)
  print(f"Integration time set to {milsec} ms")

# Grab wavelength and intensity
def capture_spectrum(spec_device):
  """
  Capture spectrum from Ocean Optics spectrometer

  Parameters
  ----------
  spec_device : object
    Callable Ocean Optics spectrometer object

  Returns
  -------
  x : float
    Array of wavelengths
  y : float
    Array of intensities

  """
  print("Capturing Spectrum...")
  x = spec_device.wavelengths()
  y = spec_device.intensities()
  print("Spectrum Captured!")
```

```
    return x, y

def capture_averaged_spectrum(spec_device, no_of_averages):
    """
    Capture averaged spectrum from Ocean Optics spectrometer

    Parameters
    ----------
    spec_device : object
        Callable Ocean Optics spectrometer object
    no_of_averages : int
        Number of captures to average over

    Returns
    -------
    wavelengths : float
        Array of wavelengths
    average_spectrum : float
        Array of averaged intensities

    """
    print(f"Capturing average of {no_of_averages}")
    wavelengths = spec_device.wavelengths()
    accummulated_spectra = spec_device.intensities()
    for i in range(no_of_averages-1):
        accummulated_spectra += spec_device.intensities()
    average_spectrum = accummulated_spectra/no_of_averages
    return wavelengths, average_spectrum

def capture_bkgd(spec_device, no_of_averages, keyword_1, keyword_2, keyword_continue):
    """
    Perform background spectra capture with Ocean Optics; manual pause and keyword entry
to allow turning on/off lamp

    Parameters
    ----------
    spec_device : function-like
        Callable Ocean Optics spectrometer object
    no_of_averages : int
        Number of captures to average over
    keyword_1 : str
        Keyword to trigger (or re-trigger) background spectrum capture
    keyword_2 : str
        Keyword to initiate a boogie
    keyword_continue : str
        Keyword to allow script to continue

    Returns
    -------
    y_bkgd : float
        Array of background signal from Ocean Optics

    """
    y_bkgd = None
```

```
    print("Ready to Capture SWIR Background!")
    while True:
        user_input = input(f"Enter '{keyword_1}' to perform dark background capture, '{keyword_2}' to perform a dance, or '{keyword_continue}' to carry on script, spectral capture starts immediately:")
        if user_input == keyword_1.lower():
            print("Performing dark background capture...")
            # x_bkgd = spec_device.wavelengths()
            # y_bkgd = spec_device.intensities()

            x_bkgd, y_bkgd = capture_averaged_spectrum(spec_device, no_of_averages)
            print("Plotting dark background...")
            plt.plot(x_bkgd, y_bkgd)
            plt.title("Dark SWIR Background")
            plt.xlabel('Wavelength (nm)')
            plt.ylabel('Intensity')
            plt.grid(True)
            plt.show()
            print("What do you think?")

        elif user_input == keyword_2.lower():
            # Perform operation 2 (displaying a little dance)
            print("Performing a little dance for you...")
            dance_function()
            print("Dance completed!")

        elif user_input == keyword_continue.lower():
            # Continue script
            print("Continuing script...")
            break
        else:
            print(f"Invalid input. Enter '{keyword_1}' to perform dark background capture, '{keyword_2}' to perform a dance, or '{keyword_continue}' to carry on script:")
    return y_bkgd

def capture_bkgd_corr_spectrum(spec_device, no_of_averages, bkgd_intens, exp):
    """
    Capture averaged spectrum from Ocean Optics and subtract the averaged background signal; return arrays of wavel and intens

    Parameters
    ----------
    spec_device : function-like
        Callable Ocean Optics spectrometer object
    no_of_averages : int
        Number of captures to average over
    bkgd_intens : array
        Array of background signal from Ocean Optics
    exp : str
        Defines subfolder from overall experiment name - keep the same

    Returns
    -------
    x_corr : array
```

```
    Array of wavelengths from Ocean Optics
y_corr : array
    Array of background corrected intensities from Ocean Optics

"""
print("Capturing Spectrum...")

x, y = capture_averaged_spectrum(spec_device, no_of_averages)

print("Spectrum Captured!")
plt.plot(x, y, label="Raw")
plt.plot(x, bkgd_intens, label="Dark Background")
# plt.title("Raw SWIR Intensity")
plt.xlabel('Wavelength (nm)')
plt.ylabel('Intensity')
# plt.grid(True)
# plt.show()

print("Subtracting Background...")
x_corr = x
y_corr = (y - bkgd_intens)
print("Background Corrected!")
plt.plot(x_corr, y_corr, label="Corrected")
plt.title(f"Background Corrected SWIR Intensity; {exp} ms, {no_of_averages} Average")
plt.xlabel('Wavelength (nm)')
plt.ylabel('Intensity')
plt.legend(loc="upper right")
plt.grid(True)
plt.show()
return x_corr, y_corr

def save_spectrum(x, y, filename, folder):
    """
    Save wavelength and intensities arrays to .csv file in subfolder

    Parameters
    ----------
    x : array
        Wavelength values
    y : array
        Intensity values
    filename : str
        .csv filename, should store some metadata here (no date added here)
    folder : str
        Subfolder to save .csv to

    Returns
    -------
    None.

    """
    print("Saving Spectrum to File...")

    file_path = os.path.join(folder, filename)
```

```
    with open(file_path, 'w') as file: #Open file and put in writing mode
        file.write("Wavelength (nm), Intensity\n")
        for wavel, inten in zip(x,y):
            file.write(f"{wavel}, {inten}\n")
    print("Spectrum Saved to File!")

# Plot spectrum and show graph
def plot_spectrum(x ,y, milsec, avg, spec_device, png_name, x_coord, theta_coord, folder):
    """
    Plot and Save graph of spectrum, metadata recorded in filename

    Parameters
    ----------
    x : array
        Wavelength values
    y : array
        Intensity values
    milsec : TYPE
        DESCRIPTION.
    avg : TYPE
        DESCRIPTION.
    spec_device : TYPE
        DESCRIPTION.
    png_name : TYPE
        DESCRIPTION.
    x_coord : TYPE
        DESCRIPTION.
    theta_coord : TYPE
        DESCRIPTION.
    folder : TYPE
        DESCRIPTION.

    Returns
    -------
    None.

    """
    print("Plotting Spectrum...")
    plt.plot(x, y)
    plt.xlabel('Wavelength (nm)')
    plt.ylabel('Intensity')
    plt.title(f"SWIR at {x_coord} um, {theta_coord} º, Exp: {milsec} ms , {avg} Average")
    plt.grid(True)
    # plt.text(f"From {spec_device}")
    file_path = os.path.join(folder, png_name)
    plt.savefig(file_path)
    print("Spectrum Plotted!")
    plt.show()

# ========== 6. CYLINDRICAL SWIR FUNCTION ==========

def SWIR_CYLINDER_3D_xy_theta_scan(th_pos_list, x_pos_list, fixed_y_pos, rot_device,
radius_value, spec_device, integ_time, pycro_core, averages):
```

```
    """
    Rotate through predefined x and theta position list and capture background corrected,
averaged spectra from Ocean Optics

    Parameters
    ----------
    th_pos_list : array
        Predefined list of theta positions from previous function & brightfield scan
    x_pos_list : array
        Predefined list of x position from previous function & brightfield scan
    fixed_y_pos : float
        Predefined fixed y position from previous function & brightfield scan
    rot_device : function-like
        Callable KCube object
    radius_value : float
        Default from previously defined: cylinder_radius_global
    spec_device : function_like
        Callable NIRQuest spectrometer object
    integ_time : float
        Integration time for file name metadata
    pycro_core : function-like
        Callable pycromanager MM_Core
    averages : int
        Number of captures to average over

    Returns
    -------
    None.

    """
    # Capture background spectra
    swir_background = capture_bkgd(spec_device, averages, 'background', 'dance', 'carryon')

    # Initialize an empty list to store the z position data and index tuples
    main_df = []
    x_theta_index_tuples = []

    # Prepare theta positions to iterate over (previously defined)
    print(f"Theta Positions: {th_pos_list}")
    # Prepare x positions to iterate over (previously defined)
    print(f"X Positions: {x_pos_list}")
    # Fixed y position (previously defined)
    FIXED_Y_POS = fixed_y_pos  # Use CAPS to fit convention of this function
    # Take fixed y position (previously defined) as argument
    print(f"Fixed Y Position: {fixed_y_pos}")

    # Create subfolder if it doesn't exist already
    subfolder = create_subfolder(experiment_name_global)

    # For cylinder, fixed z and r value
    # Capture z position
    Z_VALUE = z_check_position(pycro_core)
    # Grab radiius value (previously defined)
    R_VALUE = radius_value
```

```
  # For each xy position
  # X_POS is the next position to move to after having finished rotating and capture spectra
  for X_POS in tqdm(x_pos_list, desc='Total X Positions', unit='row'):
    # For each theta position
    # Can start from pos_list[1:] if homed since this would otherwise produce 3 zero deg positions
    # Therefore THETA_POS is actually the next position to move to
    for THETA_POS in tqdm(th_pos_list[1:], desc='Total Theta Positions', unit='angles'):
      # Check current theta position
      CURRENT_THETA = theta_check_position(rot_device)
      # Check current x position
      CURRENT_X, CURRENT_Y = xy_check_position(pycro_core)
      print(f"Currently at theta={CURRENT_THETA}°, x={CURRENT_Y}")

      # Want to save z and r position for every x_pos and theta_pos
      current_header = np.asarray(['Z','R'])
      current_values = np.asarray([Z_VALUE, R_VALUE])

      # Want header to be list of ['Z', 'R', lambda1, lambda2, ..., lambda512]
      # Want results to be list of [z_position, r_value, I(lambda1), I(lambda2), ..., I(lambda512)]

      # Capture spectrum
      print(f"\rCapturing SWIR at X: {X_POS} um; Theta Position: {THETA_POS} deg ", flush=True)
      # Wavelengths and intensities data as list objects
      # wavelengths, intensities = capture_spectrum(spec_device)
      wavelengths, intensities = capture_bkgd_corr_spectrum(spec_device, averages, swir_background, integ_time)

      # Plot & Save Spectrum Graph
      graph_name = f"{date.today()}_{experiment_name_global}_SWIRgraph_{int(CURRENT_THETA)}deg_{CURRENT_X}xpos.png"
      plot_spectrum(wavelengths, intensities, integ_time, averages, spec_device, graph_name, CURRENT_X, CURRENT_THETA, subfolder)

      # Append spectral data to list to be added to dataframe
      full_current_header = np.append(current_header, wavelengths)
      full_current_values = np.append(current_values, intensities)

      # Convert current position results to labelled dataframe
      current_position_df = convert_spectrum_to_dataframe(full_current_header, full_current_values, CURRENT_X)
      # Save spectrum dataframe as .csv
      current_position_df_name = f"{date.today()}_{experiment_name_global}_SWIRdata_ZR_I(lambda)_{int(CURRENT_THETA)}deg_{CURRENT_X}xpos.csv"
      save_dataframe_to_csv(current_position_df, current_position_df_name, subfolder)

      # Add z and r position to zr position data list (convert to main dataframe later)
      # Create an index tuple with two levels ('x' and 'y')
      index_tuple = (CURRENT_X, CURRENT_THETA)
```

```
        # Append z data and index tuple to the respective lists
        main_df.append(full_current_values)

        x_theta_index_tuples.append(index_tuple)

        # Move to next theta position
        print("Move to next theta position...")
        theta_absolute_move(THETA_POS, rot_device)
        wait_for_theta_stage(rot_device)
        print(f"Now at position: {theta_check_position(rot_device)}°")

    # Move to next x
    print("Move to next x position...")
    xy_absolute_move(pycro_core, X_POS, FIXED_Y_POS)
    wait_for_xy_stage(pycro_core)
    x_check, y_check = xy_check_position(pycro_core)
    print(f"Now at position: {x_check} x position")

print ("All positions reached!")
# Now save all data from dataframe into .csv
print("Creating Z R Position Dataframe...")
# Header data list should be defined from last iteration of loop
z_r_lambda_columns = full_current_header
print("Creating X, THETA Multi Index...")
# Create a MultiIndex from the list of index tuples
multi_index = pd.MultiIndex.from_tuples(x_theta_index_tuples, names=['X', 'THETA'])
```

```
    print("Creating Full 3D Dataframe...")
    # Create a DataFrame with the MultiIndex and use the wavelength data as columns
    full_3D_dataframe = pd.DataFrame(main_df, index=multi_index,
columns=z_r_lambda_columns)
    print(full_3D_dataframe)



    # Save Main Dataframe to .csv
    print("Saving Main Dataframe...")
    save_dataframe_to_csv(full_3D_dataframe,
f"{date.today()}_{experiment_name_global}_SWIR_FULL_DATAFRAME.csv", subfolder)

    print ("All done! Great job!")
    dance_function()

# ---------- CARRY OUT SWIR SCAN ----------
print("========== STARTING UP SWIR SCAN ==========")

if __name__ == "__main__":
    try:
        # ---------- Initialise NIRQuest Spectrometer ----------
        # Scan ports for Ocean Optics spectrometers, print device list
        look_for_spectrometers()
        # Choose spectromter via serial number
        spectrometer_serial = "NQ25B0171" #NIRQuest
        # Create spectrometer device
        NIRQuest = initialise_spectrometer(spectrometer_serial)
```

```
    # Set SWIR capture parameters
    integration_time_ms_swir = 10
    no_of_averages_swir = 1000
    set_integration_time(NIRQuest, integration_time_ms_swir)

    SWIR_CYLINDER_3D_xy_theta_scan(THETA_POSITIONS_LIST, X_POSITIONS_LIST, ORIGIN_Y, KCube, cylinder_radius_global, NIRQuest, integration_time_ms_swir, MM_Core, no_of_averages_swir)

  except Exception as e:
    print(f"UH OH! An error occurred in SWIR 3D CYLINDER Execution: {e}")

    # If there's an issue then disconnect KCUbe here - otherwise will stay connected for Raman
    # Disable Rotation Stage
    disable_rotation_stage(KCube)

    # Disconnect Rotation Stage
    disconnect_rotation_stage(KCube)

  finally:
    print("========== FINISHED SWIR, SWITCHING OFF NIRQuest ==========")
    print ("Shutting Down NIRQuest...")
    time.sleep(2.0)

    # Close spectrometer
    close_spectrometer(NIRQuest)

    print("SWIR All ShutDown Complete!")

print("========== FINISHED SWIR SCAN ==========")

# Move Prior tage back to first position
print("Moving back to first position (x, fixed y)")
xy_absolute_move(MM_Core, int(ORIGIN_X), int(ORIGIN_Y))

# ========== 7. SWITCH MODALITIES ==========

# Wait for terminal input allowing time to switch out optics from SWIR to Raman
print("GET READY for RAMAN spectral capture...")
print("Switch kinematic cube for RAMAN beampath...")
wait_for_keyword("raman")   # Wait for "raman" keyword before continuing


# ---------- CYLINDRICAL RAMAN SCAN ----------

# ---------- Import sif_parser to handle Andor camera images ----------
import sif_parser

# ---------- Import Andor camera modules ----------
from pyAndorSDK2 import atmcd, atmcd_codes, atmcd_errors

cam_sdk = atmcd()     # Camera library known as atmcd
codes = atmcd_codes
```

```
# ---------- Import Andor spectrograph modules ----------
# Import Andor spectrograph modules
from pyAndorSpectrograph.spectrograph import ATSpectrograph

spec_sdk = ATSpectrograph()    # Spectrograph library known as ATSpectrograph

# ---------- Raman Andor Camera Functions ----------
# Some API functions need to remain in main code for global vairables and or quirks of
system
# Some functions deprecated - keep all for now

def andor_initialise_camera():
    """
    Initialise Andor iDus camera, and return status value to check for errors

    Returns
    -------
    ret_val_local : bool-like
        Status value (Andor specific) that checks for errors

    """
    print("Initialising Andor camera...")
    # Need first instance of ret_val here
    ret_val_local = cam_sdk.Initialize("")      # Initialise camera library
    print("Function Initialize returned {}".format(ret_val_local))
    # shamrock = spec_sdk.Initialize("")      # Initialise spectrograph library
    # print("Function Initialize returned
{}".format(spec_sdk.GetFunctionReturnDescription(shamrock, 64)[1]))
    return ret_val_local

def andor_get_serial(ret_val_local):
    """
    Get serial number of iDus camera, performs internal status error check

    Parameters
    ----------
    ret_val_local : bool-like
        Status value (Andor specific) that checks for errors

    Returns
    -------
    ret_val_local : bool-like
        Updated status value (Andor specific) that checks for errors
    iSerialNumber : str
        Serial number of iDus camera

    """
    if atmcd_errors.Error_Codes.DRV_SUCCESS == ret_val_local:
        (ret_val_local, iSerialNumber) = cam_sdk.GetCameraSerialNumber()    # Get camera
serial no.
        print("Function GetCameraSerialNumber returned {}; Serial No: {}".format(ret_val_local,
iSerialNumber))
        time.sleep(1.0)
```

```
    return ret_val_local, iSerialNumber

def andor_cool_camera(ret_val_local, target_temp):
    """
    Cool down iDus camera, prints update in terminal whilst camera is cooling down

    Parameters
    ----------
    ret_val_local : bool-like
        Status value (Andor specific) that checks for errors
    target_temp : int
        Target temperature for iDus camera

    Returns
    -------
    ret_val_local : bool-like
        Updated status value (Andor specific) that checks for errors

    """
    if atmcd_errors.Error_Codes.DRV_SUCCESS == ret_val_local:
        ret_val_local = cam_sdk.SetTemperature(target_temp)   # Set camera temperature to - 60
C
        print("Function SetTemperature returned {}; Target temperature {} C".format(ret_val_local,
target_temp))

        ret_val_local = cam_sdk.CoolerON()      # Cool down camera
        print("Function CoolerON returned {}".format(ret_val_local))
        print("Waiting for Temperature to stabilise...")
        while ret_val_local != atmcd_errors.Error_Codes.DRV_TEMP_STABILIZED:  # Visualise
cooling down progress
            time.sleep(5)
            (ret_val_local, temperature) = cam_sdk.GetTemperature()
            print("Function GetTemperature returned {}; Current temperature = {}
C".format(ret_val_local, temperature), end='\r')
            print("")
        # Catches the above print statement and preserves the below print statement
        print("")
        print("Temperature stabilised!")
        time.sleep(1.0)
    return ret_val_local

def andor_set_exp_time(ret_val_local, exp_time):
    """
    Set exposure time for Andor iDus camera in ms, get confirmation from Andor status codes

    Parameters
    ----------
    ret_val_local : bool-like
        Status value (Andor specific) that checks for errors
    exp_time : float
        Set Raman exposure time (secs) for Andor iDus

    Returns
```

```
    -------
    ret_val_local : bool-like
        Updated status value (Andor specific) that checks for errors
    fminExposure : float
        Confirmation from Andor iDus for exposure time
    fAccumulate : float
        Confirmation from Andor iDus for accumulation(?)
    fKinetic : float
        Confirmation from Andor iDus for kinetic(?)

    """
    if atmcd_errors.Error_Codes.DRV_SUCCESS == ret_val_local:
        ret_val_local = cam_sdk.SetExposureTime(exp_time)
        print("Function SetExposureTime returned {} time = {}".format(ret_val_local, exp_time))
        # Check Acqusition parameters?
        (ret_val_local, fminExposure, fAccumulate, fKinetic) = cam_sdk.GetAcquisitionTimings()
        print("Function GetAcquisitionTimings returned {} exposure = {} accumulate = {} kinetic =
{}".format(
            ret_val_local, fminExposure, fAccumulate, fKinetic))
    return ret_val_local, fminExposure, fAccumulate, fKinetic

def andor_make_acquisition(ret_val_local):
    """
    Perform capture with Andor iDus; doesn't return an image so requires another function to
grab array

    Parameters
```

```
    ----------
    ret_val_local : bool-like
        Status value (Andor specific) that checks for errors

    Returns
    -------
    ret_val_local : bool-like
        Updated status value (Andor specific) that checks for errors

    """
    if atmcd_errors.Error_Codes.DRV_SUCCESS == ret_val_local:
        ret_val_local = cam_sdk.PrepareAcquisition()  # Prepare for Acquisition - triggered by
GetAcquisition
        print("Function PrepareAcquisition returned {}".format(ret_val_local))

        ret_val_local = cam_sdk.StartAcquisition()
        print("Function StartAcquisition returned {}".format(ret_val_local))

        ret_val_local = cam_sdk.WaitForAcquisition()
        print("Function WaitForAcquisition returned {}".format(ret_val_local))
    return ret_val_local

def andor_grab_2D_image(ret_val_local, xpixels_local, ypixels_local, arr_local):
    """
    Grab image from Andor iDus following acquisition

    Parameters
```

```
    ----------
    ret_val_local : bool-like
        Status value (Andor specific) that checks for errors
    xpixels_local : int
        Image width (pixels)
    ypixels_local : int
        Image height (pixels)
    arr_local : array
        Image data array

    Returns
    -------
    None.

    """
    if atmcd_errors.Error_Codes.DRV_SUCCESS == ret_val_local:
        ret_val_local = cam_sdk.SetImage(1, 1, 1, xpixels_local, 1, ypixels_local)
        print("Function SetImage returned {} hbin = 1 vbin = 1 hstart = 1 hend = {} vstart = 1 vend =
{}".format(
                ret_val_local, xpixels_local, ypixels_local))
    # If I want to show 2D image
        arr_local = np.fliplr(np.rot90(np.reshape(arr_local, (xpixels_local, ypixels_local)), 1))
        plt.matshow(arr_local)
        plt.show()
    return(ret_val_local)

def andor_save_siffile(ret_val_local, subfolder, exposure_time, x_posit, y_posit, exp_name):
```

```
    """
    DEPRECIATED: Use "singelpoint" below with xy position in "sif_label" Save image array as
.sif before handling as Python friendly image

    Parameters
    ----------
    ret_val_local : bool-like
        Status value (Andor specific) that checks for errors
    subfolder : str
        Subfolder to save .sif file to
    exposure_time : float
        Raman exposure time in sec
    x_posit : float
        X position on Prior stage
    y_posit : float
        Y position on Prior stage

    Returns
    -------
    ret_val_local : bool-like
        Status value (Andor specific) that checks for errors
    sif_filename : str
        Final filename for .sif image file

    """
    print ("Saving as .sif...")
```

```
    sif_filename =
f'{date.today()}_{exp_name}_RAMANsif_{int(exposure_time)}sec_{int(x_posit)}_xpos_{y_posit}
_ypos.sif'
    sif_filepath = os.path.join(subfolder, sif_filename)
    # Important to have "subfolder/sif file name" to save in correct place
    ret_val_local = cam_sdk.SaveAsSif(sif_filepath)
    print("Function SaveAsSif returned {}".format(ret_val_local))
    print (".sif Saved!")
    time.sleep(1.0)
    return ret_val_local, sif_filepath

def andor_save_siffile_single_position(ret_val_local, subfolder, exposure_time, sif_label,
exp_name):
    """
    Save image array as .sif before handling as Python friendly image

    Parameters
    ----------
    ret_val_local : bool-like
        Status value (Andor specific) that checks for errors
    subfolder : str
        Subfolder to save .sif file to
    exposure_time : float
        Raman exposure time in sec
    iteration : str
        Label to identify the sif file e.g. "Repeat_no._1"
```

```
    Returns
    -------
    ret_val_local : bool-like
        Status value (Andor specific) that checks for errors
    sif_filename : str
        Final filename for .sif image file

    """
    print ("Saving as .sif...")
    sif_filename =
f'{date.today()}_{exp_name}_RAMANsif_{int(exposure_time)}sec_{sif_label}.sif'
    sif_filepath = os.path.join(subfolder, sif_filename)
    # Important to have "subfolder/sif file name" to save in correct place
    ret_val_local = cam_sdk.SaveAsSif(sif_filepath)
    print("Function SaveAsSif returned {}".format(ret_val_local))
    print (".sif Saved!")
    time.sleep(1.0)
    return ret_val_local, sif_filepath

def andor_plot_spectra(subfolder, x, y, x_position, y_position, exp_name):
    """
    Plot and save .png of Raman spectrum

    Parameters
    ----------
    subfolder : str
        Subfolder directory to save Raman spectrum .png to
```

```
    x : array
        Wavelength values to plot
    y : array
        Raman intensity values to plot
    x_position : float
        X position on Prior stage
    y_position : float
        Y position on Prior stage

    Returns
    -------
    None.

    """
    print("Plotting Raman Spectrum...")
    plt.plot(x,y)
    plt.xlabel('Pixel')
    plt.ylabel('Intensity')
    plt.title(f"Raman at {x_position} um, {y_position} deg")
    plt.grid(True)
    png_name =
f"{date.today()}_{exp_name}_RAMANgraph_{int(x_position)}_xpos_{int(y_position)}_deg.png"
    png_path = os.path.join(subfolder, png_name)
    plt.savefig(png_path)
    plt.show()
    print("Raman Spectrum Saved!")
    time.sleep(1.0)
```

```
def andor_save_csv(subfolder, x, y, exp_name):
    """
    DEPRECIATED: Now prefer dataframe to csv. Save Raman spectra as .csv

    Parameters
    ----------
    subfolder : str
        Subfolder to save Raman .csv file to
    x : array
        Wavelength v
    y : TYPE
        DESCRIPTION.

    Returns
    -------
    None.

    """
    print("Saving as .csv...")
    csv_name = f'{date.today()}_{exp_name}_RAMANtest.csv'
    csv_path = os.path.join(subfolder, csv_name)
    csv_df = pd.DataFrame({"Pixels" : x, "Intensity" : y})
    csv_df.to_csv(csv_path, index=False)
    print(".csv Saved!")
    time.sleep(1.0)
```

```
def andor_make_and_save_average_acquisition(ret_val_local, no_of_averages, subfolder,
exp_time, acquisition_label, exp_name):
    """
    Make Raman acquisition, repeat and produce average spectra. Saves each iteration (.sif,
common df) and returns intensities as array.

    Parameters
    ----------
    ret_val_local : bool-like
        Status value (Andor specific) that checks for errors
    no_of_averages : int
        Number of repeats to average over
    subfolder : str
        Data folder to hold all .sif and .csv files
    exp_time : float
        Exposure time for Raman acquisitions
    sif_label : str
        Particular acquisition e.g. "[coordinate]" or "Background"

    Returns
    -------
    ret_val_local : bool-like
        Status value (Andor specific) that checks for errors
    raman_avg_array : array
        Averaged intensities as array
    raman_single_spectrum_x : array
        Pixels (wavelengths) as array
    """

    # Create blank DataFrame to hold acquisition repeats and averaged data
    raman_avg_df = pd.DataFrame()
    # Repeat and average
    for i in range(no_of_averages):
        print(f"Carrying out {acquisition_label} Acquisition: Spectrum {i+1} of {no_of_averages}.
Wait {exp_time} secs...")
        # Wavelengths and intensities data as list objects
        ret_val_local = andor_make_acquisition(ret_val_local)
        # ---------- Deal with 1D FVB Data (Needs Global Variables) ----------
        print("Handling 1D spectra...")
        imageSize = xpixels    # For 1D image capture
        # imageSize = xpixels * ypixels    # For 2D image capture
        (ret_val_local, arr, validfirst, validlast) = cam_sdk.GetImages16(1, 1, imageSize)
        print("Function GetImages16 returned {}; first pixel = {}; size = {}".format(ret_val_local,
arr[0], imageSize))
        # ---------- Pixel Size Info (Keep in API Format) ----------
        (ret_val_local, xsize, ysize) = cam_sdk.GetPixelSize()
        print("Function GetPixelSize returned {}; X Size = {}; Y Size = {}".format(ret_val_local, xsize,
ysize))
        # ---------- Save Image Data as .sif ----------
        ret_val_local, sif_file_name = andor_save_siffile_single_position(ret_val_local, subfolder,
exp_time, f"{acquisition_label}_Repeat_{i+1}", exp_name)
        sif_data, info = sif_parser.np_open(sif_file_name)      # Handle .SIF file as numpy array
        print(f"Shape of SIF data = {np.shape(sif_data)}")
```

```
    print(f"Metadata = {info}")

    print("Creating intensity and pixel position array...")
    raman_single_spectrum_y = sif_data[0,0,:]   # Raman intensity
    raman_single_spectrum_x = np.arange(1,len(raman_single_spectrum_y)+1)    # Pixel of
sensor

    print(f"Retrieved Raman {acquisition_label} Spectrum!")
    print(f"Intensity = {raman_single_spectrum_y}")
    print(f"Pixels = {raman_single_spectrum_x}")

    # ---------- Add background spectrum to labelled dataframe ----------
    raman_avg_df[f"Signal_{i+1}"] = raman_single_spectrum_y

  # ---------- Calculate mean background ----------
  raman_avg_df["Mean_Signal"] = raman_avg_df.mean(axis=1)
  raman_avg_df["Pixel"] = raman_single_spectrum_x

  # ---------- Extract mean signal as 1D array ----------
  raman_avg_array = raman_avg_df["Mean_Signal"].to_numpy()
  print(f"Raman {acquisition_label} now an array object...")

  # ---------- Save spectrum to csv in subfolder ----------
  print("Converting Signal to Dataframe...")
  # Save spectrum dataframe as .csv
  raman_avg_df_name = f"{date.today()}_RAMANdata_Raw_{acquisition_label}.csv"
  print("Saving Dataframe to .csv...")
  save_dataframe_to_csv(raman_avg_df, raman_avg_df_name, subfolder)

  return ret_val_local, raman_avg_array, raman_single_spectrum_x

print("========== STARTING UP RAMAN SCAN ==========")
print("Starting SPECTOGRAPH prerequisites...")
ret_val_shamrock = spec_sdk.Initialize("")
print("Function Initialize returned {}".format(
  spec_sdk.GetFunctionReturnDescription(ret_val_shamrock, 64)[1]))
print("SPECTROGRAPH Initialised!")

# ========== 8. INITIALISING SPECTROGRAPH ==========
if ATSpectrograph.ATSPECTROGRAPH_SUCCESS == ret_val_shamrock:
  try:
    # Get spectrograph serial no.
    (ret_val_shamrock, serial) = spec_sdk.GetSerialNumber(0, 64)
    print("Function GetSerialNumber returned : {} Serial No: {}".format(
      spec_sdk.GetFunctionReturnDescription(ret_val_shamrock, 64)[1], serial))

    # Set Slitwidth and check
    print("Setting Slit Width, Index 1...")
    slit_width_intended = 20.0     # In microns
    (ret_val_shamrock) = spec_sdk.SetSlitWidth(0,1,slit_width_intended)

    (ret_val_shamrock, slit_width_actual) = spec_sdk.GetSlitWidth(0, 1)
    print("Function GetSlitWidth returned : {} Slit Width: {}".format(
      spec_sdk.GetFunctionReturnDescription(ret_val_shamrock, 64)[1], slit_width_actual))
```

```
    print(f"Successfully set slit width to {slit_width_actual}")

    # Set Grating Position (central wavelength, nm) and check
    print("Setting Wavelength...")
    grating_centre_intended = 926.03
    (ret_val_shamrock) = spec_sdk.SetWavelength(0, grating_centre_intended)

    (ret_val_shamrock, grating_centre_actual) = spec_sdk.GetWavelength(0)
    print("Function GetWavelength returned : {} Wavelength No: {}".format(
        spec_sdk.GetFunctionReturnDescription(ret_val_shamrock, 64)[1],
grating_centre_actual))

    print(f"Successfully set slit width to {grating_centre_actual}")

    # Open shutter and check
    print("Opening Shutter...")      # 0 - Closed, 1 - Open
    (ret_val_shamrock) = spec_sdk.SetShutter(0, 1)
    (ret_val_shamrock, shutter_mode_set) = spec_sdk.GetShutter(0)
    print("Function GetShutter returned : {} Mode: {}".format(
        spec_sdk.GetFunctionReturnDescription(ret_val_shamrock, 64)[1], shutter_mode_set))
    print("Mode: -1=Shutter not set yet, 0=Closed, 1=Open")

    print(f"Successfully set shutter to {shutter_mode_set}")

  except Exception as e:
    print(f"UH OH! An error occurred in Raman (Spectrograph): {e}")
```

```
    print("Safely shutting down Spectrograph and KCube...")
    # Disable Rotation Stage
    disable_rotation_stage(KCube)

    # Disconnect Rotation Stage
    disconnect_rotation_stage(KCube)

    #Shutdown spectrograph
    ret_val_shamrock = spec_sdk.Close()
    print("Function Close returned {}".format(
      spec_sdk.GetFunctionReturnDescription(ret_val_shamrock, 64)[1]))

  finally:
    print("SPECTROGRAPH ready!")
    time.sleep(1.0)


print ("Starting CAMERA prerequisites...")
ret_val = andor_initialise_camera()
print("Function Initialize returned {}".format(ret_val))
print("CAMERA initialised!")
time.sleep(1.0)

# ========== 9. CARRY OUT RAMAN SCAN ==========
if atmcd_errors.Error_Codes.DRV_SUCCESS == ret_val:
  try:
    ret_val, iSerialNumber = andor_get_serial(ret_val)
```

```
    # ---------- Define iDus Camera Temperature ----------
    ret_val = andor_cool_camera(ret_val, target_temp=-80)

    # ---------- Prepare Acquisition (Keep API Functions) ----------
    print("Preparing Acquisition...")
    ret_val = cam_sdk.SetAcquisitionMode(codes.Acquisition_Mode.SINGLE_SCAN)    # Single Scan
    print("Function SetAcquisitionMode returned {} mode = Single Scan".format(ret_val))

    ret_val = cam_sdk.SetReadMode(codes.Read_Mode.FULL_VERTICAL_BINNING)    # Read mode is 1D profile FVB not 2D "IMAGE"
    print("Function SetReadMode returned {} mode = FVB".format(ret_val))

    ret_val = cam_sdk.SetTriggerMode(codes.Trigger_Mode.INTERNAL)
    print("Function SetTriggerMode returned {} mode = Internal".format(ret_val))

    # ---------- Get Detector (Needs Global Variables) ----------
    (ret_val, xpixels, ypixels) = cam_sdk.GetDetector()    # Retrieve detector height and width, also pixel width
    print("Function GetDetector returned {} xpixels = {} ypixels = {}".format(ret_val, xpixels, ypixels))

    # ---------- Set Exposure time for camera in secs ----------
    # Protocol reccomends 10 um slit, 10 sec acquisition, 1% power (ND Filter) for PS standard
    print("Setting exposure parameters...")
    raman_exp_time = 20.0
```

```
    ret_val, fminExposure, fAccumulate, fKinetic = andor_set_exp_time(ret_val, raman_exp_time)

    # ---------- Select subfolder to hold raman data ----------
    print("Creating data subfolder...")
    andor_data_folder = create_subfolder(f"{experiment_name_global}") # Hard code for now

    # ========== RAMAN BACKGROUNDING and Si STANDARD CAPTURE ==========
    # 1. Capture Raman Background with "make and save average" script as "raman_bkgnd_spectrum_y" array
    # 2. Save average for that position as a "background" csv
    # Saves raw data repeats and average
    # Capture laser off spectrum with same exposure parameters and average over a few captures

    print("TURN OFF Laser to prepare for dack background capture...")
    wait_for_keyword("laseroffready")    # Wait for "laseroffready" keyword before continuing

    andor_bkgd_no_of_averages = 1
    andor_acq_no_of_averages = 1

    print("Ready to Capture Raman Background!")
    while True:
        user_input = input("Enter 'raman_bkgd' to perform dark background capture, 'groove' to perform a dance, or 'letsgo' to carry on script:")
        if user_input == "raman_bkgd".lower():
            print("Performing dark background capture...")
```

```
            ret_val, raman_background_intensities, raman_background_pixels =
andor_make_and_save_average_acquisition(ret_val, andor_bkgd_no_of_averages,
andor_data_folder, raman_exp_time, "Background", experiment_name_global)

            print("Plotting dark background...")
            plt.plot(raman_background_pixels, raman_background_intensities)
            plt.title("Dark Raman Background")
            plt.xlabel('Pixels')
            plt.ylabel('Intensity')
            plt.grid(True)
            plt.show()
            print("What do you think?")

        elif user_input == "groove".lower():
            # Perform operation 2 (displaying a little dance)
            print("Performing a little dance for you...")
            dance_function()
            print("Dance completed!")

        elif user_input == "letsgo".lower():
            # Continue script
            print("Continuing script...")
            break
        else:
            print("Invalid input. Enter 'raman_bkgd' to perform dark background capture, 'groove'
to perform a dance, or 'letsgo' to carry on script:")
```

```
    #  Plot and save Background Spectrum
    andor_plot_spectra(andor_data_folder, raman_background_pixels,
raman_background_intensities, 0.0, 0.0, f"{experiment_name_global}_Background")



    # 3. Capture (Bkgd Corrected) Raman of silicon sample via standalone script
    print("Remember to Capture Raman of Si or PS standard for pixel-wavelength
calibration!")
    print("TURN ON Laser to prepare for next capture...")
    wait_for_keyword("laseronready")

    # ========== RAMAN SCANNING MAIN CODE START ==========
    # 1. Capture (Bkgd Corrected) Averaged Raman of each cylinder position with "make and
save average" script as array
    # 2. Save average (with iterations) for that position as "x, theta, z" csv - some may be
dodgy so can identify erroneous ones
    # 3. Add the Averaged Raman for each position to main dataframe

    # Initialize an empty list to store the main data and index tuples
    print("Creating empty main Raman dataframe and tuples...")
    raman_main_df = []
    raman_x_theta_index_tuples = []

    # Prepare theta positions to iterate over (previously defined)
    print(f"Theta Positions: {THETA_POSITIONS_LIST}")
    # Prepare x positions to iterate over (previously defined)
    print(f"X Positions: {X_POSITIONS_LIST}")
```

```
    # Fixed y position (previously defined)
    Y_POS_RAMAN = ORIGIN_Y  # Grab global y position (fixed for cylindrical scan)
    print(f"Fixed Y Position: {Y_POS_RAMAN}")

    # # ---------- Create subfolder for Raman data (if it doesn't exist already) ----------
    # raman_subfolder = create_subfolder(experiment_name_global)

    # For cylinder, fixed z and r value
    # Capture z position
    Z_VALUE_RAMAN = z_check_position(MM_Core)
    # Grab radius value (previously defined)
    R_VALUE_RAMAN = cylinder_radius_global

    # For each x position; using global X_POSITIONS_LIST
    for X_POS_RAMAN in tqdm(X_POSITIONS_LIST, desc='Total X Positions', unit='row'):
      time.sleep(1.0)  # Wait for Stage Movement
      # print(f"\rWorking on X: {x_position} um ", flush=True)

      # For each theta position; using global THETA_POSITIONS_LIST
      # Wait till actions finished before moving to next position
      # Can start from position_list[1:] if homed since this would otherwise produce 3 zero deg positions
      # Therefore THETA_POS_RAMAN is actually the next position to move to
      for THETA_POS_RAMAN in tqdm(THETA_POSITIONS_LIST[1:], desc='Total Theta Positions', unit='angles'):
        # Check current theta position
        CURRENT_THETA_RAMAN = theta_check_position(KCube)
        # Check current x position
        CURRENT_X_RAMAN, CURRENT_Y_RAMAN = xy_check_position(MM_Core)
        print(f"Currently at theta={CURRENT_THETA_RAMAN}º, y={CURRENT_Y_RAMAN}")

        # Want to save z and r position for every x_pos and theta_pos
        current_header_raman = np.asarray(['Z','R'])
        current_values_raman = np.asarray([Z_VALUE_RAMAN, R_VALUE_RAMAN])

        # Want header to be list of ['Z', 'R', lambda1, lambda2, ..., lambda512]
        # Want results to be list of [z_position, r_value, I(lambda1), I(lambda2), ..., I(lambda512)]

        # Capture spectrum
        # Capture (Bkgd Corrected) Averaged Raman of each cylinder position with "make and save average" script as array
        # Save average (with iterations) for that position as "x, theta, z" as .csv - some may be dodgy so can identify erroneous ones
        # Add the Averaged Raman for each position to main dataframe

        print(f"\rCapturing Raman at X: {CURRENT_X_RAMAN} um; Theta Position: {CURRENT_THETA_RAMAN} deg ", flush=True)
        # Wavelengths and intensities data as list objects
        raman_position_label = f"ZR_I(lambda)_{int(CURRENT_THETA_RAMAN)}deg_{CURRENT_X_RAMAN}xpos"
        ret_val, raman_spectrum_y_nobkgdcorr, raman_spectrum_x = andor_make_and_save_average_acquisition(ret_val, andor_acq_no_of_averages, andor_data_folder, raman_exp_time, raman_position_label, experiment_name_global)
```

```
        raman_spectrum_y = raman_spectrum_y_nobkgdcorr -
raman_background_intensities

        print("Retrieved Andor Raman Spectrum!")
        print(f"Intensity = {raman_spectrum_y}")   # Array for Raman Spectrum
        print(f"Pixels = {raman_spectrum_x}")  # Array for Raman wavelengths



        # Append spectral data to list to be added to dataframe
        full_current_header_raman = np.append(current_header_raman, raman_spectrum_x)
        full_current_values_raman = np.append(current_values_raman, raman_spectrum_y)

        # Add spectrum to main data list (convert to main dataframe later)
        # Create an index tuple with two levels ('x' and 'theta')
        raman_index_tuple = (CURRENT_X_RAMAN, CURRENT_THETA_RAMAN)

        # Append data and index tuple to the respective lists
        raman_main_df.append(full_current_values_raman)
        raman_x_theta_index_tuples.append(raman_index_tuple)

        #  Plot Spectrum
        andor_plot_spectra(andor_data_folder, raman_spectrum_x, raman_spectrum_y,
CURRENT_X_RAMAN, CURRENT_THETA_RAMAN, experiment_name_global)

        # Convert current position results to labelled dataframe
        andor_current_position_df =
convert_spectrum_to_dataframe(full_current_header_raman, full_current_values_raman,
CURRENT_X_RAMAN)
        # Save spectrum dataframe as .csv
        andor_current_position_df_name =
f"{date.today()}_{experiment_name_global}_RAMANdata_ZR_I(lambda)_{int(CURRENT_THET
A_RAMAN)}deg_{CURRENT_X_RAMAN}xpos.csv"
        save_dataframe_to_csv(andor_current_position_df,
andor_current_position_df_name, andor_data_folder)

        # Move to next theta position
        print("Move to next theta position...")
        theta_absolute_move(THETA_POS_RAMAN , KCube)
        wait_for_theta_stage(KCube)
        print(f"Now at position: {theta_check_position(KCube)}°")

    # Move to next x
    print("Move to next x position...")
    xy_absolute_move(MM_Core, X_POS_RAMAN, Y_POS_RAMAN)
    wait_for_xy_stage(MM_Core)
    x_check, y_check = xy_check_position(MM_Core)
    print(f"Now at position: {x_check} X position")

print ("All positions reached!")
# Now save all data from dataframe into .csv
print("Creating Z R Position Dataframe...")
# Header data list should be defined from last iteration of loop
```

```
    raman_z_r_lambda_columns = full_current_header_raman
    print("Creating X, THETA Multi Index...")
    # Create a MultiIndex from the list of index tuples
    raman_multi_index = pd.MultiIndex.from_tuples(raman_x_theta_index_tuples,
names=['X', 'THETA'])
    print("Creating RAMAN Full 3D Dataframe...")
    # Create a DataFrame with the MultiIndex and use the wavelength data as columns
    raman_full_3D_dataframe = pd.DataFrame(raman_main_df, index=raman_multi_index,
columns=raman_z_r_lambda_columns)
    print(raman_full_3D_dataframe)



    # Save Main Dataframe to .csv
    print("Saving Main RAMAN Dataframe...")
    save_dataframe_to_csv(raman_full_3D_dataframe,
f"{date.today()}_{experiment_name_global}_RAMAN_FULL_DATAFRAME.csv",
andor_data_folder)
    # ========== RAMAN SCANNING MAIN CODE END ==========

    print ("All done! Great job!")
    dance_function()



  except Exception as e:
    print(f"UH OH! An error occurred in Raman Scan (Camera and 3D Scan): {e}")

  finally:
```

```
  # ---------- g. Clean up and Shutdown ----------
    print("========== FINISHED RAMAN, SWITCHING OFF iDUS, SPECTROGRAPH, KCube
==========")
    # Disable Rotation Stage
    disable_rotation_stage(KCube)

    # Disconnect Rotation Stage
    disconnect_rotation_stage(KCube)

    print ("Shutting Down Raman CAMERA...")
    time.sleep(2.0)
    ret_val = cam_sdk.ShutDown()  # Shutdown camera
    print("Function ShutDown returned {}".format(ret_val))
    time.sleep(1.0)

    print("Shutting Down Raman SPECTROGRAPH...")
    if ATSpectrograph.ATSPECTROGRAPH_SUCCESS == ret_val_shamrock:
      try:
        ret_val_shamrock = spec_sdk.Close()  # Shutdown spectrograph
        print("Function Close returned
{}".format(spec_sdk.GetFunctionReturnDescription(ret_val_shamrock, 64)[1]))
      except Exception as e:
        print(f"UH OH! An error occurred in Raman (Spectrograph) during final Shutdown: {e}")

    print("Raman All finished!")
    print ("All Done! Good Job!")
```

```
    print("========== FINISHED RAMAN SCAN ==========")


print("SWIR and RAMAN ALL DONE!")
```

Appendix E Python Code for 3D Spherical HSI

“20240812_3D_spherical_manual_focus_swir_raman_bkgdcorr_v3_1”

```
# -*- coding: utf-8 -*-
"""
3D Hyperspectral Spherical Scan: SWIR and Raman

1. Initialise pycromanager camera, xy-stage
2. Initialise Kinesis (theta)

3. Define x, theta position list

4. SWIR Scan: Background (take gold reference separately)
4.1. Scan through positions and allow manual refocus
4.2. Save SWIR with (x, theta, r) position
4.3. Save Hyperspectral Dataframe

5. Switch Modalities

6. Initialise Andor Spectrograph (shutter, slit, grating position)

7. Raman Scan: Background (take standard spectrum for manual x calibration separately)
7.1. Scan through positions and allow manual refocus (z and lens height)
7.2. Save Raman with (x, theta, r) position
7.3. Save Hyperspectral Dataframe

Once established want each numbered section as a separate python file with functions that
can be called in the main script

@author: Hiro
"""

# ---------- OS and Standard Functions ----------

import os
from datetime import date
import time
from tqdm import tqdm
import numpy as np
import matplotlib.pyplot as plt
import tifffile as tf

def create_subfolder(exp_name):
    """
    Creates subfolder in existing directory where current .py file is

    Parameters
    ----------
    exp_name : str
        Verbose name of experiment - adds the current date
```

```
    Returns
    -------
    subfolder : str
        Subfolder named with current date and experiment name

    """
    subfolder = f"./{date.today()}_{exp_name}"
    if not os.path.exists(subfolder):
        os.makedirs(subfolder)
    print ("Subfolder ready!")
    return subfolder

def wait_for_keyword(keyword):
    """
    Makes a pause in the script for a manual action, requires keyword input

    Parameters
    ----------
    keyword : str
        Case sensitive custom keyword

    Returns
    -------
    None.

    """
```

```
    def get_input():
        """
        Takes use input via keyboard

        Returns
        -------
        None.

        """
        return input(f"Type '{keyword}' and press Enter to continue:")
    # Keep prompting until desired input is received
    while True:
        user_input = get_input()
        if user_input.lower() == keyword.lower():
            break
        else:
            print(f"Invalid input! Please type '{keyword}'")
    # Continue with rest of programme
    print("Continuing with the programme...")
    time.sleep(1.0)

def dance_function():
    """
    Test function, prints some boogie fever

    Returns
    -------
```

```
    None.

    """
    print("\o "); print(" |\\"); print("/ \\"); time.sleep(0.5)
    print(" o "); print("<|>"); print("/ \\"); time.sleep(0.5)
    print(" o/"); print("/| "); print("/ \\"); time.sleep(0.5)
    print(" o "); print("<|>"); print("/ \\"); time.sleep(0.5)

# ---------- Pandas Dataframe Functions ----------
import pandas as pd

# ---------- Pandas Dataframe Functions ----------
# Create pandas data frame to wrangle hyperspectral data

def convert_spectrum_to_dataframe(wvlgth, intnsty, y_pos):
    """
    Want wavelengths as column headings, intensities as row entries, position as index

    Parameters
    ----------
    wvlgth : array
        Wavelengths from spectrometer
    intnsty : array
        Signal valeues from spectrometer
    y_pos : float
        Coordinate value to save as data label
```

```
    Returns
    -------
    df_converted : float
        Pandas datafranme with index label from y_pos coordinate value

    """
    # column_string_list = [str(item for item in [x])]
    # print("columns =", column_string_list)
    # df_converted = pd.DataFrame([y], index=[f"{theta}"], columns=column_string_list)
    df_converted = pd.DataFrame([intnsty], index=[f"{y_pos}"], columns=[wvlgth])
    return df_converted

def save_spectrum_to_dataframe(main_df, spectrum_entry):
    """
    Save latest spectrum to main dataframe, append rows with common column headings

    Parameters
    ----------
    main_df : dataframe
        Take in current state of main dataframe
    spectrum_entry : float
        Take in latest spectrum to append to dataframe

    Returns
    -------
    main_df : dataframe
        Updated main dataframe
```

```
    """
    print("Saving Spectrum to Database...")
    # Want to append rows to dataframe with common column headings
    main_df = pd.concat([main_df, spectrum_entry])
    print("Spectrum Saved to Database!")
    return main_df

def save_dataframe_to_csv(df, df_name, folder):
    """
    Save main dataframe as .csv

    Parameters
    ----------
    df : dataframe
        Take in final main dataframe
    df_name : str
        Define name for final .csv containing main data
    folder : str
        Takes in designated folder for saving the data

    Returns
    -------
    None.

    """
    file_path = os.path.join(folder, df_name)
    # Save the DataFrame to a CSV file
    df.to_csv(file_path, index=True)

# ========== 1. INITIALISE PYCROMANAGER ==========
# Micromanager running simultaneously with correct config file
from pycromanager import Core

# ---------- Pycromanager Functions ----------

def initialise_pycromanager(core):
    """
    Start up pycromanager; requires micromanager to be running in background

    Parameters
    ----------
    core : function-like
        Core imported from pycromanager module

    Returns
    -------
    core : function-like
        Renamed micromanager core object MMCore
    xy_device : function-like
        Renamed micromanager stage object XY_stage
    camera_device : function-like
        Renamed micromanager stage object Camera
```

```
    """
    print("========== Initialising PycroManager ==========")
    print("MicroManager Core =", core)
    # Retrieve name for pycro_xy_device
    xy_device = core.get_xy_stage_device()
    print(f"Stage Device = {xy_device}")
    # Retrieve name for pycro_cam_device
    camera_device = core.get_camera_device()
    print(f"Camera Device = {core.get_camera_device()}")
    print("========== PycroManager Ready! ==========")
    return core, xy_device, camera_device

def wait_for_xy_stage(core):
    """
    (Doesn't seem to work) Wait for XY Stage to stop moving

    Parameters
    ----------
    core : function-like
        Core imported from pycromanager module

    Returns
    -------
    None.

    """
    print("Waiting for XY Stage Motion Complete...")
    # core.waitForDeviceType('XYStageDevice')
    time.sleep(2.0)
    print("XY Stage Ready!")

def xy_check_position(core):
    """
    Get current XY position from Prior stage

    Parameters
    ----------
    core : function-like
        Core imported from pycromanager module

    Returns
    -------
    current_x : float
        Absolute X position in um
    current_y : float
        Absolute Y position in um

    """
    print("Getting Current XY Position...")
    current_x = core.get_x_position()
    current_y = core.get_y_position()
    print(f"Current X is = {current_x} um")
    print(f"Current Y is = {current_y} um")
    return current_x, current_y
```

```
def z_check_position(core):
    """
    Get current Z position from Nikon Ti

    Parameters
    ----------
    core : function-like
        Core imported from pycromanager module

    Returns
    -------
    current_z : float
        Absolute Z position in um

    """
    print("Getting Current Z Position...")
    current_z = core.get_position()
    print(f"Current Z is = {current_z} um")
    return current_z

def xy_absolute_move(core, x_abs, y_abs):
    """
    Move to absolute XY position on Prior stage

    Parameters
    ----------
    core : function-like
        Core imported from pycromanager module
    x_abs : float
        Absolute X position coordinate in um
    y_abs : float
        Absolute Y position coordinate in um

    Returns
    -------
    None.

    """
    current_x = core.get_x_position()
    current_y = core.get_y_position()
    print(f"Starting at ({current_x},{current_y})")
    print(f"Aiming for ({x_abs},{y_abs})")
    core.set_xy_position(x_abs,y_abs) # Important for positions to be int()
    # May need to add wait function, or wait for motion finishing etc.
    time.sleep(1.0)
    check_x = core.get_x_position()
    check_y = core.get_y_position()
    print(f"Finishing at ({check_x},{check_y})")

def z_absolute_move(core, z_abs):
    """
    Move to absolute Z position on Nikon Ti
```

```
    Parameters
    ----------
    core : function-like
        Core imported from pycromanager module
    z_abs : float
        Absolute Z position coordinate in um

    Returns
    -------
    None.

    """
    current_z = core.get_position()
    print(f"Starting at ({current_z})")
    print(f"Aiming for ({z_abs})")
    core.set_position(z_abs)
    # May need to add wait function, or wait for motion finishing etc.
    check_z = core.get_position()
    print(f"Finishing at ({check_z})")

def xy_relative_move(core, x_jog, y_jog):
    """
    Relative XY move on Prior stage

    Parameters
    ----------
    core : function-like
        Core imported from pycromanager module
    x_jog : float
        Relative X move coordinate in um
    y_jog : float
        Relative Y move coordinate in um

    Returns
    -------
    None.
    """
    current_x = core.get_x_position()
    current_y = core.get_y_position()
    print(f"Starting at ({current_x},{current_y})")
    print(f"Moving xy step ({x_jog},{y_jog})")
    core.set_relative_xy_position(x_jog,y_jog)
    # May need to add wait function, or wait for motion finishing etc.
    check_x = core.get_x_position()
    check_y = core.get_y_position()
    print(f"Finishing at ({check_x},{check_y})")

def z_relative_move(core, z_jog):
    """
    Relative Z move on Nikon Ti

    Parameters
    ----------
    core : function-like
```

```
    Core imported from pycromanager module
  z_jog : float
    Relative Z move coordinate in um

  Returns
  -------
  None.

  """
  current_z = core.get_position()
  print(f"Starting at ({current_z})")
  print(f"Moving z step ({z_jog})")
  core.set_relative_position(z_jog)
  # May need to add wait function, or wait for motion finishing etc.
  check_z = core.get_position()
  print(f"Finishing at ({check_z})")

def brightfield_initialise(core):
  """
  Initialise Hamamatsu Camera via pycromanager

  Parameters
  ----------
  core : function-like
    Core imported from pycromanager module

  Returns
  -------
  None.

  """
  core.initialize_device("HamamatsuHam_DCAM")
  print ("Hamamatsu Camera Initialised")

def brightfield_snap(core):
  """
  Snaps image data with Hamamatsu, retrieves image tags and reshapes into image

  Parameters
  ----------
  core : function
    Core imported from pycromanager module

  Returns
  -------
  pixels : array
    2D Array of image data from Hamamatsu camera
  tagged_image_height : int
    Image height in pixels
  tagged_image_width : int
    Image width in pixels

  """
  print("Snapping Image with Hamamatsu...")
```

```
    core.snap_image()
    # Produce numpy array of camera image
    tagged_image = core.get_tagged_image()
    tagged_image_height = tagged_image.tags['Height']
    tagged_image_width = tagged_image.tags['Width']
    # Must import numpy as np
    pixels = np.reshape(tagged_image.pix,
newshape=[tagged_image_height,tagged_image_width])
    print ("Image Captured, Exported as Array!")
    # Return numpy array of pixel values
    return pixels, tagged_image_height, tagged_image_width

def brightfield_view_save(image_array, exp_name, image_name, x_pos, theta_pos,
view_bool, tiff_bool):
    """
    Take image data array (Hamamatsu) and saves with position metadata in title

    Parameters
    ----------
    image_array : array
        Take in image data from camera (Hamamatsu)
    exp_name : str
        Defines subfolder from overall experiment name - keep the same
    image_name : str
        Name to save image file under
    x_pos : float
        X position to name image file (metadata in title)
    y_pos : float
        Y position to name image file (metadata in title)
    view_bool : bool
        True = view in terminal; False = don't view - may be necessary for saving as employs
imshow (possible bug, keep as True)
    tiff_bool : bool
        True = save as TIFF file; False = don't save as TIFF

    Returns
    -------
    None.

    """
    folder = create_subfolder(exp_name)
    file_path = os.path.join(folder, image_name)
    # Take brightfield image as numpy array
    # Must import matplotlib.pyplot as plt
    if view_bool:

        plt.title(f"{exp_name}_{image_name}: x={x_pos} um theta={theta_pos} um")
        plt.imshow(image_array)
    print("Saving as .png ...")
    plt.imsave(f'{file_path}_x_{int(x_pos)}um_{int(theta_pos)}deg.png', image_array)
    if tiff_bool:
        # Must import tifffile as tf
        print("Saving as .tif ...")
        tf.imwrite(f"{file_path}_x_{int(x_pos)}um_{int(theta_pos)}deg.tif", image_array)
```

```
    print ("Hamamatsu Images Saved!")



# ---------- Pycromanager Initialise ----------
# Get object representing micro-manager core
# Also define pycromanager device labels for Prior Stage and Hamamatsu Camera
MM_Core, XY_Stage, Camera = initialise_pycromanager(Core())

# ========== 2. INITIALISE KINESIS ==========
# ---------- Kinesis Modules ----------

import py_thorlabs_ctrl.kinesis # Import rwalle's frontend module
# init function automatically determines if the installation path is valid
# This must contain Thorlabs.MotionControl.Controls.dll
py_thorlabs_ctrl.kinesis.init(r'C:\Program Files\Thorlabs\Kinesis')
# Import module from downloaded github folders
# Seems to have nested classes: KCubeDCServo(KCubeMotor(Motor)))
from py_thorlabs_ctrl.kinesis.motor import KCubeDCServo

# ---------- Rotation Stage Functions ----------
def initialise_rotation_stage(ser_no):
    """
    Initialise Kinesis KCube and create stage object

    Parameters
    ----------
    ser_no : int
        Serial no. of KCube

    Returns
    -------
    stage : object
        KCube object with functions such as home etc.

    """
    print( "========== Initialising Kinesis ==========")
    stage = KCubeDCServo(ser_no)
    print("Kinesis Initialised!")
    return stage

def enable_rotation_stage(rot_device):
    """
    Create and Enable KCube (Initialise, Start Polling, Enable, Load Motor Config)

    Parameters
    ----------
    rot_device : function-like
        Callable KCube object

    Returns
    -------
    None.

    """
```

```
    print("Creating KCube Controller...")
    rot_device.create()
    print("Controller Created!")
    print("Enabling KCube Controller...")
    rot_device.enable()
    print(f"Enabled K-Cube Named {rot_device.get_name()}, Serial
No.{rot_device.get_serial_number()}")

def home_rotation_stage(rot_device):
    """
    Home KCube: Check if homed, visualise homing, and confirm

    Parameters
    ----------
    rot_device : function-like
        Callable KCube object

    Returns
    -------
    None.

    """
    # Check whether the rotation stage is homed: True/False?
    print(f"Homed? {rot_device.is_homed()}")
    if not rot_device.is_homed():
        print("Start Homing")
        rot_device.home()
        #  Visualise as rotation stage is homing
        while not rot_device.is_homed():
            # Check if rotation stage is busy / still moving
            print (f"Homing... Moving? {rot_device.is_moving()}; Position =
{rot_device.get_position()}")
            time.sleep(0.5)

    time.sleep(1.0)
    print(f"========== Now Homed! Position = {rot_device.get_position()} ==========")

def disable_rotation_stage(rot_device):
    """
    Disable KCube Controller before turning off

    Parameters
    ----------
    rot_device : function-like
        Callable KCube object

    Returns
    -------
    None.

    """
    # Disable Device
    print ("Disabling KCube Controller...")
    rot_device.disable()
```

```
    print("Disabled KCube Controller!")
    time.sleep(1.0)

def disconnect_rotation_stage(rot_device):
    """
    Disconnect KCube from PC

    Parameters
    ----------
    rot_device : funciton-like
        Callable KCube object

    Returns
    -------
    None.

    """
    # Disconnect Device
    print("Disconnecting KCube Controller...")
    rot_device.disconnect()
    print("Disconnected KCube Controller!")
    time.sleep(1.0)

def set_vel_accel_rotation_stage(rot_device, max_velocity, acceleration):
    """
    Set max velocity and acceleration parameters for rotation stage

    Parameters
    ----------
    rot_device : function-like
        Callable KCube object
    max_velocity : float
        Define max velocity in degrees/sec
    acceleration : float
        Define acceleration in degrees/sec/sec

    Returns
    -------
    current_velo : float
        Newly defined velocity value
    current_accel : float
        Newly defined acceleration value

    """
    # Backend: set_velocity function seems to have bug with undefined "params" - replaced
with velocity_params
    print(f"Setting max velocity to {max_velocity}, acceleration to {acceleration}")
    rot_device.set_velocity(max_velocity, acceleration)
    # Confirm whether velocity parameters set properly
    current_velo = rot_device.get_velocity()
    current_accel = rot_device.get_accelaration()
    print(f"Velocity set to {current_velo}, Accel set to {current_accel}")
    time.sleep(1.0)
    return current_velo, current_accel
```

```
def theta_check_position(rot_device):
    """
    Check current theta position from KCube

    Parameters
    ----------
    rot_device : funciton-like
        Callable KCube object

    Returns
    -------
    current_pos : float
        Current theta position (degrees)

    """
    current_pos = rot_device.get_position()
    return current_pos

def wait_for_theta_stage(rot_device):
    """
    Wait for KCube to stop moving; if true wait 0.1 sec

    Parameters
    ----------
    rot_device : function-like
        Callable KCube object

    Returns
    -------
    None.

    """
    while rot_device.is_moving():
        print(f"Still Moving; now at {rot_device.get_position()}")
        time.sleep(0.1)

def theta_absolute_move(theta_position, rot_device):
    """
    Move to absolute theta position on KCube; wait for stage to start moving before polling position

    Parameters
    ----------
    theta_position : float
        Theta value (degrees) to move round to
    rot_device : function-like
        Callable KCube object

    Returns
    -------
    None.

    """
```

```
    rot_device.move_absolute(theta_position)
    # Important to let stage start moving before polling whether it is moving
    time.sleep(2.0)

# ---------- Kinesis Rotation Stage Initialise----------
try:
    # Serial number of KCube
    kcube_serial = 27264246
    KCube = initialise_rotation_stage(kcube_serial)
    # Create K-Cube controller instance
    enable_rotation_stage(KCube)
    # Set max velocity and acceleration parameters for rotation stage
    velocity = 20.0
    acceleration = 10.0
    set_velocity, set_acceleration = set_vel_accel_rotation_stage(KCube, velocity,
acceleration)

    # Kinesis Stage Homing
    # Check position - seems to return the value in degrees
    check_theta_once = theta_check_position(KCube)
    print(f"What's the position? At {check_theta_once}")
    #  Home Rotation Stage
    home_rotation_stage(KCube)

    # Wait a bit
    print("Waiting for 2 seconds...")
    time.sleep(2.0)
```

```
except Exception as e:
    print(f"UH OH! An error occurred in KCube: {e}")

    print ("Shutting Down KCube...")
    # Disable Rotation Stage
    disable_rotation_stage(KCube)

    # Disconnect Rotation Stage
    disconnect_rotation_stage(KCube)

print("========== Kinesis Rotation Stage Ready! ==========")


# ---------- Radius value functions ----------
def get_radius_value(spacer_height_c, z_position, origin_f):
    """
    Get radius position (distance of focal volume from axis of rotation)

    Parameters
    ----------
    spacer_height_c : float
        Lens tube height (cm) to raise objective lens
    z_position : float
        Z position of Nikon Ti
    origin_f : float
        Default = 136.9 cm; Total distance between bottom of Nikon Ti to axis of rotation
```

```
    Returns
    -------
    r_position : float
        Radius value from axis of rotation (cm)

    """
    while True:
        try:
            c_value = float(input(spacer_height_c))
            print(f"You entered: c= {c_value} mm")
            lens_height = z_position*0.001 + c_value + 24.0 + 38.6
            print(f"So lens height: h = {lens_height} mm")
            r_position = origin_f - lens_height
            print(f"So r position value: r = {r_position} mm")

            return r_position
        except ValueError:
            print("Invalid input. Please enter a valid float value.")

def manual_focus_pause(core, get_z_keyword, dance_keyword, continue_keyword):
    """
    Pause script to allow manual focusing using camera feed in micromanager

    Parameters
    ----------
    core : function-like
        Core imported from pycromanager module
    get_z_keyword : str
        Custom keyword to trigger reading of Z position on Nikon Ti
    dance_keyword : str
        Custom keyword to initiate boogie time
    continue_keyword : str
        Custom keyword to allow rest of script to run

    Returns
    -------
    optimal_z : float
        Record Z position as recorded from camera - use to calculate radius r

    """
    optimal_z = None
    print("Manually focus camera to acheive optimal z position!")
    while True:
        user_input = input(f"Enter '{get_z_keyword}' to capture focused z position,
'{dance_keyword}' to perform a dance, or '{continue_keyword}' to carry on script:
").strip().lower()
        if user_input == get_z_keyword.lower():
            print("Capturing z position...")
            optimal_z = z_check_position(core)
            print(f"Optimal z position saved as {optimal_z}. Happy?")

        elif user_input == dance_keyword.lower():
            # Perform operation 2 (displaying a little dance)
            print("Performing a little dance for you...")
```

```
        dance_function()
        print("Dance completed!")
    elif user_input == continue_keyword.lower():
        # Continue script
        print("Continuing script...")
        break
    else:
        print(f"Invalid input. Enter '{get_z_keyword}' to capture focused z position,
'{dance_keyword}' to perform a dance, or '{continue_keyword}' to carry on script: ")

  return optimal_z

origin_f = 136.9 # mm

current_z_position = z_check_position(MM_Core)
# Want to find radius value manually at each (x, theta) position
# Therefore comment out a global radius value:
# cylinder_radius_global = get_radius_value("Enter the spacer height (c) mm: ",
current_z_position, origin_f)

# ========== 3. DEFINE X, THETA POSITIONS ==========

# Global experiment name without date
experiment_name_global = "FEM_HEAD_1"

# ---------- Cylinder Acquisition Parameters ----------
number_of_theta_steps = 9
```

```
starting_x_position = 6487
finishing_x_position = -23487
number_of_x_steps = 8

ORIGIN_X, ORIGIN_Y  = xy_check_position(MM_Core)
# Move Prior stage to first position
print("Move to first position (x, fixed y)")
xy_absolute_move(MM_Core, int(ORIGIN_X), int(ORIGIN_Y))

# Create positions to iterate through
def make_cylindrical_position_list(th_step_no, x_start, x_finish, x_step_no):
  """
  Make list of theta and x positions to iterate through for cylindrical scan

  Parameters
  ----------
  th_step_no : int
    Total number of positions for rotation in theta
  x_start : float
    Starting stage position (um)
  x_finish : float
    Sinishing stage position (um)
  x_step_no : int
    Total number of positions for x translation

  Returns
  -------
```

```
    th_pos_list : float
        Array of absolute theta positions (degrees)
    x_pos_list : float
        Array of absolute x positions (um)

    """
    # Define theta position list
    th_pos_list = np.linspace(0, 360, th_step_no)
    # Define x position list
    x_pos_list = np.linspace(x_start, x_finish, x_step_no)

    return th_pos_list, x_pos_list


THETA_POSITIONS_LIST, X_POSITIONS_LIST =
make_cylindrical_position_list(number_of_theta_steps, starting_x_position,
finishing_x_position, number_of_x_steps)

# ========== 4. SPHERICAL SWIR SCAN ==========
print("GET READY for SWIR spectral capture...")
print("Switch kinematic cube for SWIR beampath...")
wait_for_keyword("swir")   # Wait for "swir" keyword before continuing
#  Initialise SWIR Spectrometer
# ---------- Ocean Optics Modules ----------
import seabreeze.spectrometers as sb
# Can call dictionary of supported features via
sb.Spectrometer.from_serial_number(spectrometer_serial).features
```

```
# ---------- SWIR Ocean Optics Spectrometer Functioncs ----------
# Initialise: Look for devices, Connect, Define spectrometer to use

def look_for_spectrometers():
    """
    Searches for spectrometer and prints as list, raised error if none connected

    Raises
    ------
    ValueError
        DESCRIPTION.

    Returns
    -------
    None.

    """
    print("Looking for Ocean Optics spectrometers...")
    devices_list = sb.list_devices()
    if not devices_list:
        raise ValueError("No Ocean Optics spectrometer found!")
    print(f"Devices List = {devices_list}")

def initialise_spectrometer(ser_no):
    """
    Initialise specific OO spectrometer via serial number: NIRQuest = "NQ25B0171", USB2K =
"USB2+R00019"
```

```
    Parameters
    ----------
    ser_no : str
        Serial no. NIRQuest = "NQ25B0171", USB2K = "USB2+R00019"

    Returns
    -------
    spectrometer : function-like
        Callable Ocean Optics spectrometer object

    """
    spectrometer = sb.Spectrometer.from_serial_number(ser_no)
    print(f"Chosen spectrometer {spectrometer}")

    return spectrometer

def close_spectrometer(spec_device):
    """
    Disconnect and close spectrometer

    Parameters
    ----------
    spec_device : funciton-like
        Callable Ocean Optics spectrometer object

    Returns
    -------
    None.

    """
    print("Closing Spectrometer...")
    spec_device.close()
    time.sleep(1.0)
    print ("Spectrometer Closed!")

# Set integration time in milliseconds
def set_integration_time(spec_device, milsec):
    """
    Set integration time of Ocean Optics spectrometer (ms)

    Parameters
    ----------
    spec_device : object
        Callable Ocean Optics spectrometer object
    milsec : int
        Integration time in ms

    Returns
    -------
    None.

    """
    spec_device.integration_time_micros(milsec * 1000)
```

```
    print(f"Integration time set to {milsec} ms")

# Grab wavelength and intensity
def capture_spectrum(spec_device):
    """
    Capture spectrum from Ocean Optics spectrometer

    Parameters
    ----------
    spec_device : object
        Callable Ocean Optics spectrometer object

    Returns
    -------
    x : float
        Array of wavelengths
    y : float
        Array of intensities

    """
    print("Capturing Spectrum...")
    x = spec_device.wavelengths()
    y = spec_device.intensities()
    print("Spectrum Captured!")
    return x, y

def capture_averaged_spectrum(spec_device, no_of_averages):
    """
    Capture averaged spectrum from Ocean Optics spectrometer

    Parameters
    ----------
    spec_device : object
        Callable Ocean Optics spectrometer object
    no_of_averages : int
        Number of captures to average over

    Returns
    -------
    wavelengths : float
        Array of wavelengths
    average_spectrum : float
        Array of averaged intensities

    """
    print(f"Capturing average of {no_of_averages}")
    wavelengths = spec_device.wavelengths()
    accummulated_spectra = spec_device.intensities()
    for i in range(no_of_averages-1):
        accummulated_spectra += spec_device.intensities()
    average_spectrum = accummulated_spectra/no_of_averages
    return wavelengths, average_spectrum

def capture_bkgd(spec_device, no_of_averages, keyword_1, keyword_2, keyword_continue):
```

```
    """
    Perform background spectra capture with Ocean Optics; manual pause and keyword entry to allow turning on/off lamp

    Parameters
    ----------
    spec_device : function-like
        Callable Ocean Optics spectrometer object
    no_of_averages : int
        Number of captures to average over
    keyword_1 : str
        Keyword to trigger (or re-trigger) background spectrum capture
    keyword_2 : str
        Keyword to initiate a boogie
    keyword_continue : str
        Keyword to allow script to continue

    Returns
    -------
    y_bkgd : float
        Array of background signal from Ocean Optics

    """
    y_bkgd = None
    print("Ready to Capture SWIR Background!")
    while True:
        user_input = input(f"Enter '{keyword_1}' to perform dark background capture, '{keyword_2}' to perform a dance, or '{keyword_continue}' to carry on script:")
        if user_input == keyword_1.lower():
            print("Performing dark background capture...")
            # x_bkgd = spec_device.wavelengths()
            # y_bkgd = spec_device.intensities()

            x_bkgd, y_bkgd = capture_averaged_spectrum(spec_device, no_of_averages)
            print("Plotting dark background...")
            plt.plot(x_bkgd, y_bkgd)
            plt.title("Dark SWIR Background")
            plt.xlabel('Wavelength (nm)')
            plt.ylabel('Intensity')
            plt.grid(True)
            plt.show()
            print("What do you think?")

        elif user_input == keyword_2.lower():
            # Perform operation 2 (displaying a little dance)
            print("Performing a little dance for you...")
            dance_function()
            print("Dance completed!")

        elif user_input == keyword_continue.lower():
            # Continue script
            print("Continuing script...")
            break
```

```
    else:
        print(f"Invalid input. Enter '{keyword_1}' to perform dark background capture,
'{keyword_2}' to perform a dance, or '{keyword_continue}' to carry on script:")
    return y_bkgd

def capture_bkgd_corr_spectrum(spec_device, no_of_averages, bkgd_intens, exp):
    """
    Capture averaged spectrum from Ocean Optics and subtract the averaged background
signal; return arrays of wavel and intens

    Parameters
    ----------
    spec_device : function-like
        Callable Ocean Optics spectrometer object
    no_of_averages : int
        Number of captures to average over
    bkgd_intens : array
        Array of background signal from Ocean Optics
    exp : str
        Defines subfolder from overall experiment name - keep the same

    Returns
    -------
    x_corr : array
        Array of wavelengths from Ocean Optics
    y_corr : array
        Array of background corrected intensities from Ocean Optics
    """
    print("Capturing Spectrum...")

    x, y = capture_averaged_spectrum(spec_device, no_of_averages)

    print("Spectrum Captured!")
    plt.plot(x, y, label="Raw")
    plt.plot(x, bkgd_intens, label="Dark Background")
    # plt.title("Raw SWIR Intensity")
    plt.xlabel('Wavelength (nm)')
    plt.ylabel('Intensity')
    # plt.grid(True)
    # plt.show()

    print("Subtracting Background...")
    x_corr = x
    y_corr = (y - bkgd_intens)
    print("Background Corrected!")
    plt.plot(x_corr, y_corr, label="Corrected")
    plt.title(f"Background Corrected SWIR Intensity; {exp} ms, {no_of_averages} Average")
    plt.xlabel('Wavelength (nm)')
    plt.ylabel('Intensity')
    plt.legend(loc="upper right")
    plt.grid(True)
    plt.show()
    return x_corr, y_corr
```

```
def save_spectrum(x, y, filename, folder):
    """
    Save wavelength and intensities arrays to .csv file in subfolder

    Parameters
    ----------
    x : array
        Wavelength values
    y : array
        Intensity values
    filename : str
        .csv filename, should store some metadata here (no date added here)
    folder : str
        Subfolder to save .csv to

    Returns
    -------
    None.

    """
    print("Saving Spectrum to File...")

    file_path = os.path.join(folder, filename)

    with open(file_path, 'w') as file: #Open file and put in writing mode
        file.write("Wavelength (nm), Intensity\n")
        for wavel, inten in zip(x,y):
            file.write(f"{wavel}, {inten}\n")
    print("Spectrum Saved to File!")

# Plot spectrum and show graph
def plot_spectrum(x ,y, milsec, avg, spec_device, png_name, x_coord, theta_coord, folder):
    """
    Plot and Save graph of spectrum, metadata recorded in filename

    Parameters
    ----------
    x : array
        Wavelength values
    y : array
        Intensity values
    milsec : TYPE
        DESCRIPTION.
    avg : TYPE
        DESCRIPTION.
    spec_device : TYPE
        DESCRIPTION.
    png_name : TYPE
        DESCRIPTION.
    x_coord : TYPE
        DESCRIPTION.
    theta_coord : TYPE
        DESCRIPTION.
```

```
    folder : TYPE
        DESCRIPTION.

    Returns
    -------
    None.

    """
    print("Plotting Spectrum...")
    plt.plot(x, y)
    plt.xlabel('Wavelength (nm)')
    plt.ylabel('Intensity')
    plt.title(f"SWIR at {x_coord} um, {theta_coord} º, Exp: {milsec} ms , {avg} Average")
    plt.grid(True)
    # plt.text(f"From {spec_device}")
    file_path = os.path.join(folder, png_name)
    plt.savefig(file_path)
    print("Spectrum Plotted!")
    plt.show()

# ---------- CYLINDRICAL SWIR FUNCTION ----------

def SWIR_SPHERE_3D_xy_theta_scan(th_pos_list, x_pos_list, fixed_y_pos, rot_device,
spec_device, integ_time, pycro_core, averages):
    """
    Rotate through predefined x and theta position list and capture radius value, and
background corrected, averaged spectra from Ocean Optics

    Parameters
    ----------
    th_pos_list : array
        Predefined list of theta positions from previous function & brightfield scan
    x_pos_list : array
        Predefined list of x position from previous function & brightfield scan
    fixed_y_pos : float
        Predefined fixed y position from previous function & brightfield scan
    rot_device : function-like
        Callable KCube object
    spec_device : function_like
        Callable NIRQuest spectrometer object
    integ_time : float
        Integration time for file name metadata
    pycro_core : function-like
        Callable pycromanager MM_Core
    averages : int
        Number of captures to average over

    Returns
    -------
    None.

    """
    # Capture background spectra
    swir_background = capture_bkgd(spec_device, averages, 'background', 'dance', 'carryon')
```

```
# Initialize an empty list to store the z position data and index tuples
main_df = []
x_theta_index_tuples = []

# Prepare theta positions to iterate over (previously defined)
print(f"Theta Positions: {th_pos_list}")
# Prepare x positions to iterate over (previously defined)
print(f"X Positions: {x_pos_list}")
# Fixed y position (previously defined)
FIXED_Y_POS = fixed_y_pos  # Use CAPS to fit convention of this function
# Take fixed y position (previously defined) as argument
print(f"Fixed Y Position: {fixed_y_pos}")

# Create subfolder if it doesn't exist already
subfolder = create_subfolder(experiment_name_global)

# For sphere, capture z and r value at each (x, theta) position

# For each xy position
# X_POS is the next position to move to after having finished rotating and capture spectra
for X_POS in tqdm(x_pos_list, desc='Total X Positions', unit='row'):
    # For each theta position
    # Can start from pos_list[1:] if homed since this would otherwise produce 3 zero deg
positions
    # Therefore THETA_POS is actually the next position to move to
    for THETA_POS in tqdm(th_pos_list[1:], desc='Total Theta Positions', unit='angles'):
```

```
        # Check current theta position
        CURRENT_THETA = theta_check_position(rot_device)
        # Check current x position
        CURRENT_X, CURRENT_Y = xy_check_position(pycro_core)
        print(f"Currently at theta={CURRENT_THETA}º, x={CURRENT_Y}")

        print("Now pausing script to allow manual focusing via camera...")
        print("Switch mirrors for CAMERA beampath...")
        # Capture z position
        Z_VALUE = manual_focus_pause(MM_Core, 'grab', 'dance', 'asyouwere')

        R_VALUE = get_radius_value("Enter the spacer height (c) mm: ", Z_VALUE, origin_f)

        # Want to save z and r position for every x_pos and theta_pos
        current_header = np.asarray(['Z','R'])
        current_values = np.asarray([Z_VALUE, R_VALUE])

        # Want header to be list of ['Z', 'R', lambda1, lambda2, ..., lambda512]
        # Want results to be list of [z_position, r_value, I(lambda1), I(lambda2), ...,
I(lambda512)]

        # Pause to change from camera to SWIR path
        print("GET READY for SWIR spectral capture...")
        print("Switch mirrors for SWIR beampath...")
        wait_for_keyword('swir')

        # Capture spectrum
```

```
        print(f"\rCapturing SWIR at X: {X_POS} um; Theta Position: {CURRENT_THETA} deg ",
flush=True)
        # Wavelengths and intensities data as list objects
        # wavelengths, intensities = capture_spectrum(spec_device)
        wavelengths, intensities = capture_bkgd_corr_spectrum(spec_device, averages,
swir_background, integ_time)

        # Plot & Save Spectrum Graph
        graph_name =
f"{date.today()}_{experiment_name_global}_SWIRgraph_{int(CURRENT_THETA)}deg_{CURRE
NT_X}xpos.png"
        plot_spectrum(wavelengths, intensities, integ_time, averages, spec_device,
graph_name, CURRENT_X, CURRENT_THETA, subfolder)

        # Append spectral data to list to be added to dataframe
        full_current_header = np.append(current_header, wavelengths)
        full_current_values = np.append(current_values, intensities)

        # Convert current position results to labelled dataframe
        current_position_df = convert_spectrum_to_dataframe(full_current_header,
full_current_values, CURRENT_X)
        # Save spectrum dataframe as .csv
        current_position_df_name =
f"{date.today()}_{experiment_name_global}_SWIRdata_ZR_I(lambda)_{int(CURRENT_THETA)}
deg_{CURRENT_X}xpos.csv"
        save_dataframe_to_csv(current_position_df, current_position_df_name, subfolder)
```

```
    # Add z and r position to zr position data list (convert to main dataframe later)
    # Create an index tuple with two levels ('x' and 'y')
    index_tuple = (CURRENT_X, CURRENT_THETA)

    # Append z data and index tuple to the respective lists
    main_df.append(full_current_values)

    x_theta_index_tuples.append(index_tuple)

    # Move to next theta position
    print("Move to next theta position...")
    theta_absolute_move(THETA_POS, rot_device)
    wait_for_theta_stage(rot_device)
    print(f"Now at position: {theta_check_position(rot_device)}°")

  # Move to next x
  print("Move to next x position...")
  xy_absolute_move(pycro_core, X_POS, FIXED_Y_POS)
  wait_for_xy_stage(pycro_core)
  x_check, y_check = xy_check_position(pycro_core)
  print(f"Now at position: {x_check} x position")

print ("All positions reached!")
# Now save all data from dataframe into .csv
print("Creating Z R Position Dataframe...")
# Header data list should be defined from last iteration of loop
z_r_lambda_columns = full_current_header
```

```
    print("Creating X, THETA Multi Index...")
    # Create a MultiIndex from the list of index tuples
    multi_index = pd.MultiIndex.from_tuples(x_theta_index_tuples, names=['X', 'THETA'])
    print("Creating Full 3D Dataframe...")
    # Create a DataFrame with the MultiIndex and use the wavelength data as columns
    full_3D_dataframe = pd.DataFrame(main_df, index=multi_index,
columns=z_r_lambda_columns)
    print(full_3D_dataframe)



    # Save Main Dataframe to .csv
    print("Saving Main Dataframe...")
    save_dataframe_to_csv(full_3D_dataframe,
f"{date.today()}_{experiment_name_global}_SWIR_FULL_DATAFRAME.csv", subfolder)

    print ("All done! Great job!")
    dance_function()

# ---------- CARRY OUT SWIR SCAN ----------
print("========== STARTING UP SWIR SCAN ==========")


if __name__ == "__main__":
    try:
        # ---------- Initialise NIRQuest Spectrometer ----------
        # Scan ports for Ocean Optics spectrometers, print device list
        look_for_spectrometers()
        # Choose spectromter via serial number
        spectrometer_serial = "NQ25B0171" #NIRQuest
        # Create spectrometer device
        NIRQuest = initialise_spectrometer(spectrometer_serial)

        # Set SWIR capture parameters
        integration_time_ms_swir = 10
        no_of_averages_swir = 1000
        set_integration_time(NIRQuest, integration_time_ms_swir)

        SWIR_SPHERE_3D_xy_theta_scan(THETA_POSITIONS_LIST, X_POSITIONS_LIST,
ORIGIN_Y, KCube, NIRQuest, integration_time_ms_swir, MM_Core, no_of_averages_swir)

    except Exception as e:
        print(f"UH OH! An error occurred in SWIR 3D CYLINDER Execution: {e}")

        # If there's an issue then disconnect KCUbe here - otherwise will stay connected for
Raman
        # Disable Rotation Stage
        disable_rotation_stage(KCube)

        # Disconnect Rotation Stage
        disconnect_rotation_stage(KCube)

    finally:
        print("========== FINISHED SWIR, SWITCHING OFF NIRQuest ==========")
        print ("Shutting Down NIRQuest...")
        time.sleep(2.0)
```

```
    # Close spectrometer
    close_spectrometer(NIRQuest)

    print("SWIR All ShutDown Complete!")

print("========== FINISHED SWIR SCAN ==========")

# Move Prior tage back to first position
print("Moving back to first position (x, fixed y)")
xy_absolute_move(MM_Core, int(ORIGIN_X), int(ORIGIN_Y))

# ========== 5. SWITCH MODALITIES ==========

# Wait for terminal input allowing time to switch out optics from SWIR to Raman
print("GET READY for RAMAN spectral capture...")
print("Switch kinematic cube for RAMAN beampath...")
wait_for_keyword("raman")   # Wait for "raman" keyword before continuing


# ========== CYLINDRICAL RAMAN SCAN ==========

# ---------- Import sif_parser to handle Andor camera images ----------
import sif_parser

# ---------- Import Andor camera modules ----------
from pyAndorSDK2 import atmcd, atmcd_codes, atmcd_errors
```

```
cam_sdk = atmcd()     # Camera library known as atmcd
codes = atmcd_codes

# ---------- Import Andor spectrograph modules ----------
# Import Andor spectrograph modules
from pyAndorSpectrograph.spectrograph import ATSpectrograph

spec_sdk = ATSpectrograph()    # Spectrograph library known as ATSpectrograph

# ---------- Raman Andor Camera Functions ----------
# Some API functions need to remain in main code for global vairables and or quirks of
system
# Some functions deprecated - keep all for now

def andor_initialise_camera():
    """
    Initialise Andor iDus camera, and return status value to check for errors

    Returns
    -------
    ret_val_local : bool-like
        Status value (Andor specific) that checks for errors

    """
    print("Initialising Andor camera...")
    # Need first instance of ret_val here
    ret_val_local = cam_sdk.Initialize("")     # Initialise camera library
```

```
    print("Function Initialize returned {}".format(ret_val_local))
    # shamrock = spec_sdk.Initialize("")      # Initialise spectrograph library
    # print("Function Initialize returned
{}".format(spec_sdk.GetFunctionReturnDescription(shamrock, 64)[1]))
    return ret_val_local

def andor_get_serial(ret_val_local):
    """
    Get serial number of iDus camera, performs internal status error check

    Parameters
    ----------
    ret_val_local : bool-like
        Status value (Andor specific) that checks for errors

    Returns
    -------
    ret_val_local : bool-like
        Updated status value (Andor specific) that checks for errors
    iSerialNumber : str
        Serial number of iDus camera

    """
    if atmcd_errors.Error_Codes.DRV_SUCCESS == ret_val_local:
        (ret_val_local, iSerialNumber) = cam_sdk.GetCameraSerialNumber()     # Get camera
serial no.
        print("Function GetCameraSerialNumber returned {}; Serial No: {}".format(ret_val_local,
iSerialNumber))
        time.sleep(1.0)
    return ret_val_local, iSerialNumber

def andor_cool_camera(ret_val_local, target_temp):
    """
    Cool down iDus camera, prints update in terminal whilst camera is cooling down

    Parameters
    ----------
    ret_val_local : bool-like
        Status value (Andor specific) that checks for errors
    target_temp : int
        Target temperature for iDus camera

    Returns
    -------
    ret_val_local : bool-like
        Updated status value (Andor specific) that checks for errors

    """
    if atmcd_errors.Error_Codes.DRV_SUCCESS == ret_val_local:
        ret_val_local = cam_sdk.SetTemperature(target_temp)    # Set camera temperature to - 60
C
        print("Function SetTemperature returned {}; Target temperature {} C".format(ret_val_local,
target_temp))
```

```
    ret_val_local = cam_sdk.CoolerON()      # Cool down camera
    print("Function CoolerON returned {}".format(ret_val_local))

    print("Waiting for Temperature to stabilise...")
    while ret_val_local != atmcd_errors.Error_Codes.DRV_TEMP_STABILIZED:  # Visualise
cooling down progress
        time.sleep(5)
        (ret_val_local, temperature) = cam_sdk.GetTemperature()
        print("Function GetTemperature returned {}; Current temperature = {}
C".format(ret_val_local, temperature), end='\r')
        print("")
    # Catches the above print statement and preserves the below print statement
    print("")
    print("Temperature stabilised!")
    time.sleep(1.0)
  return ret_val_local

def andor_set_exp_time(ret_val_local, exp_time):
  """
  Set exposure time for Andor iDus camera in ms, get confirmation from Andor status codes

  Parameters
  ----------
  ret_val_local : bool-like
    Status value (Andor specific) that checks for errors
  exp_time : float
    Set Raman exposure time (secs) for Andor iDus

  Returns
  -------
  ret_val_local : bool-like
    Updated status value (Andor specific) that checks for errors
  fminExposure : float
    Confirmation from Andor iDus for exposure time
  fAccumulate : float
    Confirmation from Andor iDus for accumulation(?)
  fKinetic : float
    Confirmation from Andor iDus for kinetic(?)

  """
  if atmcd_errors.Error_Codes.DRV_SUCCESS == ret_val_local:
    ret_val_local = cam_sdk.SetExposureTime(exp_time)
    print("Function SetExposureTime returned {} time = {}".format(ret_val_local, exp_time))
    # Check Acqusition parameters?
    (ret_val_local, fminExposure, fAccumulate, fKinetic) = cam_sdk.GetAcquisitionTimings()
    print("Function GetAcquisitionTimings returned {} exposure = {} accumulate = {} kinetic =
{}".format(
        ret_val_local, fminExposure, fAccumulate, fKinetic))
  return ret_val_local, fminExposure, fAccumulate, fKinetic

def andor_make_acquisition(ret_val_local):
  """
```

```
    Perform capture with Andor iDus; doesn't return an image so requires another function to
grab array

    Parameters
    ----------
    ret_val_local : bool-like
        Status value (Andor specific) that checks for errors

    Returns
    -------
    ret_val_local : bool-like
        Updated status value (Andor specific) that checks for errors

    """
    if atmcd_errors.Error_Codes.DRV_SUCCESS == ret_val_local:
        ret_val_local = cam_sdk.PrepareAcquisition()   # Prepare for Acquisition - triggered by
GetAcquisition
        print("Function PrepareAcquisition returned {}".format(ret_val_local))

        ret_val_local = cam_sdk.StartAcquisition()
        print("Function StartAcquisition returned {}".format(ret_val_local))

        ret_val_local = cam_sdk.WaitForAcquisition()
        print("Function WaitForAcquisition returned {}".format(ret_val_local))
    return ret_val_local

def andor_grab_2D_image(ret_val_local, xpixels_local, ypixels_local, arr_local):
    """
    Grab image from Andor iDus following acquisition

    Parameters
    ----------
    ret_val_local : bool-like
        Status value (Andor specific) that checks for errors
    xpixels_local : int
        Image width (pixels)
    ypixels_local : int
        Image height (pixels)
    arr_local : array
        Image data array

    Returns
    -------
    None.

    """
    if atmcd_errors.Error_Codes.DRV_SUCCESS == ret_val_local:
        ret_val_local = cam_sdk.SetImage(1, 1, 1, xpixels_local, 1, ypixels_local)
        print("Function SetImage returned {} hbin = 1 vbin = 1 hstart = 1 hend = {} vstart = 1 vend =
{}".format(
            ret_val_local, xpixels_local, ypixels_local))
    # If I want to show 2D image
        arr_local = np.fliplr(np.rot90(np.reshape(arr_local, (xpixels_local, ypixels_local)), 1))
        plt.matshow(arr_local)
```

```
    plt.show()
  return(ret_val_local)

def andor_save_siffile(ret_val_local, subfolder, exposure_time, x_posit, y_posit, exp_name):
  """
  DEPRECIATED: Use "singelpoint" below with xy position in "sif_label" Save image array as .sif before handling as Python friendly image

  Parameters
  ----------
  ret_val_local : bool-like
    Status value (Andor specific) that checks for errors
  subfolder : str
    Subfolder to save .sif file to
  exposure_time : float
    Raman exposure time in sec
  x_posit : float
    X position on Prior stage
  y_posit : float
    Y position on Prior stage

  Returns
  -------
  ret_val_local : bool-like
    Status value (Andor specific) that checks for errors
  sif_filename : str
    Final filename for .sif image file
  """
  print ("Saving as .sif...")
  sif_filename = f'{date.today()}_{exp_name}_RAMANsif_{int(exposure_time)}sec_{int(x_posit)}_xpos_{y_posit}_ypos.sif'
  sif_filepath = os.path.join(subfolder, sif_filename)
  # Important to have "subfolder/sif file name" to save in correct place
  ret_val_local = cam_sdk.SaveAsSif(sif_filepath)
  print("Function SaveAsSif returned {}".format(ret_val_local))
  print (".sif Saved!")
  time.sleep(1.0)
  return ret_val_local, sif_filepath

def andor_save_siffile_single_position(ret_val_local, subfolder, exposure_time, sif_label, exp_name):
  """
  Save image array as .sif before handling as Python friendly image

  Parameters
  ----------
  ret_val_local : bool-like
    Status value (Andor specific) that checks for errors
  subfolder : str
    Subfolder to save .sif file to
  exposure_time : float
    Raman exposure time in sec
```

```
    iteration : str
        Label to identify the sif file e.g. "Repeat_no._1"

    Returns
    -------
    ret_val_local : bool-like
        Status value (Andor specific) that checks for errors
    sif_filename : str
        Final filename for .sif image file

    """
    print ("Saving as .sif...")
    sif_filename =
f'{date.today()}_{exp_name}_RAMANsif_{int(exposure_time)}sec_{sif_label}.sif'
    sif_filepath = os.path.join(subfolder, sif_filename)
    # Important to have "subfolder/sif file name" to save in correct place
    ret_val_local = cam_sdk.SaveAsSif(sif_filepath)
    print("Function SaveAsSif returned {}".format(ret_val_local))
    print (".sif Saved!")
    time.sleep(1.0)
    return ret_val_local, sif_filepath

def andor_plot_spectra(subfolder, x, y, x_position, y_position, exp_name):
    """
    Plot and save .png of Raman spectrum

    Parameters
    ----------
    subfolder : str
        Subfolder directory to save Raman spectrum .png to
    x : array
        Wavelength values to plot
    y : array
        Raman intensity values to plot
    x_position : float
        X position on Prior stage
    y_position : float
        Y position on Prior stage

    Returns
    -------
    None.

    """
    print("Plotting Raman Spectrum...")
    plt.plot(x,y)
    plt.xlabel('Pixel')
    plt.ylabel('Intensity')
    plt.title(f"Raman at {x_position} um, {y_position} deg")
    plt.grid(True)
    png_name =
f"{date.today()}_{exp_name}_RAMANgraph_{int(x_position)}_xpos_{int(y_position)}_deg.png"
    png_path = os.path.join(subfolder, png_name)
    plt.savefig(png_path)
```

```
    plt.show()
    print("Raman Spectrum Saved!")
    time.sleep(1.0)

def andor_save_csv(subfolder, x, y, exp_name):
    """
    DEPRECIATED: Now prefer dataframe to csv. Save Raman spectra as .csv

    Parameters
    ----------
    subfolder : str
        Subfolder to save Raman .csv file to
    x : array
        Wavelength v
    y : TYPE
        DESCRIPTION.

    Returns
    -------
    None.

    """
    print("Saving as .csv...")
    csv_name = f'{date.today()}_{exp_name}_RAMANtest.csv'
    csv_path = os.path.join(subfolder, csv_name)
    csv_df = pd.DataFrame({"Pixels" : x, "Intensity" : y})
    csv_df.to_csv(csv_path, index=False)
    print(".csv Saved!")
    time.sleep(1.0)

def andor_make_and_save_average_acquisition(ret_val_local, no_of_averages, subfolder,
exp_time, acquisition_label, exp_name):
    """
    Make Raman acquisition, repeat and produce average spectra. Saves each iteration (.sif,
common df) and returns intensities as array.

    Parameters
    ----------
    ret_val_local : bool-like
        Status value (Andor specific) that checks for errors
    no_of_averages : int
        Number of repeats to average over
    subfolder : str
        Data folder to hold all .sif and .csv files
    exp_time : float
        Exposure time for Raman acquisitions
    sif_label : str
        Particular acquisition e.g. "[coordinate]" or "Background"

    Returns
    -------
    ret_val_local : bool-like
        Status value (Andor specific) that checks for errors
    raman_avg_array : array
```

```
    Averaged intensities as array
  raman_single_spectrum_x : array
    Pixels (wavelengths) as array

  """

  # Create blank DataFrame to hold acquisition repeats and averaged data
  raman_avg_df = pd.DataFrame()
  # Repeat and average
  for i in range(no_of_averages):
    print(f"Carrying out {acquisition_label} Acquisition: Spectrum {i+1} of {no_of_averages}.
Wait {exp_time} secs...")
    # Wavelengths and intensities data as list objects
    ret_val_local = andor_make_acquisition(ret_val_local)
    # ---------- Deal with 1D FVB Data (Needs Global Variables) ----------
    print("Handling 1D spectra...")
    imageSize = xpixels    # For 1D image capture
    # imageSize = xpixels * ypixels    # For 2D image capture
    (ret_val_local, arr, validfirst, validlast) = cam_sdk.GetImages16(1, 1, imageSize)
    print("Function GetImages16 returned {}; first pixel = {}; size = {}".format(ret_val_local,
arr[0], imageSize))
    # ---------- Pixel Size Info (Keep in API Format) ----------
    (ret_val_local, xsize, ysize) = cam_sdk.GetPixelSize()
    print("Function GetPixelSize returned {}; X Size = {}; Y Size = {}".format(ret_val_local, xsize,
ysize))
    # ---------- Save Image Data as .sif ----------
```

```
    ret_val_local, sif_file_name = andor_save_siffile_single_position(ret_val_local, subfolder,
exp_time, f"{acquisition_label}_Repeat_{i+1}", exp_name)
    sif_data, info = sif_parser.np_open(sif_file_name)    # Handle .SIF file as numpy array
    print(f"Shape of SIF data = {np.shape(sif_data)}")
    print(f"Metadata = {info}")

    print("Creating intensity and pixel position array...")
    raman_single_spectrum_y = sif_data[0,0,:]  # Raman intensity
    raman_single_spectrum_x = np.arange(1,len(raman_single_spectrum_y)+1)  # Pixel of
sensor

    print(f"Retrieved Raman {acquisition_label} Spectrum!")
    print(f"Intensity = {raman_single_spectrum_y}")
    print(f"Pixels = {raman_single_spectrum_x}")

    # ---------- Add background spectrum to labelled dataframe ----------
    raman_avg_df[f"Signal_{i+1}"] = raman_single_spectrum_y

  # ---------- Calculate mean background ----------
  raman_avg_df["Mean_Signal"] = raman_avg_df.mean(axis=1)
  raman_avg_df["Pixel"] = raman_single_spectrum_x

  # ---------- Extract mean signal as 1D array ----------
  raman_avg_array = raman_avg_df["Mean_Signal"].to_numpy()
  print(f"Raman {acquisition_label} now an array object...")

  # ---------- Save background spectrum to csv in subfolder ----------
```

```
    print("Converting Background Signal to Dataframe...")
    # Save spectrum dataframe as .csv
    raman_avg_df_name = f"{date.today()}_RAMANdata_Raw_{acquisition_label}.csv"
    print("Saving Dataframe to .csv...")
    save_dataframe_to_csv(raman_avg_df, raman_avg_df_name, subfolder)

    return ret_val_local, raman_avg_array, raman_single_spectrum_x

print("========== STARTING UP RAMAN SCAN ==========")
print("Starting SPECTOGRAPH prerequisites...")
ret_val_shamrock = spec_sdk.Initialize("")
print("Function Initialize returned {}".format(
    spec_sdk.GetFunctionReturnDescription(ret_val_shamrock, 64)[1]))
print("SPECTROGRAPH Initialised!")

# ========== 6. INITIALISE SPECTROGRAPH ==========
if ATSpectrograph.ATSPECTROGRAPH_SUCCESS == ret_val_shamrock:
    try:
        # Get spectrograph serial no.
        (ret_val_shamrock, serial) = spec_sdk.GetSerialNumber(0, 64)
        print("Function GetSerialNumber returned : {} Serial No: {}".format(
            spec_sdk.GetFunctionReturnDescription(ret_val_shamrock, 64)[1], serial))

        # Set Slitwidth and check
        print("Setting Slit Width, Index 1...")
        slit_width_intended = 20.0     # In microns
        (ret_val_shamrock) = spec_sdk.SetSlitWidth(0,1,slit_width_intended)
        (ret_val_shamrock, slit_width_actual) = spec_sdk.GetSlitWidth(0, 1)
        print("Function GetSlitWidth returned : {} Slit Width: {}".format(
            spec_sdk.GetFunctionReturnDescription(ret_val_shamrock, 64)[1], slit_width_actual))

        print(f"Successfully set slit width to {slit_width_actual}")

        # Set Grating Position (central wavelength, nm) and check
        print("Setting Wavelength...")
        grating_centre_intended = 926.03
        (ret_val_shamrock) = spec_sdk.SetWavelength(0, grating_centre_intended)

        (ret_val_shamrock, grating_centre_actual) = spec_sdk.GetWavelength(0)
        print("Function GetWavelength returned : {} Wavelength No: {}".format(
            spec_sdk.GetFunctionReturnDescription(ret_val_shamrock, 64)[1],
grating_centre_actual))

        print(f"Successfully set slit width to {grating_centre_actual}")

        # Open shutter and check
        print("Opening Shutter...")      # 0 - Closed, 1 - Open
        (ret_val_shamrock) = spec_sdk.SetShutter(0, 1)
        (ret_val_shamrock, shutter_mode_set) = spec_sdk.GetShutter(0)
        print("Function GetShutter returned : {} Mode: {}".format(
            spec_sdk.GetFunctionReturnDescription(ret_val_shamrock, 64)[1], shutter_mode_set))
        print("Mode: -1=Shutter not set yet, 0=Closed, 1=Open")
```

```
    print(f"Successfully set shutter to {shutter_mode_set}")

  except Exception as e:
    print(f"UH OH! An error occurred in Raman (Spectrograph): {e}")
    print("Safely shutting down Spectrograph and KCube...")
    # Disable Rotation Stage
    disable_rotation_stage(KCube)

    # Disconnect Rotation Stage
    disconnect_rotation_stage(KCube)

    #Shutdown spectrograph
    ret_val_shamrock = spec_sdk.Close()
    print("Function Close returned {}".format(
      spec_sdk.GetFunctionReturnDescription(ret_val_shamrock, 64)[1]))

  finally:
    print("SPECTROGRAPH ready!")
    time.sleep(1.0)


print ("Starting CAMERA prerequisites...")
ret_val = andor_initialise_camera()
print("Function Initialize returned {}".format(ret_val))
print("CAMERA initialised!")
time.sleep(1.0)

# ========== 7. CARRY OUT 3D SPHERICAL RAMAN SCAN ==========
```

```
if atmcd_errors.Error_Codes.DRV_SUCCESS == ret_val:
  try:
    ret_val, iSerialNumber = andor_get_serial(ret_val)

    # ---------- Define iDus Camera Temperature ----------
    ret_val = andor_cool_camera(ret_val, target_temp=-80)

    # ---------- Prepare Acquisition (Keep API Functions) ----------
    print("Preparing Acquisition...")
    ret_val = cam_sdk.SetAcquisitionMode(codes.Acquisition_Mode.SINGLE_SCAN)   #
Single Scan
    print("Function SetAcquisitionMode returned {} mode = Single Scan".format(ret_val))

    ret_val = cam_sdk.SetReadMode(codes.Read_Mode.FULL_VERTICAL_BINNING)   # Read
mode is 1D profile FVB not 2D "IMAGE"
    print("Function SetReadMode returned {} mode = FVB".format(ret_val))

    ret_val = cam_sdk.SetTriggerMode(codes.Trigger_Mode.INTERNAL)
    print("Function SetTriggerMode returned {} mode = Internal".format(ret_val))

    # ---------- Get Detector (Needs Global Variables) ----------
    (ret_val, xpixels, ypixels) = cam_sdk.GetDetector()   # Retrieve detector height and width,
also pixel width
    print("Function GetDetector returned {} xpixels = {} ypixels = {}".format(ret_val, xpixels,
ypixels))

    # ---------- Set Exposure time for camera in secs ----------
```

```
    # Protocol reccomends 10 um slit, 10 sec acquisition, 1% power (ND Filter) for PS standard
    print("Setting exposure parameters...")
    raman_exp_time = 20.0
    ret_val, fminExposure, fAccumulate, fKinetic = andor_set_exp_time(ret_val, raman_exp_time)

    # ---------- Select subfolder to hold raman data ----------
    print("Creating data subfolder...")
    andor_data_folder = create_subfolder(f"{experiment_name_global}") # Hard code for now

    # ========== RAMAN BACKGROUNDING and Si STANDARD CAPTURE ==========
    # 1. Capture Raman Background with "make and save average" script as "raman_bkgnd_spectrum_y" array
    # 2. Save average for that position as a "background" csv
    # Saves raw data repeats and average
    # Capture laser off spectrum with same exposure parameters and average over a few captures

    print("TURN OFF Laser to prepare for dack background capture...")
    wait_for_keyword("laseroffready")   # Wait for "laseroffready" keyword before continuing

    andor_bkgd_no_of_averages = 3
    andor_acq_no_of_averages = 1

    print("Ready to Capture Raman Background!")
    while True:
```

```
        user_input = input("Enter 'raman_bkgd' to perform dark background capture, 'groove' to perform a dance, or 'letsgo' to carry on script:")
        if user_input == "raman_bkgd".lower():
            print("Performing dark background capture...")
            ret_val, raman_background_intensities, raman_background_pixels = andor_make_and_save_average_acquisition(ret_val, andor_bkgd_no_of_averages, andor_data_folder, raman_exp_time, "Background", experiment_name_global)

            print("Plotting dark background...")
            plt.plot(raman_background_pixels, raman_background_intensities)
            plt.title("Dark Raman Background")
            plt.xlabel('Pixels')
            plt.ylabel('Intensity')
            plt.grid(True)
            plt.show()
            print("What do you think?")

        elif user_input == "groove".lower():
            # Perform operation 2 (displaying a little dance)
            print("Performing a little dance for you...")
            dance_function()
            print("Dance completed!")

        elif user_input == "letsgo".lower():
            # Continue script
            print("Continuing script...")
            break
```

```
        else:
            print("Invalid input. Enter 'raman_bkgd' to perform dark background capture, 'groove' to perform a dance, or 'letsgo' to carry on script:")

    #  Plot and save Background Spectrum
    andor_plot_spectra(andor_data_folder, raman_background_pixels, raman_background_intensities, 0.0, 0.0, f"{experiment_name_global}_Background")


    # 3. Capture (Bkgd Corrected) Raman of silicon sample via standalone script
    print("Remember to Capture Raman of Si or PS standard for pixel-wavelength calibration!")
    print("TURN ON Laser to prepare for next capture...")
    wait_for_keyword("laseronready")

    # ========== RAMAN SCANNING MAIN CODE START ==========
    # 1. Capture (Bkgd Corrected) Averaged Raman of each cylinder position with "make and save average" script as array
    # 2. Save average (with iterations) for that position as "x, theta, z" csv - some may be dodgy so can identify erroneous ones
    # 3. Add the Averaged Raman for each position to main dataframe

    # Initialize an empty list to store the main data and index tuples
    print("Creating empty main Raman dataframe and tuples...")
    raman_main_df = []
    raman_x_theta_index_tuples = []
```

```
    # Prepare theta positions to iterate over (previously defined)
    print(f"Theta Positions: {THETA_POSITIONS_LIST}")
    # Prepare x positions to iterate over (previously defined)
    print(f"X Positions: {X_POSITIONS_LIST}")
    # Fixed y position (previously defined)
    Y_POS_RAMAN = ORIGIN_Y  # Grab global y position (fixed for cylindrical scan)
    print(f"Fixed Y Position: {Y_POS_RAMAN}")

    # # ---------- Create subfolder for Raman data (if it doesn't exist already) ----------
    # raman_subfolder = create_subfolder(experiment_name_global)

    # For sphere, capture z and r value at each (x, theta) position

    # For each x position; using global X_POSITIONS_LIST
    for X_POS_RAMAN in tqdm(X_POSITIONS_LIST, desc='Total X Positions', unit='row'):
        time.sleep(1.0)  # Wait for Stage Movement
        # print(f"\rWorking on X: {x_position} um ", flush=True)

        # For each theta position; using global THETA_POSITIONS_LIST
        # Wait till  actions finished before moving to next position
        # Can start from position_list[1:] if homed since this would otherwise produce 3 zero deg positions
        # Therefore THETA_POS_RAMAN is actually the next position to move to
        for THETA_POS_RAMAN in tqdm(THETA_POSITIONS_LIST[1:], desc='Total Theta Positions', unit='angles'):
            # Check current theta position
            CURRENT_THETA_RAMAN = theta_check_position(KCube)
```

```
        # Check current x position
        CURRENT_X_RAMAN, CURRENT_Y_RAMAN = xy_check_position(MM_Core)
        print(f"Currently at theta={CURRENT_THETA_RAMAN}º, y={CURRENT_Y_RAMAN}")

        print("Now pausing script to allow manual focusing via camera...")
        print("Switch mirrors for CAMERA beampath...")
        # Capture z position
        Z_VALUE_RAMAN = manual_focus_pause(MM_Core, 'grab', 'dance', 'asyouwere')

        R_VALUE_RAMAN = get_radius_value("Enter the spacer height (c) mm: ",
Z_VALUE_RAMAN, origin_f)



        # Want to save z and r position for every x_pos and theta_pos
        current_header_raman = np.asarray(['Z','R'])
        current_values_raman = np.asarray([Z_VALUE_RAMAN, R_VALUE_RAMAN])

        # Want header to be list of ['Z', 'R', lambda1, lambda2, ..., lambda512]
        # Want results to be list of [z_position, r_value, I(lambda1), I(lambda2), ...,
I(lambda512)]

        # Pause to change to RAMAN
        print("Radius value recorded! Ensure LASER ON...")
        print("GET READY for RAMAN spectral capture...")
        print("Switch mirrors for RAMAN beampath...")
        wait_for_keyword('raman')
```

```
        # Capture spectrum
        # Capture (Bkgd Corrected) Averaged Raman of each cylinder position with "make
and save average" script as array
        # Save average (with iterations) for that position as "x, theta, z" as .csv - some may be
dodgy so can identify erroneous ones
        # Add the Averaged Raman for each position to main dataframe

        print(f"\rCapturing Raman at X: {CURRENT_X_RAMAN} um; Theta Position:
{CURRENT_THETA_RAMAN} deg ", flush=True)
        # Wavelengths and intensities data as list objects
        raman_position_label =
f"ZR_I(lambda)_{int(CURRENT_THETA_RAMAN)}deg_{CURRENT_X_RAMAN}xpos"
        ret_val, raman_spectrum_y_nobkgdcorr, raman_spectrum_x =
andor_make_and_save_average_acquisition(ret_val, andor_acq_no_of_averages,
andor_data_folder, raman_exp_time, raman_position_label, experiment_name_global)

        raman_spectrum_y = raman_spectrum_y_nobkgdcorr -
raman_background_intensities

        print("Retrieved Andor Raman Spectrum!")
        print(f"Intensity = {raman_spectrum_y}")   # Array for Raman Spectrum
        print(f"Pixels = {raman_spectrum_x}")  # Array for Raman wavelengths



        # Append spectral data to list to be added to dataframe
        full_current_header_raman = np.append(current_header_raman, raman_spectrum_x)
        full_current_values_raman = np.append(current_values_raman, raman_spectrum_y)
```

```
        # Add spectrum to main data list (convert to main dataframe later)
        # Create an index tuple with two levels ('x' and 'theta')
        raman_index_tuple = (CURRENT_X_RAMAN, CURRENT_THETA_RAMAN)

        # Append data and index tuple to the respective lists
        raman_main_df.append(full_current_values_raman)
        raman_x_theta_index_tuples.append(raman_index_tuple)

        #  Plot Spectrum
        andor_plot_spectra(andor_data_folder, raman_spectrum_x, raman_spectrum_y,
CURRENT_X_RAMAN, CURRENT_THETA_RAMAN, experiment_name_global)

        # Convert current position results to labelled dataframe
        andor_current_position_df =
convert_spectrum_to_dataframe(full_current_header_raman, full_current_values_raman,
CURRENT_X_RAMAN)
        # Save spectrum dataframe as .csv
        andor_current_position_df_name =
f"{date.today()}_{experiment_name_global}_RAMANdata_ZR_I(lambda)_{int(CURRENT_THET
A_RAMAN)}deg_{CURRENT_X_RAMAN}xpos.csv"
        save_dataframe_to_csv(andor_current_position_df,
andor_current_position_df_name, andor_data_folder)

        # Move to next theta position
        print("Move to next theta position...")
        theta_absolute_move(THETA_POS_RAMAN , KCube)
        wait_for_theta_stage(KCube)
        print(f"Now at position: {theta_check_position(KCube)}°")

    # Move to next x
    print("Move to next x position...")
    xy_absolute_move(MM_Core, X_POS_RAMAN, Y_POS_RAMAN)
    wait_for_xy_stage(MM_Core)
    x_check, y_check = xy_check_position(MM_Core)
    print(f"Now at position: {x_check} X position")

print ("All positions reached!")
# Now save all data from dataframe into .csv
print("Creating Z R Position Dataframe...")
# Header data list should be defined from last iteration of loop
raman_z_r_lambda_columns = full_current_header_raman
print("Creating X, THETA Multi Index...")
# Create a MultiIndex from the list of index tuples
raman_multi_index = pd.MultiIndex.from_tuples(raman_x_theta_index_tuples,
names=['X', 'THETA'])
print("Creating RAMAN Full 3D Dataframe...")
# Create a DataFrame with the MultiIndex and use the wavelength data as columns
raman_full_3D_dataframe = pd.DataFrame(raman_main_df, index=raman_multi_index,
columns=raman_z_r_lambda_columns)
print(raman_full_3D_dataframe)



# Save Main Dataframe to .csv
```

```
    print("Saving Main RAMAN Dataframe...")
    save_dataframe_to_csv(raman_full_3D_dataframe,
f"{date.today()}_{experiment_name_global}_RAMAN_FULL_DATAFRAME.csv",
andor_data_folder)
    # ========== RAMAN SCANNING MAIN CODE END ==========

    print ("All done! Great job!")
    dance_function()



  except Exception as e:
    print(f"UH OH! An error occurred in Raman Scan (Camera and 3D Scan): {e}")

  finally:
  # ---------- g. Clean up and Shutdown ----------
    print("========== FINISHED RAMAN, SWITCHING OFF iDUS, SPECTROGRAPH, KCube
==========")
    # Disable Rotation Stage
    disable_rotation_stage(KCube)

    # Disconnect Rotation Stage
    disconnect_rotation_stage(KCube)

    print ("Shutting Down Raman CAMERA...")
    time.sleep(2.0)
    ret_val = cam_sdk.ShutDown()   # Shutdown camera
    print("Function ShutDown returned {}".format(ret_val))
    time.sleep(1.0)

    print("Shutting Down Raman SPECTROGRAPH...")
    if ATSpectrograph.ATSPECTROGRAPH_SUCCESS == ret_val_shamrock:
      try:
        ret_val_shamrock = spec_sdk.Close()   # Shutdown spectrograph
        print("Function Close returned
{}".format(spec_sdk.GetFunctionReturnDescription(ret_val_shamrock, 64)[1]))
      except Exception as e:
        print(f"UH OH! An error occurred in Raman (Spectrograph) during final Shutdown: {e}")

    print("Raman All finished!")
    print ("All Done! Good Job!")

  print("========== FINISHED RAMAN SCAN ==========")

print("SWIR and RAMAN ALL DONE!")
```

Appendix F “From Mars to Humans” Handbook

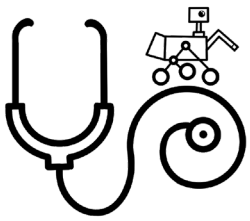

Contents

Learning Outcomes and Key Messages

1. **Diagnostic power of Raman Spectroscopy**
    a. A technique central to the medical technologies developed by the InLightenUs research programme
    b. How Raman spectroscopy uses the tiny vibrations of molecules to give insight into life

2. **The need and benefits of interdisciplinary research**
    a. Visitors will be able to appreciate that the spectroscopic techniques, artificial intelligence, optical physics and light-shaping technologies being developed within the InLightenUs programme work together for transforming the diagnosis of musculoskeletal diseases.
    b. We will demonstrate how NASA’s Mars Perseverance Rover also uses Raman spectroscopy to detect life on Mars.
    c. Interdisciplinary research is intrinsically inclusive as it appreciates and utilises diverse skills; multifunctional teams

3. **Medical innovations go hand-in-hand with amazing discoveries in space**
    a. Visitors will thus journey from ‘Mars to Humans’ to experience that fundamental scientific research, development and innovations can have diverse applications ranging from diagnostics on Earth to finding life on Mars.
    b. Experience how powerful innovations in medical technologies on earth go hand in hand with amazing discoveries in space

Mars to Humans: Labelled Floor Plan

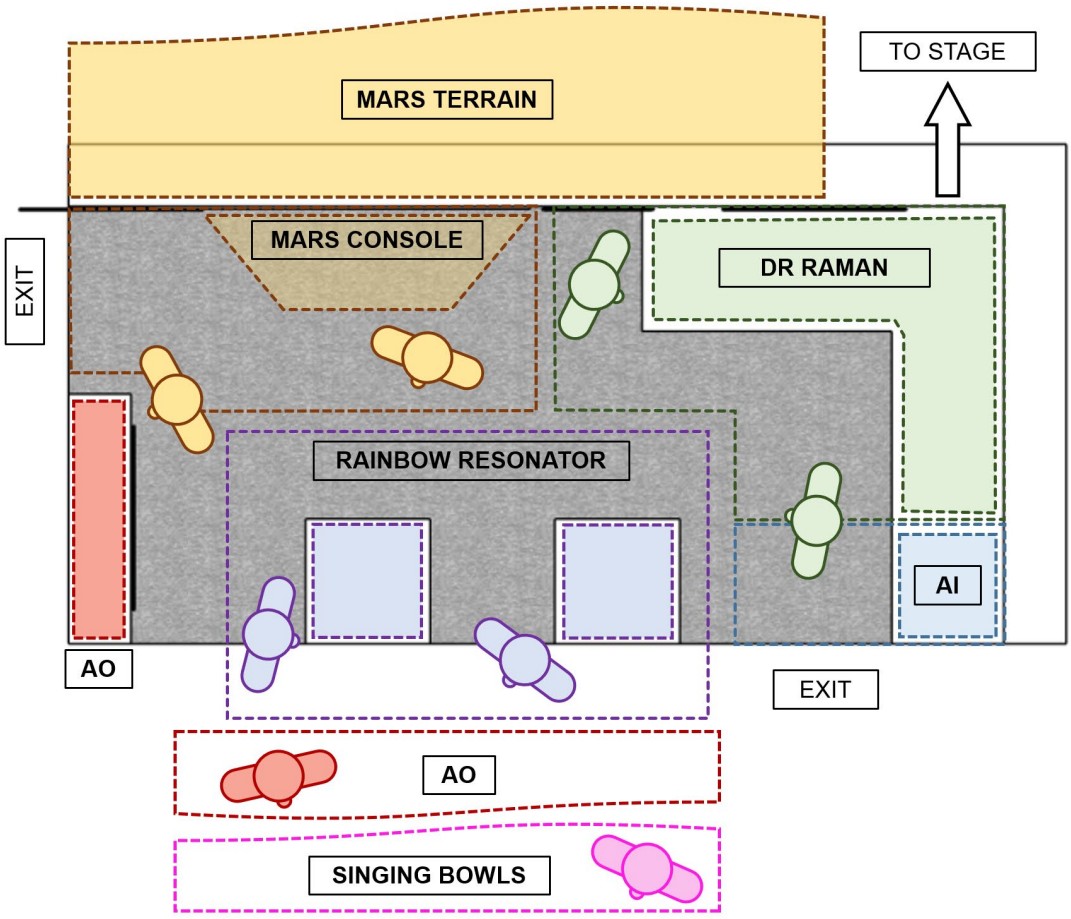

- The entrance to the exhibit is through the middle. The exits are as indicated. One of the blue tables (the left one) will be almost close to the left wall. Except for the aforementioned change the layout is accurate but the relative sizes are approximately to scale.
- The positions of shift members looking after each exhibit are indicated above. This can be less if it is less busy.
- We will rotate between different exhibits and everyone should be able to demonstrate every exhibit
- It is going to depend on how busy things are but the general principle is that we should all have a break every 2-3 hours.

Script and key points for each activity

1. “Singing Bowls”: Acoustic Vibrations

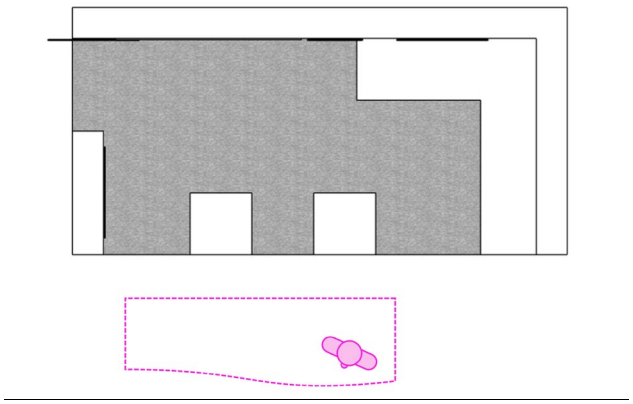

Our aim: to draw public in, enthuse and direct to the main stand

Learning Outcomes: Vibrational resonances can be distinct for different objects. Analogous to matching light energy with resonant frequencies of molecules.

Script and demonstration:

- “Would you like to see something cool?”
- “How can you make a bowl sing?”
- “Can you tell me anything about vibrations?”
- “How loud can we make these bowls sound?” (Use sparingly, please)
- Do you think that the frequency (pitch) will be higher or lower for a larger bowl? (it will be lower - larger bowl means longer wavelength of standing waves, lower frequency)

Demonstrate with one bowl first and then, if time permits, show another sized bowl. Resonant frequency will scale depending on the size of the bowl.Demonstrate to a whole group if possible but obviously do not overlook individuals. This will be useful for our crowd control, engagement and guiding people to queuing for the larger activities.

Teaching points include:

Explain that moving the mallet around the rim creates vibrations and waves that travel around the rim. Resonance occurs when the vibrational frequency matches the natural frequency of the bowl resulting in a loud sound. The effect is similar to that observed by many in wine glasses by running their finger around the rim. The effect is related to the whispering gallery effect in which resonant standing waves are created around the circumference of objects.

- Relate this to light (like the mallet) supplying energy to molecules (like the bowls) to give different colours (frequency or wavelengths) that are measured in Raman spectroscopy.

Measuring Success: Learnt about **vibrational resonances** and excited to learn more about what measuring vibrations can do for us including on Mars to look for life. Aware of how different objects can resonate at different frequencies (sound) which we can measure (hear). Happily go to the Rainbow resonator.

2. “Adaptive Optics Web App”: Aberration Correction

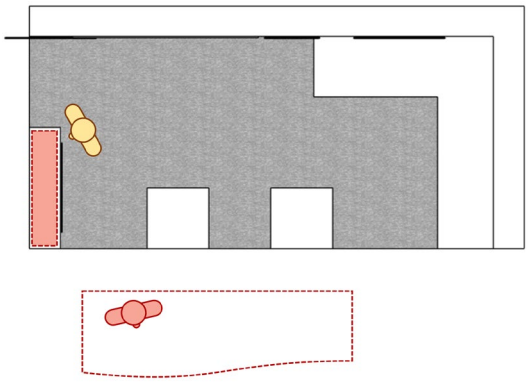

Our aim: To draw public in, enthuse and direct to main stand - mobile tablets with roving demonstrators, plus same interactive demonstrator shown on larger screen.

Learning Outcomes: signals and images can get distorted when passing through material such as the earth’s atmosphere or the human body. We can apply optical corrections to the light to remove these distortions and reveal the object we are trying to image. This technique is called Adaptive Optics. It is used by astronomers to image stars and planets from Earth and we are using it in the InLightenUs project to image inside the body to detect/monitor disease.

Script and demonstration:

The tablet demonstrator is identical to the bigger screen version. The tablet version can be used to draw people into the stand, or if the stand is busy and space limited the demonstration can take place on the tablet alone. At quieter times, for particularly interested visitors, or when explaining to a group, visitors can be guided to the big screen to see a larger version of the demonstration.

The demonstration consists of 3-4 different images of parts of the human body and 3-4 different images of stars and planets. Visitors will look at one image at a time. Initially the image will appear blurred and unrecognizable, using three slider bars the visitor will be able to apply different optical corrections to the image to improve the image and reveal the object. The three optical corrections are defocus, astigmatism and coma.

Visitors can be asked:

- “Can you guess what this picture is?”
- “Can you improve the picture by using the three slider bars? Now can you guess?”
- “Can you find the positions of the slider bars to give you the ‘best’ image?”
- “Do you want to try a different image/example? You can try an example in the body and you can try an example in space”

Explanations:

- Light gets distorted when it travels through the human body by the different tissues/materials present e.g skin, blood vessels, bones, organs. This makes it hard to image inside the body as the images appear blurred and often completely unrecognizable.

- It is possible to correct for this blurring by adding different amounts and types of optical correction. If the right combinations of corrections are added we can remove the blurring and produce good images/reveal the object we are interested in. Similar to how the demonstrator works.
- The lenses used in glasses apply one (sometimes two) types of optical corrections to help people see better. This correction is called defocus (and sometimes astigmatism too). The distortion when imaging inside the body is more complicated and therefore we have to apply many different types of optical corrections to improve our images, not only defocus. The demonstrator shows an example of three corrections we often add - defocus, astigmatism, coma.
- The optical corrections we need to apply to produce good images are different depending on where in the body we are imaging and what we are imaging. Therefore we need to find clever ways to guess/predict the optical corrections that are required.
- Currently we use optimisation approaches to do this - similar to moving the slider bars on the demonstrator and homing in on the 'best' image. We are working on using AI to predict/guess the correction required with a single click of the button.
- This is very important and it would make the correction process much quicker and therefore make it easier to use in hospitals by doctors to detect and monitor disease.
- A similar problem exists in astronomy when scientists want to view stars and planets from the earth. The atmosphere messes up the images and makes the images appear blurred. Astronomers also add optical corrections to improve their images. Similar to the demonstrator.
- This technique is called Adaptive Optics. The astronomers were the first to develop it and then it was used in microscopes to help produce better images. On the InLightenUs project, we are now trying to adapt this method to produce images inside the body.
- It is a great example of one area of science learning from another and different disciplines working together.

Definition of defocus, coma and astigmatism.

- A 'perfect' image is formed by a lens when the object is placed the focal distance away from a lens and when the size of the focal spot formed by the lens is small, symmetrical, and circular.
- Defocus - this optical correction would be the equivalent of not placing the object the focal distance away from the lens. The object appears blurred as it is either too far away or too close to the lens. Adding the defocus optical correction is equivalent to changing the focal length of the lens to bring the object into focus.
- Coma - when coma is present the focal spot is no longer circular but is blurred to one side and produces a comet-like shape. This leads to a distorted and poor quality image. One cause of coma is light entering the lens at an angle.
- Astigmatism - when astigmatism is present the focal spot is no longer circular but elliptical like a rugby ball. At one distance from the lens the rugby ball shaped focal spot will appear horizontal and the image in the vertical direction will be sharp/in focus. At a different distance to the lens the rugby ball shaped focal spot will appear vertical and the image in the horizontal direction will be sharp and in focus. Applying astigmatism makes these two distances overlap so the image is sharp and in focus in the vertical and horizontal direction.

Measuring Success: Understand that signals can get distorted while travelling through a medium and can be corrected. Excited to learn more about technologies that are used in space that can also be used to understand disease. Excited to learn more about how we are using AI to automate and speed up processes.

3. “Rainbow Resonator”: Light-Matter Interactions

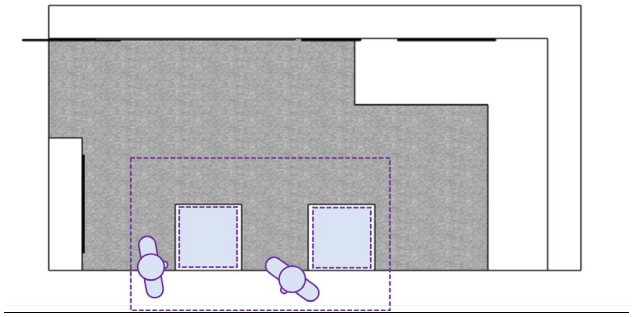

Our aim: Explain the physical mechanism of Raman spectroscopy, to lead on to Mars rover and / or Dr Raman activity

Learning Outcomes: Simple message- shine a laser and different colours come out for each vibrational resonance in a material/molecule. Laser light induced vibrational resonances can lead to distinct colours of light (frequency or wavelengths) which we can measure in the technique of Raman spectroscopy. The pattern of colours scattered by a material is characteristic of its constituent molecules, hence, by using Raman spectroscopy one can identify molecules and hence, whether they correspond to a diseased state or not and whether they indicate life or not.

Script and demonstration:

The two Rainbow Resonator devices will be mounted on floating island type table surfaces at the front edge of the stand. The operator will lead the discussion trying to build on the concept of vibrational resonances demonstrated by singing bowls. Make the connection that while ‘singing bowls’ are a demonstration of the sound-based/acoustic version of Raman spectroscopy where vibrations are triggered by mechanical force (moving the mallet) while in Raman spectroscopy (the tiny) vibrations of molecules are triggered by lasers.

Importantly the colour that we see on the rainbow resonator corresponds to the scattered light from the vibrational resonances of molecules/materials and not the excitation. In Raman spectroscopy a single laser wavelength is used and the different vibrations slice off different amount of energies and thus shift the colour to longer wavelengths. In this demonstration, the laser will be at UV wavelengths (hence, invisible) while the Raman scattering where the vibrational resonances occur are in the blue, green and red.

The main unit will light up accordingly in each of the colours to represent low, medium, and high frequency, respectively, and one of the three atoms will begin to vibrate vigorously (resonance). Chemical bond energies are shown analogously via different spring constants and masses of the “atoms”. (A-level students study IR spectroscopy but may not have the physical understanding of vibrations and how vibrations are measured in IR). The participant can further interact directly with the device via a physical slider from red to green to blue.

The units can change mode via a three-way switch on the rear: “Manual” will respond directly to the slider movement and sleep after a while, “Auto” will cycle through each colour automatically and demonstrate resonance (and “Off” will stop the skull-shaking noises, use liberally, please).

Hook and teaching points include:

Participants will be aware of how different objects can resonate at different frequencies (sound) which we can measure (hear) from singing bowls. The purpose here is to make them understand Raman spectroscopy which is the light-based or optical equivalent of ‘singing bowls’ activity.

- “Have you seen how we can cause things to vibrate / at different frequencies?
- “How else can we make things vibrate?”
- “Did you know that we can use lasers to make things vibrate?”

Molecules need energy to vibrate. This energy can be supplied by light because light is a form of energy - that is why prolonged exposure to light makes a surface feel warm. When molecules interact with lasers they can slice off the amount of energy required to vibrate and scatter the remaining light, causing a shift in the colour of the laser. By measuring the colours scattered and the shifts that have happened one can work out the vibrational pattern of a material/molecule. This vibrational pattern is a characteristic ‘Fingerprint’ of the material. Using the fingerprint of the material one can detect molecules of Life as shown with the Mars Rover or signatures of disease for diagnostics as in Dr Raman demonstration.

- “Light (lasers) is a type of energy”
- Light can trigger vibrations in molecules (bonds start vibrating)
- “Different vibrations slice off different amounts of energy and change the colour (slightly) of excitation light
- The vibrational patterns are characteristic of each material - hence can identify molecules of life on Mars or in Humans

We don’t need to prepare the material in anyway so it lets us measure these properties without touching, modifying or moving them” = it is non-invasive and non-destructive

The scattered colours go from blue to red on the Rainbow resonator. This also means that a UV laser is incident on the box wherein each of the 3 molecules is slicing off (or absorbing) a small amount of energy shifting the colour that is scattered (emitted) to blue, green or red. The blue molecule slices off the least amount of energy while the the red molecule slices off the most energy and hence, shifts the colour by the largest amount.

“This technique is called Raman spectroscopy”

- Name the jargon and use repeatedly
- “Spectrum” = Latin, image; “Skopia” = Greek, observation; C.V. Raman discovered this phenomena in 1928

“We can use this here on Earth to tell us about things like our own bodies or in space to look at life on other planets”

Measuring Success: Understand how vibrational resonances are excited by lasers and can give us the identity of molecules. Excited to learn more about how this is utilised in studies of space environments and to understand disease on Earth. Aware of the term “Raman spectroscopy” how this involves laser light causing characteristic vibrations of materials - alien or otherwise.

4. “Dr Raman”: Diagnostic Power of Spectroscopy

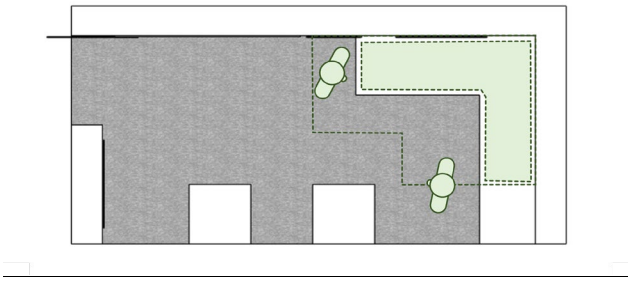

Our aim: Show the diagnostic power of Raman spectroscopy, which is central to the medical technologies being developed in the InLightenUs team

Learning Outcomes:

- Raman spectroscopy uses lasers to produce a “chemical fingerprint” which can be used to identify a material
- This has been applied to study disease in humans as a powerful label free and non-invasive technique for biological sample assessment
- Together with artificial intelligence, optical physics and light-shaping technologies, this can then allow accurate detection of early-stage bone and joint diseases
- The InLightenUs programme is developing technologies that can improve healthcare for older individuals on earth

Script and demonstration:

The physical layout follows the patient's journey from taking biopsy samples in surgery, to spectral measurements in the lab by a biomedical scientist, to diagnosis aided by AI.

For a some audiences it might be a good start to say that we live in an aging population where bone/joint disease problems need to be detected early as then we can do something about it.

1. **Biopsies taken via surgery**

   A demonstrator dressed either in scrubs (clinical surgeon) or white coat (biomedical scientist) can start by using any of the hooks. It does not matter whether the person in scrubs or the white coat does the whole demonstration as one can say add a line that both scientists and clinicians work together to bring about such new methods for the benefit of people (see hooks and teaching points).

   Bone & cartilage looking samples will be taken from the model of our patient (dressed in surgical linen) stored in a container at the hips (pelvis model will show “biopsies” taken from the hip sockets). There will be two types of samples - healthy and diseased. The public member engages with the demonstrator who picks the sample for them and places them on the sample holder. The sample holder will slot into the manually positioned stage on the microscope stand.

Hooks and teaching points include:

- Did you know that a majority of us will get knee or joint pain as we grow up and we may not even realise that things are going wrong?
- Wouldn't it be wonderful if we could know what might go wrong in our bodies (joints) much in advance so that we can take corrective action?
- Scientists must work closely with clinicians and doctors in order to use cutting edge technologies to help patients
- "When a doctor wants to diagnose diseases they can ask for a small piece of tissue to be taken from the body for further tests (biopsy)"
- "These are carefully removed by a surgeon and sent to the biomedical scientist for testing" the test involves cutting the tissue sample into thin slices and then dyeing them in various colourants. Then a trained operator looks down a microscope and makes a judgement (which is subjective)
- Wouldn't it be fantastic if this whole colouring process can be avoided and objective diagnosis made within seconds? Or better if the whole process of taking a biopsy and colouring it etc was avoided?
- While currently we demonstrate how Raman spectroscopy will work with biopsy samples, it can be done directly on the patient which is one of the goals in the larger InLightenUs project.

2. Raman spectroscopy measurement

The sample holder is inserted into a slot built in a light proof box on the Dr Raman microscope stage. The participant is asked to press a button for analysis, they can press either button "1" and then "2" in turn (or the other way round) to take spectra of both samples.

In reality, the "biopsy" samples are spoofed and spectra will actually be taken from clear plastic window embedded into the sample holder. This means the Raman signal will be robust and intense. Results will then return "1 = healthy" & "2 = diseased" or vice versa, depending on the sample holder chosen. This should be random between participants. Note that the samples will look identical and hence, we can assert that while to the eye things may look identical Raman spectroscopy based analysis can pick up differences.

The main thing is that the demonstrator should ensure the sample holder is positioned correctly over the microscope objective lens (effort has been that this is automatically taken care of by the manual stage with two preset positions). Also note that the 'biopsy' samples only look the part and hence, their positioning is not super important.

Hook and teaching points include:

- This technique uses lasers to detect tiny vibrations of different molecules and provides a "chemical fingerprint"
- "If we can test and see what chemicals are in a piece of tissue we can start to detect disease fingerprints"
- The biopsies can be taken directly from the patient and measured without having to add any chemicals to the sample
- Raman spectroscopy can make the invisible differences become visible

3. **Reading spectra for diagnosis**

The demonstrator will guide the participant through the interpretation of spectra to identify which sample is healthy and which is diseased.

Spectra are shown after each acquisition as part of the graphical user interface (Python) and the participant must now identify which biopsy was healthy and which diseased by its spectrum.

Teaching points include:

- Manual, human interpretation engaging the participant by looking at differences between the spectra and talking to the healthy and diseased spectra that will be displayed on the screen.
- This is indicative of how Raman spectroscopy can be used for assessing the health of the patient
- "We look closely at the fingerprint of the biopsy to tell if the part of the body is healthy or diseased."
- Manual human input can then be aided by powerful AI interpretation in the next stage. Hence, advisable to not spend too much time on the interpretation and move to triggering the AI graphic animation.

Measuring Success:

Understanding of how Raman spectroscopy can be used for disease diagnosis. Awareness that this work requires close collaboration between scientists (physicists, biochemists) and clinicians. Prepped for learning how AI interpretation of results can aid this process.

Further talking points:

Biophotonics goals: "Faster, early, affordable, accurate detection and monitoring; Non-invasive, non-destructive, label-free multiscale (nm to cm) and multimodal imaging-based diagnostics"

Raman spectroscopy is the fastest growing spectroscopic technique in the world:

- No sample preparation needed
- Non-invasive and non-destructive
- Quantitative readout
- Water does not interfere – brilliant for biology, medicine

5. “Artificial Intelligence Web App”: Diagnostic Interpretation of Spectra

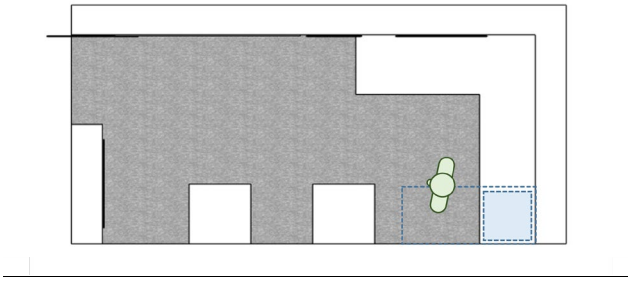

***Note: This section should be read as a continuation of Section 4 (Dr Raman) as the demonstrator of the diagnosis part will run this as well.**

Our aim: Show how AI technology can be used to speed up the detection process.

Learning Outcomes:

Deep Neural Network can automatically determine the biologically relevant wavelengths of raw spectra to help with disease diagnosis.

AI can be used to quickly identify the ‘signatures’ produced by the spectrometer. The matching of signatures to different materials that is done by humans in section 4, can be done automatically in the computer using AI. The computer looks at the shapes of the ‘signatures’ and where peaks occur and uses these to determine the type material. For example, by looking at these signatures, the AI will be able to tell automatically if the material in a hip joint is healthy or diseased, if arthritis is present and the type of arthritis that is present.

Script and demonstration:

The web app will be displayed on a desktop monitor immediately next to Dr Raman, with our narrative describing how the spectra will now be fed into the neural network for diagnosis using AI. Demonstrators will interact directly with the web app via a numeric keypad mapped in the following way:

Keypress no. 1 : diseased

Keypress no. 2 : healthy

Keypress ‘Enter’: blank state

Demonstrators will press 1 on the numeric keypad if the sample shown is diseased and 2 if the sample is healthy following the results from Dr Raman. Press ‘Enter’ after the demo to go back to blank state.

The monitor will show how the important features of the spectra are propagated through the network and a prediction is made at the end to indicate if it's a healthy or diseased sample.

Explain that neural network can be applied to raw spectra and learn to determine the most biologically relevant wavelengths that help in the decision making of disease diagnosis:

1. After we obtain the spectra from the spectroscopy, we feed the raw spectra into a trained network (which is a Machine Learning algorithm that has been trained to recognise and process these spectra features to make predictions).
2. The trained neural network will propagate the spectra information through the layers to process the relevant features to contribute to the diagnosis of the disease at the output layer.

Talking points

Adults/teenagers [long version]:

- "Anyone heard of AI? (Audience: It's very clever.) What does it do?"/"How does the neural network work?"
- "Think of it like how the brain works. We learn through past experiences to make a decision. This is the same for the neural network."
- "For example, you want to identify cats and dogs. How would you train an AI to do that? What could you possibly do? (Audience: GIve it a lot of samples/pictures)"
    - "That's exactly what I need if I want my AI model to determine whether my cartilage is healthy or not. We feed the AI with lots of spectra detected from the cartilage. Most of you will have very similar spectra, but some may have weaker cartilage, in that case, they will have different states of spectra. What we want to be able to do is to predict that."
- "Shall we see if the AI can predict the bone state from the spectra? Which sample shall we analyse first? (if sample is diseased, keypress 1, else keypress 2)" [*Audience will have both healthy and diseased samples, do both]
- "Look at these spectra and you can see all these different peaks. Remember we talked about being able to identify cats and dogs. How do we identify them? We identify them based on their appearance like colour and shape, right? So if I want to identify if my spectrum is healthy or not, we look at these peaks (features/signatures).
- "What the AI/neural network will do is they will learn from these spectra samples and it will start to adjust the weights of the connections between neurons in order to extract these peaks/features to tell you whether the spectra is healthy or not (controlling the strength and the significance of information passed between them)."
- Neural network is a powerful tool that has been successfully applied to various tasks because it can learn from experience/large amounts of data to make predictions on unseen data.

Kids [short version]:

- "Let's think of the neural network as a robot. You want your robot to recognise cats and dogs. What would you do to train your robot to recognise them? You show your robot lots of pictures of cats and dogs. The robot then learns from the shape, the colour of the animal to recognise the animals correctly."
- "Once the robot has learned enough, you can give it a new picture of either a dog or cat and ask it to guess at it."
- "This is the same for this work. Look at this spectrum, many healthy people will have similar spectra, but some people may be weak and have very different spectra.
- "Shall we see if the AI can predict the bone state from the spectra? Which sample shall we analyse first? (if sample is diseased, keypress 1, else keypress 2)" [*Audience will have both healthy and diseased samples, do both]
- Just like how your robot can recognise cats and dogs from their appearances, what the robot will do is they will learn from these differences (the peaks/features), do its magic and tell you if your cartilage is healthy or not."

How far are we from using AI in a real world setting in the medicine field?

"We have already implemented AI in the classification of spectra from 19 Osteoporosis and 45 Osteoarthritis patients and showed that the neural network can automatically learn and recognise the spectra peaks to contribute to the disease diagnosis. We are currently working to publish this work."

Measuring Success: Excited to learn more about what neural network can do to solve the various tasks in life and being applied in the medical field for disease diagnosis.

6. “Mars Rover”: Searching for Alien Life with Spectroscopy

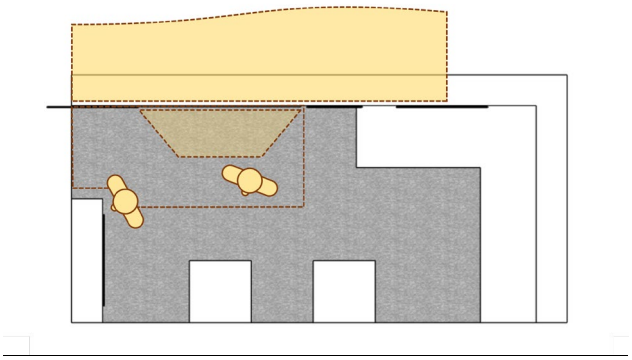

Our aim: Show how Raman spectroscopy is being used on Mars to find potential/past signs of life

Learning Outcomes:

- Raman spectroscopy uses lasers to produce a “chemical fingerprint” which can be used to identify a material
- Since life depends and uses molecules, one can identify molecules of life
- This has been applied to detect signs of life on Mars
- Perseverance rover has cutting edge detection technologies: “SuperCam” mounted on the body and “SHERLOC” on the arm both host Raman spectrometers to analyse samples on the surface of Mars
- These technologies are created through interdisciplinary approaches
- The InLightenUs programme is developing technologies that can improve healthcare for older individuals on earth, which are also enabling the search for alien life.

Script and demonstration:

The physical layout is in two parts: the console where the participant and demonstrator observe (in the stand) and remotely operate the rover, and the Martian terrain (on the stage) upon which the rover will drive, looking for “alien life”.

Participants will be directed to queue for a go at controlling the rover as part of our "Finding Life" game, a time-limited session driving around a pre-determined track. The rover will approach the targets and take spectra to see if each contain "life".

1. **"Mission Control" Console**

A table-top mounted interface will house the joystick and large buttons for the participant to sit at and use to control the rover in three modes: wheel movement for driving, robotic arm movement for aligning the spectrometer, and spectral acquisition where the Raman laser fires and captures the "alien fingerprint". Some controls are accessible only to the demonstrator to ensure laser safety and ensure no damage comes to the rover due to poor handling. This will also include an emergency stop which will shut-down the rover immediately.

1.a. Participant Controls

The rover's movements are controlled by a flight-stick style joystick on the Console.
The wheel movement mode is triggered by pressing the large green “wheel” button below the screen, and the rover will move forward / backward, and turn left / right. The screen will display the POV camera mounted on the rover body ("SuperCam").
The arm movement similarly starts with its (yellow) button pressed, and the spectrometer will move up / down, left / right. The screen will display the camera mounted next to the spectrometer ("SHERLOC and WATSON").
The wheels cannot be moved in arm mode and vice versa.

The rover's spectrometer will take a Raman spectra when the orange “laser” button is pressed. The motors will be locked to ensure no movement during laser operation and a dead-man switch ensures the demonstrator must confirm correct alignment before the laser fires.

Teaching points include:

- Scientists of different disciplines must work together to make and send a rover like this to operate on Mars, 140 million miles away
- "Can you tell me what kinds of scientists / engineers would be a part of the rover team?"
- “Our team is made up of physicists, chemists, biologists, computer scientists etc.”
- We have used a number of tools to build our model rover: 3D CAD, 3D printing, programming (Python, Java, Arduino), Single-board computers (SBCs) and microcontrollers (Raspberry Pi and Arduino), laser cutting
- "Have you heard of / used in school [technique]?"

1.b. Demonstrator Controls

The console buttons and joystick are mirrored on an Xbox controller held by the demonstrator. This will be wireless primarily (long charging cable available when low battery) and held at all times by the demonstrator. The controller joystick has the same functions as that of the console to allow the demonstrator to take over control of the wheels / arm when necessary. Control can be taken and restored between the demonstrator and participant at the press of a button. This allows some aid for finer positioning of the rover if the participant is struggling.

Also included is a dead-man switch for safe operation of the laser and emergency stop to kill power to the rover when necessary.

1. The **dead-man switch** means the demonstrator must first confirm the spectrometer output is pointed directly at the target and away from anyone’s line of vision (should be fine if people remain within the exhibit bounds, in front of the backdrop). Satisfying this, the Xbox controller **trigger “RT” must be fully depressed**, the participant presses the “laser” button, and then the Raman spectra will be triggered.
2. The **emergency stop** is triggered by pressing and holding shoulder buttons **“RB” + “LB” simultaneously**. This will kill power to the rover, and the activity will need to be reset (~5 mins). Safety is paramount so **please do not hesitate** to use the emergency stop.

2. "Finding Life" Game

2.a. Objectives

The rover will be driven around the simulated Mars terrain on the stage in order to scan targets and identify which contain “life”. These will be plastic targets made visible via LEDs, and observed through the large window cut-out on the exhibit backdrop.

Participants must drive the rover from the starting point to each target (wheel mode), position the arm so that the spectrometer is pointed at the target (arm mode), and press the laser button. Spectra will then display on the console screen to allow confirmation of the “life” fingerprint or a “no life” fingerprint. The game will end either if the rover finds “life” or time runs out.

Teaching points include:

- Perseverance is searching for signs of past microbial life by analyzing rocks and soil samples for biosignatures - organic molecules and microbial fossils
- “How can you tell if something is alive?”
- “MRS GREN”; NASA say: “A self-sustaining chemical system capable of Darwinian evolution.”

- Perseverance Rover is packed full of the latest and best sensors for detecting fingerprints that indicate astrobiology
- "Look carefully at the rover: what do you notice about the wheels / arm?"
- “SHERLOC spectrometer and WATSON camera in the arm of Perseverance are looking for chemical fingerprints that alien life might leave behind”

- The same technology operated on Mars to look for alien life is being used on Earth to study human life and diagnose diseases
- “Can you tell me what you have learned today about Raman spectroscopy?”
- Name the jargon and repeat the key words to allow this to stick, “…Raman spectroscopy, where we use lasers to cause vibrations to identify materials”

2.b. Scoring

Our narrative describes a limited amount of power reserve for the rover to operate. This means participants have a time limit in order to complete the course and find “life”. Participants under the age of 10 (Key Stage 1 and 2) have 5:00 mins, and over 10’s will have 4:00 mins. High scores are measured by how much time remains upon completion. (This handicap may have to be adjusted should we find practical issues on the day).

Participants are identified by a numbering stamp on their exhibit card and recorded in our database. The scoring time will then be uploaded to a live or quasi-live leaderboard accessible via the QR code printed on the exhibit card. The overall competition winner will receive space art from Jackie, daily winners a smaller prize, likely Lego.

- Gamifying the activity should allow for quick turn-around times and engagement.
- Perseverance makes its own electrical power using its thermoelectric generator heated via radioisotope plutonium
- "Can you see the large box coming out of the back of the rover?"

Extra notes:

The Rover's mission objectives include:

- Collecting and storing rock and soil samples for later retrieval and return to Earth.
- Searching for signs of past microbial life by analyzing rocks and soil samples for biosignatures, such as organic molecules and microbial fossils.
- Studying the geology and climate of Mars, including the planet's past habitability and potential for future human exploration.
- Testing new technologies, such as the Mars Oxygen In-Situ Resource Utilization Experiment (MOXIE), which aims to produce oxygen from the Martian atmosphere to demonstrate the feasibility of producing oxygen for future human missions.

SHERLOC Raman spectrometer findings thus far:

- Mars has a liberal dosing of the building blocks of life, and that these organic molecules are resilient
- Organic carbon has been found - aromatics (molecules with ring structures)
- Organics in sulfate deposits have been found - this is the latest Sept 2022. These are associated with fossilized microbes on Earth.

Measuring Success

Excited to learn more about how discoveries in space are facilitated by technologies used on Earth for biomedical applications Aware that this work requires close collaboration between various scientists and engineers: physicists, chemists, biologists, geologists etc etc.

Fielding further **space-science specific questions:** NASA provide a very nice 3D model and explanation of Perseverance - SuperCam and SHERLOC are well described https://mars.nasa.gov/mars2020/spacecraft/rover/ UK Space Agency are currently running "I'm a Space Person" and "Space for Everyone" tours over summer 2023 - do point toward their resources: https://spaceperson.co.uk/rocket-tour/

(Though of course we hope the questions will be more related to our science)